Development and simulation of a highly integrated Solid Oxide Fuel Cell

Von der Fakultät für Maschinenbau
der Technischen Universität Carolo-Wilhelmina zu Braunschweig
zur Erlangung der Würde eines

Doktor-Ingenieurs (Dr.-Ing.)

genehmigte Dissertation

von:	Dipl.-Phys. Christian Wesemeyer
aus (Geburtsort):	Peine
eingereicht:	26. Januar 2015
mündliche Prüfung am:	19. Juni 2015
Vorsitzende:	Prof. Dr.-Ing. Ulrike Krewer
Berichterstatter:	Prof. Dr. techn. Reinhard Leithner
	Prof. Dr.-Ing. Otto Carlowitz

2015

Contents

List of Tables

List of Figures

Acronyms

$k_{\text{TURB}} - \omega_{\text{TURB}}$	$k_{\text{turb}} - \omega_{\text{turb}}$ turbulence model
$k_{\text{TURB}} - \varepsilon_{\text{TURB}}$	$k_{\text{turb}} - \varepsilon_{\text{turb}}$ turbulence model
0D	Zero(0)-Dimensional
1D	One(1)-Dimensional
2D	Two(2)-Dimensional
3D	Three(3)-Dimensional
AB	Active Boundary (electrochemically active region around the electrolyte, represented by a boundary plane)
AE	Arrhenius Equation
AFC	Alcaline Fuel Cell
ANSYS	ANalysis SYStem, Inc.
AR	Autothermal Reformation
BC	Boundary Condition
BE	Balance Equation
BFC	Biological Fuel Cell
BRIC	Brazil, Russia, India, and China
BVE	Butler-Volmer Equation
CAD	Computer Aided Design
CEE	Chapman-Enskogg Equation
CFCL	Ceramic Fuel Cells Limited
CFD	Computational Fluid Dynamics
CFX	CFD simulation software
CHP	Combined Heat and Power
CPOX	Catalyzed Partial OXidation
CPU	Central Processing Unit
CRC	Chemical Rubber Company; today a publishing group specialized on scientific and technical literature
CV	Control Volume
DBE	Darcy-Brinkman Equation
DCFC	Direct Carbon Fuel Cell
DE	Darcy Equation
DETCHEM	DETailed CHEMistry

DF-SOFC	Direct Flame SOFC
DGM	Dusty Gas Model
DIR	Direct Internal Reformation
DMFC	Direct Methanol Fuel Cell
DR	Dry Reformation
DTU	Danmarks Tekniske Universitet (engl.: Technical University of Denmark)
ER	External Reformation
ESC	Electrolyte Supported Cell
EU	European Union
FACTSAGE	Thermochemical software and database package
FDM	Finite Difference Method
FEM	Finite Element Method
FVM	Finite Volume Method
GDC	Gadolinium Doped Cerium $\left(Ce_{0.8}Gd_{0.2}O_{2-\omega}\right)$
GEMT	Generalized Effective Media Theory
GND	GrouND (electrical reference potential)
HEXIS-CELL	Heat Exchanger Integrated System-cell
HPC	High Potential Case
HPD-SOFC	High Power Density-SOFC
IC	Interconnect
IIR	Indirect Internal Reformation
IP-SOFC	Integrated Planar-SOFC
IR	Internal Reformation
IT-SOFC	Intermediate Temperature-SOFC
IWBT	Institut für Wärme und Brennstofftechnik (engl.: institute of heat- and fuel-technology)
JANAF	Joint-Army-Navy-Air Force thermochemical tables
KIT	Karlsruher Institut für Technologie (engl. Karlsruhe Institute of Technology)
LFFC	Laminar Flow Fuel Cell
LHK	Langmuir-Hinshelwood Kinetics
LI	Langmuir Isotherm
LPC	Low Potential Case
LSCF	Lanthanum Strontium Cobalt Ferrite $\left(La_{0.2}Sr_{0.8}Co_{0.2}Fe_{0.8}O_{3-\omega}\right)$
LSM	Lanthanum Strontium Manganite $\left(La_{0.84}Sr_{0.16}MnO_3\right)$
LTA-SOFC	Liquid Tin Anode SOFC

MAFC	Metal Air Fuel Cell
MATLAB	MATrix LABoratory
MAX	MAXimal value
MCFC	Molten Carbonate Fuel Cell
MEA	Membrane Electrodes Assembly ≡ PEN
MHI	Mitsubishi Heavy Industries
MIEC	Mixed Ionic and Electronic Conductor
MOLB-TYPE SOFC	Mono Layer Block Built type SOFC
MSM	Maxwell-Stefan Model
MT-SOFC	Micro-Tubular-SOFC
NASA	National Aeronautics and Space Administration (space agency of the United States of America (USA))
NEE	Nernst-Einstein Equation
NPE	Nernst-Planck Equation
NSE	Navier-Stokes Equation
PAFC	Phosphoric Acid Fuel Cell
PDE	Partial Differential Equation
PEMFC	Proton Exchange Membrane Fuel Cell
PEN	Positive electrode Electrolyte Negative electrode ≡ MEA
POX	Partial Oxidation
PT-SOFC	Planar Tubular-SOFC
PTPPC	Physical and Thermodynamic Properties of Pure Chemicals data compilation
REC	REference Case
RMS	Root Mean Square
RZK	Roginskij-Zel'dovic Kinetics
SBL	Stefan-Boltzmann Law
SC-SOFC	Single Chamber-SOFC
SOFC	Solid Oxide Fuel Cell
SPFC	Solid Polymer Fuel Cell
SR	Steam Reformation
SS-SOFC	Segmented-in-Series-SOFC
SSC	$Sm_{0.5}Sr_{0.5}CO_{3-\chi}$
SST	Shear Stress Transport
TEC	Thermal Expansion Coefficient (see also γ_{th})
TPB	Three Phase Boundary
UCEM	Unit Cell Electrochemistry Model
USA	United States of America

USSR	Union of Soviet Socialist Republics
WGS	Water-Gas-Shift
YSZ	Yttrium Stabilized Zirconium
ÖPNV	Öffentlicher Personen NahVerkehr (engl.: public transport)

Chemical elements, compounds and ions

BaO	barium oxide
Ba	barium
CH_2	ethyl intermediate
CH_3OH	methanol
CH_3	methylium
CH_4	methane
CH	methylidyne radical
CO_2	carbon dioxide
CO_3^{2-}	carbonate
CO	carbon monoxide
CaO	calcium oxide
Ca	calcium
Ce	cerium
Cr	chrome
C	carbon
H^+	hydron (positively charged hydrogen ion)
H_2O	water
H_2	(molecular) hydrogen
H_3O^+	hydronium
H_3PO_4	phosphoric acid
$HCOOH$	formic acid
HCO	hydrocarbon intermediate
H	hydrogen
KOH	potassium hydroxide
K	potassium
$La_{1-\chi}Ca_\chi CrO_3$	lanthanum calcium chromite
$LaCrO_3$	lanthanum chromite
La	lanthanum
Li	lithium
$M_2'O_3$	metal oxide, with M' as wildcard for various metals
MO_2	metal oxide, with M as wildcard for various metals
M	wildcard for a metal in a metal oxide
N_2	(molecular) nitrogen
Na_2CO_3	sodium carbonate

Na_2O	sodium oxide
NaOH	sodium hydroxide
NiO	nickel oxide
Ni	nickel
O^{2-}	two times negatively charged oxygen ions
O_2	molecular oxygen
OH^-	hydroxide
OH	hydroxyl radical
O	oxygen
Pd	palladium
P	phosphor
Pt	platinum
Ru	ruthenium
SO_2	sulfur dioxide
Sc	scandium
SiO_2	silicon dioxide
SrO	strontium oxide
Sr	strontium
Y_2O_3	yttrium oxide
Yb	ytterbium
Y	yttrium
ZnO	zinc oxide
Zn	zinc
ZrO_2	zirconium dioxide
Zr	zirconium

Cyrillic symbols

Б	target function in a Legendre-transformation	
Ъ	effective TPB length per effective surface	m/m^2
Ц	wildcard for model parameters	var.
Д	original function in a Legendre-transformation	
Э	pseudo-random number	
$Ь_{scat}$	scattering diameter	Å
Г	wildcard for model parameters	var.
Ъ	interaction parameter for thermal conductivity	
И	adsorption function	
Ъ	dimensionless model parameter for Roginkij-Zel'dovich kinetics	
К	wildcard for model parameters	var.
$Л_{stoich}$	ratio relative to stoichiometry (index specifies media)	
Н	wildcard for model parameters	var.
Ш	local adsorption probability	$(m^3/mol)^x/m$
Ц	empirical correlation formula	var.
Я	relative number of a species belonging to percolating clusters	
Ю	wildcard for calculated quantities in fitting equations	var.
Ж	canonic variable of the original function in a Legendre-transformation	
З	canonical variable of a function in a Legendre-transformation	
ѳ	oxygen non-stoichiometry coefficient	
ђ	number of moles of a quantity in a chemical compound	
є	exchange energy	J
и	fraction of the maximal current density	
k	permeability	m^2
љ	standard deviation	
ҙ	number of moles of a quantity in a chemical compound	
ы	number of elementary charges	
ъ	number of elementary charges	

Greek symbols

If not otherwise noted, the values of the constants are taken out of Gerthsen's textbook on physics (Meschede 2006).

Γ_{visc}	dynamic viscosity	kg/m s
Γ	exchange coefficient	1/m s
Ω_{coll}	diffusion collision integral	
Θ_{perc}	surface coverage	1/100 %
Ξ_{mol}	surface site density of adsorption places	mol/m^2
α_{th}	heat transfer coefficient	W/m^{2}K
α	general transfer coefficient	var.
β	symmetry factor of the energy barrier	
χ	number of moles of a quantity in a chemical compound	
δ	dipole moment	Debye
η	overpotential	V
ε_0	electric permittivity of free space $\left(\varepsilon_0 = 8,854 \cdot 10^{-2}\ \text{A s/V m}\right)$	A s/V m
ε_{rad}	emissivity	1/100 %
$\varepsilon_{\text{turb}}$	isotropic dissipation rate	m^2/s^3
$\eta_{\%}$	efficiency	%
γ_{th}	thermal expansion coefficient	1/K
κ	reaction order	
λ_{En}	thermal conductivity	W/m K
$\mu_{\text{elchem}\blacktriangle\text{mol}}$	molar electrochemical potential	J/mol
μ_{mol}	molar chemical potential	J/mol
ν	stoichiometric coefficient	
ω_{turb}	characteristic frequency of the turbulent curls	1/s
ϕ	electric potential	V
π	number pi ($\pi \approx 3.1413$)	
ι	radius	m
$\rho_{\text{Mass}\blacktriangle\text{vol}}$	volumetric mass density	kg/m^3
ρ_{vol}	volumetric density	1/m^3
σ_{rad}	Stefan-Boltzmann constant $\left(\sigma_{\text{rad}} = 5.67 \cdot 10^{-8}\ \text{W/m}^2\,\text{K}^4\right)$	W/m^2 K^4
$\underline{\underline{\sigma}}$	electric/ionic conductivity	S/m

τ	residence time	s
τ	tortuosity	
Φ	generalized conserved quantity	
Υ	source term	1/s
σ_{ad}	surface site for adsorption	
ξ	arbitrary constitutive fluid property	var.
ζ_{ad}	adsorption coefficient	var.

Indices

Indices starting with a capital letter are used in this study to indicate if a quantity is either expressed as mass ($_{\mathrm{Mass}}$ in kg), moles ($_{\mathrm{Mol}}$ in mol), volume ($_{\mathrm{Vol}}$ in m^3), energy ($_{\mathrm{En}}$ in J), or charge ($_{\mathrm{Ch}}$ in C). Density-like expressions are indicated by indices too. Here lower case letters are applied to distinguish references to mass ($_{\mathrm{mass}}$ in 1/kg), moles ($_{\mathrm{mol}}$ in 1/mol), volume ($_{\mathrm{vol}}$ in $1/m^3$), and normalized percents ($_{\%}$ in 1/100 %). Domains are emphasized by an abbreviation in capital letters (e.g. a quantity inside the electrolyte is indicated by $_{\mathrm{ELE}}$). The definition of the standard conditions (25 °C, p = 1013 hPa, pH = 0, ionic activity = 1) is taken from the CRC handbook (Lide 2010).

0	reference condition, e.g. standard conditions
1	counting number
2	counting number
3	counting number
4	counting number
5	counting number
6	counting number
7	counting number
$\mathcal{A}$	species A
ANO	anode
$\mathcal{B}$	species B
Boudouard	Boudouard reaction
CAT	cathode
CH_4	methane
$\mathcal{C}$	species C
CO_2	carbon dioxide
CO	carbon monoxide
CV	control volume
Carnot	Carnot
C	carbon
C,ad$_{\blacktriangle}$Ni	carbon adsorbed/deposited on nickel surface
Ch	charge
Coul	Coulomb
ELE	electrolyte
En	energy / heat
H_2	molecular hydrogen
H_2O	steam
H	hydrogen

Knud	Knudsen diffusion
LSCF	located at the LSCF surface
LSM	located at the LSM surface
Mass	quantity expressed in mass
Mol	quantity expressed in moles
N_2	molecular nitrogen
N	nitrogen
Nernst	Nernst
Ni	located at the nickel surface
O_2	molecular oxygen
O^{2-}	two times negatively charged oxygen ions
O	oxygen
Ohm	ohmic
TPB	located at the three-phase-boundaries
Volt	voltage
Vol	volume
YSZ	located at the YSZ surface
a	fitting coefficient
act	activation / activity
(ad,LSM)	adsorbed at LSM location
(ad,Ni)	adsorbed at nickel location
(ad,ς)	adsorbed at adsorption site σ_{ad}
ad	adsorbed / adsorption
air	air
arb	arbitrary
ave	average
back	backward
cata	catalyst
cell	cell / fuel cell
chem	chemical
χ	number of moles of a quantity in a chemical compound
conc	concentration
cond	conduction
cont	contact
convec	convective
conv	converted
crit	critical
ɒ	number of moles of a quantity in a chemical compound
ʒ	number of moles of a quantity in a chemical compound
des	desorption
dia	diameter
diff	diffusive
↓	low
eff	effective
elchem	electrochemical

el	electronic
equi	equilibrium
exch	exchange
fl	fluid
forw	forward
fuel	fuel
(g)	gaseous, gas phase
grav	gravity
i	counting index
int	internal
in	inflow, input, inward
ion	ionic
j	counting index
k	counting index
kin	kinetic
l	counting index
local	local
mass	referenced to mass
max	maximal value, maximum
mech	mechanical
min	minimal value, minimum
mole	molecular
mol	referenced to moles
nucl	nuclear
out	outflow, output, outward
%	normalized percents
pore	pore
pot	potential
prov	provided
rad	radiative, radiation
reac	reaction
red	reduced
ref	reference state
rev	reversible
(s)	solid, solid phase
simpl	simplified
species	species
surf	surface
th	thermal
tot	total
↑	high
vol	volumetric
wall	wall
x	x-direction in a Cartesian coordinate system
y	y-direction in a Cartesian coordinate system

y_i	molar fraction of the i-th species
z	z-direction in a Cartesian coordinate system

Latin symbols

Indices starting with a capital letter are used in this study to indicate if a quantity is either expressed as mass ($_{\mathrm{Mass}}$ in kg), moles ($_{\mathrm{Mol}}$ in mol), volume ($_{\mathrm{Vol}}$ in m^3), energy ($_{\mathrm{En}}$ in J), or charge ($_{\mathrm{Ch}}$ in C). Density-like expressions are indicated by indices too. Here lower case letters are applied to distinguish references to mass ($_{\mathrm{mass}}$ in 1/kg), moles ($_{\mathrm{mol}}$ in 1/mol), volume ($_{\mathrm{vol}}$ in $1/m^3$), and normalized percents ($_{\%}$ in 1/100 %). Domains are emphasized by an abbreviation in capital letters (e.g. a quantity inside the electrolyte is indicated by $_{\mathrm{ELE}}$). The definition of the standard conditions (25 °C, p = 1013 hPa, pH = 0, ionic activity = 1) is taken from the CRC handbook (Lide 2010).

$A_{\mathrm{cata}\blacktriangle\mathrm{mass}}$	effective surface area per mass catalyst	m^2/g
$A_{\mathrm{eff}\blacktriangle\mathrm{vol}}$	effective surface per cubic meter	m^2/m^3
$\mathcal{A}$	species A	
A	area	m^2
$\mathcal{B}$	species B	
$\mathcal{C}$	species C	
$\underline{\underline{D}}_{\mathrm{elchem}\blacktriangle\mathrm{mol}}$	diffusion coefficient of the molar electrochemical potential $\mu_{\mathrm{elchem}\blacktriangle\mathrm{mol}}$	$mol^2/J\,m\,s$
D	diffusion coefficient	m^2/s
$\dot{E}_{\mathrm{En}}$	energy flow	J/s
$E_{\mathrm{En,int}\blacktriangle\mathrm{mass}}$	internal energy per unit of mass	J/kg
$E_{\mathrm{En,int}\blacktriangle\mathrm{mol}}$	molar internal energy	J/mol
$\vec{\mathbb{E}}$	electric field	V/m
E_{En}	energy	J
$\mathfrak{F}_{\mathrm{En,Helm}\blacktriangle\mathrm{mol}}$	molar Helmholtz free energy	J/mol
$F_{\mathrm{Ch}\blacktriangle\mathrm{mol}}$	Faraday's number $\left(F_{\mathrm{Ch,mol}} = e_{\mathrm{Ch}}^{-} \cdot N_{\mathrm{A}\blacktriangle\mathrm{mol}} = 96485.34\ \mathrm{A\,s/mol}\right)$	A s/mol
$\mathfrak{G}_{\mathrm{En,elchem}\blacktriangle\mathrm{mol}}$	molar electrochemical Gibbs free energy	J/mol
$G_{\mathrm{En}\blacktriangle\mathrm{mol}}$	molar Gibbs free energy	J/mol
$\dot{H}_{\mathrm{En}}$	enthalpy flow	J/s
$H_{\mathrm{En}\blacktriangle\mathrm{mol}}$	molar enthalpy	J/mol
I	current	A
$\vec{J}$	flow (index defines kind of flow)	$1/m^2\,s$
K	equilibrium constant	
L	length	m
MPC	Material and Production Costs	EUR/unit
$\dot{M}_{\mathrm{Mol}}$	molar flow	mol/s

$M_{\mathrm{Mass}\blacktriangle\mathrm{mol}}$	molar mass	kg/mol
$N_{\mathrm{A}\blacktriangle\mathrm{mol}}$	Avogadro's number / Loschmidt's number $\left(N_{\mathrm{A}} = 6.022 \cdot 10^{23}\ 1/\mathrm{mol}\right)$	1/mol
Nu	Nußelt number	
N_{Mol}	number of particles	mol
$O_{\%}$	occupation probability	1/100 %
$Pe_{\%}$	permeability	1/100 %
$Po_{\%}$	porosity	1/100 %
Pr	Prandtl's number	
P_{En}	power	W
$\dot{Q}_{\mathrm{En}}$	heat / thermal energy flow	W
$Q_{\mathrm{En}\blacktriangle\mathrm{mol}}$	molar heat / molar thermal energy	J/mol
R_{Ohm}	electric/ionic resistance	Ω
Re	Reynolds number	
$\Re_{\mathrm{En}\blacktriangle\mathrm{mol}}$	universal gas constant $\left(R_{\mathrm{En,mol}} = k_{\mathrm{En,B}}\ N_{\mathrm{A}\blacktriangle\mathrm{mol}} = 8.314\ \mathrm{J/mol\,K}\right)$	J/mol K
$S_{\mathrm{En}\blacktriangle\mathrm{mol}}$	molar entropy	J/mol K
T	(absolute) temperature	K
U	voltage	V
$V_{\mathrm{O}\blacktriangle\mathrm{Mol}\blacktriangle\mathrm{vol}}^{\bullet\bullet}$	oxygen ion vacancy concentration	mol/m^3
V_{Vol}	volume	m^3
$X_{\mathrm{Mass,mass}}$	mass fraction	$\mathrm{kg_{species}/kg_{tot}}$
Y_{mech}	Young's modulus	Pa
a_{act}	activity	
a	fit coefficient	
b	fit coefficient	
$c_{\mathrm{Mol}\blacktriangle\mathrm{surf}}$	molar surface concentration	mol/m^2
$c_{\mathrm{Mol}\blacktriangle\mathrm{vol}}$	volumetric molar concentration	mol/m^3
$c_{\%}$	relative concentration	%
$c_{\mathrm{En,p}}$	(molar) heat capacity at constant pressure (third index defines reference)	J/kg K or J/mol K
$c_{\mathrm{En,v}}$	(molar) heat capacity at constant volume (third index defines reference)	J/kg K or J/mol K
$e_{\bar{\mathrm{Ch}}}$	elementary charge $\left(e_{\bar{\mathrm{Ch}}} = 1.602 \cdot 10^{-19}\ \mathrm{A\,s}\right)$	A s
$\vec{\mathbf{e}}$	unity vector	m
f	activity coefficient	
$\vec{g}_{\mathrm{grav}}$	earth's gravitational acceleration $\left(\vec{g}_{\mathrm{grav}} = 9.81\ \mathrm{m/s^2}\right)$	m/s^2
h_{mass}	specific enthalpy per unit mass	J/kg
i	counting variable	
$\vec{j}$	current density	A/m^2

j	counting variable	
$k_{\mathrm{En,B}}$	Boltzmann's constant $\left(k_{\mathrm{En,B}} = 1.381 \cdot 10^{-23}\ \mathrm{J/K}\right)$	J/K
$\Re_{\mathrm{reac}}$	reaction rate constant	var.
k_{turb}	turbulent kinetic energy	$\mathrm{m^2/s^2}$
k	counting variable	
l	counting variable	
$\dot{m}_{\mathrm{Mass}}$	mass flow	kg/s
m_{Mass}	mass	kg
n	number of species	
$\mathfrak{p}_{\mathrm{vol}}$	volumetric power density	$\mathrm{W/m^3}$
$\mathfrak{p}$	power density	$\mathrm{W/m^2}$
p_{part}	partial pressure of a species in a mixture	$\mathrm{Pa_{species}/Pa_{tot}}$
p	pressure	Pa
q_{Ch}	charge	A s
r_{reac}	reaction rate	l/s
t	time	s
$\vec{u}$	velocity	m/s
x	x-direction in a Cartesian coordinate system	m
y	y-direction in a Cartesian coordinate system	m
$y_{\mathrm{Mol\blacktriangle mol}}$	molar fraction	$\mathrm{mol_{species}/mol_{tot}}$
z	z-direction in a Cartesian coordinate system	m
z	number of elementary charges	

Operators and symbols

Indices starting with a capital letter are used in this study to indicate if a quantity is either expressed as mass ($_{\mathrm{Mass}}$ in kg), moles ($_{\mathrm{Mol}}$ in mol), volume ($_{\mathrm{Vol}}$ in m^3), energy ($_{\mathrm{En}}$ in J), or charge ($_{\mathrm{Ch}}$ in C). Density-like expressions are indicated by indices too. Here lower case letters are applied to distinguish references to mass ($_{\mathrm{mass}}$ in 1/kg), moles ($_{\mathrm{mol}}$ in 1/mol), volume ($_{\mathrm{vol}}$ in $1/m^3$), and normalized percents ($_{\%}$ in 1/100 %). Domains are emphasized by an abbreviation in capital letters (e.g. a quantity inside the electrolyte is indicated by $_{\mathrm{ELE}}$). The definition of the standard conditions (25 °C, p = 1013 hPa, pH = 0, ionic activity = 1) is taken from the CRC handbook (Lide 2010).

:=	definition
DEN	denominator
$\underline{\Delta}$	Laplace operator
$\lvert\ \rvert$	absolute value
$\langle\ \rangle$	arithmetic mean value
Δ	difference
div	divergence
$\dot{}$	partial derivative with respect to time
$\downarrow$	low
d	change, derivative
exp	exponential function, Euler's number ($e \approx 2.718$ (Bronstein 2008))
grad	gradient
$(\ )_i$	operation performed at i = constant
ln	natural logarithm
max	maximum
min	minimum
∂	partial derivative
$\prod$	product
$\sum$	sum
$\overline{\overline{\ }}$	tensor
$\uparrow$	high
$\vec{\ }$	vector

Acknowledgments

"Knowledge is in the end based on acknowledgement."

Ludwig Wittgenstein
(On Certainty (Über Gewissheit), J. & J. Harper Editions, New York, 1969, p. 378)

After more than four years my time at the Institut für Wärme und Brennstoff-technik (engl.: institute of heat- and fuel-technology) (IWBT) and finally after more than seven years my research activities as a PhD-student finally have come to an end. In my opinion, when such a long and laborious project is over, the time has come to say "thank you" to a lot of people.

First of all I would like to thank my wife Anita, for all your patience and the never ending support you gave to me on this far too long journey. I also would like to thank my family, without you I never would have been here. In particular I want to acknowledge Anna, Emma, and Jakob.

From my professional background first of all I have to say "thank you" to my friend and colleague Rune Staeck and my supervisor Prof. Dr. techn. Reinhard Leithner. You always had faith in me and the very often unorthodox ideas of a "physicist". Last but not least on the one hand I want to acknowledge my colleague Ina Schunke, without your help I would have lost the war on bureaucracy. Shaofei Chen, Gulzhan Tleukenova, and Sohail Ahmed, from which I was able to learn much about how things work elsewhere in the world, and Wilfried Janssen, who taught me way more than just electronics. On the other hand I would like to mention all those students that decided to accompany me for a while on my way. Special thanks go to Conrad Zeidler, Constantin Malorny, Markus Ramm, and Tarek Tounsi who have been my "Swiss army knifes" for a very long time. Jendrik Seiler, who helped me to broadcast not only myself over the Internet. Jonathan Lefebvre, Steffen Heinke, and Yannick Femppel, who were willing to follow me deep into physics, and finally Birte Horn and Yvonne Jocher, who have spent days and weeks in not getting lost in a catalytic, porous maze. To all of you and all those I forgot to mention, thank you very much.

Once a wise man told me that all people want to shine a bit in the eyes of the others, for me all of you have been lighthouses, brightly illuminating my way through the night.

Christian Wesemeyer
Peine, June 2015

Abstract

The present work focuses on the development and investigation of Solid Oxide Fuel Cells (SOFCs) with Direct Internal Reformation (DIR) of methane. To optimize their performance, key aspects for design, materials, and manufacturing are derived from the basic operational principles. Together with the results of a detailed review on the current state of the art in the field of SOFCs design concepts they are used to develop a novel janiform configuration of an anode supported Integrated Planar-SOFC (IP-SOFC) system.

As preparative studies for a 3D investigation of the concept with a Computational Fluid Dynamics (CFD) model, the possible influences of the anode microstructure and composition as well as of elementary surface reactions on the overall cell performance and numerical results are studied. Additionally, individual submodels for the physical phenomena of interest are set up and verified. For the electrochemical reactions, next to an alternative approach based on a local description of the potential dependent equations, two additional approaches, applicable to different levels of geometrical complexity, are proposed.

Together with the results of the microstructural investigation it is derived that, due to the small ionic conductivity of Yttrium Stabilized Zirconium (YSZ), the optimal equivolumetric mixture of the anode's cermet components should only be applied to a thin active layer close to the electrolyte surface. Inside the support structure the focus should lie on a high electric conductivity and gas penetration.

The CFD simulation focuses on a three-cell series connection and covers a parameter study on the cell voltage and inlet temperature. Both parameters can be applied to balance the effects of electrochemistry and reformation in order to minimize the temperature differences inside the anode. Although the contribution of CO to the overall current density increases in flow direction to almost 10 %, the system in total converts the hydrogen first. Finally, it is figured out that the system shows a high system efficiency for long cascade of more than ten cells.

Zusammenfassung

Die vorliegende Arbeit beschäftigt sich mit der Entwicklung und Untersuchung von oxdikeramischen Brennstoffzellen (engl.: Solid Oxide Fuel Cell (SOFC)) mit direkter interner Reformierung von Methan. Zur Optimierung ihrer Leistungsfähigkeit werden ausgehend von den physikalischen Grundprinzipien, Randbedingungen für das Design, die Materialauswahl und Herstellungsweise abgeleitet. Aufbauend auf dem aktuellen Stand der Technik im Bereich der SOFC Konstruktion wird aus den gewonnenen Erkenntnissen ein neuartiges Design mit janusförmig angeordneten Elektroden entwickelt.

Zur Vorbereitung auf eine dreidimensionale Untersuchung des Konzepts mit den Methoden der numerischen Strömungsmechanik (engl.: Computational Fluid Dynamics (CFD)) werden mögliche Einflussparameter auf die Zellleistung und die numerischen Ergebnisse hinterfragt. Dabei handelt es sich einerseits um Abhängigkeiten von der Mikrostruktur und Zusammensetzung der Anode und andererseits um die Bedeutung elementarer Oberflächenreaktionen. Zusätzlich dazu werden für alle relevanten physikalischen Phänomene separate Submodelle entwickelt und verifiziert. Neben einem alternativen Ansatz, welcher von einer lokalen Beschreibung der potentialabhängigen Gleichungen ausgeht, werden zwei weitere Beschreibungen für die elektrochemischen Reaktionen in verschieden komplexen Rechengitter formuliert.

Die Berechnungsergebnisse zeigen, dass in Folge der geringen ionischen Leitfähigkeit von mit Yttrium stabilisiertem Zirkoniumoxid (engl.: Yttrium Stabilized Zirconium (YSZ)) die optimale isovolumetrische Mischung der Bestandteile des Anodencermets nur innerhalb einer dünnen, elektrochemisch aktiven Reaktionsschicht an der Grenze zum Elektrolyten verwendet werden sollte. Innerhalb der stützenden Anode sollte die Zusammensetzung zu Gunsten der elektrischen Leitfähigkeit und Gasdurchlässigkeit angepasst werden.

Bei den CFD-Simulationen wird eine Reihenschaltung aus drei Zellen einer Parameterstudie bezüglich Einlasstemperatur und Betriebsspannung unterzogen. Es zeigt sich, dass beide Parameter dazu verwendet werden können die thermischen Auswirkungen von Elektrochemie und Reformierung gegeneinan-

der auszubalancieren und so die Temperaturgradienten innerhalb der Anodenstruktur zu minimieren. Ferner folgt, dass obwohl der Kohlenmonoxid (CO)-Anteil an der Gesamtstromdichte in Richtung des Gasflusses zunimmt, er nie einen Wert von etwa 10 % überschreitet. Global betrachtet konvertiert das System daher zunächst den Wasserstoff und nachfolgend das CO. Abschließend wird gezeigt, dass das entwickelte System für lange Kaskaden von mehr als zehn Zellen einen hohen Gesamtwirkungsgrad aufweist.

1. Introduction

It is well known that one of the basic aspects of life is the transformation of energy (Smil 1994, p. 223). This artificial definition of life can be easily extended from the biological point of view on human existence towards a sociological perspective on our species (Perls 1947). Since our ancestors have formed the first hordes, humans socially interact with each other in multiple ways whereby natures resources are utilized (Schmidt-Bleek 2006, p. 29). Although it is obvious that human existence cannot be explained only in terms of biology, from a purely materialistic point of view the majority of our needs[1] can be satisfied by the production and utilization of goods, which in all cases is associated with a conversion of energy. (Smil 1994, p. 1)

In a technical context conversion of energy means e.g. conversion of kinetic energy to electricity (wind turbines), radiation to thermal energy (solar-thermal absorber), nuclear to thermal energy (nuclear fission and fusion) or chemical to kinetic and thermal energy (combustion engine, human body) (Smil 1994). From all the aforesaid primary energies mankind has a particular interest in chemical energy ever since, because it is long term storable, easily portable and tradable, and can be utilized in a demand driven way. (Smil 1994, p. 157 et seqq.)(Wagner 2007, p. 93 et seqq.) For long, the conversion rate of chemical to kinetic energy (i.e. work) was essentially limited to the amount humans or animals were able to supply[2]. With the invention of the steam engine and the following dawn of industrialization in England at the end of the 18$^{\text{th}}$ century the situation changed dramatically. Before that time "high power prime movers" like wind- or watermills[3] were based either on location bound (water power) or unsteady (wind) sources of primary energy coming more or less directly from the sun (Smil 2005, p. 14). With this new type of prime mover in the 19$^{\text{th}}$ century the source of primary energy moved from solar to

[1] e.g. air, communication, food, labor, shelter, transport (Hahlbrock 2007, p. 43)(Wagner 2007, p. 30)(Printz 2008, p. 152)

[2] $P_{\text{En mech}} \approx 50 - 800\,\text{W}_{\text{mech}}$ (Smil 1994, p. 223 et seqq.)(Smil 2005, p. 14)

[3] $P_{\text{En mech}} \approx 1 - 4\,\text{kW}_{\text{mech}}$ (Smil 1994, p. 103 et seqq.)(Smil 2005, p. 14 et seqq.)

fossil energy changing the way of living not only in England but also in almost all countries of the world in a way unknown before in history (Radkau 2006)(Wagner 2007, p. 36 et seqq.). As a side effect of the industrialization a dramatic increase in primary energy demand[4] was the consequence.

Since the demise of the USSR in the years around 1990 the world has become multi-polar. Besides "old" global players like the USA or the EU "new" societies[5] are demanding more and more energy on the global market (Lior 2010; Müller-Kraenner 2007). Almost 30 years after the Brundtland report (Brundtland et al. 1987, p. 20 et seqq.) its conclusions are still valid: As the differences in ideology in the past century, an increased demand for energy in combination with rising prices (Eisenbeiß 2006; Seeliger et al. 2011) might lead to serious international tensions within the next decades (Müller-Kraenner 2007). Additional challenges from environmental impacts of human activities[6] and the expected consequences of the (maybe anthropogenic) greenhouse effect (Solomon et al. 2007)[7] also have to be addressed in the future (Latif 2007, p. 135 et seqq.). Altogether, to secure a sustainable development for the generations to come and to prevent global conflicts on energy will be one of the main topics of the 21st century (Müller-Kraenner 2007).

In consequence to the challenges of the time, the majority of authors in the literature expect a tremendous increase in the share of renewable energy sources in the satisfaction of the primary energy demand within the next decades (Angelis-Dimakis et al. 2010; Graça Carvalho, Bonifacio, and Dechamps 2011; Lund, Östergärd, and Stadler 2011; Metz et al. 2007; PriceWaterhouseCoopers LLP 2010). Unfortunately, these sources still suffer from their time and location dependence (Wagner 2007, p. 52). Although intercontinental electric grids and storage concepts for renewable produced electricity like pumped storage power plants or compressed air power plants (Nielsen and Leithner 2009)[8] were developed, the realizable potential of constant carbon free energy production is limited (Mauser 2007, p. 66 et seqq.) (Timilsina and Shrestha

[4] e.g. from about 5.86 EJ in 1957 to about 10.55 EJ in 1976 in the federal republic of Germany (Der Bundesminister für Forschung und Technologie 1977, p.19)

[5] e.g. Brazil, Russia, India, and China (BRIC)

[6] e.g. acid rain, nuclear contamination, eutrophication (Mauser 2007, p. 145 et seqq.) and acidification of rivers, lakes and oceans (Rahmstorf and Richardson 2007, p. 159 et seqq.)

[7] e.g. rising of the sea level by a value between 18 cm and 59 cm till 2100 (Latif 2007, p. 162)(Solomon et al. 2007) or global migration due to desertification (Parry et al. 2007)

[8] e.g. operated with air or hydrogen from electrolysis

2010). Other alternatives to fossil sources for (chemical) energy, like biological processes[9] might be in concurrence to food production, leading to increased prices for agricultural products and social tensions (Ajanovic 2011; Eisenbeiß 2006; Müller-Kraenner 2007). As long as non depleting, high output energy sources[10] are either not readily available within a foreseeable future (Lior 2010) or associated with high costs,[11] chemical energy from fossil fuels and its conversion (mainly to electricity) will still play an important role in future energy systems (Lund 2010). To extend the range of the available resources, energy has to be harvested, stored (Graça Carvalho, Bonifacio, and Dechamps 2011), and used (decentralized) in all its diversity (Timilsina and Shrestha 2010)(Wagner 2007, p. 281), in all scales (Watts to Megawatts), and as efficient as possible[12] (Jäger 2007, p. 151)(Schorsch 2009; Woodside 2011)(Wagner 2007, p. 207 and 274).

Although they are no panacea, in this context fuel cells, and in particular highly integrated Solid Oxide Fuel Cells (SOFCs) are of great interest. Their scalability, fuel flexibility and high electric efficiency make SOFCs feasible for decentralized small scale Combined Heat and Power (CHP) applications[13]. In particular highly integrated SOFC concepts based on a cascaded structure with internal reformation of CH_4 seem to be promising for this (Leithner and Schlitzberger 2007). Not only their outstanding power to heat ratio, but also an off-gas consisting only of fuel, CO_2, and H_2O are beneficial; giving SOFC-systems with increased fuel utilization an intrinsic possibility for CO_2 separation (Leithner 2007). To come closer to the technical and financial goals, which have to be met before production and finally a significant market penetration seems possible (Lior 2010), a profound understanding of the counteracting internal processes inside the system is necessary. For this issue numerical simulations offer a flexible and efficient way to obtain insights at various operational conditions.

Since numerical models can be set up for different numbers of geometrical

[9] e.g. biogas plants or gas from landfills

[10] e.g. cheap solar cells with high efficiency, energy from space, nuclear fusion...

[11] e.g. large geothermal power plants, solar power production in the Sahara region (Larsen 2010)

[12] e.g. make use of synergy effects in combined heat and power generation (Leithner 2002, p. 47)

[13] e.g. scenarios indicate that the average heating demand for residential buildings in Germany is expected to decrease from about 145 kWh_{th} to less than 100 kWh_{th} per square meter and year by 2020 (Blome 2008; Eisenbeiß 2006)

dimensions and various length- and timescales, their influence on the system has to be investigated. The most detailed insight is possible with a 3D model, providing information on the spatial distribution of all aspects of interest. For this kind of model localized formulations of all phenomena, which try to cover as many of the real couplings among the phenomena as possible, are necessary. They can be used to obtain numerical results and finally judge over the capability of a cascaded SOFC with internal reformation.

2. Fuel Cell fundamentals

In this chapter the operating principles of fuel cells are discussed. Hereby special attention is paid to SOFCs.

The chapter begins in section 2.1 with the electrochemical fundamentals behind all galvanic cells, different types of fuel cells, and a brief review of their similarities and differences. After that sections 2.2 and 2.3 address fuel cell thermodynamics and electronics, before in sections 2.4 and 2.5 the SOFC and its materials as well as the chemical reformation reactions are emphasized. The chapter ends in section 2.6 with a summary of the basic concepts needed in the following chapters for the proposed novel cell concept and its mathematical modeling.

2.1. Electrochemical fundamentals

The ELECTROCHEMICAL DICTIONARY (Bard, Inzelt, and Scholz 2008, p. 286) defines the term "fuel cell" as:

> "... electrochemical devices that convert the chemical energy of a reaction directly into electrical energy. In contrast to batteries the fuel and the oxidant are continuously fed to the anode and to the cathode, respectively."

Since fuel cells account to the family of electrochemical cells, for the development of new cell concepts and detailed models a profound understanding of the underlying electrochemical phenomena is crucial. Again the ELECTROCHEMICAL DICTIONARY (Bard, Inzelt, and Scholz 2008, p. 197 et seqq.) gives a definition of the term "electrochemistry" and hence a direction for the focus of the successive investigation:

> "Electrochemistry, as the name suggests, is a branch of chemical science that deals with the interrelation of electrical and chemi-

cal phenomena. From the very beginning electrochemistry covers two main areas: the conversion of the energy of chemical reactions into electricity (electrochemical power sources) and the transformations of chemical compounds by the passage of an electric current (electrolysis). [...] Electrochemistry is the science of structures and processes at and through the interface between an electronic ('electrode') and an ionic conductor ('electrolyte') or between two ionic conductors."

Originating from this definition, already at this point a precise limitation of the spatial resolution and scales on which the phenomena of interest take place is necessary. Although on a molecular level interactions with surfaces are single particle phenomena the validity of a continuum mechanical treatment and hence a sufficient number of particles[1] is assumed here in any case (Meschede 2006, p. 224 et seqq.)[2]. Altogether, the possibility of a certain mismatch between results from numerical modeling and experiments has to be noticed as an intrinsic drawback of the chosen methodology. Nevertheless, numerous authors in the literature[3] have shown that a sufficiently accurate description of electrochemical phenomena in terms of continuum mechanics is possible at almost all scales and any number of dimensions (0D to 3D).

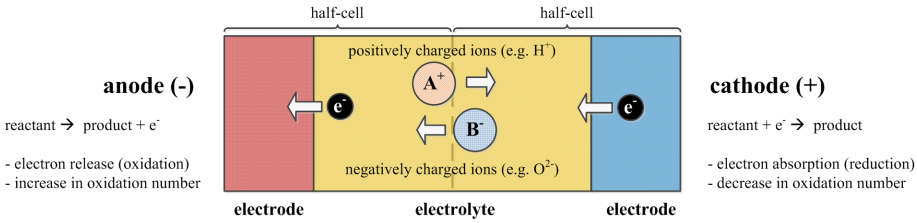

Figure 2.1.: **Basic electrochemical cell:** Inside the half-cells of an electrochemical cell (e.g. a fuel cell) electrons are either transferred from the electrode to the electrolyte (*cathode*) or the other way round (*anode*); modified from (de Haart 2009b).

[1] atoms, electrons, ions, molecules

[2] In consequence not only effects on scales below about 10 µm are only considered by their integral values over volumes of this magnitude, but also a treatment of cases where single particles interact (e.g. at very low partial pressures) is difficult.

[3] e.g. (Danilov and Tade 2009; Hecht et al. 2005; Wang et al. 2007; Yakabe 2001)

The second part of the dictionary's definition is illustrated in Figure 2.1. In contrast to other electrochemical cells where electricity is converted to chemical bound energy (electrolyzer), in fuel cells chemical energy is converted into electricity and heat via an exchange of electrons from the electrode to the electrolyte (*reduction* (Bard, Inzelt, and Scholz 2008, p. 575)) or vice versa (*oxidation* (Bard, Inzelt, and Scholz 2008, p. 478)). Summation of the two half cell reactions leads to the overall redox-reaction inside a fuel cell (de Haart 2009a; Leithner et al. 2010):

	Reactants		**Products**
Anode:	$z_{ANO}\cdot$ reductant$^{z_b+}$	$\longrightarrow$	$z_{ANO}\cdot$ oxidant$^{(z_b+z_{CAT})+}$ + $z_{ANO}z_{CAT}\cdot e^-_{Ch}$
+ Cathode:	$z_{CAT}\cdot$ oxidant$^{z_A+}$ + $z_{CAT}z_{ANO}\cdot e^-_{Ch}$	$\longrightarrow$	$z_{CAT}\cdot$ reductant$^{(z_A-z_{ANO})+}$
Total:	$z_{CAT}\cdot$ oxidant$^{z_A+}$ + $z_{ANO}\cdot$reductant$^{z_b+}$	$\longrightarrow$	$z_{CAT}\cdot$reductant$^{(z_A-z_{ANO})+}$ + $z_{ANO}\cdot$ oxidant$^{(z_b+z_{CAT})+}$.

The required chemical energy is, in a distinct delimitation to batteries, continuously fed to the electrodes by the reactants[4]. The products[5] are also constantly removed from the cell (Bard, Inzelt, and Scholz 2008, p. 286). For a continuous reaction to take place, a possibility for equilibrating the electric potentials of the anode and cathode has to be provided by an electronic conductor between them (O'Hayre et al. 2009, p. 15). Since the movement of electric charges forms an electric current (Meschede 2006, p. 318) it can be used to power electric devices (see Figure 2.2). Before the specific constructive, material,

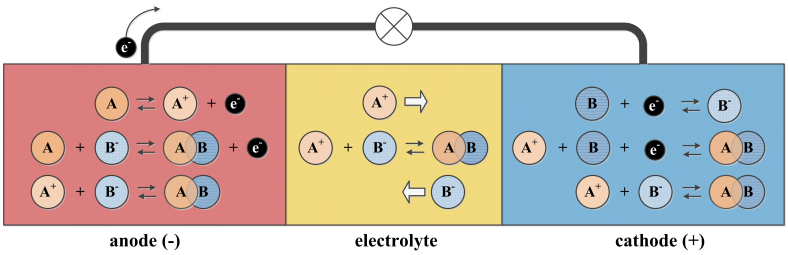

Figure 2.2.: **Operating principle of a galvanic cell:** A theoretical *galvanic cell* with mixed ionic conducting electrolyte is powering an electric device. The reductant $\mathcal{A}$ is supplied to the anode, whereas the oxidant $\mathcal{B}$ is fed to the cathode. The product $\mathcal{AB}$ is generated in all regions of the cell.

[4] like e.g. H_2 and O_2
[5] e.g. H_2O

and operational aspects will be addressed at the end of this chapter (see page 32), some more general considerations can be derived from the definitions at the beginning of this section. The electrolyte forms the heart of every fuel cell. Therefore, special attention has to be paid on it. Since the materials, phases, and conduction mechanisms differ, the operational temperature varies from ambient conditions up to more than 1000 °C (O'Hayre et al. 2009, p. 12). The latter are necessary for solid electrolytes since their ionic conductivity is

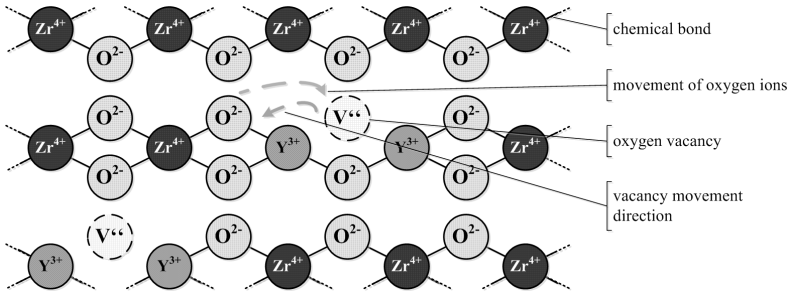

Figure 2.3.: **Conduction mechanism of YSZ:** ZrO_2 becomes conductive for two times negatively charged oxygen ions (O^{2-}) when being doped with Y_2O_3. This can be explained by the fact that yttrium has one valence-electron less than zirconium, creating vacancies for negatively charged ions; adapted from (Leithner et al. 2010).

based on semiconductor physics (Li, Gemmen, and Liu 2010) and hence increases with temperature. Another drawback is their limitation to only one type of ion[6]. Although (almost) all of today's fuel cells use only one kind of ion, a bidirectional electrolyte, conductive for positively as well as negatively charged ions, is possible; leading to an increased net current at given potential and expanding the product formation all over the cell. Unfortunately, for a solid electrolyte this would maybe result in a sudden formation of e.g. water inside its atomic structure and hence mechanical tensions. A technical summary of the aforesaid is given in Table A.2 in appendix A.2, where numerous currently investigated fuel cells with their operational conditions are listed.

Independent of the current state of the system the occurrence of an electrochemical reaction and an associated charge transfer is assumed so far. To identify the physical driving forces for this and to quantify their effects some thermodynamic considerations are made in the next section.

[6] see Figure 2.2

2.2. Thermodynamics of fuel cells

The 22nd edition of Dubbel's textbook on mechanical engineering (Grote and Feldhusen 2007, p. D1) defines *thermodynamics* as:

> "As a branch of physics, the thermodynamics is a general science of energy. It deals with the various forms of energy and its transformation into one another. It provides the general laws that any energy conversion is based on."

In the case of an energy converter like the fuel cell, any change in the energy of a system $\mathrm{d}E_{\mathrm{En,tot_{\blacktriangle}mol}}$ is given by the sum of the changes in its gravitational potential energy $\mathrm{d}E_{\mathrm{En,pot_{\blacktriangle}mol}}$, kinetic energy $\mathrm{d}E_{\mathrm{En,kin_{\blacktriangle}mol}}$, and internal energy $\mathrm{d}E_{\mathrm{En,int_{\blacktriangle}mol}}$ per mole all in J/mol (Wachter and Hoeber 1998, p. 22)(Grote and Feldhusen 2007, p. D5):

$$\begin{aligned}\mathrm{d}E_{\mathrm{En,tot_{\blacktriangle}mol}} =& \mathrm{d}E_{\mathrm{En,pot_{\blacktriangle}mol}} + \mathrm{d}E_{\mathrm{En,kin_{\blacktriangle}mol}} \\ &+ \underbrace{\mathrm{d}E_{\mathrm{En,int_{\blacktriangle}mol,mech}} + \mathrm{d}E_{\mathrm{En,int_{\blacktriangle}mol,chem}} + \mathrm{d}E_{\mathrm{En,int_{\blacktriangle}mol,Coul}} + \mathrm{d}E_{\mathrm{En,int_{\blacktriangle}mol,mole}}}_{=\mathrm{d}E_{\mathrm{En,int_{\blacktriangle}mol}}} \,. \end{aligned} \tag{2.1}$$

The first two terms in equation 2.1 are in general negligible for all fuel cells. For a certain material the term *internal energy* is a summary of the mechanical energy associated with its volumetric expansion $E_{\mathrm{En,int_{\blacktriangle}mol,mech}}$, chemical bonds $E_{\mathrm{En,int_{\blacktriangle}mol,chem}}$, Coulomb interactions $E_{\mathrm{En,int_{\blacktriangle}mol,Coul}}$, and molecular motions (heat) $E_{\mathrm{En,int_{\blacktriangle}mol,mole}}$ per mole[7].

Changes in mechanical energy are accomplished by an expansion of the system against a pressure, and can be expressed by[8] (O'Hayre et al. 2009, p. 27):

$$\mathrm{d}E_{\mathrm{En,int_{\blacktriangle}mol,mech}} = -p\mathrm{d}V_{\mathrm{Vol_{\blacktriangle}mol}} \,. \tag{2.2}$$

Here p is the pressure in Pa and $\mathrm{d}V_{\mathrm{Vol_{\blacktriangle}mol}}$ the volume change per mole in $\mathrm{m^3/mol}$. The internal energy stored in chemical bonds per mole $E_{\mathrm{En,int_{\blacktriangle}mol,chem}}$ is dependent on the number of moles of all n_i species inside the system. At

[7] Nuclear processes $E_{\mathrm{En,int_{\blacktriangle}mol,nucl}}$, and the energy stored in the mass of the material $E_{\mathrm{En,int_{\blacktriangle}mol,mass}}$ are negligible, since neither nuclear fission or fusion nor relativistic effects occur inside fuel cells.

[8] The minus is introduced in equation 2.2 since a decrease of the system volume ($\mathrm{d}V_{\mathrm{Vol_{\blacktriangle}mol}} < 0$) at constant pressure leads to a gain in internal energy ($\mathrm{d}E_{\mathrm{En,int_{\blacktriangle}mol}} > 0$).

constant chemical energy and given temperature T in K the system, can be characterized by the change of possible micro-states (molar entropy $S_{\mathrm{En}_\blacktriangle\mathrm{mol}}$ in J/mol K) in dependence of the number of particles of all species i (Bard, Inzelt, and Scholz 2008, p. 91)(Grote and Feldhusen 2007, p. N20)(Motschmann 2005, p. 22):

$$\begin{aligned}\mu_{\mathrm{mol}_\blacktriangle i} &:= \textit{molar chemical potential of species } i \\ &:= -T(\partial_{N_{\mathrm{Mol}_\blacktriangle\mathrm{mol}_\blacktriangle i}} S_{\mathrm{En}_\blacktriangle\mathrm{mol}_\blacktriangle i})_{E_{\mathrm{En,int}_\blacktriangle\mathrm{mol},\mathrm{chem}}} \quad \text{in J/mol.}\end{aligned} \tag{2.3}$$

From the definition in equation 2.3 it follows that any change $\mathrm{d}E_{\mathrm{En,int,chem}_\blacktriangle\mathrm{mol}}$ is either connected to a change in the number of particles per mole $\mathrm{d}N_{\mathrm{Mol},\mathrm{mol}_\blacktriangle i}$ or a change of the chemical potential $\mathrm{d}\mu_{\mathrm{mol}_\blacktriangle i}$ of the i-th species in the system in $\mathrm{mol_{species}/mol_{tot}}$ (O'Hayre et al. 2009, p. 49 et seqq.):[9]

$$\begin{aligned}\mathrm{d}E_{\mathrm{En,int}_\blacktriangle\mathrm{mol},\mathrm{chem}_\blacktriangle i} &= \mu_{\mathrm{mol}_\blacktriangle i}\,\mathrm{d}N_{\mathrm{Mol}_\blacktriangle\mathrm{mol}_\blacktriangle i} + \underbrace{N_{\mathrm{Mol}_\blacktriangle\mathrm{mol}_\blacktriangle i}\,\mathrm{d}\mu_{\mathrm{mol}_\blacktriangle i}}_{=0,\text{ from definition}}, \\ \Rightarrow \mathrm{d}E_{\mathrm{En,int}_\blacktriangle\mathrm{mol},\mathrm{chem}} &= \sum_i \mathrm{d}E_{\mathrm{En,int}_\blacktriangle\mathrm{mol},\mathrm{chem}_\blacktriangle i}, \\ &= \mu_{\mathrm{mol}_\blacktriangle\mathrm{tot}}\,\mathrm{d}N_{\mathrm{Mol}_\blacktriangle\mathrm{mol}_\blacktriangle\mathrm{tot}}\,.\end{aligned} \tag{2.4}$$

In the presence of an electric potential ϕ in V, charged particles experience forces coming from Coulomb interactions (Bard, Inzelt, and Scholz 2008, p. 193) (Meschede 2006, p. 296). In addition, these charged particles itself form an electric potential (Meschede 2006, p. 347). Therefore, the internal electrostatic energy[10] of a system might be changed by altering the number of particles $\mathrm{d}N_{\mathrm{Mol}_\blacktriangle\mathrm{mol}_\blacktriangle i}$ of charge $z_i{\cdot}F_{\mathrm{Ch}_\blacktriangle\mathrm{mol}}$, where $F_{\mathrm{Ch}_\blacktriangle\mathrm{mol}}$ is Faraday's number[11]

---

[9] $N_{\mathrm{Mol}_\blacktriangle\mathrm{mol}_\blacktriangle i}\mathrm{d}\mu_{\mathrm{mol}_\blacktriangle i} = N_{\mathrm{Mol}_\blacktriangle\mathrm{mol}_\blacktriangle i}\cdot\mathrm{d}\left(\underbrace{-T\left(\partial_{N_{\mathrm{Mol}_\blacktriangle\mathrm{mol}_\blacktriangle i}} S_{\mathrm{En}_\blacktriangle\mathrm{mol}}\right)_{E_{\mathrm{En,int}_\blacktriangle\mathrm{mol},\mathrm{chem}}}}_{=0,\text{ since } N_{\mathrm{Mol}_\blacktriangle\mathrm{mol}_\blacktriangle i}=\text{const.}}\right)_{N_{\mathrm{Mol}_\blacktriangle\mathrm{mol}_\blacktriangle i},\,T} = 0$

[10] In principle there is also an energy associated with the magnetic forces (Lorentz forces) when a current is formed by the flow of charged particles. Since the characteristic magnitude of its influence on the current paths is very small (Kivelson and Russel 1995, p. 29 et seqq.), and the operational temperature of a SOFC is larger than typical Curie- or Néel-temperatures (Ashcroft and Mermin 2007, p. 837 et seqq.) magnetic effects are neglected within this study.

[11] $F_{\mathrm{Ch}_\blacktriangle\mathrm{mol}} = 96485.34$ C/mol (Meschede 2006)

or the electric potential $\mathrm{d}\phi_i$ of the i-th species (Bard, Inzelt, and Scholz 2008, p. 193):[12]

$$\mathrm{d}E_{\mathrm{En,int}_{\blacktriangle}\mathrm{mol},\mathrm{Coul}_{\blacktriangle}i} = z_i F_{\mathrm{Ch}_{\blacktriangle}\mathrm{mol}} \phi_i \mathrm{d}N_{\mathrm{Mol}_{\blacktriangle}\mathrm{mol}_{\blacktriangle}i} + z_i F_{\mathrm{Ch}_{\blacktriangle}\mathrm{mol}} N_{\mathrm{Mol}_{\blacktriangle}\mathrm{mol}_{\blacktriangle}i} \mathrm{d}\phi_i \ , \quad (2.5)$$

$$\begin{aligned} \Rightarrow \mathrm{d}E_{\mathrm{En,int}_{\blacktriangle}\mathrm{mol},\mathrm{Coul}} &= \sum_i \mathrm{d}E_{\mathrm{En,int}_{\blacktriangle}\mathrm{mol},\mathrm{Coul}_{\blacktriangle}i} \ , \\ &= z_{\mathrm{tot}} F_{\mathrm{Ch}_{\blacktriangle}\mathrm{mol}} \phi_{\mathrm{tot}} \mathrm{d}N_{\mathrm{Mol}_{\blacktriangle}\mathrm{mol}_{\blacktriangle}\mathrm{tot}} \ . \end{aligned} \quad (2.6)$$

Equations 2.4 and 2.6 can be combined to describe the change of the molar internal energy of a system under electrochemical reactions:

$$\begin{aligned} \mathrm{d}E_{\mathrm{En,int}_{\blacktriangle}\mathrm{mol},\mathrm{elchem}} &= \mathrm{d}E_{\mathrm{En,int}_{\blacktriangle}\mathrm{mol},\mathrm{chem}} + \mathrm{d}E_{\mathrm{En,int}_{\blacktriangle}\mathrm{mol},\mathrm{Coul}} \ , \\ &= \mu_{\mathrm{mol}_{\blacktriangle}\mathrm{tot}} \mathrm{d}N_{\mathrm{Mol}_{\blacktriangle}\mathrm{mol}_{\blacktriangle}\mathrm{tot}} + z_{\mathrm{tot}} F_{\mathrm{Ch}_{\blacktriangle}\mathrm{mol}} \phi_{\mathrm{tot}} \mathrm{d}N_{\mathrm{Mol}_{\blacktriangle}\mathrm{mol}_{\blacktriangle}\mathrm{tot}} \ , \\ &= (\mu_{\mathrm{mol}_{\blacktriangle}\mathrm{tot}} + z_{\mathrm{tot}} F_{\mathrm{Ch}_{\blacktriangle}\mathrm{mol}} \phi_{\mathrm{tot}}) \mathrm{d}N_{\mathrm{Mol}_{\blacktriangle}\mathrm{mol}_{\blacktriangle}\mathrm{tot}} \ . \end{aligned} \quad (2.7)$$

The *molar electrochemical potential* $\mu_{\mathrm{elchem}_{\blacktriangle}\mathrm{mol}}$ in J/mol can be defined as (Bard, Inzelt, and Scholz 2008, p. 193):

$$\mu_{\mathrm{elchem}_{\blacktriangle}\mathrm{mol}} := \mu_{\mathrm{mol}} + z F_{\mathrm{Ch}_{\blacktriangle}\mathrm{mol}} \phi \ .$$

With this equation 2.7 can be written as:

$$\mathrm{d}E_{\mathrm{En,int}_{\blacktriangle}\mathrm{mol},\mathrm{elchem}} = \mu_{\mathrm{elchem}_{\blacktriangle}\mathrm{mol},\mathrm{tot}} \mathrm{d}N_{\mathrm{Mol}_{\blacktriangle}\mathrm{mol}_{\blacktriangle}\mathrm{tot}} \ . \quad (2.8)$$

The last term in equation 2.1 expresses the heat $\mathrm{d}Q_{\mathrm{En}_{\blacktriangle}\mathrm{mol}}$ in J/mol, transferred to the system per mole species. It is associated with changes in the molecular motions[13] of the particles forming the system (Demtröder 2008, p. 293). It can be seen as a change of the possible micro-states $\mathrm{d}S_{\mathrm{En}_{\blacktriangle}\mathrm{mol}}$ at constant temperature T (Baehr 2005, p. 93 et seqq.):

$$\mathrm{d}E_{\mathrm{En,int}_{\blacktriangle}\mathrm{mol},\mathrm{mole}} = \mathrm{d}Q_{\mathrm{En}_{\blacktriangle}\mathrm{mol}} = T \mathrm{d}S_{\mathrm{En}_{\blacktriangle}\mathrm{mol}} \ . \quad (2.9)$$

[12] The electric potential of a point charge is given by (Meschede 2006, p. 299): $\phi(\iota) = \frac{1}{4\pi\varepsilon_0} \frac{q_{\mathrm{Ch}}}{\iota}$ with the charge q_{Ch} in A s, the radius ι in m and the electric permittivity of free space ε_0 in A s/V m. With $q_{\mathrm{Ch}} = \sum_i z_i F_{\mathrm{Ch}_{\blacktriangle}\mathrm{mol}} N_{\mathrm{Mol}_{\blacktriangle}\mathrm{mol}_{\blacktriangle}i}$ it follows $\phi(\iota) = \sum_i \phi_i = \frac{1}{4\pi\varepsilon_0} \sum_i \frac{z_i F_{\mathrm{Ch}_{\blacktriangle}\mathrm{mol}} N_{\mathrm{Mol}_{\blacktriangle}\mathrm{mol}_{\blacktriangle}i}}{\iota}$. For a constant radius or distance ι any change $\mathrm{d}\phi_i$ is given by: $\mathrm{d}\phi_i = \frac{F_{\mathrm{Ch}_{\blacktriangle}\mathrm{mol}}}{4\pi\varepsilon_0 \iota} (z_i \mathrm{d}N_{\mathrm{Mol}_{\blacktriangle}\mathrm{mol}_{\blacktriangle}i} + N_{\mathrm{Mol}_{\blacktriangle}\mathrm{mol}_{\blacktriangle}i} \mathrm{d}z_i)$. Since $N_{\mathrm{Mol}_{\blacktriangle}\mathrm{mol}_{\blacktriangle}i}$ = const. and only the i-th species with a charge z_i = const. are considered, it follows that $\mathrm{d}N_{\mathrm{Mol}_{\blacktriangle}\mathrm{mol}_{\blacktriangle}i}$ as well as $\mathrm{d}z_i$ vanish in the equation above. This leads to $\mathrm{d}\phi_i = 0$.

[13] rotation, translation

Using equations 2.2, 2.8, and 2.9, equation 2.1 can be rearranged to give the usual formulation of the first law of thermodynamics (Gibbs' fundamental equation) (Baehr 2005, p. 55) (Motschmann 2005, p. 38) as[14]:

$$\mathrm{d}E_{\mathrm{En,int}_{\blacktriangle}\mathrm{mol}} = \underbrace{-p\mathrm{d}V_{\mathrm{Vol}_{\blacktriangle}\mathrm{mol}} + \mu_{\mathrm{elchem}_{\blacktriangle}\mathrm{mol}}\,\mathrm{d}N_{\mathrm{Mol}_{\blacktriangle}\mathrm{mol}}}_{\text{work}} + \underbrace{T\mathrm{d}S_{\mathrm{En}_{\blacktriangle}\mathrm{mol}}}_{\text{heat flow}} \,. \tag{2.10}$$

Starting from the definition of *thermodynamic potentials* as (Motschmann 2005, p. 45):

> "... functions in dependence of certain variables within their definition
>
> - the thermodynamic system can be described completely and
> - thermodynamic values of interest are deducible by differentiation of the functions.
>
> "

appropriate expressions can be derived from the internal energy $E_{\mathrm{En,int}_{\blacktriangle}\mathrm{mol}}(N_{\mathrm{Mol}_{\blacktriangle}\mathrm{mol}}, S_{\mathrm{En}_{\blacktriangle}\mathrm{mol}}, V_{\mathrm{Vol}_{\blacktriangle}\mathrm{mol}})$ by *Legendre transformation* (see Table 2.1 and appendix B.1). Here $\mathfrak{G}_{\mathrm{En,elchem}_{\blacktriangle}\mathrm{mol}}$ is the *molar electrochemical Gibbs en-*

Table 2.1.: **Thermodynamic potentials:** Listed are commonly used thermodynamic potentials, their dependencies and connection to other potentials (O'Hayre et al. 2009, p. 32) (Motschmann 2005, p. 50)

Name	**Dependency**	**Connection to other potentials**
molar internal energy	$E_{\mathrm{En,int}_{\blacktriangle}\mathrm{mol}}$ $(N_{\mathrm{Mol}_{\blacktriangle}\mathrm{mol}}, S_{\mathrm{En}_{\blacktriangle}\mathrm{mol}}, V_{\mathrm{Vol}_{\blacktriangle}\mathrm{mol}})$	
molar enthalpy	$H_{\mathrm{En}_{\blacktriangle}\mathrm{mol}}(S_{\mathrm{En}_{\blacktriangle}\mathrm{mol}}, N_{\mathrm{Mol}_{\blacktriangle}\mathrm{mol}}, p)$	$H_{\mathrm{En}_{\blacktriangle}\mathrm{mol}} = E_{\mathrm{En,int}_{\blacktriangle}\mathrm{mol}} + pV_{\mathrm{Vol}_{\blacktriangle}\mathrm{mol}}$
molar Gibbs free energy	$G_{\mathrm{En}_{\blacktriangle}\mathrm{mol}}(T, N_{\mathrm{Mol}_{\blacktriangle}\mathrm{mol}}, p)$	$G_{\mathrm{En}_{\blacktriangle}\mathrm{mol}} = E_{\mathrm{En,int}_{\blacktriangle}\mathrm{mol}} + pV_{\mathrm{Vol}_{\blacktriangle}\mathrm{mol}} - TS_{\mathrm{En}_{\blacktriangle}\mathrm{mol}}$ $= \mu_{\mathrm{mol}} N_{\mathrm{Mol}_{\blacktriangle}\mathrm{mol}}$ (see appendix B.2)
molar electrochemical Gibbs free energy	$\mathfrak{G}_{\mathrm{En,elchem}_{\blacktriangle}\mathrm{mol}}(T, N_{\mathrm{Mol}_{\blacktriangle}\mathrm{mol}}, p)$	$\mathfrak{G}_{\mathrm{En,elchem}_{\blacktriangle}\mathrm{mol}} = G_{\mathrm{En}_{\blacktriangle}\mathrm{mol}} + zF_{\mathrm{Ch}_{\blacktriangle}\mathrm{mol}}\phi N_{\mathrm{Mol}_{\blacktriangle}\mathrm{mol}}$ $= \mu_{\mathrm{elchem}_{\blacktriangle}\mathrm{mol}} N_{\mathrm{Mol}_{\blacktriangle}\mathrm{mol}}$ (see appendix B.2)

[14] Without loss of generality a single species system is assumed. Therefore, species indices are omitted.

ergy in J/mol which is equivalent to $G_{\mathrm{En}_\blacktriangle\mathrm{mol}}$ in the case of an uncharged system (Bard, Inzelt, and Scholz 2008, p. 193). With this equation 2.10 can be rewritten as (O'Hayre et al. 2009, p. 37):

$$\underbrace{\mathrm{d}E_{\mathrm{En,int}_\blacktriangle\mathrm{mol}} + p\mathrm{d}V_{\mathrm{Vol}_\blacktriangle\mathrm{mol}}}_{=\mathrm{d}H_{\mathrm{En}_\blacktriangle\mathrm{mol}},\ \text{at } p=\text{const.}} = \underbrace{\mu_{\mathrm{elchem}_\blacktriangle\mathrm{mol}}\mathrm{d}N_{\mathrm{Mol}_\blacktriangle\mathrm{mol}}}_{=\mathrm{d}\mathfrak{G}_{\mathrm{En,elchem}_\blacktriangle\mathrm{mol}}} + T\mathrm{d}S_{\mathrm{En}_\blacktriangle\mathrm{mol}}\ ,$$

$$\mathrm{d}H_{\mathrm{En}_\blacktriangle\mathrm{mol}} = \mathrm{d}\mathfrak{G}_{\mathrm{En,elchem}_\blacktriangle\mathrm{mol}} + T\mathrm{d}S_{\mathrm{En}_\blacktriangle\mathrm{mol}}\ . \tag{2.11}$$

Since the molar enthalpy $H_{\mathrm{En}_\blacktriangle\mathrm{mol}}$ in J/mol expresses the energy stored in the system on a molecular level per mole species, plus the energy content of the occupied space (O'Hayre et al. 2009, p. 31), $H_{\mathrm{En}_\blacktriangle\mathrm{mol}}$ can be interpreted as the total amount of energy available for conversion. In as much as $\mathfrak{G}_{\mathrm{En,elchem}_\blacktriangle\mathrm{mol}}$ represents the energy required to create the system minus the contribution of the environment[15], according to equation 2.11, it represents the exploitable energy potential[16] of the system (O'Hayre et al. 2009, p. 37). Since $\mathrm{d}\mathfrak{G}_{\mathrm{En,elchem}_\blacktriangle\mathrm{mol}}$ is proportional to a change in the number of particles, it is obvious that the driving forces of a fuel cell are concentration gradients of its working media[17]. This is illustrated in Figure 2.4. Thus for a treatment of the electric properties of the fuel cell as an electrochemical energy converter in the next section a further investigation of $\mathrm{d}\mathfrak{G}_{\mathrm{En,elchem}_\blacktriangle\mathrm{mol}}$ is necessary.

2.3. Fuel Cell electronics

As already mentioned in section 2.1, the electrochemical reactions take place at the interface between electrolyte and electrodes of the two half-cells. In a steady-state the electrochemical potentials of both half cells have to equilibrate, which can be expressed by:

$$\mu_{\mathrm{elchem}_\blacktriangle\mathrm{mol},\mathrm{tot}_\blacktriangle\mathrm{ANO}} = \mu_{\mathrm{elchem}_\blacktriangle\mathrm{mol},\mathrm{tot}_\blacktriangle\mathrm{ELE/ANO}} = \mu_{\mathrm{elchem}_\blacktriangle\mathrm{mol},\mathrm{tot}_\blacktriangle\mathrm{ELE/CAT}} = \mu_{\mathrm{elchem}_\blacktriangle\mathrm{mol},\mathrm{tot}_\blacktriangle\mathrm{CAT}}\ , \tag{2.12}$$

$$\Rightarrow \mu_{\mathrm{elchem}_\blacktriangle\mathrm{mol},\mathrm{tot}_\blacktriangle\mathrm{ANO}} = \mu_{\mathrm{elchem}_\blacktriangle\mathrm{mol},\mathrm{tot}_\blacktriangle\mathrm{CAT}}\ . \tag{2.13}$$

For a general chemical reaction with the stoichiometric coefficients ν

$$\sum_j \nu_j \text{ reactants } j \rightleftharpoons \sum_i \nu_i \text{ products } i \tag{2.14}$$

[15] via heat

[16] work potential

[17] see chapter 4 for a mathematical treatment of the associated transport phenomena

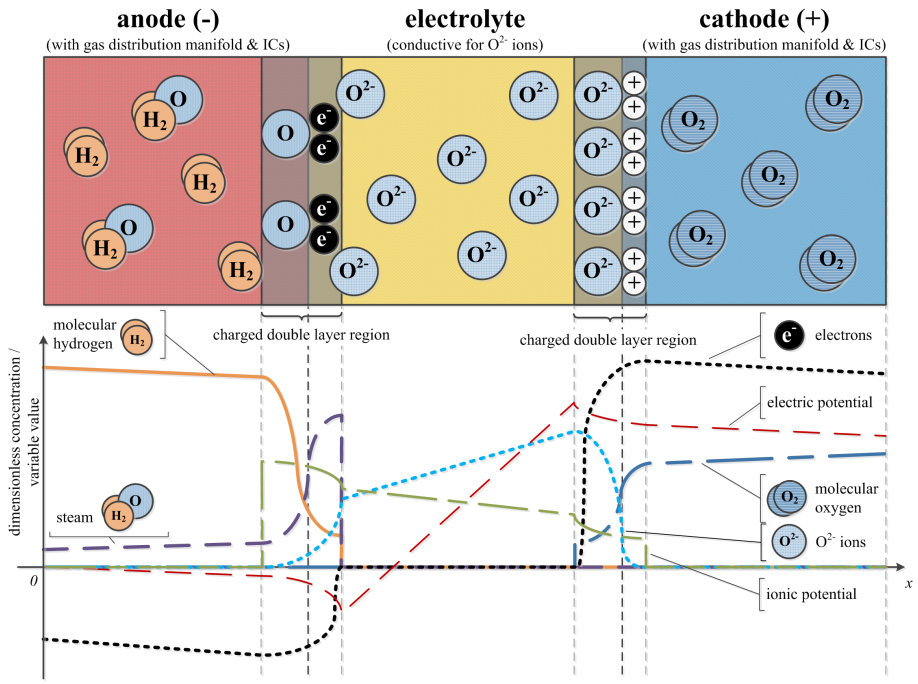

Figure 2.4.: **Particle distribution inside a fuel cell:** Inside a fuel cell, with an electrolyte conducting oxygen ions, concentration gradients of the working media are established. They act as the cells driving forces and as sources/sinks of the electronic/ionic potentials. The graphs are intended to give a qualitative impression of the situation; adapted from (Kulikovsky 2010; O'Hayre et al. 2009).

has to be valid in equilibrium, leading to the *law of mass action* (Bard, Inzelt, and Scholz 2008, p. 91):

$$\sum_{\text{reactants } j} \nu_j \mu_{\text{mol}\blacktriangle j} = \sum_{\text{products } i} \nu_i \mu_{\text{mol}\blacktriangle i} \,. \tag{2.15}$$

From this, the electric potential of both half cells can be derived as[18]:

$$\phi_{\text{el}\blacktriangle\text{ANO}} = -\frac{1}{z_{\text{tot}} F_{\text{Ch}\blacktriangle\text{mol}}} \left(\sum_{\text{products } i} \nu_{\text{ANO}\blacktriangle i} \mu_{\text{mol}\blacktriangle\text{ANO}\blacktriangle i} - \sum_{\text{reactants } j} \nu_{\text{ANO}\blacktriangle j} \mu_{\text{mol}\blacktriangle\text{ANO}\blacktriangle j} \right) , \tag{2.16}$$

[18] see appendix B.3 for calculation

$$\phi_{\mathrm{el}\blacktriangle\mathrm{CAT}} = -\frac{1}{z_{\mathrm{tot}} F_{\mathrm{Ch}\blacktriangle\mathrm{mol}}} \left(\sum_{\text{products } k} \nu_{\mathrm{CAT}\blacktriangle k}\, \mu_{\mathrm{mol}\blacktriangle\mathrm{CAT}\blacktriangle k} - \sum_{\text{reactants } l} \nu_{\mathrm{CAT}\blacktriangle l}\, \mu_{\mathrm{mol}\blacktriangle\mathrm{CAT}\blacktriangle l} \right) . \tag{2.17}$$

Since the chemical potential is highly dependent on the operating conditions, it is advisable to express its value in dependence of an *activity* a_{act} relative to a reference state[19] ${\mu_{\mathrm{mol}}}^{0}$ (Bard, Inzelt, and Scholz 2008, p. 91) (Boeyens 2008, p. 251 et seqq.):

$$\mu_{\mathrm{mol}} = {\mu_{\mathrm{mol}}}^{0} + \Re_{\mathrm{En}\blacktriangle\mathrm{mol}} T \ \ln\left(a_{\mathrm{act}}\right) . \tag{2.18}$$

For an ideal mixture the coefficient $a_{\mathrm{act}\blacktriangle i}$ of the *i*-th species of a *n*-species mixture is given by the mole fraction:

$$y_{\mathrm{Mol}\blacktriangle\mathrm{mol}\blacktriangle i} = \frac{N_{\mathrm{Mol}\blacktriangle\mathrm{mol}\blacktriangle i}}{\sum_j N_{\mathrm{Mol}\blacktriangle\mathrm{mol}\blacktriangle j}}$$

in $\mathrm{mol}_{\mathrm{species}}/\mathrm{mol}_{\mathrm{tot}}$ (Bard, Inzelt, and Scholz 2008, p. 9). In reality mixtures often do not behave ideal. Hence to retain a similar expression $a_{\mathrm{act}\blacktriangle i}$ is transformed into a *relative activity* via:

$$a_{\mathrm{act}\blacktriangle i} = f_i\, y_{\mathrm{Mol}\blacktriangle\mathrm{mol}\blacktriangle i} .$$

Here f_i denotes a dimensionless activity coefficient (Bard, Inzelt, and Scholz 2008, p. 9). The different formulations of the activity and its influence on ${\mu_{\mathrm{mol}}}^{0}$ are summarized in Table 2.2. With equation 2.18, equations 2.16 and 2.17 can

Table 2.2.: **Activities:** The activity of the *i*-th species of a *n*-component mixture can be formulated in dependence of the system to be described (Bard, Inzelt, and Scholz 2008, p. 9 et seqq.) (de Haart 2009a)

Activity	$\mathbf{a_{act}}$	**Description**	${\mu_{\mathrm{mol}}}^{0}$	**State**
constant	1	constant	chemical potential at certain temperature	solid
ideal mixtures	$y_{\mathrm{Mol}\blacktriangle\mathrm{mol}\blacktriangle i}$ (p_{part} for gases)	mole fraction / partial pressure	molar free energy of component in its pure form at certain temperature and pressure	fluid / gaseous
non-ideal mixtures	$f_i\, y_{\mathrm{Mol}\blacktriangle\mathrm{mol}\blacktriangle i}$	relative conditions	(hypothetical) standard state	fluid

[19] e.g. apparent at standard conditions; T = 25 °C, p = 1013 hPa, pH = 0, ionic activity = 1 (Lide 2010).

be written as:

$$\phi_{\mathrm{el}_{\blacktriangle}\mathrm{ANO}} = -\frac{1}{z_{\mathrm{tot}} F_{\mathrm{Ch}_{\blacktriangle}\mathrm{mol}}} \left(\sum_{\text{products } i} \nu_{\mathrm{ANO}_{\blacktriangle} i}\, {}^{0}\mu_{\mathrm{mol}_{\blacktriangle}\mathrm{ANO}_{\blacktriangle} i} - \sum_{\text{reactants } j} \nu_{\mathrm{ANO}_{\blacktriangle} j}\, {}^{0}\mu_{\mathrm{mol}_{\blacktriangle}\mathrm{ANO}_{\blacktriangle} j} + \Re_{\mathrm{En}_{\blacktriangle}\mathrm{mol}} T \cdot \ln\left(\frac{\prod_{\text{products } i} a_{\mathrm{act}_{\blacktriangle}\mathrm{ANO}_{\blacktriangle} i}^{\nu_{\mathrm{ANO}_{\blacktriangle} i}}}{\prod_{\text{reactants } j} a_{\mathrm{act}_{\blacktriangle}\mathrm{ANO}_{\blacktriangle} j}^{\nu_{\mathrm{ANO}_{\blacktriangle} j}}} \right) \right),$$

$$\phi_{\mathrm{el}_{\blacktriangle}\mathrm{CAT}} = -\frac{1}{z_{\mathrm{tot}} F_{\mathrm{Ch}_{\blacktriangle}\mathrm{mol}}} \left(\sum_{\text{products } k} \nu_{\mathrm{CAT}_{\blacktriangle} k}\, {}^{0}\mu_{\mathrm{mol}_{\blacktriangle}\mathrm{CAT}_{\blacktriangle} k} - \sum_{\text{reactants } l} \nu_{\mathrm{CAT}_{\blacktriangle} l}\, {}^{0}\mu_{\mathrm{mol}_{\blacktriangle}\mathrm{CAT}_{\blacktriangle} l} + \Re_{\mathrm{En}_{\blacktriangle}\mathrm{mol}} T \cdot \ln\left(\frac{\prod_{\text{products } k} a_{\mathrm{act}_{\blacktriangle}\mathrm{CAT}_{\blacktriangle} k}^{\nu_{\mathrm{CAT}_{\blacktriangle} k}}}{\prod_{\text{reactants } l} a_{\mathrm{act}_{\blacktriangle}\mathrm{CAT}_{\blacktriangle} l}^{\nu_{\mathrm{CAT}_{\blacktriangle} l}}} \right) \right).$$

Since isolated half cells cannot be constructed, the theoretical cell voltage U_{Nernst} (Nernst potential) in V is given by the sum of the two half cell potentials:

$$\begin{aligned} U_{\mathrm{Nernst}} &:= \phi_{\mathrm{el}_{\blacktriangle}\mathrm{CAT}} + \phi_{\mathrm{el}_{\blacktriangle}\mathrm{ANO}} \\ &= -\frac{1}{z_{\mathrm{tot}} F_{\mathrm{Ch}_{\blacktriangle}\mathrm{mol}}} \left(\left(\sum_{\text{products } k} \nu_{\mathrm{CAT}_{\blacktriangle} k}\, {}^{0}\mu_{\mathrm{mol}_{\blacktriangle}\mathrm{CAT}_{\blacktriangle} k} - \sum_{\text{reactants } l} \nu_{\mathrm{CAT}_{\blacktriangle} l}\, {}^{0}\mu_{\mathrm{mol}_{\blacktriangle}\mathrm{CAT}_{\blacktriangle} l} \right) \right. \\ &\quad + \left(\sum_{\text{products } i} \nu_{\mathrm{ANO}_{\blacktriangle} i}\, {}^{0}\mu_{\mathrm{mol}_{\blacktriangle}\mathrm{ANO}_{\blacktriangle} i} - \sum_{\text{reactants } j} \nu_{\mathrm{ANO}_{\blacktriangle} j}\, {}^{0}\mu_{\mathrm{mol}_{\blacktriangle}\mathrm{ANO}_{\blacktriangle} j} \right) \\ &\quad \left. + \Re_{\mathrm{En}_{\blacktriangle}\mathrm{mol}} T \cdot \ln\left(\frac{\prod_{\text{products } k} a_{\mathrm{act}_{\blacktriangle}\mathrm{CAT}_{\blacktriangle} k}^{\nu_{\mathrm{CAT}_{\blacktriangle} k}} \prod_{\text{products } i} a_{\mathrm{act}_{\blacktriangle}\mathrm{ANO}_{\blacktriangle} i}^{\nu_{\mathrm{ANO}_{\blacktriangle} i}}}{\prod_{\text{reactants } l} a_{\mathrm{act}_{\blacktriangle}\mathrm{CAT}_{\blacktriangle} l}^{\nu_{\mathrm{CAT}_{\blacktriangle} l}} \prod_{\text{reactants } j} a_{\mathrm{act}_{\blacktriangle}\mathrm{ANO}_{\blacktriangle} j}^{\nu_{\mathrm{ANO}_{\blacktriangle} j}}} \right) \right). \end{aligned} \tag{2.19}$$

At standard conditions the last term in equation 2.19 vanishes, what leads to:

$$\begin{aligned} U^{0}_{\mathrm{Nernst}} &= -\frac{1}{z_{\mathrm{tot}} F_{\mathrm{Ch}_{\blacktriangle}\mathrm{mol}}} \left(\mathrm{d}G^{\,0}_{\mathrm{En}_{\blacktriangle}\mathrm{mol}_{\blacktriangle}\mathrm{ANO}} + \mathrm{d}G^{\,0}_{\mathrm{En}_{\blacktriangle}\mathrm{mol}_{\blacktriangle}\mathrm{CAT}} \right) \\ &= -\frac{\mathrm{d}G^{\,0}_{\mathrm{En}_{\blacktriangle}\mathrm{mol}_{\blacktriangle}\mathrm{reac}}}{z_{\mathrm{tot}} F_{\mathrm{Ch}_{\blacktriangle}\mathrm{mol}}} \\ &:= U_{\mathrm{rev}} \ (\textit{reversible cell voltage}) \ [\mathrm{V}] \ . \end{aligned}$$

For all other conditions the Nernst potential can be calculated by (Leithner et al. 2010):

$$U_{\mathrm{Nernst}} = U_{\mathrm{rev}} + \frac{\Re_{\mathrm{En}_{\blacktriangle}\mathrm{mol}} T}{z_{\mathrm{tot}} F_{\mathrm{Ch}_{\blacktriangle}\mathrm{mol}}} \cdot \ln\left(\frac{\prod_{\text{reactants } l} a_{\mathrm{act}_{\blacktriangle}\mathrm{CAT}_{\blacktriangle} l}^{\nu_{\mathrm{CAT}_{\blacktriangle} l}} \prod_{\text{reactants } j} a_{\mathrm{act}_{\blacktriangle}\mathrm{ANO}_{\blacktriangle} j}^{\nu_{\mathrm{ANO}_{\blacktriangle} j}}}{\prod_{\text{products } k} a_{\mathrm{act}_{\blacktriangle}\mathrm{CAT}_{\blacktriangle} k}^{\nu_{\mathrm{CAT}_{\blacktriangle} k}} \prod_{\text{products } i} a_{\mathrm{act}_{\blacktriangle}\mathrm{ANO}_{\blacktriangle} i}^{\nu_{\mathrm{ANO}_{\blacktriangle} i}}} \right) . \tag{2.20}$$

2.3.1. Cell voltage and loss mechanisms

So far only an idealized current less case is assumed. Due to the flow of electrons, ions, and uncharged species in a real fuel cell the hitherto assumed equilibrium is perturbed to some extent. As it can be seen in Figure 2.5 the stationary cell voltage of a real fuel cell is highly dependent on the current density $\vec{j}$ in A/m^2.

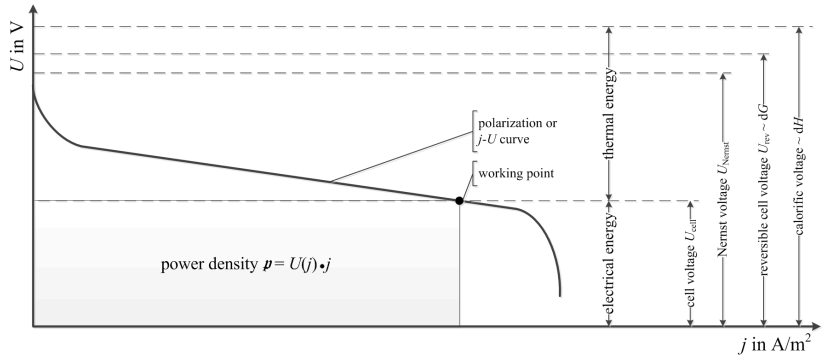

Figure 2.5.: **Polarization curve:** The current density dependence of the cell voltage can be divided into different regions. For small current densities the activation polarization dominates, whereas for higher values of j the ohmic losses are governing the curve. When j increases further, the concentration of the reactants deplete, leading to an exponential loss in cell voltage; adapted from (Scheufen 2011).

2.3.1.1. Electrochemical reactions and activation losses

In electrochemical reactions electrical charges are directly released or consumed. Therefore, the absolute value of the generated electric current density

$$|\vec{j}| = \frac{1}{A}\dot{Q}_{\mathrm{En}\blacktriangle\mathrm{el}}$$

as the change in the number of electric charges $\mathrm{d}Q_{\mathrm{En}\blacktriangle\mathrm{mol}\blacktriangle\mathrm{el}}$ in C per area A in m^2 and time interval dt in seconds is a direct measure for the molar surface reaction rate $r_{\mathrm{reac}\blacktriangle\mathrm{Mol}\blacktriangle\mathrm{surf}}$ in mol/m^{2}s (O'Hayre et al. 2009, p. 72 et seqq.) (*Faraday's law*):

$$|\vec{j}| = \frac{z_{\mathrm{tot}} F_{\mathrm{Ch}\blacktriangle\mathrm{mol}}}{A} \frac{\mathrm{d}N_{\mathrm{Mol,mol}}}{\mathrm{d}t} \tag{2.21}$$

$$= \frac{z_{\text{tot}} F_{\text{Ch}_\blacktriangle\text{mol}}}{A} r_{\text{reac}_\blacktriangle\text{Mol}_\blacktriangle\text{surf}} \cdot \tag{2.22}$$

Mathematically, a surface reaction rate involving i species might be formulated in dependence of dimensionless reaction orders κ_i, the molar surface concentrations $c_{\text{Mol}_\blacktriangle\text{surf}_\blacktriangle i}$ in $\text{mol}_{\text{species}}/\text{m}^2$ of the reacting species, and a kinetic molar reaction rate constant $\Re_{\text{reac}_\blacktriangle\text{Mol}_\blacktriangle\text{surf}}$ with appropriate units to express $r_{\text{reac}_\blacktriangle\text{Mol}_\blacktriangle\text{surf}}$ in $\text{mol}/\text{m}^2\text{s}$ (Behr, Agar, and Jörissen 2010, p. 34) (Baerns et al. 2006):

$$r_{\text{reac}_\blacktriangle\text{Mol}_\blacktriangle\text{surf}} = \Re_{\text{reac}_\blacktriangle\text{Mol}_\blacktriangle\text{surf}} \prod_i c_{\text{Mol}_\blacktriangle\text{surf}_\blacktriangle i}^{\kappa_i} \cdot \tag{2.23}$$

To take into account the temperature dependency of the reaction or charges of the reacting particles, the kinetic reaction rate constant is commonly expressed via an *Arrhenius Equation (*AE*)*

$$\Re_{\text{reac}_\blacktriangle\text{Mol}_\blacktriangle\text{surf}} = \Re^{0}_{\text{reac}_\blacktriangle\text{Mol}_\blacktriangle\text{surf}} \cdot T^{a} \cdot \exp\left(-\frac{\mathrm{d}G_{\text{En}_\blacktriangle\text{mol}_\blacktriangle\text{act}}}{\Re_{\text{En}_\blacktriangle\text{mol}} T}\right) \tag{2.24}$$

in dependence of a pre-exponential constant $\Re^{0}_{\text{reac}_\blacktriangle\text{Mol}_\blacktriangle\text{surf}}$ in $\text{mol}/\text{m}^2\,\text{s}$ and a molar *activation energy* $\mathrm{d}G_{\text{En}_\blacktriangle\text{mol}_\blacktriangle\text{act}}$ in J/mol (Bard, Inzelt, and Scholz 2008, p. 16) (Behr, Agar, and Jörissen 2010, p. 42) (Zhu et al. 2005). Altogether, for a general chemical reaction (see equation 2.14)

$$\nu_{\mathcal{A}}\mathcal{A} + \nu_{\mathcal{B}}\mathcal{B} \rightleftharpoons \nu_{C}\mathcal{C} \tag{2.25}$$

the surface reaction rates can be written as (Riedel 1999):

$$\begin{aligned} r_{\text{reac,tot}_\blacktriangle\text{Mol}} =& r_{\text{reac,forw}_\blacktriangle\text{Mol}} - r_{\text{reac,back}_\blacktriangle\text{Mol}} \\ =& \Re^{0}_{\text{reac,forw}_\blacktriangle\text{Mol}_\blacktriangle\text{surf}} \cdot T^{a_{\text{forw}}} \cdot \exp\left(-\frac{\mathrm{d}G_{\text{En}_\blacktriangle\text{mol}_\blacktriangle\text{act,forw}}}{\Re_{\text{En}_\blacktriangle\text{mol}} T}\right) \prod_{\text{reactants } i} c_{\text{Mol}_\blacktriangle\text{surf}_\blacktriangle\text{eff}_\blacktriangle i} \\ & - \Re^{0}_{\text{reac,back}_\blacktriangle\text{Mol}_\blacktriangle\text{surf}} \cdot T^{a_{\text{back}}} \cdot \exp\left(-\frac{\mathrm{d}G_{\text{En}_\blacktriangle\text{mol}_\blacktriangle\text{act,back}}}{\Re_{\text{En}_\blacktriangle\text{mol}} T}\right) \prod_{\text{products } j} c_{\text{Mol}_\blacktriangle\text{surf}_\blacktriangle\text{eff}_\blacktriangle j}\,, \end{aligned}$$

whereby the index "eff" is indicating the respective effective concentration in a direct neighborhood of the reaction site[20]. As shown in Figure 2.6, the activation energy of the backward reaction may be written by the sum of activation

[20] e.g. the surface on which the reaction takes place

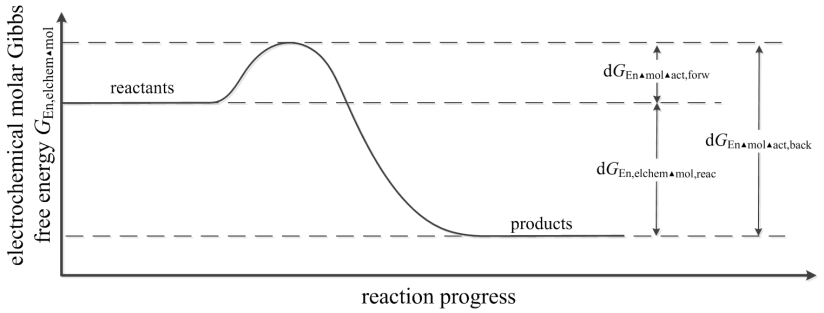

Figure 2.6.: **Activation barrier:** The conversion of reactants to products is impeded via an energetic barrier, limiting the reaction rate to a finite value. The activation energy of the backward reaction is given by the sum of the forward one and its resulting change in electrochemical free energy. Here the case $\phi = 0$ V is shown; modified from (O'Hayre et al. 2009, p. 76).

energy of the forward one and the energy released in it. With this, the current density $\vec{j}$ from equation 2.22 gives (O'Hayre et al. 2009, p. 80):

$$|\vec{j}_{\mathrm{tot}}| = \underbrace{\frac{z_{\mathrm{tot}} F_{\mathrm{Ch\blacktriangle mol}}}{A}\, \Re^{\,0}_{\mathrm{reac,forw\blacktriangle Mol\blacktriangle surf}} \cdot T^{\alpha_{\mathrm{forw}}} \cdot \exp\left(-\frac{\mathrm{d}G_{\mathrm{En\blacktriangle mol\blacktriangle act,forw}}}{\Re_{\mathrm{En\blacktriangle mol}} T}\right) \prod_{\mathrm{reactants}\ i} c_{\mathrm{Mol\blacktriangle surf\blacktriangle eff\blacktriangle}i}^{\kappa_i}}_{|\vec{j}_{\mathrm{forw}}|}$$
$$- \underbrace{\frac{z_{\mathrm{tot}} F_{\mathrm{Ch\blacktriangle mol}}}{A}\, \Re^{\,0}_{\mathrm{reac,back\blacktriangle Mol\blacktriangle surf}} \cdot T^{\alpha_{\mathrm{back}}} \cdot \exp\left(-\frac{\mathrm{d}G_{\mathrm{En\blacktriangle mol\blacktriangle act,forw}} + \mathrm{d}\mathfrak{G}_{\mathrm{En,elchem\blacktriangle mol,reac}}}{\Re_{\mathrm{En\blacktriangle mol}} T}\right) \prod_{\mathrm{products}\ j} c_{\mathrm{Mol\blacktriangle surf\blacktriangle eff\blacktriangle}j}^{\kappa_j}}_{|\vec{j}_{\mathrm{back}}|} \cdot \tag{2.26}$$

In the case of an open circuit $|\vec{j}_{\mathrm{tot}}|$ is zero, leading to:

$$|\vec{j}_{\mathrm{forw}}| = |\vec{j}_{\mathrm{back}}| = |\vec{j}_{\mathrm{exch}}|,$$

with the absolute value of the *exchange current density* $|\vec{j}_{\mathrm{exch}}|$. Although changes in the electrochemical free energy are discussed in a general meaning, only the uncharged case is considered so far. Using Table 2.1, the second term in equation 2.26 can be expressed as (Leithner et al. 2010, p. 84):

$$|\vec{j}_{\mathrm{back}}| = \frac{z_{\mathrm{tot}} F_{\mathrm{Ch\blacktriangle mol}}}{A}\, \Re^{\,0}_{\mathrm{reac,back\blacktriangle Mol\blacktriangle surf}} \cdot T^{\alpha_{\mathrm{back}}}$$
$$\cdot \exp\left(-\frac{\mathrm{d}G_{\mathrm{En\blacktriangle mol\blacktriangle act,forw}} + \mathrm{d}G_{\mathrm{En\blacktriangle mol\blacktriangle reac}} + z_{\mathrm{tot}} F_{\mathrm{Ch\blacktriangle mol}} \Delta\phi}{\Re_{\mathrm{En\blacktriangle mol}} T}\right) \prod_{\mathrm{products}\ j} c_{\mathrm{Mol\blacktriangle surf\blacktriangle eff\blacktriangle}j}^{\kappa_j} \cdot$$

As shown in Figure 2.7, in the open circuit case the activation barrier of the backward reaction is lowered by the electric potential to such an amount that forward and backward reaction are facing the same activation energy barrier (O'Hayre et al. 2009, p. 82). The situation changes when a current is drawn.

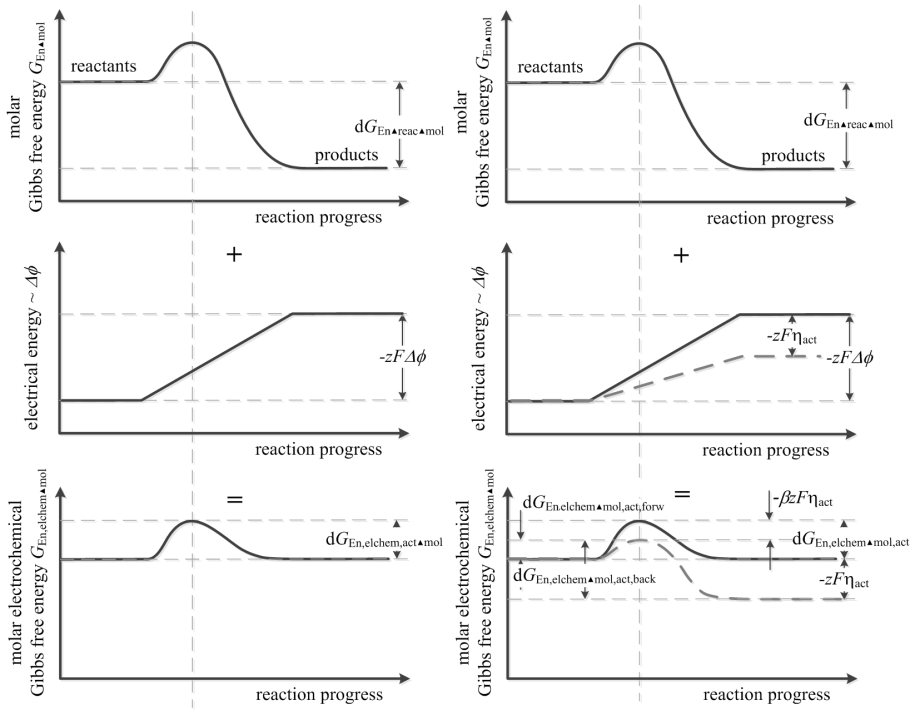

Figure 2.7.: **Electrochemical free energy at equilibrium and under load:** At equilibrium (left) the barrier in free energy across a reaction interface is balanced by the electric potential difference of reactants and products. This leads to a net reaction rate of zero. Under loading conditions (right) the level of electrochemical energy of the products is lowered by the activation overpotential η_{act}. In consequence, the activation energy barrier for the forward one decreases while it increases for the backward reaction. Adapted from (O'Hayre et al. 2009, p. 82-84).

In consequence the potential difference across the reaction surface is increased by an *activation overpotential* η_{act} (see Figure 2.7).

Mathematically, the changes in the activation energies can be considered via an empirical factor β to describe the symmetry of the energy barrier (*Butler-*

*Volmer Equation (*BVE*)*). (O'Hayre et al. 2009, p. 85) (Bard, Inzelt, and Scholz 2008, p. 63 et seqq.):

$$
\begin{aligned}
|\vec{j}_{\text{forw}}| &= |\vec{j}_{\text{exch}}| \cdot \exp\left(\frac{\beta z_{\text{tot}} F_{\text{Ch}_{\blacktriangle}\text{mol}}}{\Re_{\text{En}_{\blacktriangle}\text{mol}} T}\eta_{\text{act}}\right) , \\
|\vec{j}_{\text{back}}| &= |\vec{j}_{\text{exch}}| \cdot \exp\left(-\frac{(1-\beta) z_{\text{tot}} F_{\text{Ch}_{\blacktriangle}\text{mol}}}{\Re_{\text{En}_{\blacktriangle}\text{mol}} T}\eta_{\text{act}}\right) , \\
\Rightarrow |\vec{j}_{\text{tot}}| &= |\vec{j}_{\text{exch}}| \cdot \left\{\exp\left(\frac{\beta z_{\text{tot}} F_{\text{Ch}_{\blacktriangle}\text{mol}}}{\Re_{\text{En}_{\blacktriangle}\text{mol}} T}\eta_{\text{act}}\right) - \exp\left(-\frac{(1-\beta) z_{\text{tot}} F_{\text{Ch}_{\blacktriangle}\text{mol}}}{\Re_{\text{En}_{\blacktriangle}\text{mol}} T}\eta_{\text{act}}\right)\right\} . \qquad (2.27)
\end{aligned}
$$

2.3.1.2. Ohmic losses

The middle region of the polarization curve (see Figure 2.5) is dominated by *ohmic losses*, whose origins are the conductivities $\underline{\underline{\sigma}}_{\text{el/ion}}$ in S/m for electrons and ions. The constitutive law for this phenomena is *Ohm's law* (Bove and Ubertini 2008, p. 54) (Meschede 2006, p. 320):

$$
\begin{aligned}
\vec{j}_{\text{el/ion}} &= \underline{\underline{\sigma}}_{\text{el/ion}} \vec{\mathbb{E}}_{\text{el/ion}} \\
&= -\underline{\underline{\sigma}}_{\text{el/ion}} \operatorname{grad}\left(\phi_{\text{el/ion}}\right) . \qquad (2.28)
\end{aligned}
$$

Accordingly, for a cuboidal shaped conductor (see Figure 2.8) in a 1D-case[21]

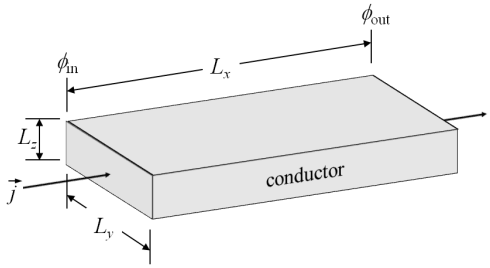

Figure 2.8.: **Schematic conductor:** The voltage loss due to conduction is proportional to its shape and material (Leithner et al. 2010, p. 95).

the change in electric/ionic potential in dependence of the conductor length $L_{\varkappa}$

[21] $\underline{\underline{\sigma}}_{\text{el/ion}}$ is a scalar

in m is given by:

$$\vec{j} = \underline{\underline{\sigma}}_{\text{el/ion}} \underbrace{\frac{\phi_{\text{in}} - \phi_{\text{out}}}{L_{\chi}}}_{\eta_{\text{Ohm}}} \ .$$

Using the electric current $I = \vec{j}/A$ in A and the cross-sectional area $A = L_y \cdot L_z$ of the conductor, the total ohmic loss inside a fuel cell follows as (Mücke 2009c, p. 31 et seqq.):

$$\eta_{\text{Ohm,tot}} = I \cdot \left\{ \sum_{\text{components } i} \left(\underbrace{\frac{L_{\chi_{\blacktriangle} i}}{L_{y_{\blacktriangle} i}\, L_{z_{\blacktriangle} i}\, \underline{\underline{\sigma}}_{\text{el}_{\blacktriangle} i}}}_{:=R_{\text{Ohm,el}_{\blacktriangle} i}} + \underbrace{\frac{L_{\chi_{\blacktriangle} i}}{L_{y_{\blacktriangle} i}\, L_{z_{\blacktriangle} i}\, \underline{\underline{\sigma}}_{\text{ion}_{\blacktriangle} i}}}_{:=R_{\text{Ohm,ion}_{\blacktriangle} i}} \right) \right\} . \tag{2.29}$$

2.3.1.3. Concentration losses

The region on the right side of the polarization curve in Figure 2.5 is dominated by *concentration losses*, which originate in a change of the reactants and products concentrations at the reaction zones. As explained in section 2.1, in fuel cells reactants and products are continuously fed into and led out of the cell. Since mass transport inside the electrodes is diffusion controlled, it competes with the (electro)chemical reactions (O'Hayre et al. 2009, p. 164 et seqq.). The evolution of the concentration profiles over time is illustrated in Figure 2.9. Under constant operational conditions a steady-state situation ($t \to \infty$) is eventually reached where the rates of reactant consumption balances the rate of their supply. In the simplest case *Fick's first law of diffusion* can be applied to describe the diffusive flux $\vec{j}_{\text{diff}}$ in mol/m^2 s (Meschede 2006, p. 238) (O'Hayre et al. 2009, p. 168):

$$\vec{j}_{\text{diff}} = -D_{\text{diff}} \operatorname{grad}\left(c_{\text{Mol}_{\blacktriangle}\text{surf}}\right) \ . \tag{2.30}$$

Here D_{diff} in m^2/s is the mass diffusion coefficient of the diffusion layer. Combining equation 2.30 with equation 2.21 gives for a scalar case:

$$|\vec{j}| = -\frac{z_{\text{tot}} F_{\text{Ch}_{\blacktriangle}\text{mol}}}{A} D_{\text{diff}} \operatorname{grad}(c) \ .$$

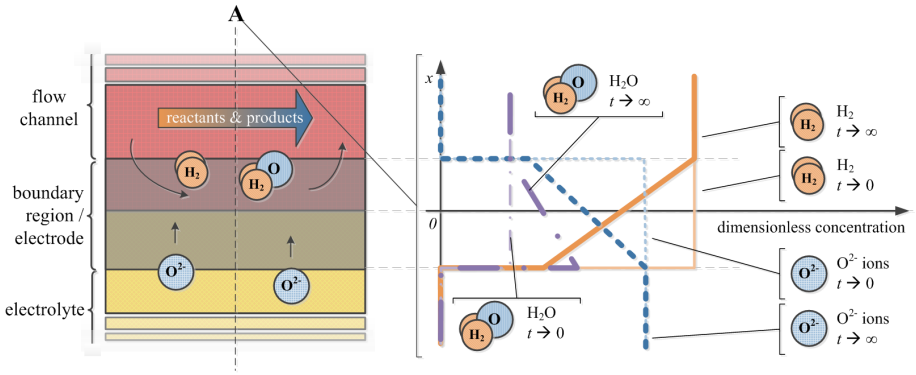

Figure 2.9.: **Concentration gradients:** Because of the electrochemical reactions during operation a concentration gradient between the bulk of the gas channel and the electrode / electrolyte surface is established. Under constant operational conditions a diffusion controlled steady-state situation is eventually reached for the effective concentrations. Here the situation at the plane (A) is shown qualitatively. Modified from (O'Hayre et al. 2009, p. 166).

For a 1D[22] steady-state situation this can be rewritten as:

$$|\vec{j}| = -\frac{z_{\text{tot}} F_{\text{Ch}_\blacktriangle\text{mol}}}{A} D_{\text{diff}} \cdot \left(\frac{c_{\text{Mol}_\blacktriangle\text{surf}_\blacktriangle\text{reac,eff}} - c^{\,0}_{\text{Mol}_\blacktriangle\text{surf}_\blacktriangle\text{reac}}}{L_\chi} \right)$$

$$\Rightarrow c_{\text{Mol}_\blacktriangle\text{surf}_\blacktriangle\text{reac,eff}} = c^{\,0}_{\text{Mol}_\blacktriangle\text{surf}_\blacktriangle\text{reac}} - \frac{|\vec{j}| L_\chi}{z_{\text{tot}} F_{\text{Ch}_\blacktriangle\text{mol}} D_{\text{diff}}} \,. \tag{2.31}$$

Summarizing the last subsections, a change of the effective reactant concentration at the electrode/electrolyte interface leads to (O'Hayre et al. 2009, p. 164 et seqq.):

- *Nernstian losses*: The Nernst voltage in equation 2.20 is decreased due to reduced reactant activities.
- *Reaction losses*: The activation loss in equation 2.27 is increased due to changes in the exchange current density (equation 2.26).

These effects can be summarized in a concentration overpotential η_{conc} in V.

[22] In a layer of width L_χ in m, diffusion only occurs in in χ-direction.

2.3.1.4. Cell voltage and power

Altogether, the cell voltage of a fuel cell U_{cell} in V in dependence of the current density is given by the difference of the Nernst voltage and the discussed overpotentials (Leithner et al. 2010, p. 107):

$$U_{\text{cell}} = U_{\text{Nernst}} - \eta_{\text{act}} - \eta_{\text{Ohm}} - \eta_{\text{conc}} \,. \tag{2.32}$$

Accordingly, the electric power $P_{\text{En}_{\blacktriangle}\text{el}}$ in W follows as (Meschede 2006, p. 400):

$$P_{\text{En}_{\blacktriangle}\text{el}} = U_{\text{cell}} \cdot I_{\text{cell}} \,. \tag{2.33}$$

2.3.2. Efficiency

The efficiency $\eta_{\%}$ in % of an energy conversion process can be defined as (Mücke 2009c, p. 18):

$$\eta_{\%} = \frac{\text{usable energy (exergy)}}{\text{total energy}} \cdot 100\,\% \,.$$

In dependence of the maximum and the rejection temperatures T_{max} and T_{min}, for a conventional heat engine the *Carnot efficiency* $\eta_{\%,\text{Carnot}}$:

$$\eta_{\%,\text{Carnot}} = \frac{T_{\text{max}} - T_{\text{min}}}{T_{\text{max}}} \cdot 100\,\% \,,$$

and for a fuel cell the *reversible efficiency* $\eta_{\%,\text{rev}}$ set upper limits for $\eta_{\%}$ (see Figure 2.10). Due to the losses discussed in the previous sections the *total efficiency* $\eta_{\%,\text{tot}}$ is always lower than $\eta_{\%,\text{rev}}$:

$$\begin{aligned}\eta_{\%,\text{tot}} &= \underbrace{\eta_{\%,\text{rev}}}_{\substack{\text{reversible}\\\text{efficiency}}} \cdot \underbrace{\eta_{\%,\text{Volt}}}_{\substack{\text{voltage}\\\text{efficiency}}} \cdot \underbrace{\eta_{\%,\text{fuel}}}_{\substack{\text{fuel}\\\text{efficiency}}} \cdot \left(\frac{1}{100\,\%}\right)^2 \,, \\ &= \frac{\mathrm{d}G_{\text{En}_{\blacktriangle}\text{mol}}}{\mathrm{d}H_{\text{En}_{\blacktriangle}\text{mol}}} \cdot \frac{U_{\text{cell}}}{U_{\text{rev}}} \cdot \underbrace{\frac{\dot{M}_{\text{Mol}_{\blacktriangle}\text{fuel,conv}}}{\dot{M}_{\text{Mol}_{\blacktriangle}\text{fuel,prov}}}}_{=\frac{|\vec{j}|\,A}{z_{\text{tot}}\,F_{\text{Ch}_{\blacktriangle}\text{mol}}}} \cdot 100\,\% \,.\end{aligned} \tag{2.34}$$

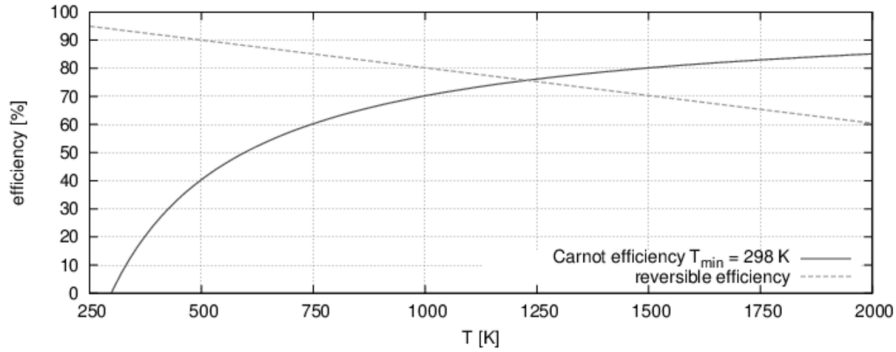

Figure 2.10.: **Reversible vs. Carnot efficiency:** The efficiencies are presented in dependence of the operational temperature in K. For the Carnot cycle a rejection temperature of $T_{\min} = 298\,\mathrm{K}$ is assumed. In particular, at low operational temperatures the reversible efficiency $\eta_{\%,\mathrm{rev}}$ of a fuel cell (green) is significantly larger than the Carnot efficiency $\eta_{\%,\mathrm{Carnot}}$ (red) (Heinzel, Mahlendorf, and Roes 2006)(O'Hayre et al. 2009, p. 60).

The *voltage efficiency* $\eta_{\%,\mathrm{Volt}}$ respects losses due to irreversible effects inside the cell by comparing the measured cell voltage with the reversible one. In contrast, the *fuel efficiency* $\eta_{\%,\mathrm{fuel}}$ respects that not the entire molar-flow of the provided fuel $\dot{M}_{\mathrm{Mol}\blacktriangle\mathrm{fuel,prov}}$ in mol/s accounts to the amount of fuel $\dot{M}_{\mathrm{Mol}\blacktriangle\mathrm{fuel,conv}}$ in mol/s, electrochemically converted by the cell. The final formulation of $\eta_{\%,\mathrm{fuel}}$ is dependent on the mode of operation, expressed through the denominator. Here either the molar flow rate can be kept constant, supplying for every point on the polarization curve a real number и of the molar flow consumed at the point where the U-$\vec{j}$-curve crosses the $\vec{j}$-axis (see Figure 2.5):

$$\eta_{\%,\mathrm{fuel}} = \frac{\vec{j}}{\text{и} \cdot \vec{j}_{\max}} \cdot 100\,\% \,. \qquad (\textit{current efficiency})$$

Alternatively, the fuel flow is adjusted at every point of the U-$\vec{j}$-curve to guarantee a constant stoichiometric ratio $\Pi_{\mathrm{stoich,fuel}}$ between the provided and converted fuel:

$$\eta_{\%,\mathrm{fuel}} = \frac{1}{\Pi_{\mathrm{stoich,fuel}}} \cdot 100\,\% \,.$$

Since the first variant of $\eta_{\%,\mathrm{fuel}}$ increases linear with $\vec{j}$, whereas the second formulation remains constant for all $\vec{j}$, the resulting efficiencies in dependence of

the current either have an extremum at part-load ($\Pi_{\text{stoich,fuel}}$ variable) or follow the voltage efficiency ($\Pi_{\text{stoich,fuel}}$ fixed). (O'Hayre et al. 2009, p. 59-63)

2.4. Solid Oxide Fuel Cells

The operational principle of a SOFC corresponds to what has been discussed in section 2.1 and is illustrated in Figure 2.11. In contrast to the majority of other fuel cells, the electrolyte is made of a solid of (almost) only ionic conductivity. Although various materials have been investigated (see section 2.4.1), variations of Yttrium Stabilized Zirconium (YSZ) are the materials of choice for this purpose ever since the first experiments were made by Baur and Preis during the 1930s (Barrio 2011; Baur and Preis 1938).

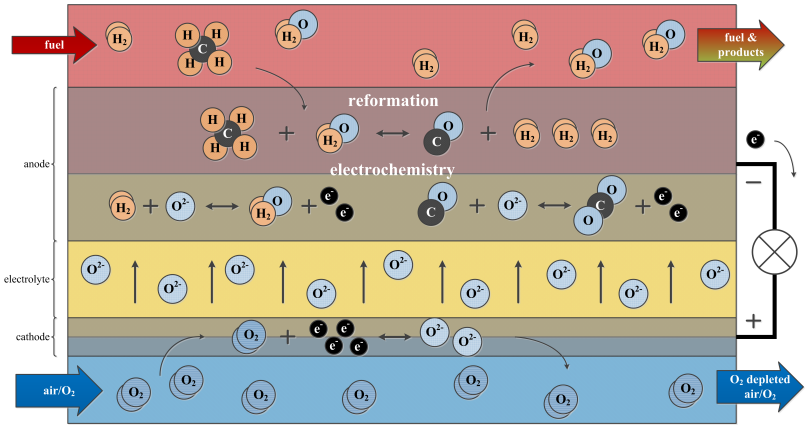

Figure 2.11.: **Schematic operational principle of a SOFC:** Fuel and air/oxygen are continuously supplied to the reaction chambers. Simultaneously, unused fuel and products as well as unused oxygen/O_2 depleted air are removed. If the cell is operated with hydrocarbons, internal reformation might produce hydrogen and CO which undergo a subsequent electrochemical reaction with oxygen ions migrating through the electrolyte. The latter itself are created from the oxygen in the cathodes gaseous domain and electrons coming from the anode via an external electric circuit; adapted from (Wesemeyer, Jocher, and Leithner 2011).

The material properties of the solid electrolyte have contradicting influences on the design of SOFCs. On the one hand the solid state allows a wide range of

possible cell geometries (see chapter 3). On the other hand its charge transport is based on semiconductor physics (see Figure 2.3), requiring a high temperature for sufficient conductivity (see section 2.4.2). Therefore, with an operational temperature of 900 to 1300 K the SOFC accounts to the high temperature fuel cells (see Table A.2 in appendix A.2) (Bove and Ubertini 2006)(Irvine and Sauvet 2001). (Heinzel, Mahlendorf, and Roes 2006, p. 15)(Vielstich, Lamm, and Gasteiger 2003a, p. 335 et seqq.)

Since the commonly used YSZ conducts oxygen ions to the anode, both hydrogen as well as carbon containing species[23] can be directly utilized electrochemically (Vielstich, Lamm, and Gasteiger 2003a, p. 335 et seqq.) (McIntosh and Gorte 2004), according to the following reaction schemes (Zehe, Gordon, and Mcbride 2002):

$$H_2 + \frac{1}{2}O_2 \rightleftharpoons H_2O \qquad (\mathrm{d}G^{\,0}_{\mathrm{En}_\blacktriangle\mathrm{mol},\mathrm{reac}} = -228.6\ \mathrm{kJ/mol})\,, \quad (2.35)$$

$$CO + \frac{1}{2}O_2 \rightleftharpoons CO_2 \qquad (\mathrm{d}G^{\,0}_{\mathrm{En}_\blacktriangle\mathrm{mol},\mathrm{reac}} = -257.2\ \mathrm{kJ/mol})\,, \quad (2.36)$$

$$CH_4 + 2\,O_2 \rightleftharpoons CO_2 + 2\,H_2O \qquad (\mathrm{d}G^{\,0}_{\mathrm{En}_\blacktriangle\mathrm{mol},\mathrm{reac}} = -800.8\ \mathrm{kJ/mol})\,. \quad (2.37)$$

Here the high operational temperature is advantageous, because the reaction rate is increased sufficiently to use non-noble metals as anode catalyst (Baur and Ehrenberg 1912) (O'Hayre et al. 2009, p. 270 et seqq.). Usually Ni is applied for this purpose. Since Ni is also a good catalyst for the reformation of hydrocarbons towards CO and hydrogen, thermal integration by internal reformation is possible and hence will be addressed in section 2.5.

Drawbacks of the high temperature are the high activity of the reformation catalyst and the limitation towards materials that can withstand the operational conditions[24]. The latter not only have to maintain their structural integrity,[25] but also the gas tightness of the cell (Vielstich, Lamm, and Gasteiger 2003a, p. 341). Therefore, despite of corrosion resistance, chemical compatibility, and little vapor pressures, in particular a sufficiently high Young's modulus Y_{mech} in Pa, and a comparable Thermal Expansion Coefficient (see also γ_{th}) (TEC) in 1/K are required for all components (de Haart 2009c) (Larminie and Dicks 2003, p. 213) (Tietz 1999).

[23] e.g. CO and lower hydrocarbons

[24] strongly oxidizing and reducing atmospheres (Wesemeyer, Jocher, and Leithner 2011) in often highly humidified gases at elevated temperatures

[25] little re-sintering and creeping

Since high electric current densities j_{el} in A/m^2 are desirable, the ohmic losses should be reduced by adjusting the electric $\underline{\underline{\sigma}}_{el}$ and ionic $\underline{\underline{\sigma}}_{ion}$ conductivities (both in S/m) of the cells components (Larminie and Dicks 2003, p. 220). Current sources and sinks are the oxidation- and reduction-reactions, taking place at the common boundaries of gas-phase, electronic, and ionic conductor,[26] the Three Phase Boundary (TPB) (Vielstich, Lamm, and Gasteiger 2003a, p. 337) (Wesemeyer, Jocher, and Leithner 2011). Therefore, for high electrochemical performance, both the anode and the cathode in total must not only be a Mixed Ionic and Electronic Conductor (MIEC) with extended networks for electronic as well as ionic conduction, but also have to have a high porosity (see Figure 2.12). To utilize the active cell volume to a high extend

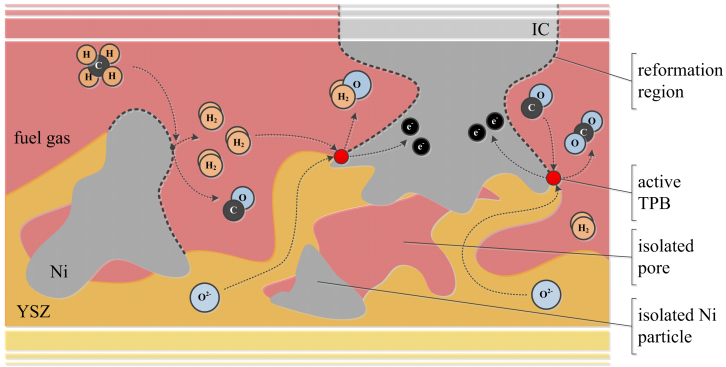

Figure 2.12.: **TPB formation inside a SOFC electrode:** Electrochemical reactions only occur at those lines (points in 2D), where uninterrupted paths of pores, ionic-, and electronic conductor meet. Ni is commonly used as electronic conductor. Since it is also catalytic towards reformation of hydrocarbons, the corresponding reactions occur at the interfaces of Ni and uninterrupted pores; adapted from (Wesemeyer, Jocher, and Leithner 2011).

and to reduce thermo-mechanical stresses, the temperature should be as homogeneously distributed as possible throughout the cell. Therefore, not only the reformation and electrochemistry have to be adjusted. Moreover, the thermal conductivity λ_{En} in W/m K of all components as well as their respective heat transfer coefficients α_{th} in W/m^2 K should be as high as possible (de Haart

[26] all having uninterrupted paths to their respective contact area

2009d; Mücke 2009a). To increase the cell performance,[27] additionally the diffusion coefficient[28] D in m^2/s should be sufficiently large to guarantee an effective gas transport (Mücke 2009b, p. 40) (Vielstich, Lamm, and Gasteiger 2003a, p. 337). For improving not only the cell but also the entire system performance, the "pressure drop" dp in Pa should be minimized (de Haart 2009c).

Finally, from a possible customers point of view, on the one hand the required volume V_{Vol} in m^3, mass m_{Mass} in kg, and Material and Production Costs MPC in €/unit should be reduced to a minimum,[29] while on the other hand service intervals and operational lifetime are maximized (Steinberger-Wilckens 2009; Steinberger-Wilckens 2010; Tietz 1999). The general aspects are sum-

Table 2.3.: **General requirements for fuel cell materials:** To build an efficiently working cell the material properties of the different cell zones have to be matched to one another. In the topmost columns the operational conditions are summarized. In the middle as well as in the footer of the table material properties, and in the bottom lines general requirements for the construction of cells/stacks are listed. The arrows indicate "as high as possible (↑)" and "as low as possible (↓)"; modified from (Leithner et al. 2010).

Interconnect (IC)	**anode (ANO) (–)**	**electrolyte (ELE)**	**cathode (CAT) (+)**	**interconnect IC**
		$\overset{e\ \bar{Ch}}{\longleftarrow}$ oxidation	$\overset{e\ \bar{Ch}}{\longleftarrow}$ reduction	
$\phi_{\text{el}\blacktriangle\text{ANO/IC}}$ $\vec{J}_{\text{el}\blacktriangle\text{ANO/IC}}$ $T_{\text{ANO/IC}}$	$\phi_{\text{el/ion}\blacktriangle\text{ANO}}$ $\vec{J}_{\text{el/ion}\blacktriangle\text{ANO}}$ T_{ANO} $\dot{m}_{\text{Mass}\blacktriangle\text{ANO}}$	$\phi_{\text{el/ion}\blacktriangle\text{ELE}}$ $\vec{J}_{\text{el/ion}\blacktriangle\text{ELE}}$ T_{ELE}	$\phi_{\text{el/ion}\blacktriangle\text{CAT}}$ $\vec{J}_{\text{el/ion}\blacktriangle\text{CAT}}$ T_{CAT} $\dot{m}_{\text{Mass}\blacktriangle\text{CAT}}$	$\phi_{\text{el}\blacktriangle\text{CAT/IC}}$ $\vec{J}_{\text{el}\blacktriangle\text{CAT/IC}}$ $T_{\text{CAT/IC}}$
	$A_{\text{eff}\blacktriangle\text{vol}\blacktriangle\text{ANO}}\uparrow$ $D_{\text{ANO}}\uparrow$ $dG_{\text{En}\blacktriangle\text{mol}\,\text{act}\blacktriangle\text{ANO}}\downarrow$ $dp_{\text{ANO}}\downarrow$		$A_{\text{eff}\blacktriangle\text{vol}\blacktriangle\text{CAT}}\uparrow$ $D_{\text{CAT}}\uparrow$ $dG_{\text{En}\blacktriangle\text{mol}\,\text{act}\blacktriangle\text{CAT}}\downarrow$ $dp_{\text{CAT}}\downarrow$	
$R_{\text{Ohm}\blacktriangle\text{el}\blacktriangle\text{ANO/IC}}\downarrow$ $Y_{\text{mech}\blacktriangle\text{ANO/IC}}\uparrow$ $\gamma_{\text{th}\blacktriangle\text{ANO/IC}}$ $\lambda_{\text{En}\blacktriangle\text{ANO/IC}}\uparrow$	$R_{\text{Ohm}\blacktriangle\text{el/ion}\blacktriangle\text{ANO}}\downarrow$ $Y_{\text{mech}\blacktriangle\text{ANO}}\uparrow$ $\gamma_{\text{th}\blacktriangle\text{ANO}}$ $\lambda_{\text{En}\blacktriangle\text{ANO}}\uparrow$	$R_{\text{Ohm}\blacktriangle\text{el/ion}\blacktriangle\text{ELE}}\downarrow$ $Y_{\text{mech}\blacktriangle\text{ELE}}\uparrow$ $\gamma_{\text{th}\blacktriangle\text{ELE}}$ $\lambda_{\text{En}\blacktriangle\text{ELE}}\uparrow$	$R_{\text{Ohm}\blacktriangle\text{el/ion}\blacktriangle\text{CAT}}\downarrow$ $Y_{\text{mech}\blacktriangle\text{CAT}}\uparrow$ $\gamma_{\text{th}\blacktriangle\text{CAT}}$ $\lambda_{\text{En}\blacktriangle\text{CAT}}\uparrow$	$R_{\text{Ohm}\blacktriangle\text{el}\blacktriangle\text{CAT/IC}}\downarrow$ $Y_{\text{mech}\blacktriangle\text{CAT/IC}}\uparrow$ $\gamma_{\text{th}\blacktriangle\text{CAT/IC}}$ $\lambda_{\text{En}\blacktriangle\text{CAT/IC}}\uparrow$
$m_{\text{Mass}\blacktriangle\text{ANO/IC}}\downarrow$ $MPC_{\text{ANO/IC}}\downarrow$ $V_{\text{Vol}\blacktriangle\text{ANO/IC}}\downarrow$	$m_{\text{Mass}\blacktriangle\text{ANO}}\downarrow$ $MPC_{\text{ANO}}\downarrow$ $V_{\text{Vol}\blacktriangle\text{ANO}}\downarrow$	$m_{\text{Mass}\blacktriangle\text{ELE}}\downarrow$ $MPC_{\text{ELE}}\downarrow$ $V_{\text{Vol}\blacktriangle\text{ELE}}\downarrow$	$m_{\text{Mass}\blacktriangle\text{CAT}}\downarrow$ $MPC_{\text{CAT}}\downarrow$ $V_{\text{Vol}\blacktriangle\text{CAT}}\downarrow$	$m_{\text{Mass}\blacktriangle\text{CAT/IC}}\downarrow$ $MPC_{\text{CAT/IC}}\downarrow$ $V_{\text{Vol}\blacktriangle\text{CAT/IC}}\downarrow$
$R_{\text{Ohm,cont}\blacktriangle\text{ANO/IC}}\downarrow$ $\alpha_{\text{th}\blacktriangle\text{ANO/IC}}\uparrow$	$R_{\text{Ohm,cont}\blacktriangle\text{ANO/ELE}}\downarrow$ $\alpha_{\text{th}\blacktriangle\text{ANO/ELE}}\uparrow$	$R_{\text{Ohm,cont}\blacktriangle\text{CAT/ELE}}\downarrow$ $\alpha_{\text{th}\blacktriangle\text{CAT/ELE}}\uparrow$	$R_{\text{Ohm,cont}\blacktriangle\text{CAT/IC}}\downarrow$ $\alpha_{\text{th}\blacktriangle\text{CAT/IC}}\uparrow$	

[27] by reduced concentration overpotential ϕ_{conc} in V

[28] see equation 2.30

[29] e.g. by readily available and easy-to-machine materials

marized in Table 2.3. Since their properties are of major importance for model creation, the materials for the different cell components are reviewed in the following subsections.

2.4.1. Anode

At the anode the oxidation of fuel occurs in the presence of oxygen ions coming from the electrolyte. Therefore, on a global scale the anode has to be penetrable for electrons, oxygen ions as well as for gas particles. To reduce the overall losses[30] and to enhance the electrochemical performance by increasing the number of TPBs, the transport of all species through it should be facilitated via extended percolating transport paths between the gas channel and the electrolyte (Keil 1999; Zhao and Virkar 2010). Additionally, a high tolerance towards degradation[31] is in particular desirable if the cell is operated with hydrocarbons. In the latter case, a large internal surface from reformation catalyst and gas-phase is beneficial for the performance too (de Haart 2010; Hauch and Mogensen 2010; Salazar-Villalpando and Reyes 2009; Wilson et al. 2006). Although some of these requirements can be addressed by the manufacturing process, the electronic and ionic resistances are also dependent on the materials used and their relative volume fractions (Mücke 2009c). Altogether, a porous, sponge like structure seems to be most promising for the anodes purposes so far, because it additionally provides sufficient mechanical strength (Aruna, Muthuraman, and Patil 1998; Hecht et al. 2005; Rajaram et al. 2008). (Vielstich, Lamm, and Gasteiger 2003a, p. 338) (Zhu and Deevi 2003a)

Since reducing conditions are governing the anode domain, metals are stable under a wide range of operating conditions. Although electric conductivity and corrosion resistance of metals decrease with temperature (Meschede 2006, p. 328) (Zeng and Natesan 2004), anodes made of mixtures from metals/alloys and ceramics (e.g. Ni-YSZ), so called *cermets*, are today's state of art. As already mentioned, in particular Ni is commonly applied, because it combines a high electrochemical and catalytic activity with low costs and chemical compatibility. The manufacturing process of a Ni-YSZ cermet follows the subsequently listed basic steps (Aruna, Muthuraman, and Patil 1998; de Haart 2009c; Mücke 2009b; Tietz, Buchkremer, and Stöver 2002):

[30] ohmic as well as concentration

[31] e.g. sulfur poisoning, soot fouling, (re-)oxidation of Ni to NiO (de Haart 2010)

- Ball milling to produce fine powders of NiO, YSZ, and filler, whereby the milling time determines the particle size (Kusy 1977; Liu et al. 2010a);
- mixing of the powders according to the expected average composition of the cermet (Simwonis et al. 1999);
- (hot-)pressing to the intended shape, whereby the pressure determines the porosity of the green cermet (Balakrishnan et al. 2010; Li et al. 2003; Zhan and Lee 2010);
- sintering, whereby the temperature, atmosphere, and time are important for the final properties (Kwon and Choi 2006; Lee et al. 2002).

Altogether, a SOFC anode-cermet consists of a sponge-like structure, made from particles of more or less the same size by sintering, whose electrochemical properties strongly depend on the manufacturing procedure. Due to its porous nature, the TPBs are spread all over the anode, greatly enhancing its performance. Nevertheless, a precise determination of its local properties is difficult and thus special attention is paid to this aspect below in section 4.3.1. (Vielstich, Lamm, and Gasteiger 2003a, p. 337-338)

2.4.2. Electrolyte

During operation the electrolyte is simultaneously in contact with two diametrical opposite domains, a highly oxidizing and a highly reducing one. Therefore, it has to constantly separate both regimes even at a temperature of up to 1300 K, while featuring superior ionic and negligible electronic conductivity (de Haart 2009d). Since ionic conductivity of solids is based on lattice defects, it is on the one hand determined by the defect concentration and grows on the other hand with temperature[32] (Ashcroft and Mermin 2007, p. 789). Although various materials and composites have been investigated, the low ionic conductivity of the electrolyte, compared to the electrodes,[33] is still the main source for internal voltage loss (Antoni 2004; Mücke 2009c). To maintain sufficient conductivity even at reduced temperature ($T \approx 900$ - 1000 K), it should be made as thin as possible (de Haart 2009d) (National Energy Technology Laboratory 2004, p. 7-2). (Vielstich, Lamm, and Gasteiger 2003a, p. 337)

[32] the mobility of defects is enhanced with temperature
[33] about 100 times less

State of the art materials are based on MO_2 and $M_2'O_3$ cermets (M = Ce, Zr and M' = rare earths, Sc, Y) with a fluorite lattice. For the metals Ce and Zr up to a certain threshold the oxygen conductivity increases with the dopant concentration. Similar results can be found for rare earths from Yb to La (Antoni 2004). For Zr highest conductivities are reached with Sc doping, but for economical reasons commonly Y with a dopant concentration of 8 to 8.5 mol% is used; so called Yttrium Stabilized Zirconium (YSZ) (Vielstich, Lamm, and Gasteiger 2003a, p. 337) (Fergus 2006) (National Energy Technology Laboratory 2004, p. 7-2). As for other semiconductors (Ashcroft and Mermin 2007, p. 726 et seqq.), the ionic conductivity of electrolytes can be expressed in dependence of T by an Arrhenius like approach (Bossel 1992, p. B13):

$$\underline{\underline{\sigma}}_{\mathrm{ion_{\blacktriangle}ELE}}(T) = \underline{\underline{\sigma}}^{0}_{\mathrm{ion_{\blacktriangle}ELE}} \exp\left(-\frac{\mathrm{d}G_{\mathrm{En_{\blacktriangle}mol,act,ion_{\blacktriangle}ELE}}}{k_{\mathrm{En,B}}T}\right). \tag{2.38}$$

Measurements made by Araki et al. (Araki et al. 2009) have shown that the conductivity of various electrolytes decreases with operational time[34]. Although usually not done, therefor for long term simulations a time dependency should be introduced in eq. 2.38. Like the other ceramic components, the electrolyte is produced in a powder process consisting of ball milling, pressing, and sintering (de Haart 2009a). In this context various studies[35] have given strong indications for an influence of the process parameters on the resulting material properties, which is commonly not considered in modeling too.

2.4.3. Cathode

Although the majority of requirements are similar to those of the anode, the cathode has to succeed in a heavily oxidizing regime. Therefore, uncoated metals cannot be applied here, requiring alternative ceramic catalyst materials for oxygen reduction and electron conduction (Vielstich, Lamm, and Gasteiger 2003a, p. 339).

Nowadays state of the art material is Lanthanum Strontium Manganite $\left(La_{0.84}Sr_{0.16}MnO_3\right)$ (LSM), whereby the ionic conductivity of the perovskite

[34] e.g. 8YSZ degrades over 1000 h of operation to about 60 % of its original value (Araki et al. 2009)

[35] e.g. (Evans et al. 2009; He et al. 2002; Jiao, Shikazono, and Kasagi 2010; Waldbillig and Kesler 2009)

is adjusted by the La/Sr ratio. Since the conductivity of this p-type semiconductor for oxygen ions is very limited, it is usually mixed with YSZ during fabrication (Haile 2003; Sato, Kinoshita, and Abe 2010). Alternative studies attempt to use intrinsic MIECs for the cathode to extend the TPBs to (almost) the entire interface of gas and solid phase[36]. The material of choice for this is Lanthanum Strontium Cobalt Ferrite $\left(La_{0.2}Sr_{0.8}Co_{0.2}Fe_{0.8}O_{3-\delta}\right)$ (LSCF) (Cain et al. 2010; Leone et al. 2008). LSCF provides not only extended TPBs but also higher oxygen exchange kinetics compared to a classical LSM-YSZ cathode. Drawbacks are a TEC mismatch[37] and chemical reactions with YSZ. The latter makes a protective layer of Gadolinium Doped Cerium $\left(Ce_{0.8}Gd_{0.2}O_{2-\delta}\right)$ (GDC) necessary (Zeidler 2010, p. 35) (Ishihara 2008, p. 25). Nevertheless, various studies[38] have shown an outstanding performance of these mixed cathodes, making high power densities even at lower temperature possible[39]. (Mücke 2009b, p. 77-85)

2.4.4. Interconnect

The main purposes of the Interconnect (IC) are the conduction of the generated electric current from one cell of a stack to another, a reliable separation of neighboring cells, and the distribution of reactants to the electrodes as well as the removal of products from them[40]. An ideal IC material should satisfy the following aspects over a full product life-cycle[41] (Alman and Jablonski 2007; Fontana et al. 2007; Jablonski, Cowen, and Sears 2010; Shen et al. 2010):

1. A high electronic[42] and almost no ionic conductivity.

2. Chemical and mechanical stability without phase transitions or reactions with other cell components or operational media under simultaneous

[36] despite of blocked pores

[37] the γ_{th} is larger

[38] e.g. (Torres-Garibay and Kovar 2009; Lv et al. 2006; Tietz et al. 2006; Tietz et al. 2007; Tucker, Cheng, and DeJonghe 2011; Park et al. 2010)

[39] e.g. $\vec{j}$ goes up to 28,000 A/m^2 at $T \approx 1050$ K measured by scientists at Forschungszentrum Jülich (Mücke 2009b, p. 85)

[40] by imprinted gas distribution manifolds

[41] about 40,000 hours (Alman and Jablonski 2007; Fontana et al. 2007; Steinberger-Wilckens 2010)

[42] $\underline{\sigma}_{\text{el}\blacktriangle\text{IC}} \geq 100$ S/m (Zhu and Deevi 2003b)

contact to highly reducing and oxidizing conditions (Liu 2008; Shaigan et al. 2010).

3. No volatile ingredients, which might react with the operational media (Fergus 2005).

4. A reliable separation of the anode and cathode chambers.

5. No TEC mismatches with other cell components ($\gamma_{th_{\blacktriangle}IC} \approx 10.5 \cdot 10^{-6}$ 1/K (de Haart 2009c; Fergus 2005; Mücke 2009b)).

6. High thermal conductivity ($\lambda_{En_{\blacktriangle}IC} \geq 5$ W/m K (Fontana et al. 2007)) to homogenize the temperature distribution inside the cell.

Moreover, it should be cheap and easy to manufacture (Fontana et al. 2007; Jablonski, Cowen, and Sears 2010). Although a sufficient corrosion resistance and a reduction of TEC mismatches are still challenging for metals,[43] their reduced weight, higher electric and thermal conductivity, better mechanical stability, gas tightness, and easier machinability compared to ceramic ones[44] are advantageous (Jablonski and Cowen 2009; Lin and Wu 2009; Liu 2008; Montero et al. 2008). In combination with the trend of decreasing the operational temperature to 900 - 1100 K the development of special, very pure stainless steel alloys like e.g. Crofer22APU (VDM 2005; VDM 2010), ZMG232, ZMG 232L or E-brite (Ludlum 2007) let metallic ICs succeed over ceramic ones during the recent years (de Haart 2009c). (Zhu and Deevi 2003b)

2.4.5. Sealant

Sealants are intended to close all holes and lids between different cell components, so that anode and cathode are gas tight and well separated (Vielstich, Lamm, and Gasteiger 2003a, p. 341). Therefore, the material should have good flow properties, neither conduct any species, nor react with cell components or operational media (Goel, Pascual, and Ferreira 2010; Batfalsky et al. 2006; Haanappel et al. 2005; Liu et al. 2011). Today various glass-ceramics based on BaO and SrO are commonly used (Jin and Lu 2010).

[43] e.g. attained by high Chromium contents or various coatings (Shaigan et al. 2010; Tucker et al. 2010)

[44] typically made from doped $LaCrO_3$ or $La_{1-\chi}Ca_{\chi}CrO_3$

2.5. Reformation of lower hydrocarbons

As already discussed in section 2.4, the oxidation occurs on the fuel gas side of a SOFC, making it possible to directly operate the cell with carbon based fuels. Although theoretically possible, the direct oxidation of methane (see equation 2.37) requires a simultaneous exchange of eight electronics. This leads to only small reaction rates (Vielstich, Lamm, and Gasteiger 2003a, p. 336) and makes (external) pre-reformation to CO and H_2 meaningful.

Table 2.4.: **Internal reformation of hydrocarbons:** Advantages and disadvantages of the internal fuel reformation inside SOFC anodes.

Advantages	**Disadvantages**
simplified system design due to waving of an external reformer	high thermal gradients lead to mechanical tensions
high system efficiency due to thermal integration and reduced cooling demand	soot deposition reduces the catalyst activity (also for DIR the electrochemical performance)
optimized reformation chemistry, since the electrochemical reactions consume H_2 and CO	larger number of parameters with an influence on the SOFC operation
precise reaction control via catalyst selection and tailored microstructure	desulfurization necessary

Fortunately, the operational temperature and the Ni catalyst open an alternative pathway for direct utilization of (desulfurized) hydrocarbons by Internal Reformation (IR)[45] (Bove and Ubertini 2008, p. 55):

$$C_\chi H_\psi O_\omega + (\chi - \omega) H_2O \rightleftharpoons \chi CO + \left(\chi - \omega + \frac{\psi}{2}\right) H_2 \,,$$

and

$$CO + H_2O \rightleftharpoons CO_2 + H_2 \,.$$

This approach is particularly advantageous because exhaust heat from the electrochemical reactions can be directly used for the energy consuming reforma-

[45] The term Indirect Internal Reformation (IIR) is used if a separate reformation chamber is incorporated into the cell; a direct reformation inside the anode chamber is termed Direct Internal Reformation (DIR).

tion (*chemical heat pump*), thereby avoiding losses and complexity from heat transfer processes (Schlitzberger, Leithner, and Zindler 2009; Schlitzberger 2012). Additionally, the systems heating demand can be reduced by an utilization of the[46] electrochemically produced steam for a Direct Internal Reformation (DIR) (see equation 2.35). In consequence, the IR offers an intrinsic heat management capability for the entire stack, what reduces the need for peripheral components (Bove and Ubertini 2008, p. 142). On the downside, the temperature reduction due to reformation leads to a decreased electrochemical activity of the cell (Timmermann et al. 2010). In addition, the possible presence of large temperature gradients within the ceramic materials results in the formation of thermo-mechanical stresses (Mogensen et al. 2011). In combination with a certain probability for soot deposition in the porous structure of the catalyst/anode, a degradation of the fuel cell performance has to be considered (Anderson et al. 2003, p. 9)(Bagotsky 2009, p. 149). Although several benefits as well as disadvantages exist for the IR of hydrocarbons in SOFCs (see Table 2.4), DIR seems promising for highly integrated systems. Hence in this study the DIR of methane is assumed.

2.5.1. Reformation reactions

A lot of technical processes,[47] including low temperature fuel cells, require purified hydrogen as reactant, making the reformation of the chemical compounds in (bio-)hydrocarbons to hydrogen and other byproducts very well known for more than a century. The main techniques for this way of hydrogen production are Steam Reformation (SR), Water-Gas-Shift (WGS), Autothermal Reformation (AR), Partial Oxidation (POX), and Dry Reformation (DR) (see Figure 2.13).

2.5.1.1. Steam reformation

Commercial production of hydrogen[48] is mainly done[49] by the Steam Reformation (SR). According to the reaction scheme:

$$\mathrm{CH_4 + H_2O \rightleftharpoons CO + 3\,H_2} \quad \text{with} \quad \mathrm{d}G^{0}_{\mathrm{En_{\blacktriangle mol},reac}} = +206\ \mathrm{kJ/mol}\,. \tag{2.39}$$

[46] at operating temperature
[47] e.g. the Haber-Bosch-Ammonia synthesis
[48] about 50 million tons per year (Leon 2008, p. 20)
[49] over 80 % (Leon 2008, p. 20)

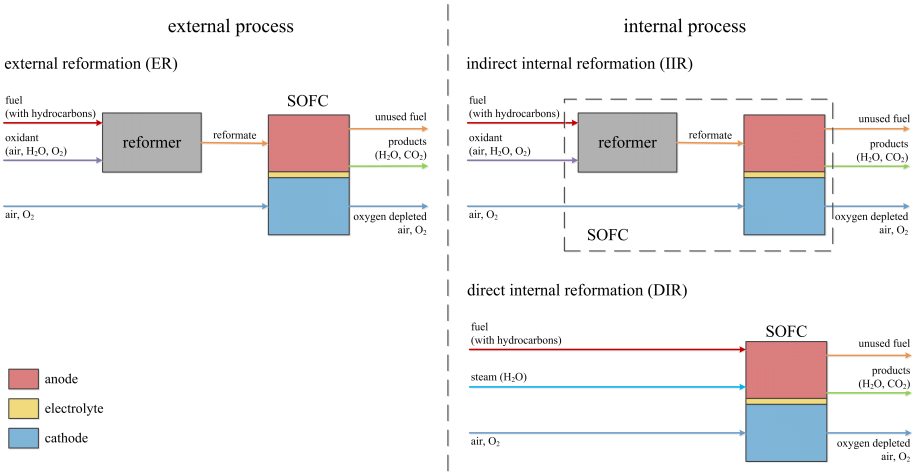

Figure 2.13.: **Operation principles of external and internal reformation processes for fuel processing in SOFC applications:** External Reformation (ER) and IIR require separate reformation chambers in the upstream direction of the fuel gas flow. In the DIR reformation and electrochemistry share the catalyst; modified from (Heinzel, Mahlendorf, and Roes 2006, p. 35).

In this process, one molecule of methane reacts under absorption of energy with one molecule of water, producing three molecules of hydrogen and one molecule of carbon monoxide. In technical systems[50] the required heat in general is either supplied by a partial oxidation of the fuel or an external heating of the system[51]. An advantage of the latter method is that since endothermic fuel reformation and heat supply[52] occur in different domains, the resulting synthesis gas is not diluted with N_2 from the air. In consequence, this method has the highest process efficiency among all reformation techniques. (Heinzel, Mahlendorf, and Roes 2006, p. 30)

Drawbacks of this process[53] are large system volumes with slow process kinetics due to the need for external heating. Here the DIR is the method of choice, since heat from the electrochemical reactions in the anode can be used to power the neighboring SR (Mogensen et al. 2011).

[50] $T \approx 800$ - 1200 K, $p \approx 1$ - 40 bar (Leithner et al. 2010, p. 5-36)
[51] like e.g. at refineries (Mogensen et al. 2011)
[52] by in general oxidation
[53] which in technical applications usually is catalyzed by Ni, Ru or Pt

2.5.1.2. Water-gas-shift

If steam is still apparent in the products of a SR, the process is followed by a Water-Gas-Shift (WGS) reaction, converting carbon monoxide and water to carbon dioxide and hydrogen:

$$CO + H_2O \rightleftharpoons CO_2 + H_2 \quad \text{with} \quad {}^{0}_{\mathrm{d}G_{\mathrm{En}_{\blacktriangle}\mathrm{mol},\mathrm{reac}}} = -41\ \mathrm{kJ/mol}\,. \tag{2.40}$$

If a sufficient amount of steam is apparent, in combination with equation 2.39 it follows an overall endothermic net-reaction:

$$CH_4 + 2\,H_2O \rightleftharpoons CO_2 + 4\,H_2 \quad \text{with} \quad {}^{0}_{\mathrm{d}G_{\mathrm{En}_{\blacktriangle}\mathrm{mol},\mathrm{reac}}} = +165\ \mathrm{kJ/mol}\,. \tag{2.41}$$

In addition it is also possible that the Dry Reformation (DR) is present, converting methane and carbon dioxide to carbon monoxide and hydrogen according to:

$$CH_4 + CO_2 \rightleftharpoons 2\,CO + 2\,H_2 \quad \text{with} \quad {}^{0}_{\mathrm{d}G_{\mathrm{En}_{\blacktriangle}\mathrm{mol},\mathrm{reac}}} = +247\ \mathrm{kJ/mol}\,. \tag{2.42}$$

As long as there is no oxygen available, reactions 2.39 to 2.42 occur in parallel inside the reformer, whereas the overall equilibrium distribution of CH_4, CO, CO_2, H_2, and H_2O is dependent on the operational temperature. Due to the parallel nature of WGS, DR, and SR the advantages, drawbacks, and technical process parameters are similar. (Heinzel, Mahlendorf, and Roes 2006, p. 30-31)

2.5.1.3. Partial oxidation

Another way to provide the heat for the reformation is to partially oxidize some fuel ($\lambda_{\mathrm{stoich}} < 1$) inside the system. This is done at a temperature of 900 K to 1200 K and a pressure from 1 bar to 50 bars by injecting a mixture of methane and oxygen into the reformer. Here they react with each other according to:

$$CH_4 + \frac{1}{2}O_2 \rightleftharpoons CO + 2\,H_2 \quad \text{with} \quad {}^{0}_{\mathrm{d}G_{\mathrm{En}_{\blacktriangle}\mathrm{mol},\mathrm{reac}}} = -36\ \mathrm{kJ/mol}\,. \tag{2.43}$$

For increasing the reaction speed, at industrial scale the process is realized over Ni, Pd or Pt-catalysts (Catalyzed Partial OXidation (CPOX)) (Chen 2013; Dietrich et al. 2009). The great advantages of the POX process are on the one hand the lack of an external heating, resulting in a fast start-up behavior and

a highly dynamical process, on the other hand a simple and compact reactor design. In addition, in the case of the CPOX, the process temperature can be decreased even below 900 K. However, disadvantages of this process are not only the low hydrogen yield[54]. Moreover, in the case of air as oxygen carrier, the dilution of the products with nitrogen, a high probability for soot formation, catalyst degradation by carbon fouling, sulfur poisoning or (re-)oxidation, and thermal impacts on the catalyst exist. (Heinzel, Mahlendorf, and Roes 2006, p. 30 et seqq.)

2.5.1.4. Autothermal reformation

The Autothermal Reformation (AR) emerges from a combination of CPOX and SR. In contrast to CPOX only one reaction chamber is apparent. Here both, partial oxidation of fuel and WGS take place according to the following reaction scheme:

$$CH_4 + \chi\frac{1}{2}O_2 + (1-\chi)H_2O \rightleftharpoons CO + (3-\chi)H_2 \quad \text{with} \quad dG^{0}_{\text{En}_{\blacktriangle}\text{mol,reac}} = \pm 0\ \text{kJ/mol}\ . \tag{2.44}$$

The process conditions, advantages, and disadvantages are very similar to those of the (C)POX reactor. Additionally, the thermal management and system complexity are simplified due to the common reaction chamber. Disadvantageously the process control has to deal with maintaining a precise balance between the endo- and exothermic reactions, what might be the reason for the low hydrogen yield of about 50 %. (Heinzel, Mahlendorf, and Roes 2006, p. 34 et seqq.)

2.5.2. Conclusions

The SR, WGS, and DR (reactions 2.39, 2.40, and 2.42) are reversible and due to the high reaction rates in general in an equilibrium state. If a sufficient amount of steam is added, the equilibrium of the WGS usually is on the products-, rather than the reactants-side, making hydrogen readily available for electrochemistry. The latter itself promotes the reformation reactions by consuming hydrogen and producing steam. Since the re-oxidation stability of the anode's Ni catalyst is poor and found to be one of the main sources for rapid degradation (de Haart 2010), free oxygen should be avoided inside the anode

[54] which can be increased by an additional downstream WGS reactor

half cell. Therefore, (C)POX and AR are not feasible for DIR. In all cases sufficient CO_2 and H_2O partial pressures are desirable to avoid soot formation by thermal decomposition of CH_4 or the Boudouard reaction (Vielstich, Lamm, and Gasteiger 2003a, p. 39 et seqq.)(Larminie and Dicks 2003, p. 244)(Yoshida et al. 1999):

$$2\,CO \rightleftharpoons C + CO_2 \quad \text{with} \quad dG_{En_{\blacktriangle}mol,reac_{\blacktriangle}mol} = +169,25\ \text{kJ/mol at 1125 K}\,.$$

2.5.3. Methane reformation in the literature

As already mentioned in the beginning of this section, the reformation of methane to hydrogen and CO is known for long and has become an industrial process at refineries. In order to improve the hydrogen yield and the operating lifetime of these installations, the kinetics of the SR have been extensively studied in the last decades. In classical approaches (Aparicio 1997; Wei and Iglesia 2004; Xu and Fromet 1989b) the kinetics are derived as power law expressions, either not taking into account the influence of the catalyst loading and the surface it provides for the reactions or considering it by multiplicative scaling factors. For instance the kinetics of Achenbach and Riensche (Achenbach and Riensche 1994), Xu and Fromet (Xu and Fromet 1989b; Xu and Fromet 1989a), and the derivations of their method by Sadeghi and Molaei (Sadeghi and Molaei 2008) are noteworthy to mention. Since these approaches are based on empirical fitting coefficients Mogensen et al. (Mogensen et al. 2011) argued that the results should be handled with care. Nevertheless, until today they are widely used in fuel cell modeling[55].

During the last two decades studies revealed that special treatment is necessary for the situation inside a SOFC anode. Since the Ni catalyst increases the reaction speed, its high amount leads to the fact that reformation reactions are fast compared to the electrochemical ones (Mogensen et al. 2011). Therefore, some models assume thermodynamic equilibrium at all times or a fixed amount of the remaining methane to be converted at each finite element/volume (Chan, Ho, and Tian 2003; Demin et al. 1992). Nevertheless, it is obvious that special attention has to be paid to the reformation kinetics to avoid large temperature gradients, soot formation, re-oxidation, and sintering under DIR

[55] e.g. (Achenbach 1995; Brus and Szmyd 2008; Paradis et al. 2011; Sanchez et al. 2008; Schlitzberger 2006; Schlitzberger 2012)

conditions. Hereby findings like a depth of the SR zone in the range of 0.15 - 0.33 mm at 1200 K (Drescher, Lehnert, and Meusinger 1998; Meusinger, Riensche, and Stimming 1998), an influence of the reaction state of the WGS on the cell voltage (Mogensen et al. 2011), or the prevention of carbon deposition by sufficiently high current densities[56] should be respected too. To investigate these issues several studies have been performed since the early 1990's. Next to simulations with Achenbach's commonly used power law expressions for the kinetics[57] recently the focus of research is redirected to surface kinetics. Here catalyst loading is taken into account by the second main approach used in SOFC modeling[58], the one of Lehnert et al. (Lehnert, Meusinger, and Thom 2000). It assumes first order dependencies on methane and water for its kinetics and is derived from the works of Xu and Fromet (Xu and Fromet 1989b; Xu and Fromet 1989a).

In their review Mogensen et al. (Mogensen et al. 2011) argued that the microstructure of the Ni catalyst, its grain size, and transient behavior are (almost) unique for every experiment. In consequence detailed surface kinetics are required to derive general results from different studies. Such micromodels were mainly developed by the groups around Deutschmann at the Karlsruher Institut für Technologie (engl. Karlsruhe Institute of Technology) (KIT) (Deutschmann et al. 2011). For instance Hecht et al. (Hecht et al. 2005) presented a model with a complete set of the kinetics for 42 elementary reactions to describe the catalyzed SR. These reactions and their application to the SOFC by Janardhanan and Deutschmann (Janardhanan and Deutschmann 2006) and Zhu et al. (Zhu et al. 2005) are discussed in detail in subsection 4.3.2. Although available, the number of studies with detailed surface reactions on a cell/stack level is still very limited[59]. A possible explanation might be the high computational effort and an insufficient experimental data basis.

Altogether is can be said that the trend tends to models with elementary surface kinetics, allowing a precise tailoring of the anode's composition and microstructure. Nevertheless, if no experimental data is available, for spatially

[56](Bebelis et al. 2000; Lin et al. 2005; Lin, Zhan, and Barnett 2006; Zhu et al. 2006)

[57](Achenbach and Riensche 1994; Achenbach 1994; Achenbach 1995; Schlitzberger 2006; Schlitzberger, Leithner, and Zindler 2009; Schlitzberger 2012)

[58](Gemmen and Trembly 2006; Haberman and Young 2004; Klein et al. 2007; Morel et al. 2005; Ni, Leung, and Leung 2008b; Ni, Leung, and Leung 2008a)

[59](Danilov and Tade 2009; Janardhanan, Heuveline, and Deutschmann 2007; Janardhanan 2007)

resolved cell/stack level simulation with DIR the kinetic approaches of Lehnert et al. (Lehnert, Meusinger, and Thom 2000) and Xu and Fromet (Xu and Fromet 1989b; Xu and Fromet 1989a) today seem to be the best compromise between accuracy and computational effort. Hence their implementation in the CFD model of this thesis is addressed below in section 5.2.3.

2.6. Conclusions

In this chapter the fundamental thermodynamical and electrochemical relations underneath all fuel cells are discussed and applied to the SOFC. Hereby the PEN structure is identified to be of particular interest for the electrochemical performance. Later the focus is directed towards three specialties of this kind of fuel cell:

1. The solid electrolyte, allowing various cell configurations;
2. the use of oxygen ions, making an utilization of carbon containing fuels possible; and
3. a high process temperature, providing high quality heat for internal reformation and / or other subsequent processes.

Latter sets high standards for the cells materials. Today's state of art materials are found to provide the requested power densities[60], but suffer from an insufficient long term stability[61] and costs, too high[62] for commercialization.

Altogether, improved cell concepts with thermal integration and a reduced operational temperature are needed to bridge the gap towards marketable products (Antoni 2004; de Haart 2009a; de Haart 2010; Liu 2008). In the next chapter various SOFC concepts are reviewed and a new one, unifying advantages, and avoiding a lot of the drawbacks of the others is proposed.

[60] up to about 10,000 W/m^2 (de Haart 2009d)

[61] less than 0,5 % degradation per 1,000 hours of operation and lifetimes of more than 10,000 operational hours are required for commercialization (Steinberger-Wilckens 2010)

[62] about 2,500 €/kW_{el} are believed as an upper limit (Steinberger-Wilckens 2010)

3. A novel concept for a highly integrated SOFC

In this chapter a novel in-plane series-segmented (cascaded) SOFC concept with the possibility of internal fuel reformation is presented.

Starting from the conclusion of the last chapter, an "ideal SOFC" has to unify various and sometimes contradicting requirements. Therefore, first of all SOFC concepts which are currently under investigation are reviewed and compared in section 3.1. Based on the obtained results, a novel cascaded SOFC concept is proposed and discussed in section 3.2. The chapter ends with a conclusion in section 3.3, explaining the aims of the modeling in the following chapters.

3.1. State of the art

When designing SOFCs the circumstance of the name giving solid electrolyte is an important difference and advantage of this type of fuel cell, because various geometrical concepts for the electrochemically active Positive electrode Electrolyte Negative electrode ≡ MEA (PEN)[1], consisting of anode, electrolyte (membrane), and cathode are possible (see Figure 3.1) (de Haart 2009a; Mücke 2009b). Next to geometrical freedom, the solid PEN structure makes it possible to adjust the electrochemical performance of its constituents by altering either their composition or dimension (Wesemeyer, Jocher, and Leithner 2011).

In dependence of the mechanical support layer for the PEN structure, SOFCs are subdivided into anode-, electrolyte-, and cathode- as well as inert-supported ones (see Figure 3.1) (Mücke 2009b). Although studies show that the electrochemical performance of anode-supported cells is superior and ohmic losses

[1] also known as Membrane Electrodes Assembly ≡ PEN (MEA)

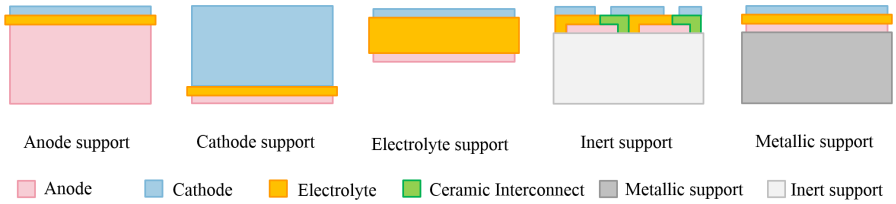

Figure 3.1.: **SOFC support types:** In dependence of the thickest layer, giving mechanical support to the rest of the PEN structure, different kinds of cell types can be distinguished: Anode-, cathode-, electrolyte-, inert-, and metallic-supported concepts. Dimensions not to scale; modified from (Mücke 2009b).

are reduced[2], in e.g. the tubular concepts alternative approaches and higher operating temperatures are still common. From the geometrical point of view there are mainly two kinds of SOFCs: The planar/monolithic[3] (Tietz, Buchkremer, and Stöver 2002) and the tubular (Singhal 2000) one. Both are so far tested for internal fuel reformation[4], but each offers design specific advantages and drawbacks. (Vielstich, Lamm, and Gasteiger 2003a, p. 343)

3.1.1. The planar concept

Planar cells (see Figure 3.2), developed e.g. at Forschungszentrum Jülich (Tietz, Buchkremer, and Stöver 2006) in Germany, HTceramix SA (Hoffmann 2009) in Switzerland or Risø DTU (RisøDTU, Topsoe, and Dantherm 2011) in Denmark feature high power densities due to short internal current paths (Costamagna et al. 2004) and cheap manufacturing costs (Repetto and Costamagna 2008). Since electrochemistry and reformation are directly linked with gas flows and thermal management, the flow design can be used for their adjustment. This is achieved e.g. by machining an appropriate flow channel structure into the IC plates separating the cells inside a stack (Danilov and

[2] allowing a reduction of the operating temperature to 1000 - 1100 K without losing efficiency (Ferguson, Fiard, and Herbin 1996; Tietz, Buchkremer, and Stöver 2006)

[3] a "monolith" is a SOFC stack built from planar cells

[4] e.g. (Colpan, Hamdullahpur, and Dincer 2010; Janardhanan, Heuveline, and Deutschmann 2007; Shiratori et al. 2010)

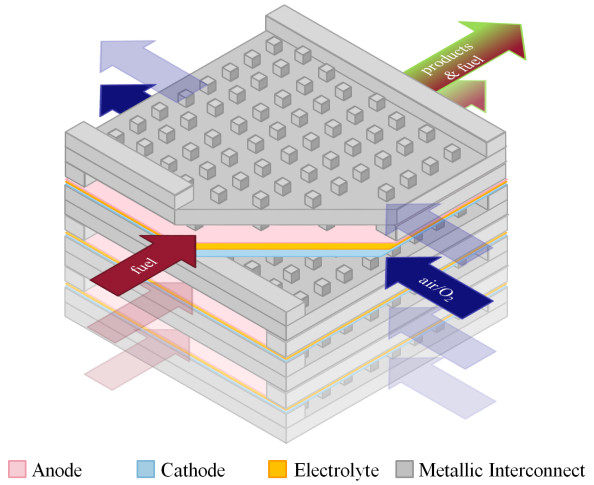

Figure 3.2.: **Schematic design principle of a planar SOFC stack:** This cell concept consists of planar layers put onto each other to form a stack. With the appropriate manifold the design can be operated under all flow configurations in either a janiform or a bipolar operation. Shown is a cross flow setup with open gas channels and external manifold; modified from (Lin et al. 2007).

Tade 2009). In dependence of their material[5], different techniques are available (Fergus 2005; Zhu and Deevi 2003b). The on- and off-gases are supplied to and removed from the cells in a stack through the gas-distribution manifold which itself can either be included into the ICs[6] or attached from the outside as an external structure. Although the first kind is more difficult to manufacture, co- and counter- as well as cross-flow configurations of fuel and air are possible (Mücke 2009b); whereas the external manifold leads to simpler ICs but is limited to a cross-flow configuration (de Haart 2009c). The main drawbacks of this concept are thermal stresses, the probability for mechanical failures, and fuel crossover originating in a TEC mismatch of the materials used (Costamagna et al. 2004; Lin et al. 2007; Tietz 1999). Additional problems are the need for large sealant planes between the cell/stack components (Liu et al. 2011) and the bipolar operation of the ICs separating the cells in-

[5]metal or ceramics
[6]internal manifold

side a stack. The latter not only leads to corrosion problems[7] originating in the direct contact with the bivalent atmospheres (Zeng and Natesan 2004). Moreover, the possibility for fuel crossover due to hydrogen diffusion (Antunes et al. 2010; Michler and Naumann 2010), an increased "pressure drop" when reducing channel dimensions, and additional volume as well as weight have to be considered. (Vielstich, Lamm, and Gasteiger 2003a, p. 343)

3.1.2. The tubular concept

The second main concept is the tubular one, first developed and investigated in the 1990s by SIEMENS-WESTINGHOUSE (Heinzel, Mahlendorf, and Roes 2006). In this concept the oxygen/air in general is fed into the cell inside ceramic tubes made by extrusion from LSM (see section 2.4.3) which are coated afterwards by YSZ and Ni-YSZ. The tubes are 1 - 2 cm in diameter and up to 150 cm long, unifying electrodes[8] and electrolyte[9]. The air flows through the tubes whereas the fuel is supplied from their outside (Fischer and Seume 2009a) (see Figure 3.3). (Vielstich, Lamm, and Gasteiger 2003a, p. 342)

In modified versions a second supply tube is positioned inside the inner pipe to realize circulation, making anode supported tubular cells possible by changing the positions of fuel and oxygen/air, the orientation of the PEN structure, and still getting rid of the products (Serincan, Pasaogullari, and Sammes 2009b). At the end of the 1990s the final versions showed power densities of up to 2,000 W/m^2 and more than 90 % fuel utilization. The advantages of this, in general still cathode-supported, concept are a reduction of the problems concerning TEC mismatches (Costamagna et al. 2004; Fischer and Seume 2009b), and decreased sealant areas compared to the planar approach (Singhal 2000). Additionally, the power output of a tubular cell based stack can easily be adjusted by both series[10] and parallel[11] connection (Ferguson, Fiard, and Herbin 1996). Furthermore, the use of open ended tubes offers an intrinsic possibility for heating the stack by burning unused fuel. Since manifold and electrical contacts can be located in the cold parts of a stack, their high temperature applicability is not mandatory. In the past several modifications like the

[7] electrical contacts, reactant crossover
[8] cathode around 2 mm, anode 100 µm
[9] about 40 µm
[10] via ceramic ICs made of $LaCrO_3$
[11] via Ni-felts

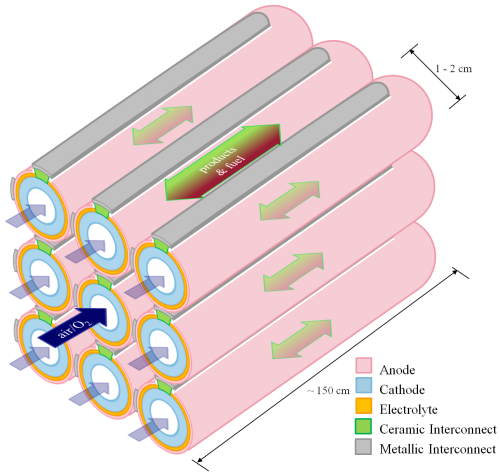

Figure 3.3.: **Schematic design principle of a tubular SOFC stack:** The cathode supported cells are supplied with oxygen/air from the inside, whereas the fuel is fed from the outside. Stacking is possible in both series as well as parallel connections; modified from (Mücke 2009b).

Micro-Tubular-SOFC (MT-SOFC) (Alston et al. 1998; Funahashi et al. 2007), which has been extensively reviewed by Lawlor et al. (Lawlor et al. 2009), the flattened tubular or the High Power Density-SOFC (HPD-SOFC) (Singhal 2000) have been developed. Also hybrids from planar and tubular concepts like e.g. the Mono Layer Block Built type SOFC (MOLB-type SOFC) (Hwang, Chen, and Lai 2005a; Hwang, Chen, and Lai 2005b) were investigated. Although in particular the MT-SOFC design is expected to be a great step ahead (Calise, Restuccia, and Sammes 2010), the tubular concept still suffers from the principle-related long current paths and resulting high ohmic losses (Costamagna et al. 2004). Since the cell diameter must be kept small, complex manufacturing procedures and thus high costs are also typical for tubular SOFCs (Costamagna et al. 2004). (Vielstich, Lamm, and Gasteiger 2003a, p. 342)

3.1.3. Alternative concepts

Apart of the two main types, several alternative designs and modifications of the two basic concepts are known. An example is the Heat Exchanger Integrated System-cell (HEXIS-cell) invented by Sulzer/InDEC B.V./Hexis

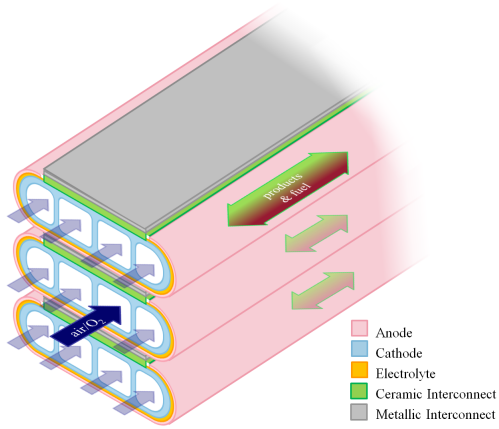

Figure 3.4.: **High Power Density-SOFC (HPD-SOFC):** The HPD-SOFC design is based on the tubular concept but tries to overcome its high ohmic losses by a flattened tube with internal ribs to shorten the current paths; modified from (Singhal 2000).

(see Figure 3.5) (Hexis 2007; Schuler 2007) which is numerically examined by e.g. Andreassi et al. (Andreassi et al. 2008). The HEXIS-CELL is based on circular disks[12], which are stacked similar to the planar concept. Fuel is supplied from the middle through a channel formed by a center hole in all disks. On its way to the outer rim of the disks, the fuel undergoes electrochemical reactions. The air is supplied through a specially designed IC from the outside, which also acts as internal heat exchanger to transfer back the heat from the combustion of the unused fuel at the outside of the cell to its interior. Due to the integration of gas distributors and electrochemical active parts into one component, the complexity of the cell is reduced to its minimum. In consequence no sealant-planes[13] are necessary. Additionally the afterburner features an intrinsic possibility for heat management. Since the manifold is designed as a channel-grid the gas distribution inside the cell and hence the operating conditions are not homogeneous, resulting in a location dependent reaction rate associated with the formation of local hot-spots (Andreassi et al. 2008). Moreover, the afterburner at the outer surface of the stack dismisses all advantages

[12] about 120 mm in diameter
[13] despite of a ring around the center hole

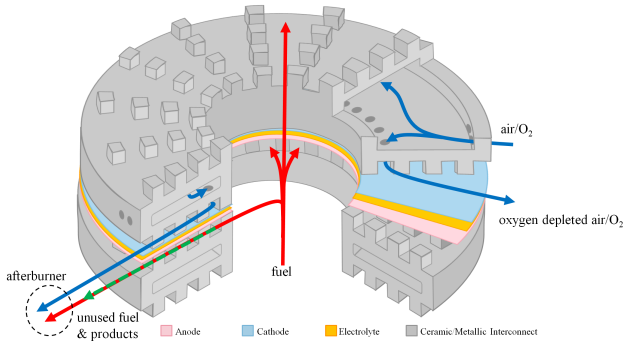

Figure 3.5.: **Heat Exchanger Integrated System-cell (HEXIS-CELL):** In this disk shaped concept, developed by Sulzer, the fuel is supplied through the hole in the middle, while the air / oxygen is fed from the outside. Both reactants mix at the outer surface and react with each other, whereby the released heat is used for heating the system. Adapted from (Vielstich, Lamm, and Gasteiger 2003a, p.345).

of SOFCs for CO_2 separation and leads to additional thermal stresses in dependence of the operating conditions. (Vielstich, Lamm, and Gasteiger 2003a, p. 345)

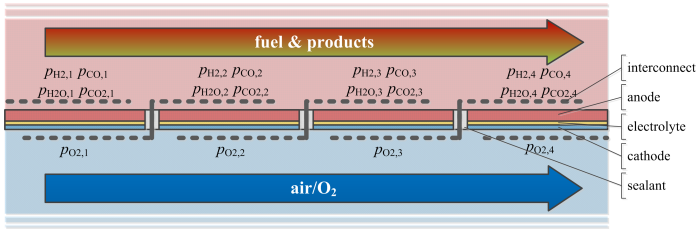

Figure 3.6.: **Segmented-in-Series-SOFC (SS-SOFC):** The SS-SOFC concept, also known as Integrated Planar-SOFC (IP-SOFC), is based on an in-series connection of small cell stripes. (Gardner et al. 2000; Leithner 2004; Leithner and Schlitzberger 2007)

With increased fuel utilization the formation of a fuel concentration gradient in the direction of the flow leads to a difference in local Nernst potentials U_{Nernst} along the electrodes[14] and hence in increased ohmic losses due to the

[14] see chapters 2 and 4

formation of in-plane currents inside them (Costamagna et al. 2004). Therefore, a cascade of numerous electrically in series connected small "cell-stripes" with short current paths and only a small change in partial pressures along the direction of the flow is beneficial (see Figure 3.6). This concept, which is substantially a mixture of the planar and the tubular concept, was first developed in the early 1990s under the name Integrated Planar-SOFC (IP-SOFC) at Rolls Royce (Gardner et al. 2000). The concept is realized with ceramic process technology on a porous ceramic substrate (Gardner et al. 2000) what reduces the problems associated with sealant planes and TEC mismatches. To avoid interactions of the reactants with bipolar plates, the cells are operated in a janiform configuration with anodes/cathodes facing each other (see Figure 3.7). Advantageous in this concept are not only the high fuel utilization of more than

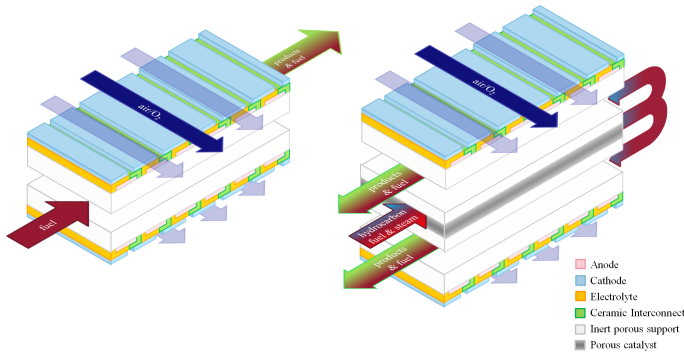

Figure 3.7.: **Integrated Planar-SOFC (IP-SOFC) design concepts:** The IP-SOFC concept offers the possibility for DIR on the anode (1-C concept, left) and IIR inside separate reformation channels (3-C concept, right). In both cases, co- and counter as well as cross-flow configurations (shown here) are possible; adapted from (Magistri et al. 2005).

70 % (Gardner et al. 2000), but also the possibility for thermal integration. In the 3-C concept (see Figure 3.7) fuel is fed into a reformer located between the heat releasing anode channels. After the reformation in the inner channel the flow is divided and enters the two anodes (Magistri et al. 2005). A tubular version of the IP-SOFC was investigated by Mitsubishi Heavy Industries (MHI)[15] (Haga et al. 2009; Tomida et al. 2007). Although the IP-SOFC concept (which

[15] providing up to 21 kW_{el} with an electrical efficiency of 35 % and 75 % fuel utilization (Vielstich, Lamm, and Gasteiger 2003a)

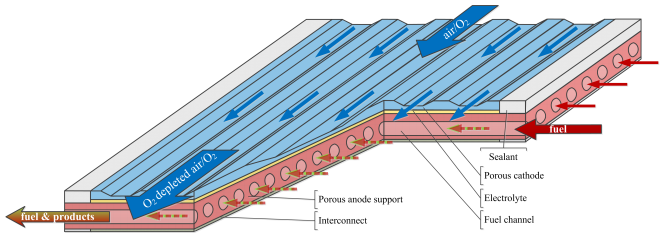

Figure 3.8.: **Planar Tubular-SOFC (PT-SOFC) concept:** The planar-tubular SOFC concept combines a porous support with internal flow channels and the possibility of an almost seal free stack formation. In this schematic illustration an anode-supported design is shown; adapted from (Chen et al. 2011).

is also known as Segmented-in-Series-SOFC (SS-SOFC)) combines advantages of the other cell concepts and satisfies almost all of the requirements from the beginning, there has not been much progress in terms of practical applications within the last decade (Bai et al. 2010; Cassidy et al. 2009; Kim et al. 2006b).

Several models for IP- and SS-SOFCs are reported in the literature (Grosso, Repetto, and Pezzini 2008; Haberman and Young 2004; Magistri et al. 2007; Mounir et al. 2009). E.g. Cui and Cheng (Cui and Cheng 2010) proposed a numerically optimized geometry for a tubular SS-SOFC. The authors expect their geometry to be promising because of reduced current paths and less sealant area compared to conventional tubular cells. The numerical results obtained by them for the steady-state behavior show on the one hand that[16] the cell potential decreases in the fuel flow direction and that on the other hand an optimum of U_{cell} in dependence of the cell length exists.

Another approach is the Planar Tubular-SOFC (PT-SOFC) concept (see Figure 3.8), proposed by Chen et al. (Chen et al. 2011). The concept is based on a porous structure acting as mechanical support, which itself might either be inert, an anode or a cathode. In this support structure parallel tubes for either fuel or oxidant are included. On one side of the porous support a dense electrolyte layer with a porous counter-electrode[17] on top of it, including a gas manifold structure, is positioned. The authors expect the PT-SOFC to be promising be-

[16] as a consequence of fuel depletion
[17] either cathode or anode

cause of the lack of special bipolar plates, enlarged operating time, reduced need for sealants, and short current paths as well as the possibility of internal reformation (Chen et al. 2011).

With reduced temperature[18] the speed of a lot of degradation phenomena is reduced significantly (Akhtar et al. 2009; Hagen 2010). This, and the possibility of direct injection of fuel as well as oxygen below their combustion temperature into a common reaction chamber, open new opportunities for SOFC concepts. Since various materials show different catalytic activities towards oxygen reduction[19] and fuel oxidation[20], the establishment of electrochemical potential differences between certain regions of these Single Chamber-SOFCs (SC-SOFCs) is possible. Advantages of this concept are the lack of any high temperature seals as well as any need for a strict separation of anode's and cathode's gas-flows by an electrolyte. Drawbacks are the danger of explosions and high parasitic losses due to not ideal selective electrode materials. (O'Hayre et al. 2009, p. 279-280)(Vielstich, Lamm, and Gasteiger 2003a, p. 347)

As the summary in Table A.1 in appendix A.1 implies, each of the described concepts offers design specific advantages and has to focus individual problems.

3.2. A novel cascaded design for SOFCs

From the discussion in the last section the following requirements for sophisticated SOFC concepts can be derived:

1. High power densities, with high fuel utilization, and reduced ohmic losses;
2. easily and cheap to manufacture with only little need for sealants; featuring a
3. possibility for thermal integration by internal reformation of hydrocarbons.
4. Easy adoption of power output via stacking; while having only a
5. little pressure drop; and a
6. homogeneous temperature distribution for reduced thermal stresses; as well as a
7. reduced operating temperature for decelerated degradation.

[18] 750 K to 900 K
[19] e.g. $Sm_{0.5}Sr_{0.5}CO_{3-\chi}$ (SSC)
[20] Ni-GDC

To meet the requirements in points one and two, new concepts should be based on an anode supported PEN structure. This is also beneficial for the internal reformation and thermal integration since the anodes Ni might directly act as reforming catalyst (Shiratori et al. 2010). Although problems arise from possible mismatches in the TEC of metals, ceramics, and sealant planes, the SOFC concept should reduce brittle ceramic parts to the minimum[21] and apply metallic components whenever possible. Here various materials are available (Tietz 2003; Tucker 2010; Zhu and Deevi 2003b), from which the commonly used stainless steel Crofer22APU from ThyssenKrupp (VDM 2005) currently seems to be the most promising compromise between stability, TEC mismatch, machinability, and price.

Since the tubular concept suffers from high ohmic losses, due to long current paths, a new concept should be based on a planar geometry. Nevertheless, the good system scalability of the tubular approach via both series and parallel connection should be maintained (see point four). To satisfy the points five and six the pressure drop can be decreased by almost open gas distribution manifolds instead of small gas channels (de Haart 2009c). Furthermore, the ratio of electrochemical active to gas channel volume might be increased, if[22] as much as possible of the channel surface is electrochemically active (Hwang, Chen, and Lai 2005b). In this case, an improved homogenization of the temperature profile even under DIR might be obtained by varying the catalyst along the fuel flow direction. To reduce thermal gradients either a co-flow (Wang et al. 2007) or a counter-flow configuration of the fuel and air streams should be used. Altogether, the novel SOFC concept can be characterized by:

- In-plane-series-segmented SOFC slices in direction of the fuel gas flow for high fuel utilization and tailored activity (cascaded structure);
- an anode-supported PEN-concept, providing the possibility for DIR;
- a janiform flow channel configuration with metallic ICs for high volumetric power-densities;
- a cascaded stack-concept, where the power output is adjusted by altering the stack current via additional cell layers, while keeping it constant for every cell layer; and

[21] i.e. the PEN

[22] like in the MOLB-TYPE SOFC concept

- an easy and cheap machinability through the use of both ceramic and metallic components.

3.2.1. Earlier designs

To meet the requirements various SOFC stack-designs are developed in joint undertakings of the scientific assistants at the IWBT (Schlitzberger 2012; Stenger 2014). Before the final concept for this thesis is presented in the next section, two earlier designs shall be mentioned briefly.

The first stack design consists just of two conventional Electrolyte Supported Cells (ESCs), which are positioned inside a metallic frame, containing the gas-distribution manifold. For stack formation two of these frames are positioned a top each other, whereby the PENs are arranged in such a way that a janiform configuration of anodes and cathodes is created. Both anodes are electrically contacted by a zig-zag-shaped plate whose external contacts are used for cascading. Advantages of this design are its simplicity and possibility to adjust the

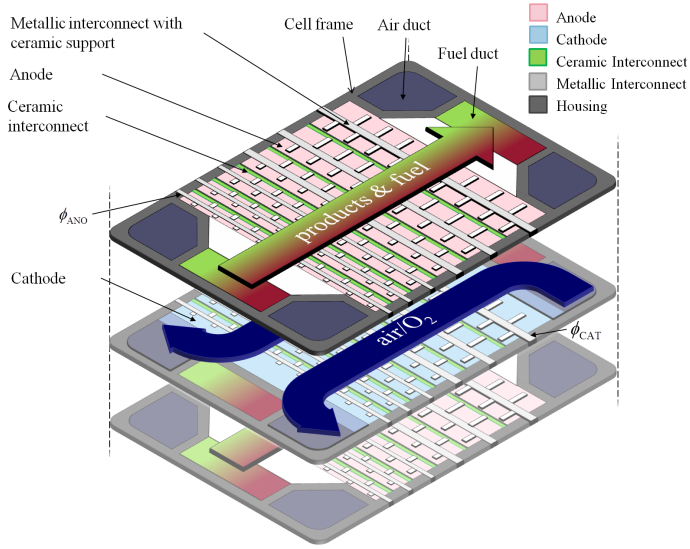

Figure 3.9.: **Herringbone interconnect cascaded SOFC concept**: The design consists of open electrodes in a janiform configuration and can be operated in co- as well as counter-flow configuration. The herringbone ICs are stabilized by a ceramic support (Wesemeyer and Leithner 2010).

stacks output voltage and current by external re-arrangement of the clamping. Disadvantages are not only the low electrochemical performance of the ESC[23]. Moreover, the extended electric equipotential planes lead to a decreased fuel utilization. Finally, the large and bulky design and the expected high ohmic losses due to long current paths (de Haart 2009d), in combination with only small contact areas between ICs and electrodes make the design unfeasible for practical applications.

The second design consists of a cascaded concept with open electrodes in a janiform configuration (see Figure 3.9) and can either be operated in a co- or a counter-flow configuration (Wesemeyer and Leithner 2010). To generate a high fuel utilization every layer is divided in numerous single cells, which grow in area along the direction of the fuel-gas flow. The herringbone-like metallic ICs act as gas-distributors and electrical connection between the cell layers. They are mechanically supported by a ceramic substructure, whereas the electrical in-plane, in-series connection is done by ceramic ICs like in the IP-SOFC concepts of MHI or Rolls Royce (Funahashi et al. 2007; de Haart 2009c; Tietz, Buchkremer, and Stöver 2002). The concept is withdrawn for this thesis, because of the difficulties in IP-SOFC manufacturing and possible problems from TEC mismatches between metallic ICs and ceramic support. Additionally, the ceramic support is difficult to manufacture. Differently sized electrode areas require special ICs for every cell, and large distances between the contacts lead to increased ohmic losses. Therefore, a third design which tries to get rid of the drawbacks of its precursors is presented in the next subsection.

3.2.2. Final design

The design consists of eight fuel cells[24] whose electrodes are rowed up in direction of the gas flows[25]. Since the fuel concentration depletes along the flow direction, the cell voltages will decrease parallel to the fuel flow direction from cell to cell. Therefore, the cells are electrically connected in-series via S-shaped ICs (see Figure 3.10). The PEN is based on an anode supported structure consisting of a 0.94 mm thick anode with decreasing porosity towards

[23] although others are possible

[24] more are possible

[25] Resulting in an active area of 204.71 cm^2 per layer, each having an active area of 25.52 cm^2 (Todt 2011).

the dense electrolyte layer of 10 µm. Atop of the electrolyte a porous cathode layer with a strength of 50 µm is positioned, leading to a total thickness of 1 mm for the PEN. If necessary an additional protection layer from GDC be-

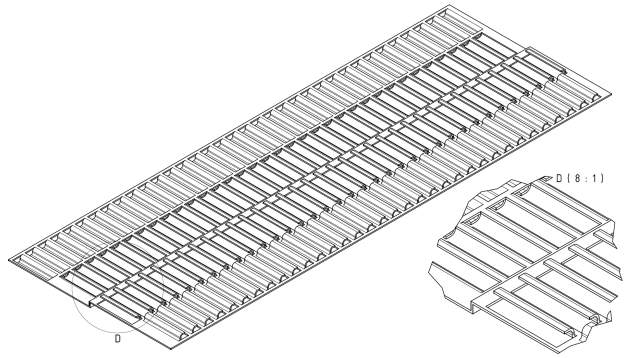

Figure 3.10.: **S-shaped IC:** The sinusoidal fins act as flow channels, and structural support (Todt 2011).

tween cathode and electrolyte (see section 2.4.3 is possible too (Todt 2011). The IC is made of Crofer22APU (VDM 2005; VDM 2010) with a strength of 0.3 mm and is identical for all cells in the layer.[26] Furthermore, it is made of only one sheet of material and can be manufactured easily by common cutting and bending techniques (Grote and Feldhusen 2007, p. S 21 et. seqq.).

On both, the anode and the cathode side, the IC is equipped with sinusoidal-shaped fins. As it can be seen in a side view of a stack in Figure 3.11 the fins are intended as contacts for the next cell layer, whereby their geometry guarantees both, a perfect fitting of the layers and a constant contacting through the sponge-like shape. Furthermore, the fins act as heat exchanger between channels flow and electrochemical active areas as well as split-and-recombine micromixers with only little "pressure drop" for the reactants (Kumar, Paraschivoiu, and Nigam 2010; Stemich 2006). If required, the material might be coated on the anode side to gather catalytic properties[27] or on the cathode side by protection layers[28] to increase its corrosion resistance (Chen et al. 2005; Fontana et al. 2007; Liu and Chen 2009; Shaigan et al. 2010; Tucker

[26] despite of those connectors forming external contacts at the very beginning and end
[27] by e.g. Ni
[28] e.g. reactive elements, perovskites or spinels

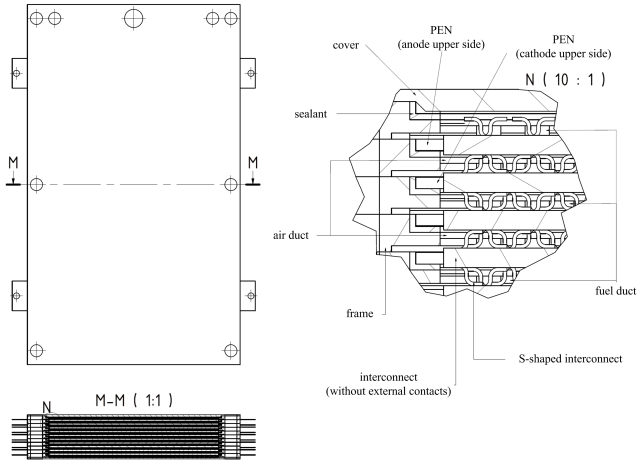

Figure 3.11.: **Top-, side- and detailed view of a cascaded SOFC stack:** External contacting is done by the extensions of the ICs at the very first and last cells of each layer. Inside the stack the fins form flow channels for the operating media (Todt 2011).

2010; Zeng and Natesan 2004). The heights of the flow channels are directly correlated with the uncovered parts of anode and cathode (see Figures 3.10 and 3.11). To offer short current paths and reduce in-plane currents, while maintaining sufficient channel dimensions, the cutouts are adjusted properly.

The assembly process of a cell-layer is illustrated in Figure 3.12. In the beginning a plate with external contacts is positioned in the metallic frame then subsequently PENs and ICs are placed until the layer is finished by a second plate with external contacts. Stack formation is done by placing additional planes with an inverted orientation of anodes and cathodes atop, and joining the external contacts by metallic bolts. This leads to a parallel connection of the cells so that the output current is increased, whereby the stack voltage is maintained constant. Since both sides of fuel and air channels are electrochemically active, high fuel utilization and volumetric power densities can be expected. More drawings are shown in section A.3 in appendix A.

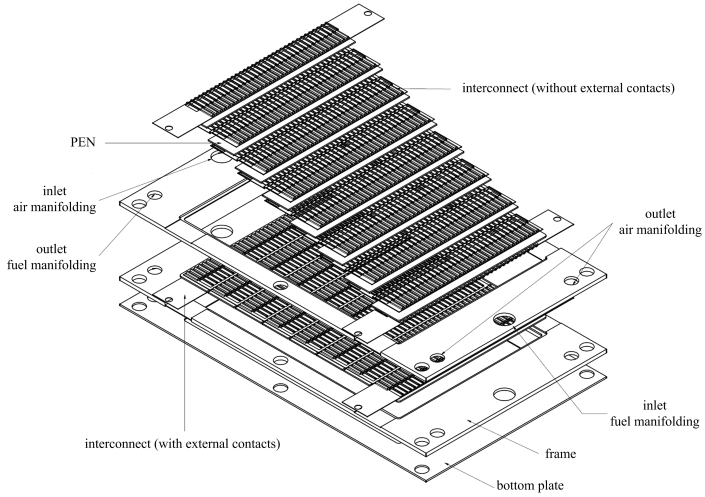

Figure 3.12.: **Exploded view of the cell-layer assembly process:** Each layer of a stack is made by subsequently positioning ICs and PENs in a metallic frame. These frames are then put atop each other for stacking (Todt 2011).

3.3. Conclusions

In this chapter current design concepts for SOFCs are reviewed and compared among each other, before a new highly integrated design is proposed.

The design, which is based on a cascaded structure of planar cells, unifies the possibility of DIR of hydrocarbons and (almost) open electrodes in either a co- or counter-flow configuration with monopolar operation and easy stacking. Nevertheless, not only the expectations towards low pressure drop and high overall performance still have to be proven. Therefore, in the subsequent chapters a 3D model is proposed, verified, and used for these purposes.

4. Modeling of SOFCs

OXFORDS DICTIONARY (Hornby 1995, p. 749) defines the term "*model*" in §3 as

> "a simple description of a system, used for explaining, calculating, etc. sth."

Therefore, the following chapter can be understood as an attempt to formulate an appropriate description of the phenomena occurring inside a SOFC in the language of mathematics. The aim of this chapter is not only to prove the potential of the introduced novel cell concept, but also to achieve a deeper understanding of the complex processes in a SOFC.

It starts in section 4.1 with a general description and mathematical formulation in terms of balance equations for the phenomena which have to be addressed in the different regions of a SOFC. Subsequently, the current state of the art in 3D modeling is reviewed in section 4.2. Recent studies[1] point out the outstanding role of micro- and meso-scale phenomena on the SOFC's overall performance. Therefore, in section 4.3.1 the influence of the anode microstructure and composition on its macro-scale properties is studied with a computational model. Afterwards, the focus is redirected to an investigation of the elementary surface kinetics at a LSM cathode. The chapter ends with a conclusion on the results of both models and their influence on the detailed 3D model which is formulated in the next chapter.

4.1. General aspects

One of the basic aspects of fuel cells is that they unify different disciplines, length-, and timescales inside one application, whereby the actual focus is dependent on the respective cell region (see Figure 4.1). In a continuum approach the balance of several conserved quantities has to be satisfied. It is possible to

[1] e.g. (Andersson, Yuan, and Sunden 2010)

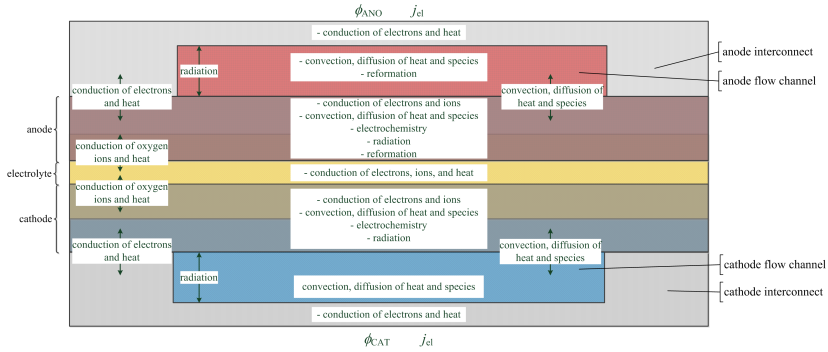

Figure 4.1.: **Physical phenomena inside a SOFC:** In the different cell regions transport phenomena for mass, species, momentum, charge, and energy as well as chemical and electrochemical reactions have to be considered in modeling. Dimensions not to scale; modified from (Lefebvre 2011).

show (Bozic et al. 2009, p. 23) that the balance equation for a general conserved quantity Φ is given by:

$$\underbrace{\frac{\partial \rho_{\mathrm{vol}_\blacktriangle \Phi} \Phi}{\partial t}}_{\text{storage term}} = \underbrace{-\mathrm{div}\left(\vec{J}_\Phi \Phi\right)}_{\text{convective term}} + \underbrace{\mathrm{div}\left(\Gamma_\Phi \ \mathrm{grad}\ (\Phi)\right)}_{\text{diffusive term}} + \underbrace{\Upsilon_{\mathrm{vol}_\blacktriangle \Phi}}_{\text{source term}} \ , \tag{4.1}$$

where $\rho_{\mathrm{vol}_\blacktriangle \Phi}$ is the volumetric density of quantity Φ in $1/\mathrm{m}^3$, $\vec{J}_\Phi$ its convective flow in $1/\mathrm{m}^2\,\mathrm{s}$, Γ_Φ an exchange coefficient in $1/\mathrm{m}\,\mathrm{s}$, and $\Upsilon_{\mathrm{vol}_\blacktriangle \Phi}$ a volumetric source term in $1/\mathrm{m}^3\mathrm{s}$. Having in mind the regions of a SOFC (see Figure 4.1) the different terms and coefficients in equation 4.1 have to be specified.

4.1.1. Mass transport

Starting from the dense, solid, and only electronic conductive IC, neither storage or convection nor diffusion or sources of mass are apparent, so all terms equal zero in this region. Going on to the gas channels, mass is transported by convection. Because there are no gradients, the mass exchange coefficient Γ_Φ is zero (Bozic et al. 2009, p. 24) and since no sources or sinks for the mass exist, $\Upsilon_{\mathrm{vol}_\blacktriangle \Phi}$ is zero too. Hence equation 4.1 simplifies to the well known mass continuity equation (Ansys Inc. 2011, p. 25):

$$\frac{\partial \rho_{\mathrm{Mass}_\blacktriangle \mathrm{vol}}}{\partial t} + \mathrm{div}\left(\rho_{\mathrm{Mass}_\blacktriangle \mathrm{vol}}\, \vec{u}\right) = 0 \ . \tag{4.2}$$

Where

$$\dot{\vec{J}}_{\text{Mass}} = \rho_{\text{Mass}_\blacktriangle\text{vol}}\,\vec{u}$$

is the mass flow in kg/m^{2}s, $\rho_{\text{Mass}_\blacktriangle\text{vol}}$ the volumetric mass density in kg/m^3 and $\vec{u}$ the fluid velocity in m/s. Directing the focus to the porous electrode regions, on the cathode side oxygen ions migrate from the gas phase to the ion conductor and leave it on the anode side as part of chemical reactions that form water or carbon dioxide. In the cell center, for the electrolyte the situation is much the same as in the ICs, leading all terms in equation 4.1 to be zero. (Bove and Ubertini 2006)

4.1.2. Species transport

Taking into account that the operating media in the anode and cathode region consist of a mixture of gases reacting either directly[2] or indirectly[3], the conservation principle for mass has to be satisfied for all i-species. As described earlier, the discussion should focus on the gas channels and the porous electrodes. For the gas channels, the general balance equation of the i-th species can be written as:

$$\begin{aligned}\frac{\partial \rho_{\text{Mass}_\blacktriangle\text{vol}}\, y_{\text{Mol}_\blacktriangle\text{mol}_\blacktriangle i}}{\partial t} + \text{div}\underbrace{\left(\rho_{\text{Mass}_\blacktriangle\text{vol}}\, y_{\text{Mol}_\blacktriangle\text{mol}_\blacktriangle i}\,\vec{u}\right)}_{\vec{J}_{\text{conv}_\blacktriangle i}} \\ -\text{div}\underbrace{\left(\rho_{\text{Mass}_\blacktriangle\text{vol}}\, D_{\text{eff}_\blacktriangle(\text{g})_\blacktriangle i}\text{grad}\left(y_{\text{Mol}_\blacktriangle\text{mol}_\blacktriangle i}\right)\right)}_{\vec{J}_{\text{diff}_\blacktriangle i}} = \Upsilon_{\text{Mass,vol}_\blacktriangle y_i}\ ,\end{aligned} \tag{4.3}$$

where $y_{\text{Mol}_\blacktriangle\text{mol}_\blacktriangle i}$ denotes the molar fraction of the i-th species in mol$_{\text{species}}$/mol$_{\text{tot}}$, $D_{\text{eff}_\blacktriangle(\text{g})_\blacktriangle i}$ the effective mass diffusion coefficient/kinematic viscosity in m^2/s, and $\Upsilon_{\text{Mass,vol}_\blacktriangle y_i}$ a volumetric source term of this species in kg/m^{3}s. Under the assumption of an ideal mixture, the volumetric density $\rho_{\text{Mass}_\blacktriangle\text{vol}}$ in 1/m^3 is given by the sum

$$\rho_{\text{Mass}_\blacktriangle\text{vol}} = \sum_{i=1}^{n} y_{\text{Mol}_\blacktriangle\text{mol}_\blacktriangle i}\,\rho_{\text{Mass}_\blacktriangle\text{vol}_\blacktriangle i} \tag{4.4}$$

[2] reformation

[3] via the electrolyte

over the volumetric densities of all n species weighted with their mass fractions $y_{\text{Mol}_\blacktriangle \text{mol}_\blacktriangle i}$ (Bove and Ubertini 2006). With the same assumption equation 4.4 can also be applied to calculate arbitrary constitutive fluid properties ξ by replacing $\rho_{\text{Mass}_\blacktriangle \text{vol}}$ with ξ and $\rho_{\text{Mass}_\blacktriangle \text{vol}_\blacktriangle i}$ with ξ_i.

Species transport is again strongly dependent on the cell region. In the gas channels it is governed by the convective flow $\vec{J}_{\text{conv}}$, here usually the *dynamic viscosity* Γ_{visc} in kg/m s:

$$\Gamma_{\text{visc}} = \rho_{\text{Mass}_\blacktriangle \text{vol}} D_{\text{eff}_\blacktriangle(\text{g})}$$

is applied to describe the diffusive transport. For pure substances various compilations based on experimental data exist (Daubert and Danner 1989).

In the porous electrodes the diffusive flux $\vec{J}_{\text{diff}}$ becomes dominant. It is strongly dependent on the value of $D_{\text{eff}_\blacktriangle(\text{g})}$ which is usually either described by Fick's law, the Maxwell-Stefan Model (MSM) (Vielstich, Lamm, and Gasteiger 2003a, p. 55) or the Dusty Gas Model (DGM). (Janardhanan and Deutschmann 2006; Pramuanjaroenkij, Kakac, and Yangzhou 2008)

4.1.3. Momentum transport

A change in momentum of a fluid volume is given by the difference of the in- and outflow of momentum and the sum of all forces acting on it (Bozic et al. 2009, p. 26). In a continuum approach the basis for all models on this aspect are the *Navier-Stokes Equations (*NSEs*)*. They can be derived from Newton's laws (Durst 2006, p. 134 et seqq.) and govern the behavior of unsteady, compressible, and viscous flows (Bove and Ubertini 2006) (Bozic et al. 2009, p. 29)(Ansys Inc. 2011, p. 25):

$$\frac{\partial \rho_{\text{Mass}_\blacktriangle \text{vol}} \vec{u}_i}{\partial t} = -\vec{u} \rho_{\text{Mass}_\blacktriangle \text{vol}} \operatorname{div}(\vec{u}) - \operatorname{grad}(p) + \Gamma_{\text{visc}} \underline{\Delta} \vec{u} + \rho_{\text{Mass}_\blacktriangle \text{vol}} \vec{g}_{\text{grav}} \ . \quad (4.5)$$

Here p is the fluid pressure in Pa, Γ_{visc} its dynamic viscosity in kg/m s, and $\vec{g}_{\text{grav}}$ earth's gravitational acceleration in m/s^2. Although the fluid velocity, and the Reynolds number (Meschede 2006, p. 117):

$$Re = \frac{\vec{u} L_x \rho_{\text{Mass}_\blacktriangle \text{vol}_\blacktriangle(\text{g})}}{\Gamma_{\text{visc}_\blacktriangle(\text{g})}} \quad (4.6)$$

usually are very small[4] inside the flow channels, in dependence of the fluid properties and geometrical dimensions, turbulence phenomena might have to be taken into account (Bove and Ubertini 2006).

In contrast, in the porous electrodes the forces from the pressure gradient and the frictional resistance of the material have to be considered simultaneously. For the flow "in the middle" of these porous regions the *Darcy Equation (*DE*)* is suitable. However, the treatment of the transition zone between the electrodes and the gas channels is difficult, since interfacial conditions have to be defined. A way to handle this is the *Darcy-Brinkman Equation (*DBE*)* which includes the NSE and the DE as limiting cases for both domains (Haberman and Young 2004):

$$\frac{\partial \rho_{\mathrm{Mass}_\blacktriangle \mathrm{vol}}\, \vec{u}_i}{\partial t} + \rho_{\mathrm{Mass}_\blacktriangle \mathrm{vol}}\, \vec{u}\, \mathrm{div}\left(\frac{\vec{u}}{Po_{\%}}\right) = -Po_{\%}\, \mathrm{grad}(p) + \Gamma_{\mathrm{visc}}\, \underline{\Delta}\, \vec{u} + Po_{\%}\, \rho_{\mathrm{Mass}_\blacktriangle \mathrm{vol}}\, \vec{g}_{\mathrm{grav}} - \frac{\Gamma_{\mathrm{visc}}\, Po_{\%}}{Pe_{\%}(Po_{\%})}\, \vec{u}\ .$$

Here $Po_{\%}$ is the porosity of the material and $Pe_{\%}$ its permeability expressed in normalized percents and m^2. (Andersson, Yuan, and Sunden 2010; Le Bars and Worster 2006)

4.1.4. Energy transport

The discussion of fuel cell thermodynamics (see chapter 2.2) shows that in SOFCs chemical energy is converted either to electricity or heat. Since charge transport is addressed in the next subsection, here the focus lies on thermal energy. In dependence of the specific internal energy per unit of mass $E_{\mathrm{En,int}_\blacktriangle \mathrm{mass}}$ in J/kg and a volumetric heat source term $\Upsilon_{\mathrm{En}_\blacktriangle \mathrm{vol}}$ in $\mathrm{J/m^3 s}$, the balance equation is given by (Bozic et al. 2009, p. 32) (Ansys Inc. 2011, p. 27):

$$\frac{\partial \rho_{\mathrm{Mass}_\blacktriangle \mathrm{vol}}\, E_{\mathrm{En,int}_\blacktriangle \mathrm{mass}}}{\partial t} = -\mathrm{div}\left(\rho_{\mathrm{Mass}_\blacktriangle \mathrm{vol}}\, \vec{u}\, E_{\mathrm{En,int}_\blacktriangle \mathrm{mass}}\right) + \mathrm{div}\left(\Gamma_{\mathrm{visc}}\, \mathrm{grad}\left(E_{\mathrm{En,int}_\blacktriangle \mathrm{mass}}\right)\right) + \Upsilon_{\mathrm{En}_\blacktriangle \mathrm{vol}}\ . \quad (4.7)$$

The specific internal energy per unit of mass is the sum of the specific internal and kinetic energies (Bove and Ubertini 2006):

$$E_{\mathrm{En,int}_\blacktriangle \mathrm{mass}} = c_{\mathrm{En,v}_\blacktriangle \mathrm{mass}} T + \frac{\vec{u}^2}{2} + \vec{g}_{\mathrm{grav}} \cdot \vec{\mathbf{e}}\ .$$

[4] $\iota \approx 0.5 \cdot 10^{-3}$ m, $\rho_{\mathrm{Mass}_\blacktriangle \mathrm{vol}} \approx 1\,\mathrm{kg/m^3}$, $\langle \vec{u} \rangle \approx 3$ m/s, $\Gamma_{\mathrm{visc}} \approx 18 \cdot 10^{-6}\,\mathrm{kg/m\,s} \Rightarrow Re \approx 166$ for the typical dimensions and properties of the investigated cases.

Here $c_{\mathrm{En,v}_{\blacktriangle}\mathrm{mass}}$ is the specific heat per unit of mass at constant volume in J/kg K. Since the last two terms are usually negligible, using the thermal conductivity

$$\lambda_{\mathrm{En}} = \Gamma_{\mathrm{visc}} c_{\mathrm{En,v}_{\blacktriangle}\mathrm{mass}} \quad \text{in } \frac{\mathrm{W}}{\mathrm{m\,K}} ,$$

equation 4.7 simplifies to:

$$c_{\mathrm{En,v}_{\blacktriangle}\mathrm{mass}} \frac{\partial \rho_{\mathrm{Mass}_{\blacktriangle}\mathrm{vol}} T}{\partial t} = -\mathrm{div}\left(\rho_{\mathrm{Mass}_{\blacktriangle}\mathrm{vol}} \vec{u} c_{\mathrm{En,v}_{\blacktriangle}\mathrm{mass}} T\right) + \lambda_{\mathrm{En}} \underline{\Delta} T + \Upsilon_{\mathrm{En}_{\blacktriangle}\mathrm{vol}} . \quad (4.8)$$

The incorporated phenomena are once again dependent on the different regions of the SOFC. In the flow channels, next to convective heat transport with the fluid flow, its transfer between the gas streams and the solid walls is of interest. It is described by Newton's law of cooling (Meschede 2006, p. 236):

$$\frac{\partial Q_{\mathrm{En}_{\blacktriangle}\mathrm{mol}_{\blacktriangle}\mathrm{convec}}}{\partial t} = \alpha_{\mathrm{th,convec}} \cdot A \cdot \left(T_{\mathrm{wall}} - T_{(\mathrm{g})}\right) \text{ in W} \quad (4.9)$$

in dependence of the temperature difference between the wall T_{wall} and the gas-phase $T_{(\mathrm{g})}$ both in K and the local convective heat transfer coefficient $\alpha_{\mathrm{th,convec}}$ in W/m^{2}K. The latter is calculated in dependence of the local Nußelt number Nu, the hydraulic diameter of the flow channel L_{dia} in m, and the thermal conductivity of the gas phase $\lambda_{\mathrm{En}_{\blacktriangle}(\mathrm{g})}$ in W/m K (Verein Deutscher Ingenieure 2006, p. Gb 6):

$$\alpha_{\mathrm{th,convec}} = \frac{Nu \cdot \lambda_{\mathrm{En}_{\blacktriangle}(\mathrm{g})}}{L_{\mathrm{dia}}} . \quad (4.10)$$

Since the Nußelt number is strongly coupled to the flow situation,[5] various approaches for its calculation exist. In SOFCs usually mixtures of gases are apparent, thus $\lambda_{\mathrm{En}_{\blacktriangle}(\mathrm{g})}$ is a function of the constituents volume fractions. Although equation 4.9 is also valid inside the porous electrodes,[6] here the heat transfer is dominated by conduction over the fluid solid interface. Hence $\alpha_{\mathrm{th,convec}}$ should be replaced by an $\alpha_{\mathrm{th,diff}_{\blacktriangle}(\mathrm{g})/(\mathrm{s})}$ and two energy balances (one for the fluid and one for the solid) need to be solved.

If the solid structures are conductive for charged species, heat is also released due to internal ohmic losses. Inside the porous electrodes additional

[5] laminar or turbulent

[6] $T_{\mathrm{wall}} = T_{\mathrm{wall}_{\blacktriangle}(\mathrm{s})}$

sources for thermal energy are the electrochemical reactions. Insofar DIR is present in the anode, heat is consumed.

A precise modeling also includes radiative heat transfer between all components[7]. Therefore, commonly the *Stefan-Boltzmann Law (*SBL*)* (Bozic et al. 2009, p. 83) (Meschede 2006, p. 579):

$$\gamma_{\mathrm{En}_{\blacktriangle}\mathrm{rad}_{\blacktriangle}\mathrm{vol}} = A_{\mathrm{rad}} \varepsilon_{\mathrm{rad}} \sigma_{\mathrm{rad}} T^4$$

in dependence of the effective radiative surface A_{rad} per volume in $\mathrm{m}^2/\mathrm{m}^3$, the dimensionless emissivity $\varepsilon_{\mathrm{rad}}$, and the Stefan-Boltzmann constant $\sigma_{\mathrm{rad}} = 5.67 \cdot 10^{-8}\ \mathrm{W/m^2\,K^4}$ is used. Since a precise treatment of the radiative heat exchange between different parts of a SOFC is difficult (Daun et al. 2006), it is often neglected in modeling [8].

Altogether, a careful treatment of equation 4.8 is essential within SOFCs to predict the temperature distribution, improve overall cell performance, and reduce thermo-mechanical stresses[9].

4.1.5. Charge transport

In fuel cells charge is transported by electrons as well as by ions[10]. To solve the problem of charge transport, the local distribution of the (scalar) potentials $\phi_{\mathrm{el/ion}}$ in V and the current density (vector) $\vec{j}_{\mathrm{el/ion}}$ in $\mathrm{A/m^2}$ have to be calculated (Bove and Ubertini 2006). Both quantities are related towards each other by Ohm's law (Meschede 2006, p. 458, 923):

$$\begin{aligned} \vec{j}_{\mathrm{el/ion}} &= -\underline{\underline{\sigma}}_{\mathrm{el/ion}} \operatorname{grad}\left(\phi_{\mathrm{el/ion}}\right) , \\ &= \underline{\underline{\sigma}}_{\mathrm{el/ion}} \vec{\mathbb{E}}_{\mathrm{el/ion}} . \end{aligned} \tag{4.11}$$

[7] e.g. (Boder and Dittmeyer 2006; Bove and Ubertini 2006; Cui and Cheng 2009; Hwang, Chen, and Lai 2005b; Janardhanan, Heuveline, and Deutschmann 2007; Li et al. 2008; Pramuanjaroenkij, Kakac, and Yangzhou 2008; Serincan, Pasaogullari, and Sammes 2009a; Stiller 2006; Tanaka et al. 2007)

[8] e.g. (Al-Sulaiman, Dincer, and Hamdullahpur 2010; Danilov and Tade 2009; Jiang and Chen 2009; Ki and Kim 2010; Paradis et al. 2011; Schlitzberger, Leithner, and Zindler 2009; Schlitzberger 2012; Wang et al. 2007)

[9] e.g. (Andersson, Yuan, and Sunden 2010; Fischer and Seume 2009b; Liu, Kim, and Chandra-Ambhorn 2010; Tietz 1999)

[10] In the case of a SOFC two-times negatively charged oxygen ions migrating from the cathode to the anode.

The proportionality constant is given by the tensor of the electric/ionic conductivity $\underline{\underline{\sigma}}_{\text{el/ion}}$ in S/m whose value depends on the region in the cell:

$$\underline{\underline{\sigma}}_{\text{el}} = \begin{cases} \approx 0 & \text{Electrolyte, gas-phase ,} \\ \neq 0 & \text{elsewhere ,} \end{cases} \quad \underline{\underline{\sigma}}_{\text{ion}} = \begin{cases} \neq 0 & \text{electrolyte + electrodes ,} \\ = 0 & \text{elsewhere .} \end{cases}$$

The ionic transport properties of e.g. YSZ are determined by the concentration and type of defects in the bulk material (Kharton, Marques, and Atkinson 2004). Hence ionic currents can either be modeled by equation 4.11 using an experimentally validated exponential Arrhenius approach for the temperature dependence of $\underline{\underline{\sigma}}_{\text{ion}}$[11]:

$$\underline{\underline{\sigma}}_{\text{ion}}(T) = a_{\text{ion}_\blacktriangle 1} T^{a_{\text{ion}_\blacktriangle 2}} \exp\left(-\frac{\mathrm{d}G_{\text{En}_\blacktriangle\text{mol},\text{act}_\blacktriangle\text{ion}}}{\Re_{\text{En}_\blacktriangle\text{mol}} T}\right),$$

in dependence of the fitting parameters $a_{\text{ion}_\blacktriangle 1}$ in $\text{S/K}^{a_{\text{ion}_\blacktriangle 2}}\text{m}$ and $a_{\text{ion}_\blacktriangle 2}$[12] as well as the molar activation energy $\mathrm{d}G_{\text{En}_\blacktriangle\text{mol},\text{act}_\blacktriangle\text{ion}}$ in J/mol, or by a diffusive flux $\vec{J}_{\text{diff}_\blacktriangle\text{ion}}$ of ionic charges in $\text{C/m}^2\text{s}$ (Bard, Inzelt, and Scholz 2008, p. 142) (Kilo et al. 2002).

In a simplified approach the latter is described by the Nernst-Planck Equation (NPE) (see appendix B.4 for a derivation):

$$\vec{J}_{\text{diff}} = -zF_{\text{Ch}_\blacktriangle\text{mol}} \underline{\underline{D}}_{\text{ion}} \operatorname{grad}\left(c_{\text{Mol}_\blacktriangle\text{vol}}\right) - \underline{\underline{\sigma}}_{\text{ion}} \vec{\mathbb{E}} . \tag{4.12}$$

If the gradient of the particle concentration is very small,[13] the first term in equation 4.12 can be neglected, merging equation 4.12 into equation 4.11. Nevertheless, it is noteworthy to mention that this commonly made simplification[14] is only valid for very thin electrolytes. Measurements of oxygen tracer diffusion profiles made by numerous authors[15] have shown an exponential decay in concentration with growing thickness of the electrolyte, making

[11] e.g. (Garbayo et al. 2010; Hattori et al. 2004; Ji, Kilner, and Carolan 2005; Li et al. 1999; Raj, Atkinson, and Kilner 2009; Valov et al. 2009; Zhou et al. 2009; Zhu et al. 2005)

[12] dimensionless

[13] e.g. because the electrolyte is very thin

[14] e.g. (Amiri et al. 2010; Andersson et al. 2011; Autissier et al. 2004; Bove and Ubertini 2006; Nam and Jeon 2006; Shi et al. 2007a; Wang et al. 2007; Yakabe and Sakurai 2004) (Bove and Ubertini 2008, p. 54)

[15] e.g. (de Souza and Kilner 1998; Kilo et al. 2002; Ji, Kilner, and Carolan 2005; Raj, Atkinson, and Kilner 2009)

it necessary to deal with equation 4.12 rather than equation 4.11. Since the electric field $\vec{\mathbb{E}}$ in V/m belongs to the family of conservative forces (Nolting 2011, p. 59), modified versions of equation 4.1 can be formulated for the sources/sinks of the electric/ionic current density or the electronic/ionic charges $q_{\mathrm{Ch}_\blacktriangle\mathrm{el/ion}}$ in C. In dependence of the charge density $\rho_{\mathrm{vol}_\blacktriangle\mathrm{Ch}_\blacktriangle\mathrm{el/ion}}$ in C/m^3 and a volumetric source term $\Upsilon_{\mathrm{Ch}_\blacktriangle\mathrm{vol}_\blacktriangle\mathrm{el/ion}}$ in C/m^3 s current conservation can be written as:

$$\frac{\partial \rho_{\mathrm{vol}_\blacktriangle\mathrm{Ch}_\blacktriangle\mathrm{el/ion}}}{\partial t} + \mathrm{div}\left(\vec{j}_{\mathrm{el/ion}}\right) = \Upsilon_{\mathrm{Ch}_\blacktriangle\mathrm{vol}_\blacktriangle\mathrm{el/ion}} \,. \tag{4.13}$$

Since deviations in the charge distribution are equilibrated almost immediately,[16] the storage term is usually negligible for electrons. According to the physical phenomena discussed in chapter 2 this source term closes the gap to electrochemistry (Bove and Ubertini 2008, p. 62):

$$\Upsilon_{\mathrm{Ch}_\blacktriangle\mathrm{vol}_\blacktriangle\mathrm{el}} = \left\{ \begin{matrix} \mathrm{div}\left(\vec{j}\right) & \text{at the anode's TPBs,} \\ -\mathrm{div}\left(\vec{j}\right) & \text{at the cathode's TPBs,} \\ 0 & \text{elsewhere,} \end{matrix} \right\} = -\Upsilon_{\mathrm{Ch}_\blacktriangle\mathrm{vol}_\blacktriangle\mathrm{ion}} \,. \tag{4.14}$$

Altogether, the following relations can be obtained for the two potentials:
Electrons:

$$\begin{aligned} \mathrm{div}(\vec{j}_{\mathrm{el}}) &= \Upsilon_{\mathrm{Ch}_\blacktriangle\mathrm{el}_\blacktriangle\mathrm{vol}} \,, \\ \Rightarrow\ \underline{\Delta}\phi_{\mathrm{el}} &= -\frac{\Upsilon_{\mathrm{Ch}_\blacktriangle\mathrm{el}_\blacktriangle\mathrm{vol}}}{\underline{\underline{\sigma}}_{\mathrm{el}}} \,. \end{aligned} \tag{4.15}$$

Ions:

$$\begin{aligned} \Upsilon_{\mathrm{Ch}_\blacktriangle\mathrm{ion}_\blacktriangle\mathrm{vol}} &= \frac{\partial \rho_{\mathrm{vol},\mathrm{Ch}_\blacktriangle\mathrm{ion}}}{\partial t} - \mathrm{div}\left(zF_{\mathrm{Ch}_\blacktriangle\mathrm{mol}} \underline{\underline{D}}_{\mathrm{ion}} \,\mathrm{grad}\left(c_{\mathrm{Mol}_\blacktriangle\mathrm{vol}}\right) - \underline{\underline{\sigma}}_{\mathrm{ion}} \,\mathrm{grad}\left(\phi_{\mathrm{ion}}\right) \right) \,, \\ \underline{\Delta}\phi_{\mathrm{ion}} &= \frac{1}{\underline{\underline{\sigma}}_{\mathrm{ion}}} \left(\frac{\partial \rho_{\mathrm{vol},\mathrm{Ch}_\blacktriangle\mathrm{ion}}}{\partial t} - zF_{\mathrm{Ch}_\blacktriangle\mathrm{mol}} \underline{\underline{D}}_{\mathrm{ion}} \underline{\Delta}\left(c_{\mathrm{Mol}_\blacktriangle\mathrm{vol}}\right) - \Upsilon_{\mathrm{Ch}_\blacktriangle\mathrm{ion}_\blacktriangle\mathrm{vol}} \right) \,. \end{aligned} \tag{4.16}$$

[16] According to Drude's model with $\vec{\mathbb{E}} = 300$ V/m and a charge mobility of about 10^{-2} m^2/V s, electron's speed can be approximated to 10^6 m/s ($\approx$ 1/300 of the speed light in the vacuum) (Meschede 2006, p. 923 et seqq.).

4.2. State of the art

In principle, on a continuum level mathematical modeling of SOFCs always has to deal with the aspects discussed in the previous section. Nevertheless, in dependence of their geometrical dimension and scope, models often simplify some aspects and make use of results from non continuum simulations (see Figure 4.2) (Andersson, Yuan, and Sunden 2010; Karakasidis and Charitidis 2007; Lippky 2011).

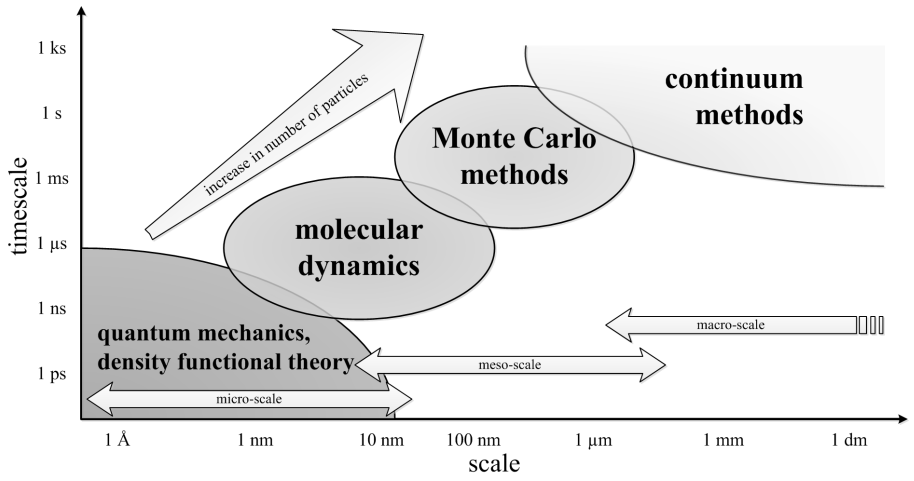

Figure 4.2.: **Characteristic length- and timescales for modeling:** In dependence of the length- and timescales of the phenomena of interest, different mathematical methods are available. So far there is no theory which unifies the worlds of micro- and macrophysics; modified from (Karakasidis and Charitidis 2007).

3D modeling allows a detailed investigation of the internal behavior of a fuel cell and hence this kind of models in general is used when detailed information about physical parameters (e.g. temperature or current density) are of interest (Lippky 2011; Wang et al. 2011). The computational domain is usually either divided into finite volumes (FVM) or finite elements (FEM) for which the governing balance equations are solved (see section 4.1). Since an accurate resolution of the physical phenomena requires large computational grids[17]

[17] where solutions have to be calculated for every Control Volume (CV) or node

the resulting simulations are usually time- and computational-resource intensive. In consequence, simple geometries, symmetric cases, and only a limited number of phenomena are commonly investigated (Bove and Ubertini 2006). Often commercial CFD codes like ANalysis SYStem, Inc. (ANSYS)/CFX (Wang et al. 2008), Comsol Multiphysics (Akhtar et al. 2009; Liu, Kong, and Lin 2009), ANSYS/FLUENT (Autissier et al. 2004; Danilov and Tade 2009; Yakabe 2001) or Star-CD (Chiang et al. 2010)(Bove and Ubertini 2008, p. 323 et seqq.) are used to solve the hydrodynamic problems, while extensions take care of the special phenomena of interest. The aims of 3D models are often either an optimization of the cell's geometry to improve operating conditions,[18] or advances in the understanding of the material properties and their influence on the electrochemical process[19].

Due to the 3D nature of the model, a spatial resolved solution of the physical phenomena and hence a 3D distribution of all quantities is calculated. Nevertheless, regarding the various models that have been proposed in the literature over the recent years, the electrochemical conversion of CO as well as the mutually coupled reformation- and charge-transfer-processes are often neglected (Wang et al. 2008). In particular advancements in the field of CO electrochemistry date back to the early works of Achenbach (Achenbach 1995). Since then almost all studies (see Table A.3 in appendix A.4) assume either a fixed ratio between CO and H_2 electrochemistry[20] or neglect the influence of CO electrochemistry even for steady-state calculations[21]. In the latter case usually CO is assumed to undergo a WGS (see section 2.5.1.2) to form CO_2 rather than contribute to electrochemistry.

Although never mentioned in this context, another strong reason for this practice is the application of "static and global information", as overpotentials, global Nernst- and cell-potentials or fixed values for e.g. activation overpotentials (polarization) in modeling. In particular for the Nernst-potential (see equation 2.20) a strict application of the methodology used for derivation would lead to higher values for U_{Nernst} compared to the pure H_2 case. To get rid of this issue e.g. Danilov and Tade (Danilov and Tade 2009) or An-

[18] e.g. homogenize temperature (Goldin et al. 2009; Lu, Schaefer, and Li 2005; Yakabe and Sakurai 2004)

[19] (Haberman and Young 2004; Yuan, Ji, and Chung 2009)

[20] often ratios of 1:4 (Gemmen and Trembly 2006) or 1:2 (Matsuzaki and Yasuda 2000) are assumed

[21] (Aguiar, Adjiman, and Brandon 2004; Sukeshini et al. 2006; Zhu et al. 2005)

dersson, Yuan, and Sundén (Andersson, Yuan, and Sundén 2012) neglected CO for U_{Nernst} calculation and Yakabe (Yakabe 2001) derived U_{Nernst} from the oxygen concentration difference between the region close the electrolyte and the bulk of the channel flow. Subsequently, the cell voltage is calculated by subtracting overpotentials from U_{Nernst}. For this, an activation overpotential corrected Nernst potential is assumed somewhere in the cell[22]. Alternatively, U_{Nernst} and U_{cell} are fixed and the activation overpotential is calculated at the reaction zones. This requires ohmic losses. These are determined by defining electrical transport properties (Akhtar et al. 2009; Goldin et al. 2009; Ho et al. 2010) and applying equivalent circuit models (Campanari and Iora 2005; Schlitzberger, Leithner, and Zindler 2009; Schlitzberger 2012). Since activation overpotential, current density, and ohmic losses are correlated, iterative techniques are required. Reaction rate and current density are in all cases connected via a BVE. In consequence, only one-step charge-transfer processes under well stirred conditions, and the charge-transfer as rate limiting step are assumed implicitly (Bard, Inzelt, and Scholz 2008, p. 63-64).

Although numerous models have been reported in the literature (see Table A.3 in appendix A.4) the development of multi-scale, multi-physics models is still in its infancy. Electrochemical models of SOFCs based on elementary kinetic processes are very rare (Andersson, Yuan, and Sunden 2010) and even in 3D modeling "global information approaches" are widely used. In particular an application of information which are from a physical point of view not available locally[23] and furthermore not very well defined[24] is prejudicial and makes an experimental validation challenging. In order to come up with the mutually coupled processes in SOFCs, Andersson, Yuan, and Sundén (Andersson, Yuan, and Sunden 2010) suggested that future models need to solve equations 4.15 and 4.16 in all domains of the cell, whereby special attention has to be paid to the source terms (Cui and Cheng 2010; Dokmaingam et al. 2010; Kang et al. 2009). Such approaches would make it possible to tailor the microstructure and material properties in order to satisfy pre-defined boundary conditions[25]. Therefore, in advance to the subsequent continuum model, the influence of micro- and meso-scale phenomena on the macro-scale properties

[22] e.g. at the surface of the electrolyte (Fergus 2005; Nam and Jeon 2006; Yakabe and Sakurai 2004)

[23] concentrations at the "other side" of the electrolyte

[24] where exactly is the "other side" of the electrolyte?

[25] e.g. temperature distribution for a given design

has to be studied and taken into account where needed.

4.3. Micro-scale phenomena and their influence on macro-scale modeling

From the aforesaid two types of influences can be identified: microstructure (scale) and reaction behavior (timescale). Therefore, in the following subsections two approaches to study their effects on a macro-scale model are presented. The first model focuses on the influence of the microstructure and composition of the anode, while the second one highlights elementary reaction kinetics at a LSM cathode.

4.3.1. Numerical investigation of the influence of anode composition and microstructure on its macro-scale properties

As discussed in section 2.4.1, anodes consist of a porous mixture of electron and ion conducting species. Therefore, the subsequent investigation has to focus on the transport properties of porous materials. Several approaches have been made to take into account not only the particle size distribution and the random topology, but also the spheroid shape of the particles and pores in porous materials (Keil 1999; Sanyal et al. 2010). In this context studies (Sahimi and Tsotsis 1985; Winterfeld, Scriven, and Davis 1981) have shown that transport and other main properties of a topologically disordered and a topologically ordered network are identical, as long as the average coordination number of both networks is equal (Ji, Yuan, and Chung 2007). Therefore, to save computational time and to reduce the complexity, a simplified Three(3)-Dimensional (3D) microstructure is assumed.

The idealized microstructure consists of a regular lattice of small cubes representing the particles of the cermet. The cubes, and therefore all the particles, have the same size. According to experimental results obtained by different authors[26] this is an acceptable simplification to the physical reality. Each cube can be filled with only one species. The probability that a certain cube is occupied by a nickel particle is given by the average nickel con-

[26](Alzate-Restrepo and Hill 2010; Lee et al. 2002; Oliveira and Grande 2010; Simwonis, Tietz, and Stöver 2000; Storjohann et al. 2009)

tent of the cermet $c_{\%,\mathrm{Ni}}$. Accordingly, the probability for a YSZ particle to block a certain cube is $c_{\%,\mathrm{YSZ}}$, whereas the probability for a pore is given by $c_{\%,\mathrm{pore}} = 1 - c_{\%,\mathrm{Ni}} - c_{\%,\mathrm{YSZ}}$. Under the assumption of an ideal mixture of the starting powders, the occupation probability $O_{\%}$ for every cube i in dependence of a pseudo-random number Θ[27] is independent from the other cubes and can be determined by the average composition of the cermet:

$$O_{\%,i}(\Theta) = \begin{cases} \mathrm{Ni} & 0 \leq \Theta \leq c_{\%,\mathrm{Ni}}\,, \\ \mathrm{YSZ} & c_{\%,\mathrm{Ni}} < \Theta\, c_{\%,\mathrm{Ni}} + c_{\%,\mathrm{YSZ}}\,, \\ \mathrm{gas} & c_{\%,\mathrm{Ni}} + c_{\%,\mathrm{YSZ}} < \Theta \leq 1\,. \end{cases} \tag{4.17}$$

For the formation of cluster structures it is further assumed that all species flows (electrons, ions, and gas-particles) can only happen through the faces of the cubes. Common boundaries between three volumes of arbitrary shape always have to be lines. Therefore, it is assumed, that TPBs are given by the edges between the three different constituents. The existence of a TPB is only assumed in the case that each of the three species is part of an uninterrupted path between TPB and its respective contact area ("contact cluster", see Figure 4.3).

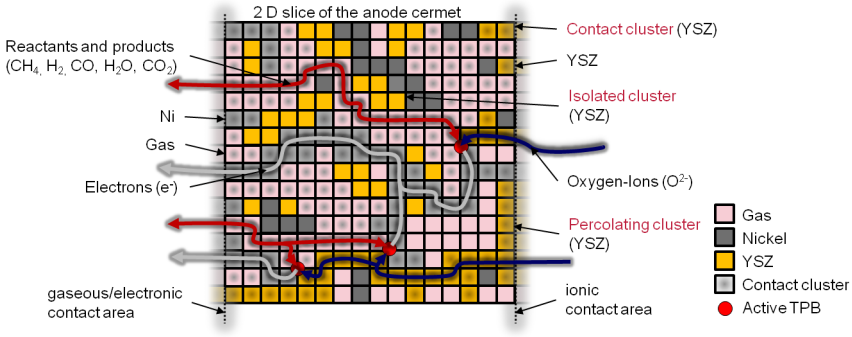

Figure 4.3.: **Two dimensional slice of the modeled anode cermet:** Electrochemical reactions only occur on TPBs having uninterrupted paths to all contact areas (Wesemeyer, Jocher, and Leithner 2011).

[27] $0 \leq \Theta \leq 1$

The contact areas for electrons (Ni as conductor) and gas phase (pores as conductor) are assumed to be on one of the surfaces of the computational domain (i.e. x-y-plane, $z = \text{min.}$) and the contact area for ions (YSZ as conductor) is assumed to be a second x-y-plane at $z = \text{max.}$. These assumptions represent the situation inside a SOFC, where the IC and the gas channel are on one side of the electrode, whereas the electrolyte is on the other side. Keeping the overall thickness of the electrode fixed to some value (e.g. 100 µm (de Haart 2009c)), a variation of the number of cubes in z-direction is equal to a reduction in particle size, resulting in the possibility to study its influence on the anode properties.

The procedure discussed so far is a modified version of an algorithm first described by Hoshen and Kopelman (Hoshen and Kopelman 1976). All cubes in the computational domain are one after another randomly filled by one of the three species, starting from the origin at $x = y = z = 0$ and going on in layers in the x-y-plane with increasing z. To reduce computation time and to simplify the following steps three copies of the computational domain are made, one for each species. In the subsequent text the methodology is just described for one of the species, but in reality has to be consistently carried out for all three in the same way. In accordance to Hoshen and Kopelman (Hoshen and Kopelman 1976) the labeling of the cubes and a preliminary cluster identification can be performed simultaneously. If a certain cube is assigned to a species the algorithm checks whether the adjacent cubes in x- or y-direction belong to the same species (label $\neq 0$) or not (label $= 0$). If an adjacent cube with a label not equal to zero is found this label is used, otherwise the value of the species counter is applied and subsequently incremented by one. After the labeling and the preliminary cluster identification is done for all $z = \text{const.}$ planes the cubes are checked once again for cluster formation in all spatial directions. If one of the neighbors of a certain cube is also occupied by the same species, but with a different labeling index all cubes with the larger of both numbers are relabeled with the smaller one. As a consequence some of the originally assigned k_i cluster-numbers are not needed any more. Therefore, in a final stage all clusters are re-labeled starting from one in an ascending order, resulting in l_i clusters for each species i (see Figure 4.4). As a consequence of the application of this modified Hoshen-Kopelman-algorithm (Hoshen and Kopelman 1976) it is not only possible to determine the number of clusters in dependence of the particle size, but also to easily investigate percolation and electrochemical properties. To realize this, layer $z = 1$ is assumed to be in contact with both

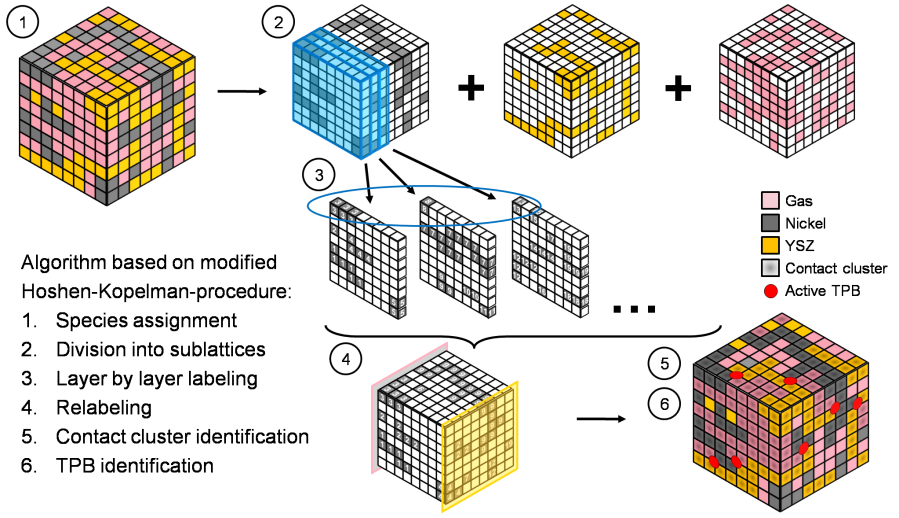

Figure 4.4.: **Virtual division of the anode cermet in three sublattices:** Starting with Ni, the cube labeling algorithm is applied subsequently to YSZ and gas. It automatically checks for clusters in $z = \text{const.}$ planes. Finally, an identification of clusters in z-direction and a re-labeling is done (Wesemeyer, Jocher, and Leithner 2011).

the electron conducting IC and the gas channel and the layer $z = z_{\max}$ to be in contact with the ion conducting electrolyte. In consequence, only those clusters which are in contact with one of these layers (Ni and gas-phase with the layer at $z = z_{\min}$ and YSZ with the layer at $z = z_{\max}$), so called "contact clusters" are of interest for the subsequent determination of the TPBs. Since the algorithm also counts the number of cubes in each cluster, a determination of the TPBs also generates direct information on the electrochemically active volume fractions of each species.

The identification of the TPBs is done very similar to the procedure described so far. Starting with Ni, for each cube of the lattice it is ascertained whether it belongs to a contact cluster. If that is the case, all adjacent cubes are successively checked first to see if they belong to a YSZ-contact cluster. If this is true, the remaining cubes that share a common edge with the other two are checked whether they belong to a gas-phase contact cluster. If any of the conditions is not satisfied the algorithm terminates and proceeds with

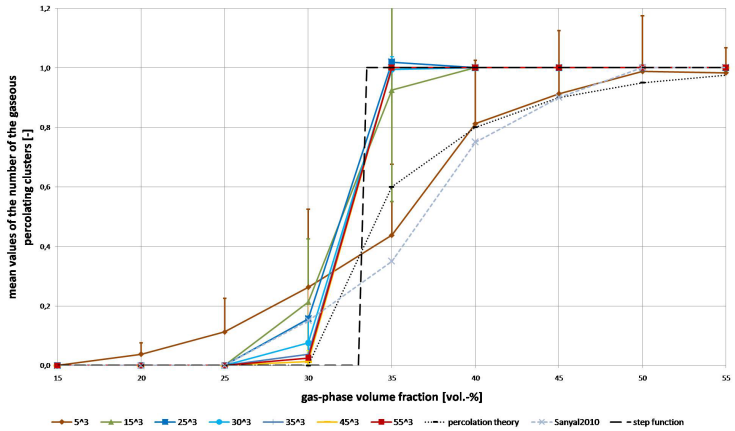

Figure 4.5.: **Percolation probability as a function of the gas-phase volume fraction:** For several grid sizes the obtained results (average over then repetitions) are compared with those of Sanyal et al. (Sanyal et al. 2010), Ji et al. (Ji, Yuan, and Chung 2007), and percolation theory (McLachlan, Blaszkiewicz, and Newnham 1990); (Wesemeyer, Jocher, and Leithner 2011).

the YSZ-condition for the next adjacent cube. If no more adjacent YSZ-cubes are found, it proceeds with the Ni-condition for the next cube. The algorithm terminates with summing up the numbers of TPBs, cubes belonging to each species, cubes in contact- and completely percolating-clusters (clusters going through the entire lattice), and those cubes in electrochemically active clusters (clusters to which at least one TPB belongs).

As it can be seen in Figure 4.5, the obtained results for the percolation probability as a function of the gas-phase volume fraction is in good agreement with the results of several other studies[28], and with percolation theory (McLachlan, Blaszkiewicz, and Newnham 1990). For all three species i the calculated rapid increase in percolation probability is in the range of $0.3 \leq c_{\%,i} \leq 0.4$. Altogether, the obtained results not only fit well to numerical findings, but also to experimental data (Ji, Yuan, and Chung 2007; Lee et al. 2002). Therefore, strong indications are apparent that the computational approach provides reasonable representations of the microstructure. Since the increase in the porosity improves the gas transport properties of the cermet it is desirable.

[28](Ji, Yuan, and Chung 2007; Sanyal et al. 2010; Shi et al. 2007a; Shi et al. 2007b)

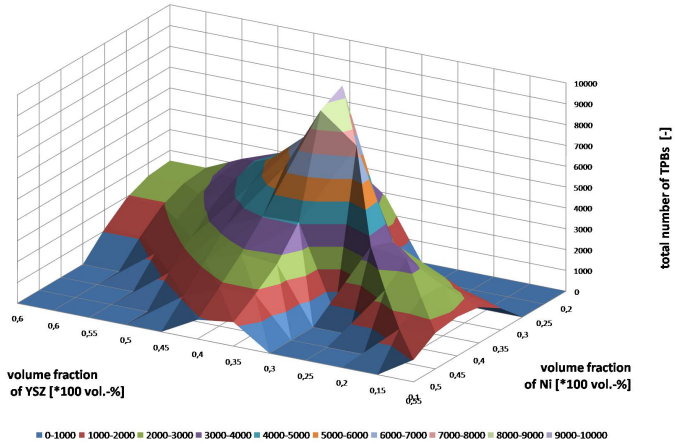

Figure 4.6.: **Total number of TPBs in dependence of the cermet composition:** Presented are average values over ten repetitions for 50 particle layers in each spatial direction (Wesemeyer, Jocher, and Leithner 2011).

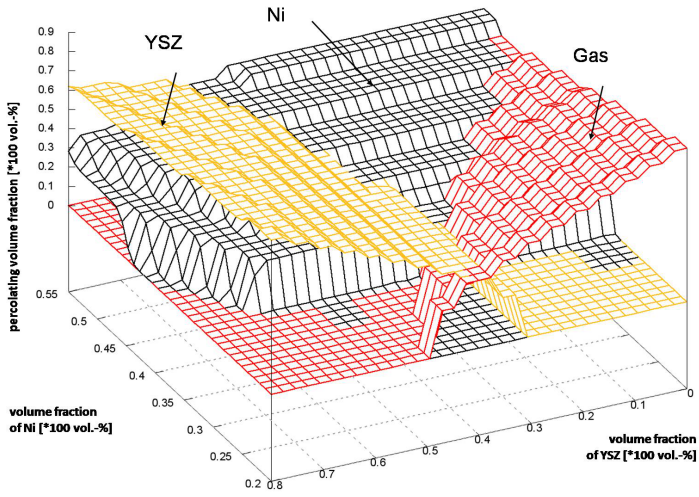

Figure 4.7.: **Relative volume fractions of percolating elements in dependence of the cermet composition:** Presented are average values over ten repetitions for 50 particle layers in each spatial direction (Wesemeyer, Jocher, and Leithner 2011).

Unfortunately, an improvement of the gas transport simultaneously decreases the electrochemically active volumes of the solid fractions. In Figure 4.7 the relative volume fractions of percolating gas- and solid-phase clusters in dependence of the porosity are presented. It is apparent that for a porosity of 40 % a crossing in the relative number of particles belonging to percolating clusters from solid state $Я_{(s)}$ to gas-phase $Я_{pore}$ occurs. Above this value the increase in $Я_{pore}$ is almost directly proportional to an increase in porosity $Po_{\%}$, whereas, due to the binary isovolumetric mixture, the deviation of $Я_{(s)}$ from an ideal anti-proportional behavior is larger. For an ideal cermet the optimum of the relative number of particles belonging to percolating clusters as well as of the number of TPBs has to be evaluated in dependence of the cermet composition (see Figures 4.6 and 4.7).

Although a large number of TPBs is desirable for a high electrochemical activity of the cermet, the transport properties cannot be neglected. As Figure 4.7 indicates, those are highly dependent on the cermet composition too. Since each of the three components accounts to a different transport phenomena, the average properties of the cermet are easily adjusted by a variation of the composition and will always be a compromise between the electronic-, ionic-, and gas-phase conductivities. A comparison of Figure 4.6 and Figure 4.7 reveals a relative minimum in the overall transport properties (almost no percolation is apparent) for the composition with the maximum in the total number of TPBs. Since the relative volume fractions are close to the percolation threshold, the formation of large complexes of contact clusters for each species without complete penetration of the entire structure, are a possible explanation for this. With respect to the results in Figure 4.6 the optimal number of TPBs is reached, if the concentration of all species is as close to the percolation limit as possible.

In summary it can be said that percolation theory gives suitable results for the composition dependence of all transport phenomena. For concentrations much higher than the percolation threshold the overall transport properties can be approximated by those of the non-porous material. When simulating mixtures of three or more constituents, usually there is no percolating cluster for at least one of the species. Here either some differences between model and reality have to be accepted[29] or local micro-models are required.

[29] assuming percolating clusters for all species

4.3.2. Surface electrochemistry

The results of the last subsection reveal that micro-scale submodels can help to understand local phenomena. Nevertheless, average values for properties are in general an acceptable approximation for continuum simulations. This subsection deals with the interaction of fluid and solid phase and the influence of elementary reactions on overall reaction kinetics. The aim is to determine the importance of these micro-timescale processes on continuum models. For this purpose first of all a brief review on sorption modeling and the current state of the art are given, before a detailed surface reactions model is proposed for a LSM cathode.

4.3.2.1. Sorption modeling

In order to highlight the role of the catalyst, the global reactions have to be divided into several sub-reactions including ad- and desorption as well as surface ones. In the literature various approaches to model such processes exist (Brivio and Grimley 1993).

The elementary idea for catalyst modeling is that of an *adsorption isotherm* covering the surface of the catalyst. Here the most common one is the *Langmuir Isotherm (*LI*)* (Hoinkins and Lindner 2007). The basic assumption of this model is that during sorption on energetically equivalent places just one layer of non-interacting molecules is formed at the catalyst surface. The gas phase is treated as a continuum so that the behavior of the adsorbed species can be described by that of the two-phase interface. Here the focus lies on the surface coverage of the catalyst by a species *i*:

$$\Theta_{\mathrm{perc}\blacktriangle i} = \frac{c_{\mathrm{Mol}\blacktriangle\mathrm{vol}\blacktriangle\mathrm{ad}\blacktriangle i}}{\Xi_{\mathrm{mol}} A_{\mathrm{eff}\blacktriangle\mathrm{vol}}}$$

which is the ratio of the adsorbent concentration $c_{\mathrm{Mol}\blacktriangle\mathrm{vol}\blacktriangle\mathrm{ad}\blacktriangle i}$ in mol/m^3 to the product of the total surface site density Ξ_{mol} in mol/m^2, and the effective surface per volume $A_{\mathrm{eff}\blacktriangle\mathrm{vol}}$ in m^2/m^3. Since only monolayer adsorption is apparent $\sum_i \Theta_{\mathrm{perc}\blacktriangle i} = 1$. In the case of a fully kinetic description of the sorption process by an Arrhenius approach (see equation 2.24), the surface coverage can be taken into consideration by introducing the concentration of free surface sites as reactants in the ad- and products in the desorption reactions. Here usually ei-

ther the Langmuir-Hinshelwood Kinetics (LHK)[30] or the Roginskij-Zel'dovic Kinetics (RZK)[31] are used. For a species $\mathcal{A}$ and an adsorption surface site σ_{ad} both assume the following basic reaction scheme, whereby RZK's coverage dependency is added by the dimensionless model parameter K (Bard, Inzelt, and Scholz 2008, p. 16)(Deutschmann et al. 2011, p. 18):

$$\begin{aligned}
&\mathcal{A} + \sigma_{\mathrm{ad}} \rightleftharpoons \mathcal{A}_{(\mathrm{ad},\varsigma)} \\
\Rightarrow r_{\mathrm{reac}\blacktriangle\mathrm{surf}\blacktriangle\mathcal{A}} &= \frac{\mathrm{d}\Theta_{\mathrm{perc}\blacktriangle\mathcal{A}}}{\mathrm{d}t} = \underbrace{r_{\mathrm{reac}\blacktriangle\mathrm{ad}\blacktriangle\mathcal{A}}}_{\text{adsorption}} - \underbrace{r_{\mathrm{reac}\blacktriangle\mathrm{des}\blacktriangle\mathcal{A}}}_{\text{desorption}}, \\
&= \Re_{\mathrm{reac}\blacktriangle\mathrm{Vol,mol}\blacktriangle\mathrm{ad}\blacktriangle\mathcal{A}} \cdot c_{\mathrm{Mol}\blacktriangle\mathrm{vol}\blacktriangle\mathcal{A}} \cdot \left(1 - \Theta_{\mathrm{perc}\blacktriangle\mathcal{A}}\right) \cdot T^{a_{\mathrm{ad}}} \cdot \exp\left(-\frac{\mathrm{d}G_{\mathrm{En}\blacktriangle\mathrm{mol}\blacktriangle\mathrm{act}\blacktriangle\mathrm{ad}}}{\Re_{\mathrm{En}\blacktriangle\mathrm{mol}} T} + \mathrm{K}_{\mathrm{ad}}\Theta_{\mathrm{perc}\blacktriangle\mathcal{A}}\right) \\
&\quad - \Re_{\mathrm{reac}\blacktriangle\mathrm{des}\blacktriangle\mathcal{A}} \cdot \Theta_{\mathrm{perc}\blacktriangle\mathcal{A}} \cdot T^{a_{\mathrm{des}}} \cdot \exp\left(-\frac{\mathrm{d}G_{\mathrm{En}\blacktriangle\mathrm{mol}\blacktriangle\mathrm{act}\blacktriangle\mathrm{des}}}{\Re_{\mathrm{En}\blacktriangle\mathrm{mol}} T} + \mathrm{K}_{\mathrm{des}}\Theta_{\mathrm{perc}\blacktriangle\mathcal{A}}\right). \qquad (4.18)
\end{aligned}$$

Here $\Re_{\mathrm{reac}\blacktriangle\mathrm{Vol,mol}\blacktriangle\mathrm{ad}\blacktriangle\mathcal{A}}$ and $\Re_{\mathrm{reac}\blacktriangle\mathrm{des}\blacktriangle\mathcal{A}}$ are the forward and backward reaction rate constants of the ad- and desorption in $\mathrm{m}^3/\mathrm{s\,mol\,K}^{a_{\mathrm{ad}}}$ and $1/\mathrm{s\,K}^{a_{\mathrm{des}}}$. If charge exchanges are apparent too, equation 4.18 needs to be extended by a term proportional to the difference $\Delta\phi$ in electric/ionic potential which acts as an additional driving force:

$$\begin{aligned}
&\mathcal{A} + \sigma_{\mathrm{ad}} + e^-_{\mathrm{Ch}} \rightleftharpoons \mathcal{A}^-_{(\mathrm{ad},\varsigma)}; \\
\Rightarrow r_{\mathrm{reac}\blacktriangle\mathrm{surf}\blacktriangle\mathcal{A}} &= \Re_{\mathrm{reac}\blacktriangle\mathrm{Vol,mol}\blacktriangle\mathrm{ad}\blacktriangle\mathcal{A}} \cdot c_{\mathrm{Mol}\blacktriangle\mathrm{vol}\blacktriangle\mathcal{A}} \left(1 - \Theta_{\mathrm{perc}\blacktriangle\mathcal{A}}\right) \cdot T^{a_{\mathrm{ad}}} \\
&\quad \cdot \exp\left(-\frac{\mathrm{d}G_{\mathrm{En}\blacktriangle\mathrm{mol}\blacktriangle\mathrm{act}\blacktriangle\mathrm{ad}} + zF_{\mathrm{Ch}\blacktriangle\mathrm{mol}}\Delta\phi}{\Re_{\mathrm{En}\blacktriangle\mathrm{mol}} T} + \mathrm{K}_{\mathrm{ad}}\Theta_{\mathrm{perc}\blacktriangle\mathcal{A}}\right) \\
&\quad - \Re_{\mathrm{reac}\blacktriangle\mathrm{des}\blacktriangle\mathcal{A}} \cdot \Theta_{\mathrm{perc}\blacktriangle\mathcal{A}} \cdot T^{a_{\mathrm{des}}} \cdot \exp\left(-\frac{\mathrm{d}G_{\mathrm{En}\blacktriangle\mathrm{mol}\blacktriangle\mathrm{act}\blacktriangle\mathrm{des}} - zF_{\mathrm{Ch}\blacktriangle\mathrm{mol}}\Delta\phi}{\Re_{\mathrm{En}\blacktriangle\mathrm{mol}} T} + \mathrm{K}_{\mathrm{des}}\Theta_{\mathrm{perc}\blacktriangle\mathcal{A}}\right). \qquad (4.19)
\end{aligned}$$

By way of contrast, the sorption kinetics is often assumed to be very fast and hence always in an equilibrium state. Therefore, steady-state expressions in dependence of the partial pressure p_i in Pa in a direct neighborhood of the reaction sites and dimensionless adsorption coefficients $\zeta_{\mathrm{ad}\blacktriangle i}$ can be derived (Behr, Agar, and Jörissen 2010, p. 47):

$$\Theta_{\mathrm{perc}\blacktriangle i} = \frac{\zeta_{\mathrm{ad}\blacktriangle i}\, p_i}{p_{\mathrm{tot}} + \sum_{j=1}^{N_{\mathrm{Mol}}} \zeta_{\mathrm{ad}\blacktriangle j} p_j}. \qquad (4.20)$$

[30] no surface interactions of the adsorbate

[31] coverage dependent adsorption energy

In the case of a charged surface, equation 4.20 might also be modified by a potential dependent term. When describing surface coverage by a LI both surface non-idealities as well as lateral interactions of the adsorbed species are neglected. The latter might be taken into account either by introducing surface activity coefficients into equation 4.20 or making the $\zeta_{\text{ad}\blacktriangle j}$ a function of the surface coverage *(Frumkin- and Temkin-isotherms)* (Bard, Inzelt, and Scholz 2008, p. 15).

An alternative approach neglects the chemical kinetics of the adsorption process and tries to describe the phenomena by the probability ($0 \leq \text{Ш}_{\text{ad}} \leq 1$) that particles from the gas phase are adsorbed when they hit the catalyst surface. Assuming a Boltzmann distribution of molecular velocities near the surface, the volumetric molar adsorption rate of the i-th species $r_{\text{reac}\blacktriangle\text{ad}\blacktriangle\text{Mol,vol}\blacktriangle i}$ in $\text{mol/m}^3\,\text{s}$ can be written as (Deutschmann et al. 2011, p. 18):

$$r_{\text{reac}\blacktriangle\text{ad}\blacktriangle\text{Mol,vol}\blacktriangle i} = \text{Ш}_{\text{ad}\blacktriangle i}\sqrt{\frac{\Re_{\text{En}\blacktriangle\text{mol}}T}{2\pi M_{\text{Mass}\blacktriangle\text{mol}\blacktriangle i}}}\, c_{\text{Mol}\blacktriangle\text{vol}\blacktriangle i}\cdot c_{\text{Mol}\blacktriangle\text{vol}\blacktriangle\text{Ni}}^{\kappa_i}\,. \tag{4.21}$$

In dependence of the specific approach, $\text{Ш}_{\text{ad}\blacktriangle i}$ is a function И of the available surface adsorption sites, lateral interactions with other adsorbents a.s.o. (Deutschmann et al. 2011, p. 18):

$$\text{Ш}_{\text{ad}\blacktriangle\text{eff}\blacktriangle i} = \text{Ш}^0_{\text{ad}\blacktriangle i}\cdot \text{И}(\Theta_{\text{perc}\blacktriangle i}, T, ...)\ \text{in}\ \frac{1}{\text{m}}\left(\frac{\text{m}^3}{\text{mol}}\right)^{\kappa_i}.$$

The surface reactions of the adsorbates can be described by the usual Arrhenius approaches in equations 2.23 and 2.24 or an extended version

$$r_{\text{reac}\blacktriangle\text{elchem}\blacktriangle\text{Mol,vol}} = \Re_{\text{reac}}{}^0\cdot T^a \exp\left(-\frac{\text{d}G_{\text{En}\blacktriangle\text{mol,act}} + zF_{\text{Ch}\blacktriangle\text{mol}}\Delta\phi}{\Re_{\text{En}\blacktriangle\text{mol}}T} + \text{Ъ}\Theta_{\text{perc}}\right)\prod_i c_{\text{Mol}\blacktriangle\text{vol}\blacktriangle i}^{\kappa_i}\ \text{in}\ \frac{\text{mol}}{\text{m}^3\text{s}}, \tag{4.22}$$

which also respects lateral interactions of the adsorbate and charge transfer processes.

Since both, catalyzed reformation as well as electrochemistry, are surface bound processes, in principle detailed surface reaction schemes are required for a precise modeling. For instance the reformation of methane can be described by the very sophisticated reaction scheme of Hecht et al. (Hecht et al. 2005). It subdivides the global reactions from section 2.5 into 42 elementary reactions. The mechanism was applied to electrochemical problems by Zhu et al. (Zhu et al. 2005) and has today become a part of the DETailed

CHEMistry (DETCHEM)-SOFC package (Deutschmann et al. 2011). To take into account electrochemistry at least the following three reactions[32] have to be implemented (Zhu et al. 2005):

$$\mathrm{H}_{2_{\blacktriangle}(\mathrm{g})} + \mathrm{O}^{\times}_{\mathrm{O}_{\blacktriangle}\mathrm{ELE}} \rightleftharpoons \mathrm{H_2O}_{\blacktriangle(\mathrm{g})} + V_{\mathrm{O}_{\blacktriangle}\mathrm{Mol}_{\blacktriangle}\mathrm{vol}_{\blacktriangle}\mathrm{ELE}}^{\bullet\bullet} + 2e^{-}_{\mathrm{Ch}_{\blacktriangle}\mathrm{ANO}},$$

$$\mathrm{CO}_{\blacktriangle(\mathrm{g})} + \mathrm{O}^{\times}_{\mathrm{O}_{\blacktriangle}\mathrm{ELE}} \rightleftharpoons \mathrm{CO}_{2_{\blacktriangle}(\mathrm{g})} + V_{\mathrm{O}_{\blacktriangle}\mathrm{Mol}_{\blacktriangle}\mathrm{vol}_{\blacktriangle}\mathrm{ELE}}^{\bullet\bullet} + 2e^{-}_{\mathrm{Ch}_{\blacktriangle}\mathrm{ANO}},$$

$$2e^{-}_{\mathrm{Ch}_{\blacktriangle}\mathrm{CAT}} + \frac{1}{2}\mathrm{O}_{2_{\blacktriangle}(\mathrm{g})} + V_{\mathrm{O}_{\blacktriangle}\mathrm{Mol}_{\blacktriangle}\mathrm{vol}_{\blacktriangle}\mathrm{ELE}}^{\bullet\bullet} \rightleftharpoons \mathrm{O}^{\times}_{\mathrm{O}_{\blacktriangle}\mathrm{ELE}} \,.$$

For both, anode[33] as well as cathode[34], numerous possible elementary reaction pathways and rate-limiting steps have been proposed. For the anode side the different models (see Figure 4.8) are similar for the sorption processes and the formation of hydroxyl radicals (OH). Differences can be found primarily in the locations of the electrochemical reactions, the interstitial behavior of O^{2-} inside YSZ, the charge transfer steps, and the sorption behavior of water (Bieberle 2000, p. 14) (Horita et al. 2006). Mogensen et al. (Mogensen et al. 2007) argued that the great variety of proposed mechanisms and intermediates might be a consequence of different amounts of impurities on the YSZ surface[35] and hence related to operational conditions and specimen preparation (Utz et al. 2011a). Although spatial-resolved kinetic studies reveal that methane is steam reformed at the anode rather than being directly utilized electrochemically (Kleis et al. 2009), some reaction mechanisms have been proposed for the electro-oxidation of carbon based species as well. Nevertheless, due to the high number of possible intermediates compared to hydrogen, the mechanisms are still less investigated and understood[36].

On the cathode side the situation is somehow simpler, since only the reduction of oxygen has to be considered. Nevertheless, numerous possible surface reaction paths have been proposed as well[37].

[32] written in *Kröger-Vink notation*

[33] (Bieberle 2000; Boer 1998; Holtappels, de Haart, and Stimming 1999; Holtappels et al. 1999; Kee, Zhu, and Goodwin 2005; Kresse and Hafner 2000; Liu et al. 1995; Mizusaki et al. 1994; Wang, Nakagawa, and Kato 2001)

[34] (Adler 2004; Co, Xia, and Birss 2005; de Souza and Kilner 1998; Fleig 2003; Kenney and Karan 2006; Kim et al. 2006a; Kuznecov et al. 2004; Mitterdorfer and Gauckler 1999a; Mitterdorfer and Gauckler 1999b; Östergärd and Mogensen 1993; Prestat, Koenig, and Gauckler 2007) (Vielstich, Lamm, and Gasteiger 2003b, p. 543 et seqq.)

[35] mainly SiO_2

[36] (Kleis et al. 2009; Utz et al. 2011b; Yurkiv et al. 2011)

[37] (Vielstich, Lamm, and Gasteiger 2003b, p. 595 et seqq.) (Armstrong et al. 2011; Mitterdor-

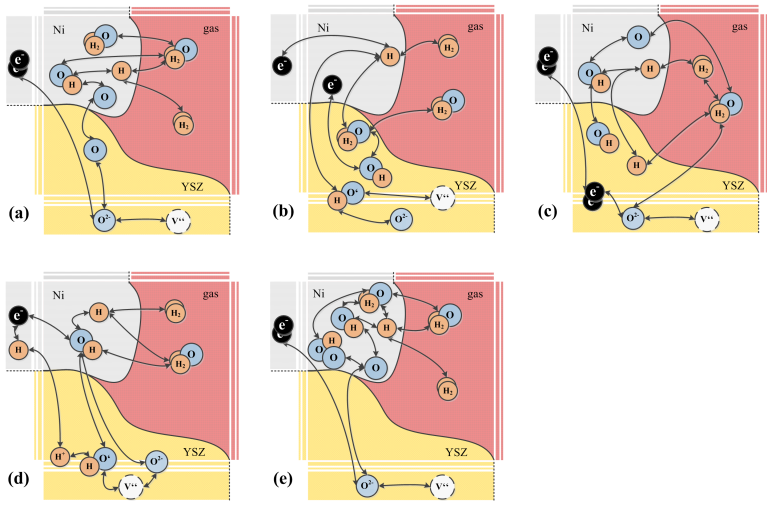

Figure 4.8.: **Electrochemical models proposed for the hydrogen kinetics of SOFC anodes:** Mizusaki et al. (Mizusaki et al. 1994) supposes oxygen migration to the Ni surface ⓐ, whereas de Boer (Boer 1998) and others (Goodwin et al. 2009; Zhu and Kee 2008) expect hydronium ions and the YSZ surface as primary reactants ⓑ. In contrast Jiang and Badwal (Jiang and Badwal 1997) ⓒ, Holtappels et al. (Holtappels, de Haart, and Stimming 1999; Holtappels et al. 1999) ⓓ, as well as Bieberle (Bieberle 2000) and successors ⓔ (Bieberle and Gauckler 2002; Mukherjee and Linic 2007; Vogler et al. 2009) again suggest the Ni surface to be the main location for hydrogen electrochemistry.

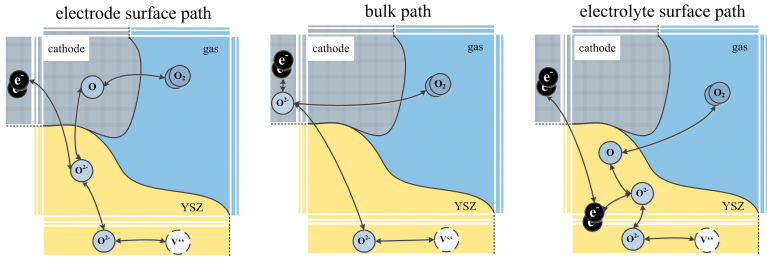

Figure 4.9.: **Reaction pathways for oxygen reduction:** The oxygen might either be adsorbed by the LSM first (left and middle) and then transferred to the electrolyte or directly by the latter, whereby the cathode just acts as an electron provider. In dependence of the modeling assumptions, modifications and combinations of the paths are possible; modified from (Fleig 2003).

fer and Gauckler 1999a)

In accordance to Fleig (Fleig 2003) they can be divided into the three main pathways shown in Figure 4.9. Oxygen might either be adsorbed by the cathode material and subsequently transported to the electrolyte or directly incorporated into the formers atomic grid under adsorption of electrons coming from the bulk. Since the overall reaction rate is dominated by the path with the fastest rate determining step, often only one reaction pathway is assumed (Smith et al. 2006; Svensson 1998). Nevertheless, it is noteworthy to mention that different reaction paths can coexist and affect each other, making the choice of the dominant reaction mechanism dependent on the manufacturing process, the material composition, and on operating conditions (Fleig 2003).

4.3.2.2. A surface reaction model based on elementary reaction kinetics

In order to set up a sub-model for the cathode side, a preparative study of a LSM-YSZ cathode with both a bulk path and a surface path for oxygen reduction is performed (see Figure 4.10). The mechanism is based on the study

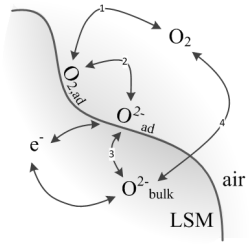

Figure 4.10.: **Oxygen reduction mechanism:** Molecular oxygen is either adsorbed, charged, and then transferred into the bulk material or directly incorporated into the latter.

of Choi et al. (Choi et al. 2009) who investigate the reaction enthalpies of various adsorption mechanisms via molecular dynamic calculations. Molecular oxygen is adsorbed first, before the molecules subsequently rearrange their electron hulls to form "peroxo-like" species of adsorbed O_2^{2-}-ions. These ions are afterwards dissociated into atoms and integrated into the bulk structure. Alternatively, a direct transition between gas-phase and bulk structure is also possible (Choi et al. 2009). To simplify the situation during calculation, in contradiction to Choi et al., in this study the adsorbed "superoxo-like"

species are assumed to be uncharged. Since potential dependent reaction rates

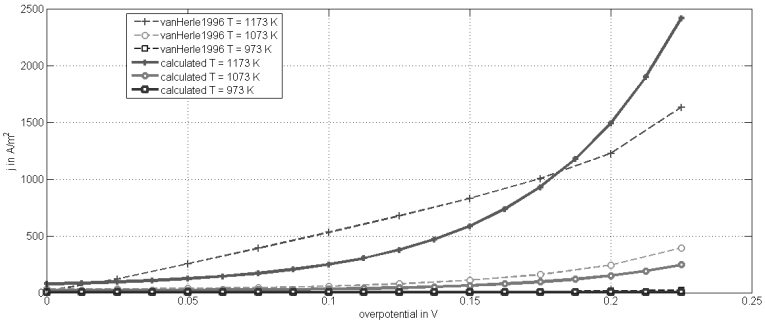

Figure 4.11.: **Cathodic polarization curves:** The curves are measured by von Herle, McEvoy, and Thampi (van Herle, McEvoy, and Thampi 1996) in air at 1000 - 1200 K for porous LSM electrodes. The parameters of the calculated curves are determined by a Gauss-Seidel algorithm and are summarized in Table 4.1 and Table 4.2.

are not determined by Choi et al. (Choi et al. 2009), a Gauss-Seidel algorithm is implemented in MATLAB in order to make a temperature dependent least squares fit to experimental data obtained by van Herle, McEvoy, and Thampi (van Herle, McEvoy, and Thampi 1996) for porous LSM (see Figure 4.11).

Table 4.1.: **Cathode properties:** Parameters needed in modeling of the heterogeneous oxygen reduction at a LSM cathode.

Quantity	**Value**	**Dimension**	**References**
$A_{\text{eff}\blacktriangle\text{vol}}$	$1.0{\cdot}10^{3}$	m^2/m^3	(Svensson 1998)
$Po_{\%}$	0.25		(Svensson 1998)
β	0.5		assumed
$\Xi_{\text{mol}\blacktriangle\text{LSM}}$	$1.0{\cdot}10^{-1}$	mol/m^2	(Svensson 1998)
$V_{\text{O}\blacktriangle\overset{\bullet\bullet}{\text{M}}\text{ol}\blacktriangle\text{vol}\blacktriangle\text{LSM}} = V_{\text{O}\blacktriangle\overset{\bullet\bullet}{\text{M}}\text{ol}\blacktriangle\text{vol}\blacktriangle\text{YSZ}}$	20.0	mol/m^3	(Svensson 1998)

The reaction mechanism and the calculated quantities are summarized in Table 4.2. It is obvious that the calculated curves are in a qualitative agreement with the measured ones. Nevertheless, the quantitative agreement is not very high. Reasons for this might on the one hand the simple structure of the proposed mechanism and on the other hand the very limited amount of experimental data. When trying to put the obtained results in a relationship with the

findings in the literature, it can be said that although detailed reaction mechanisms, including the reformation of methane (Hecht et al. 2005), and CO electrochemistry (Yurkiv et al. 2011), have been proposed for both anode (Vogler et al. 2009) as well as cathode (Choi et al. 2009), cell/stack modeling literature based on them is rare (Danilov and Tade 2009; Janardhanan, Heuveline, and Deutschmann 2007). A possible explanation for this might be, that surface reactions are very fast compared to fluid or thermal flow phenomena. Hence the former can be assumed to be always in an equilibrium state and therefore are only important as rate limiting steps. If the equilibrium assumption is waived, the reaction rates get strongly dependent on the surface coverage and the number of available surface sites.

Further studies in the context of this thesis, concerning an implementation of Hecht et al.'s surface reaction scheme (Hanke 2011b; Hanke 2011a) and the electrochemistry mechanisms proposed by Vogler et al. (Vogler et al. 2009) and Yurkiv et al. (Yurkiv et al. 2011), reveal not only a very high computational effort for calculation, since very small time steps[38] are required (Horn 2012).

Table 4.2.: **Oxygen reduction on LSM:** The reaction scheme describes the oxygen reduction mechanism for porous LSM cathodes. Values for $\mathrm{d}G_{\mathrm{En_{\blacktriangle mol}},act}$ and $\mathrm{d}G_{\mathrm{En_{\blacktriangle mol}},reac}$ are given in kJ/mol and are taken from Choi et al. (Choi et al. 2009).

reaction	$\Re_{reac}{}^{0}$	**a**	$\mathbf{d}G_{\mathbf{En_{\blacktriangle mol}},act}$ **or** $\mathbf{d}G_{\mathbf{En_{\blacktriangle mol}},reac}$
$O_2 + LSM_{surf} \longrightarrow O_{2_{\blacktriangle(ad,LSM)}}$	$9.44 \cdot 10^{4}$	-1.55	1.0
$O_{2_{\blacktriangle(ad,LSM)}} \longrightarrow O_2 + LSM_{surf}$	$3.92 \cdot 10^{16}$	-0.35	-113.86
$O_{2_{\blacktriangle(ad,LSM)}} + 2e^{-}_{Ch_{\blacktriangle LSM}} \longrightarrow O^{2-}_{\blacktriangle(ad,LSM)}$	$1.0 \cdot 10^{10}$	-4.0	1.0
$O^{2-}_{\blacktriangle(ad,LSM)} \longrightarrow O_{2_{\blacktriangle(ad,LSM)}} + 2e^{-}_{Ch_{\blacktriangle LSM}}$	$9.0 \cdot 10^{12}$	-1.65	-257.62
$O^{2-}_{\blacktriangle(ad,LSM)} \longrightarrow O^{2-}_{LSM} + LSM_{surf}$	$2.99 \cdot 10^{5}$	0.5	1.0
$O^{2-}_{LSM} + LSM_{surf} \longrightarrow O^{2-}_{\blacktriangle(ad,LSM)} + YSZ$	$3.13 \cdot 10^{5}$	0	133.15
$O_2 + 4e^{-}_{Ch_{\blacktriangle LSM}} + 2LSM \longrightarrow 2O^{2-}_{LSM}$	$1.42 \cdot 10^{3}$	-3.45	12.543
$2O^{2-}_{LSM} \longrightarrow O_2 + 4e^{-}_{Ch_{\blacktriangle LSM}} + 2LSM$	$4.0 \cdot 10^{1}$	3.95	-238.33

Moreover, due to the limited number of surface sites, problems with numerical stability and simulation time arise, making it necessary to uncouple the surface coverage from the reactions by increasing their number to very high values. This leads to the before mentioned assumption of a sufficient number

[38] $t \approx 10^{-12}$ s

of available locations for reactions at every time. In the end, for steady-state continuum simulations detailed surface electrochemistry models are not feasible at the moment. Thus, the subsequently proposed models neglect detailed surface reaction mechanisms and only focus on macro-scale reaction kinetics.

4.4. Conclusions

To develop a detailed model, a profound understanding of the physical phenomena is crucial. Therefore, as a preparatory work for the current state of the art in 3D-SOFC modeling, in this chapter general aspects and their mathematical treatment are described. From this it follows that only little attention is paid to CO electrochemistry and that a real local description of all phenomena is still missing too. In order to close this gap, the influence of microstructure and elementary reaction kinetics is investigated with numerical models. Microstructural effects are studied for the anode. It is figured out that above a certain threshold in volume fraction, uninterrupted pathways of every species, penetrating the entire structure, exist. For this situation the average cermet properties come close to those of the pure substances. Elementary reaction kinetics are investigated for a simplified oxygen reduction mechanism at a LSM cathode. Although the results agree to some extend with literature data, due to numerical reasons, limited numbers of surface sites are not feasible for steady-state continuum simulations. Therefore, simplified models are required. They, and the modeling of the other phenomena of interest, are the topic of the subsequent chapter.

5. Model description

In this chapter the necessary submodels for the final Three(3)-Dimensional (3D) model are developed and verified as preparative studies for the detailed investigation of the electrochemical and thermal situation inside the novel cell concept during operation.

In the beginning the underlying numerical methods and the computer based problem setup are discussed in section 5.1. Because of the strong coupling between the different phenomena, a validation of the entire model is challenging. Therefore, in section 5.2 the submodels for the different phenomena are explained and verified. Hereby in particular a detailed as well as two simplified models of the SOFC electrochemistry are proposed. The chapter ends in section 5.3 with a conclusion on the model itself, and the pathway for the final numerical experiments.

5.1. Numerical methods and problem setup

Starting point for every numerical method is the mathematical model of the system of interest. In the case of a fuel cell this means in particular the Balance Equations (BEs) described in the previous chapter. Since they form a set of Partial Differential Equations (PDEs) not only appropriate Boundary Conditions (BCs) and initial values have to be provided. Moreover, a suitable method for transferring them into a system of algebraic equations[1] must be chosen. (Bozic et al. 2009, p. 159)

For this study the method of choice is the Finite Volume Method (FVM). To apply it, the computational domain has to be divided into small Control Volumes (CVs). At e.g. the centroids of the CVs are the computational nodes at which the values of the variables are determined. During calculation the integral formulation of the BEs for each CV is solved. Thereby it is necessary to

[1] discretization

approximate the integrals[2] by appropriate quadrature methods, resulting in an algebraic expression for each variable at a node in dependence of some neighboring nodal values. Because of Gauss' divergence theorem all sources/sinks inside and fluxes through a CV can be expressed as integrals over its surfaces. Hence, as long as those integrals are equal for two CVs sharing a boundary, the FVM is conservative by construction. In consequence, the grid only defines the locations and shapes of the surfaces, making it possible to use FVM for any kind of grid and (almost) arbitrarily complex geometries. (Ahmed 2010, p. 18)(Ferziger and Perić 2008, p. 43)

In dependence of the discretization and the nature of the underlying PDEs the resulting system of algebraic equations is usually non-linear. In this case, iterative techniques are applied. They consist of guessing a solution, solving the linear equations, and finally improving the solution until convergence is reached. By defining the size and the type[3] of the convergence criteria it is possible to adjust the accuracy and required computation time of a solution[4]. (Ahmed 2010, p. 19)(Ansys Inc 2011, p. 439 et. seqq.)

In this thesis the FVM program ANSYS/CFX version 14.0 is used. The problem setup with this software is the subject of the next subsection.

5.1.1. Problem setup

The basic workflow of a CFD simulation is illustrated in Figure 5.1. It starts with the preparation of an assembled 3D-Computer Aided Design (CAD) model containing all parts of interest in the system under investigation[5]. Figure 5.2 shows the extraction and assembly of the CFD model from the CAD[6] one. To save computation time the original geometry is reduced to the smallest self-repeating unit. It consists of six domains from different materials. The anode's and cathode's flow channels are modeled as gas-phases whereas the electrodes itself are defined as "porous media". Here fluid as well as solid phase coexist, making a special treatment for almost all transport phenomena necessary. The

[2] surface and volume

[3] The Root Mean Square (RMS), the MAXimal value (MAX), and the overall flow balances of every variable are in general of interest (Ansys Inc 2011, p. 439).

[4] In accordance to the ANSYS/CFD simulation software (CFX) "solver modeling guide" "double precision" calculation accuracy and a normalized MAX residual level of $1 \cdot 10^{-4}$ is in general applied in this thesis (Ansys Inc 2011, p. 440).

[5] In this thesis the fluid as well as the solid parts are included.

[6] see chapter 3.2

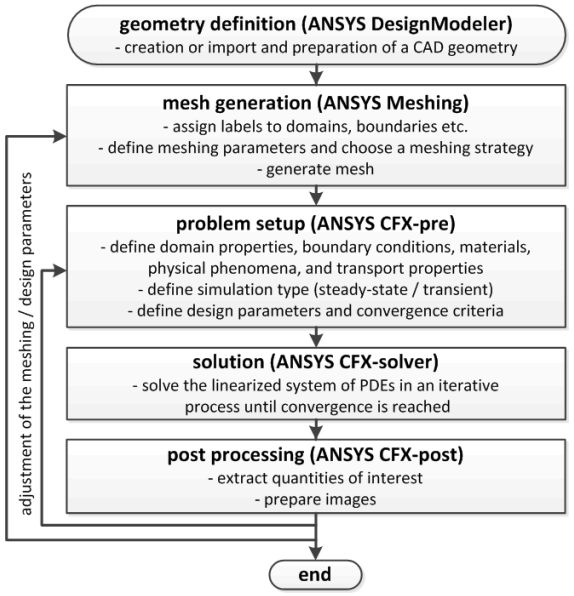

Figure 5.1.: **CFD workflow:** The workflow of a CFD simulation starts with geometry and mesh generation. They are followed by problem setup and solution, before finally the post-processing is done. If design parameters are varied, the process is re-entered either at the meshing or the setup stage.

electrolyte, the IC, and the sealant[7] are modeled as "solid domains" where any gas-transport is possible. The materials of the domains are as follows:

- **anode:** porous cermet from Ni and 8YSZ ;
- **cathode:** porous structure made of LSCF ;
- **electrolyte:** solid from 8YSZ ;
- **gas-phase (anode side):** gas mixture from CH_4, CO, CO_2, H_2, H_2O, N_2 ;
- **gas-phase (cathode side):** gas mixture from N_2 and O_2 ;
- **Interconnect (IC):** solid from Crofer22APU ;

[7]In the following the sealant is usually suppressed during calculation, since it is no active component of the cell.

- **sealant:** solid from $\left(SiO_2\right)_{0.65}\left(Na_2O\right)_{0.2}(CaO)_{0.12}(BaO)_{0.03}$.

Since the temperature has an outstanding influence on the transport properties, temperature dependent expressions from the literature are applied whenever possible. A summary of the required material parameters, fitting expressions, and numerical values is included in appendix C. In the simulations the smaller front and end faces of the gaseous domains act as gas in- and outlets and those of the IC as electrical contacts. For the other surfaces symmetry is assumed.

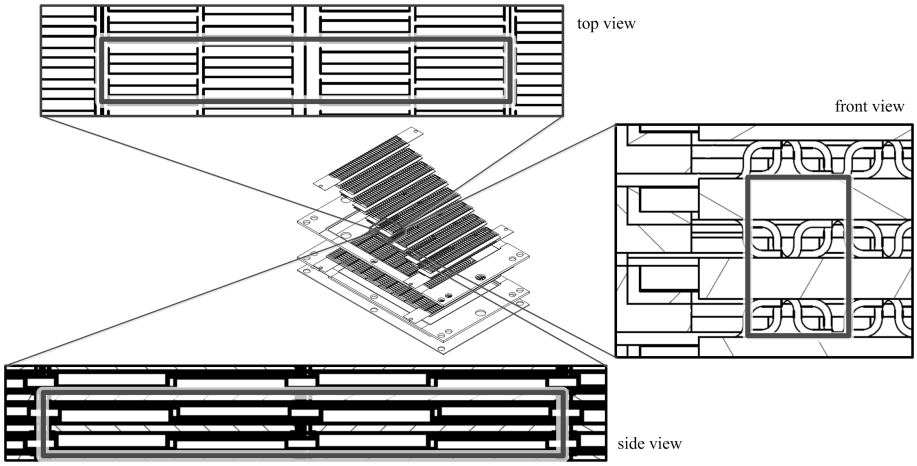

Figure 5.2.: **Extraction of the smallest self repeating unit:** From the original geometry the smallest self-repeating unit is extracted for CFD model creation; modified from (Todt 2011).

The geometry is subsequently passed to the mesh generator which tries to approximate it with CVs using different strategies. The mesh has to be fine enough to sufficiently represent the geometry and to have no influence on the physical phenomena of interest. Nevertheless, it has to be coarse enough to minimize computation time and required resources. Additionally the "numerical quality" of the mesh should be sufficient to inhibit numerical problems. Figure 5.4 compares the results of a flow simulation with different numbers of CVs. Since the results are (almost) identical for more than approximately two million nodes this resolution is used as minimum for the electrochemical simulations.

Due to problems with convergence of the thermal effects, variations of the original geometry are investigated (see Figure 5.3) in order to minimize the

number of “degenerated elements” at the bended ends of the fins. Moreover, the “straight fin” and the “discrete fin geometry” allow mesh creation from one part instead of an “assembly”. This leads to a steady mesh among all regions rather than one where interpolation between non-steady meshes is needed at domain boundaries. Finally, grid refinement is performed close to the surfaces of the porous regions in order to reduce the remaining residuals during solution.

Problem setup is done with ANSYS/CFX-pre which allows to define all domains, their materials, and BCs as well as variables for additional quantities of interest. The program can be extended by self written Fortran routines[8] which are afterwards linked to the CFD solver. Since it is not possible to write “UserFortran” routines for paralleled computation all simulations have to be performed with a single processor, leading to calculation times of two to three weeks on a Intel® Core™ i5-2500 K Central Processing Unit (CPU). The large number of almost 6.5 million elements for a single cell of the “discrete fin” geometry also precludes the simulation of a series connection of non-isothermal cells. The latter is only possible for the rather coarsely meshed “original” geometry, but for which non-isothermal convergence is hard to attain. Since all of the so far mentioned geometries require rather fine meshing and thus long computation times, the final simulations are made with a “simplified geometry”. Here the fins at the cathode side are slightly shifted and the “covered regions” are reduced to the thickness of the IC. Together with a growth of the cathode from $5 \cdot 10^{-5}$ m to $1 \cdot 10^{-4}$ m, this leads to a significant reduction in meshing complexity, computation time[9], and enhanced convergence behavior. Information about the respective meshes are listed in the captions of Figure 5.5. Finally, the results are post-processed in ANSYS/CFX-post.

In order to verify the simulation results they have to be compared with known analytical solutions or other simulations. Since all processes in a fuel cell are strongly coupled this has to be done separately for all submodels in the next subsection.

[8] so called “UserFortran”

[9] With an appropriate replacement of the “UserFortran” routines parallel computation and thus computation times of four to eight hours on the above mentioned machine are possible.

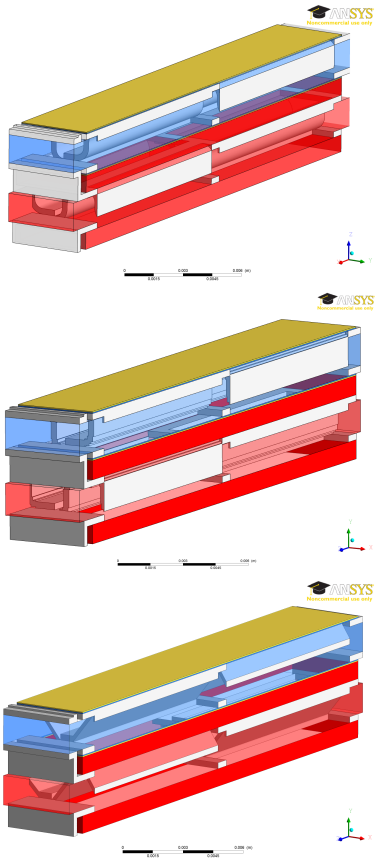

“Original geometry”
Nodes: 1.85 million
Elements: 0.44 million

Aspect ratio: 2.69 (min = 1.0, max ≈ 139.69, лъ ≈ 2.33)
Quality: 0.70 (min ≈ $3.91{\cdot}10^{-2}$, max ≈ 0.99, лъ ≈ 0.22)
Skewness: $1.45{\cdot}10^{-1}$ (min ≈ $1.31{\cdot}10^{-10}$, max ≈ 0.99, лъ ≈ $1.98{\cdot}10^{-1}$)

“Discrete fin geometry”
Nodes: 6.36 million
Elements: 6.54 million

Aspect ratio: 1.80 (min = 1.0, max ≈ 11.46, лъ ≈ 0.52)
Quality: 0.85 (min ≈ 0.20, max ≈ 0.99, лъ ≈ 0.11)
Skewness: $4.88{\cdot}10^{-2}$ (min ≈ $1.31{\cdot}10^{-10}$, max ≈ 0.81, лъ ≈ $9.67{\cdot}10^{-2}$)

“Straight fin geometry”
Nodes: 5.89 million
Elements: 18.11 million

Aspect ratio: 1.79 (min = 1.0, max ≈ 48.33, лъ ≈ 0.55)
Quality: 0.85 (min ≈ $4.65{\cdot}10^{-2}$, max ≈ 0.99, лъ ≈ 0.11)
Skewness: $1.99{\cdot}10^{-1}$ (min ≈ $1.31{\cdot}10^{-10}$, max ≈ 0.98, лъ ≈ $1.39{\cdot}10^{-1}$)

Figure 5.3.: **3D-CAD model of the “original geometry” and variations:** While the “original geometry” possesses sinusoidal shaped fins, the “discrete fin geometry” simplifies the curved parts by discrete steps. The “straight fin geometry” discards the original curved fins and replaces them by direct connections. The meshing differs between the three geometries, since each of them features specific challenges for the ANSYS/CFX-pre meshing algorithm. The “discrete fin geometry” can be easily meshed with a hex-based mesh. However, due to the geometry of the discrete steps and the quality criteria for the thin elements inside the cathode, a lot of nodes are required. The same accounts for the “straight fin geometry”, which even requires tetrahedral elements because of the diagonal baffles. The “original geometry” leads to problems with degenerated elements in those areas where the curved fins get in contact with the electrodes. Since both hexahedrons and tetrahedrons are used, a significant decrease in the number of elements and thus a serial connection of several cells is possible.

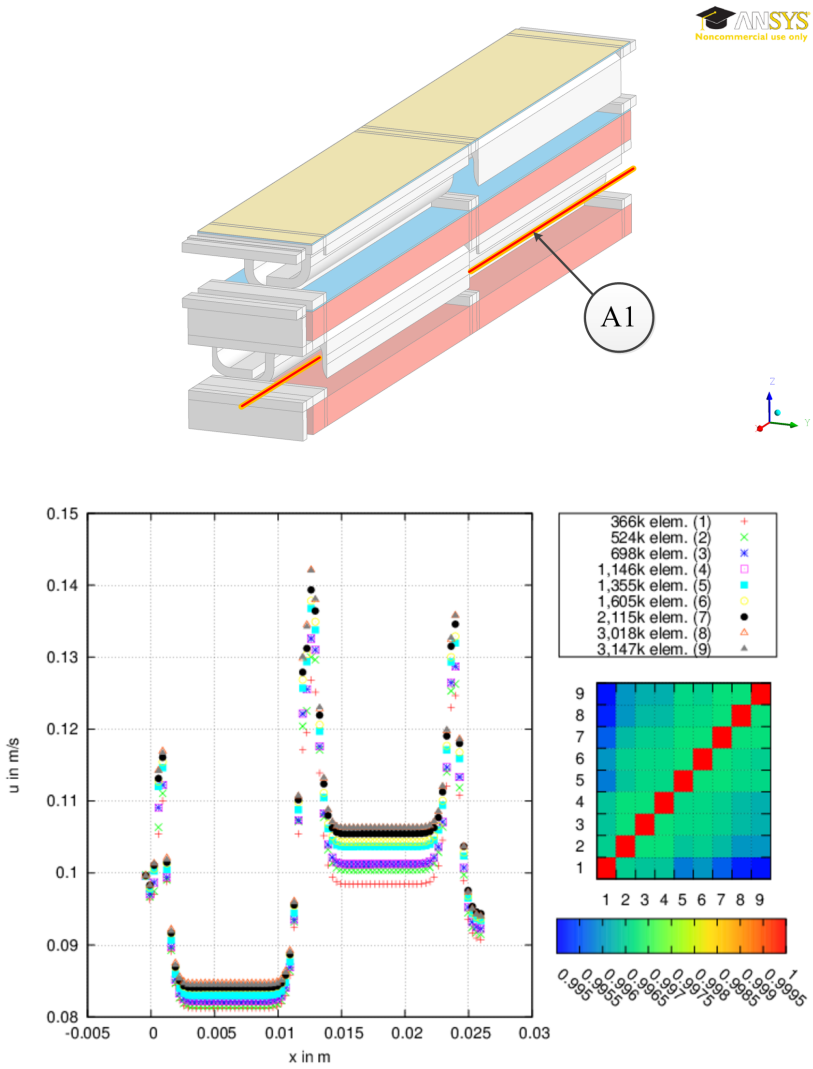

Figure 5.4.: **CV convergence study:** The results of isothermal, turbulent flow simulations with the original geometry are examined at the line (A1) (top) for different numbers of CVs. It can be seen that a high correlation exists among the different grid sizes (bottom right).

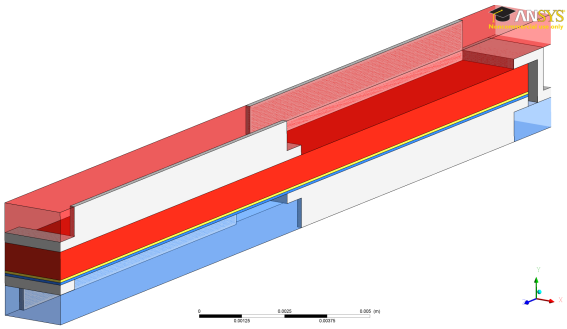

“Simplified geometry”
Nodes: 7.12 million
Elements: 6.75 million

Aspect ratio: 1.59
(min = 1.01, max ≈ 3.44, ЛЬ ≈ 0.66)
Quality: 0.87
(min ≈ 0.49, max ≈ 0.99, ЛЬ ≈ 0.15)
Skewness: $3.70{\cdot}10^{-2}$
(min ≈ $1.31{\cdot}10^{-10}$, max ≈ 0.59, ЛЬ ≈ $7.51{\cdot}10^{-2}$)

Figure 5.5.: **3D-CAD model of the simplified geometry:** In the “simplified geometry” the flow direction is altered from the x- to the z-direction and the anode and cathode side of the PEN are flipped. To simplify the geometry, the fins are reduced to straight contacts with the thickness of the IC’s material. Compared to the other geometries, this, and a shifting on the cathode side in x-direction, leads to a reduction of the geometry by 50 % in x- as well as y-direction.

5.2. Submodels

In order to describe the fuel cell process with a CFD model, the physical phenomena discussed in chapter 4.1 have to be implemented into the problem setup. Before the submodels are explained and verified separately some general remarks and modeling assumptions have to be made:

- **Electrochemistry:**
  - No intermediates from surface reactions.
  - $\lambda_{\text{stoich}_{\blacktriangle}\text{air/fuel}} > 1$.
- **Energy:**
  - Radiative heat transfer is neglected.
- **Fluid flow:**
  - The gases enter the flow channels with pre-defined and homogeneous temperatures; $T_{\text{in}_{\blacktriangle}\text{ANO}}$ and $T_{\text{in}_{\blacktriangle}\text{CAT}}$.

  - A fully developed laminar flow profile is assumed at the inlet (shape see subsection 5.2.2).
  - Only gaseous components enter and leave the fuel cell.
  - Operating media are CH_4, CO, CO_2, H_2, H_2O, N_2, and O_2.

- **General aspects:**
  - 3D, steady-state model.
  - All gases are assumed to behave like ideal gases.
  - Validity limited to $650\,\mathrm{K} \leq T \leq 1200\,\mathrm{K}$ due to fitting parameters.
  - The PEN structure has the geometrical dimensions introduced in section 3.2.2[10].
  - Transient effects like sintering are neglected.
  - The investigated self repeating unit is taken from the middle of the cell stack, thus in accordance to Tanaka et al. (Tanaka et al. 2007) interactions with the environment are negligible.

- **Porous electrodes:**
  - Parts of percolating clusters from all species are apparent at every CV.
  - The average composition of the electrodes is valid for every CV[11] and the length of the TPBs is directly proportional to the composition.

5.2.1. Diffusion and dynamic viscosity

For the convective flow in the gas channels the average dynamic viscosity of the medium is required. Based on the results of Todd and Young (Todd and Young 2002), in the model Reichenberg's method is applied to calculate the average dynamic viscosity[12] Γ_{visc} of the gas phase (Poling, Prausnitz, and

[10] For the "simplified geometry" the cathode thickness is doubled.

[11] no changes due to e.g. sintering

[12] For the different species temperature dependent expressions for $\Gamma_{\mathrm{visc}\,i}$ are summarized in appendix C.

O'Connell 2001, p. 9.15 et. seqq.):

$$\Gamma_{\mathrm{visc}_\blacktriangle(\mathrm{g})} = 10^{-7} \cdot \sum_{i=1}^{n} \mathbb{K}_i \cdot \left\{ 1 + 2 \cdot \sum_{j=1}^{i-1} \left(\mathrm{H}_{i/j} \mathbb{K}_j \right) + \sum_{\substack{j=1 \\ j \neq i}}^{n} \sum_{\substack{k=1 \\ k \neq i}}^{n} \left(\mathrm{H}_{i/j} \mathrm{H}_{i/k} \mathbb{K}_j \mathbb{K}_k \right) \right\} \text{ in } \frac{\mathrm{kg}}{\mathrm{m\,s}}, \quad (5.1)$$

where

$$\mathbb{K}_i = \frac{10^7 \cdot y_{\mathrm{Mol}_\blacktriangle \mathrm{mol}_\blacktriangle i} \Gamma_{\mathrm{visc}_\blacktriangle i}}{y_{\mathrm{Mol}_\blacktriangle \mathrm{mol}_\blacktriangle i} + 10^7 \cdot \Gamma_{\mathrm{visc}_\blacktriangle i} \cdot \sum_{\substack{k=1 \\ k \neq i}}^{n} \left(y_{\mathrm{Mol}_\blacktriangle \mathrm{mol}_\blacktriangle k} \mathrm{H}_{i/k} \cdot \left(3 + \frac{2 M_{\mathrm{Mass}_\blacktriangle \mathrm{mol}_\blacktriangle k}}{M_{\mathrm{Mass}_\blacktriangle \mathrm{mol}_\blacktriangle i}} \right) \right)}$$

and

$$\mathrm{H}_{i/j} = \sqrt{\frac{M_{\mathrm{Mass}_\blacktriangle \mathrm{mol}_\blacktriangle i} M_{\mathrm{Mass}_\blacktriangle \mathrm{mol}_\blacktriangle j}}{32 \cdot \left(M_{\mathrm{Mass}_\blacktriangle \mathrm{mol}_\blacktriangle i} + M_{\mathrm{Mass}_\blacktriangle \mathrm{mol}_\blacktriangle j} \right)^3}} \cdot \left(\Gamma_i + \Gamma_j \right)^2 \cdot \frac{\left(1 + 0.36 T_{\mathrm{red}_\blacktriangle i/j} \cdot \left(T_{\mathrm{red}_\blacktriangle i/j} - 1 \right) \right)^{\frac{1}{6}} \mathbb{K}_{\mathrm{red}_\blacktriangle i/j}}{\sqrt{T_{\mathrm{red}_\blacktriangle i/j}}} .$$

The design parameter Γ_i, the reduced temperature of the i-th and the j-th species $T_{\mathrm{red}_\blacktriangle i/j}$, and the reduced polar correction of both species $\mathbb{K}_{\mathrm{red}_\blacktriangle i/j}$ are given by:

$$\Gamma_i = \frac{M_{\mathrm{Mass}_\blacktriangle \mathrm{mol}_\blacktriangle i}^{\frac{1}{4}}}{\sqrt{10^7 \cdot \Gamma_{\mathrm{visc}_\blacktriangle i} \amalg_i}}, \qquad \amalg_i = \frac{\left(1 + 0.36 T_{\mathrm{red}_\blacktriangle i} \cdot \left(T_{\mathrm{red}_\blacktriangle i} - 1 \right) \right)^{\frac{1}{6}} \mathbb{K}_{\mathrm{red}_\blacktriangle i}}{\sqrt{T_{\mathrm{red}_\blacktriangle i}}},$$

$$T_{\mathrm{red}_\blacktriangle i} = \frac{T_{(\mathrm{g})}}{T_{\mathrm{crit}_\blacktriangle(\mathrm{g})_\blacktriangle i}}, \qquad T_{\mathrm{red}_\blacktriangle i/j} = \frac{T_{(\mathrm{g})}}{\sqrt{T_{\mathrm{crit}_\blacktriangle(\mathrm{g})_\blacktriangle i} T_{\mathrm{crit}_\blacktriangle(\mathrm{g})_\blacktriangle j}}},$$

$$\mathbb{K}_{\mathrm{red}_\blacktriangle i} = \frac{T_{\mathrm{red}_\blacktriangle i}^{3.5} + (10 \cdot \delta_{\mathrm{red}_\blacktriangle i})^7}{T_{\mathrm{red}_\blacktriangle i}^{3.5} \cdot \left(1 + (10 \cdot \delta_{\mathrm{red}_\blacktriangle i})^7 \right)}, \qquad \mathbb{K}_{\mathrm{red}_\blacktriangle i/j} = \frac{T_{\mathrm{red}_\blacktriangle i/j}^{3.5} + \left(10 \cdot \delta_{\mathrm{red}_\blacktriangle i/j} \right)^7}{T_{\mathrm{red}_\blacktriangle i/j}^{3.5} \cdot \left(1 + \left(10 \cdot \delta_{\mathrm{red}_\blacktriangle i/j} \right)^7 \right)}.$$

Here, $T_{\mathrm{crit}_\blacktriangle(\mathrm{g})_\blacktriangle j}$ is the critical temperature of the i-th gas species. The dimensionless reduced dipole moment of the i-th component $\delta_{\mathrm{red}_\blacktriangle i}$ is calculated in dependence of the critical pressure p_{crit} in bars from (Poling, Prausnitz, and O'Connell 2001, p. 9.9):

$$\delta_{\mathrm{red}_\blacktriangle i} = 52.46 \cdot \frac{\delta_i^2 p_{\mathrm{crit}}}{T_{\mathrm{crit}}^2}, \qquad \delta_{\mathrm{red}_\blacktriangle i/j} = \sqrt{\delta_{\mathrm{red}_\blacktriangle i} \delta_{\mathrm{red}_\blacktriangle j}} .$$

To verify the implemented procedure in Figure 5.6 calculated values are referenced to literature data. For the diffusive species transport for every species i

in a n-species mixture an effective molecular diffusion coefficient $D_{\text{eff}_\blacktriangle(\text{g})_\blacktriangle i}$ in dependence of the molar fractions $y_{\text{Mol}_\blacktriangle\text{mol}_\blacktriangle j}$ of the other j species in $\text{mol}_{\text{species}_\blacktriangle j}/\text{mol}_{\text{tot}}$ and the binary diffusion coefficient $D_{\text{mole}_\blacktriangle(\text{g})_\blacktriangle i/j}$ in m^2/s have to be calculated (Yakabe et al. 2000):

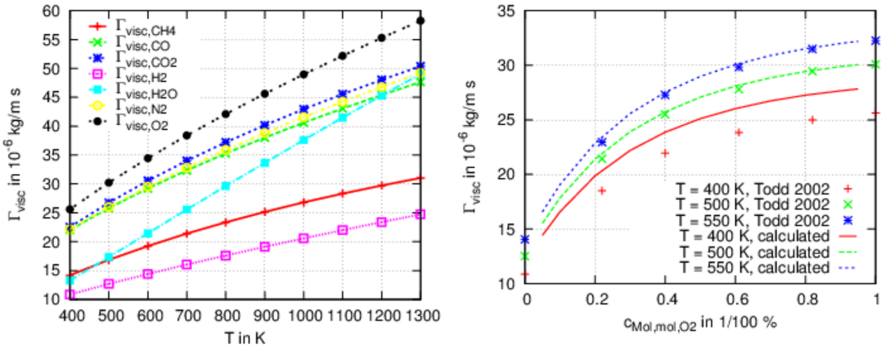

Figure 5.6.: **Dynamic viscosities of pure substances and gas-mixtures:** The values are calculated in dependence of the temperature T in K. The left figure shows $\Gamma_{\text{visc}_\blacktriangle\text{ave}_\blacktriangle(\text{g})}$ for selected pure substances based on the PTPPC data. The right one displays a comparison of experimental and calculated results for a O_2-H_2 mixture in dependence of the oxygen content. The data is taken from (Todd and Young 2002).

$$D_{\text{mole}_\blacktriangle(\text{g})_\blacktriangle i} = \left(1 - y_{\text{Mol}_\blacktriangle\text{mol}_\blacktriangle i}\right) \cdot \left(\sum_{\substack{j=1 \\ j \neq i}}^{n} \frac{y_{\text{Mol}_\blacktriangle\text{mol}_\blacktriangle j}}{D_{\text{mole}_\blacktriangle(\text{g})_\blacktriangle i/j}} \right)^{-1} . \tag{5.2}$$

In this thesis, the latter are calculated using Hirschfelder's adaption of the Chapman-Enskogg Equation (CEE)(Bozic et al. 2009, p. 59):

$$D_{\text{mole}_\blacktriangle(\text{g})_\blacktriangle i/j} = 1.8583 \cdot 10^{-7} \cdot \frac{T^{\frac{3}{2}} \left(\frac{M_{\text{Mass}_\blacktriangle\text{mol}_\blacktriangle i} + M_{\text{Mass}_\blacktriangle\text{mol}_\blacktriangle j}}{M_{\text{Mass}_\blacktriangle\text{mol}_\blacktriangle i} \cdot M_{\text{Mass}_\blacktriangle\text{mol}_\blacktriangle j}} \right)^{\frac{1}{2}}}{p \text{Þ}^{2}_{\text{scat}_\blacktriangle i/j} \Omega_{\text{coll}}} \text{ in } \frac{\text{m}^2}{\text{s}}$$

in dependence of the gas pressure p in atm, the molar masses $M_{\text{Mass}_\blacktriangle\text{mol}_\blacktriangle i}$ and $M_{\text{Mass}_\blacktriangle\text{mol}_\blacktriangle j}$ in kg/mol, the scattering-diameter (*Lennard-Jones-length*) of the molecules $\text{Þ}_{\text{scat}_\blacktriangle i/j}$, and the dimensionless diffusion collision integral Ω_{coll}. According to Todd and Young (Todd and Young 2002) for mixtures more accurate

results for Ω_{coll} are obtained using the equation given by Poling, Prausnitz, and O'Connell (Poling, Prausnitz, and O'Connell 2001, p. 11.6):

$$\Omega_{\text{coll}} = \frac{1.06036}{\left(\frac{k_{\text{En,B}}T}{\epsilon_{i/j}}\right)^{0.1561}} + \frac{0.193}{\exp\left(0.47635\frac{k_{\text{En,B}}T}{\epsilon_{i/j}}\right)} + \frac{1.03587}{\exp\left(1.52996\frac{k_{\text{En,B}}T}{\epsilon_{i/j}}\right)} + \frac{1.76474}{\exp\left(3.89411\frac{k_{\text{En,B}}T}{\epsilon_{i/j}}\right)},$$

compared to the usual application of the mixing law to the PTPPC data. Hereby is $\epsilon_{i/j}$ the exchange energy between the i-th and the j-th species in J[13].

The diffusive flux in the porous electrodes is modeled using the DGM. Here the diffusion of an ideal gas consists of molecular diffusion $D_{\text{mole}_\blacktriangle(\text{g})_\blacktriangle i}$ and Knudsen diffusion $D_{\text{Knud}_\blacktriangle(\text{g})_\blacktriangle i}$ (Bozic et al. 2009, p. 62). The latter respects the influence of the interactions with the walls on the movement of the gas particles (Garcia-Camprubi, Sanchez-Insa, and Fueyo 2010; Pramuanjaroenkij, Kakac, and Yangzhou 2008):

$$\frac{1}{D_{\text{eff}_\blacktriangle(\text{g})_\blacktriangle i}} = \frac{\tau}{Po_{\%}} \cdot \left(\frac{\left(1 - y_{\text{Mol}_\blacktriangle\text{mol}_\blacktriangle i}\right)}{D_{\text{mole}_\blacktriangle(\text{g})_\blacktriangle i}} + \frac{1}{D_{\text{Knud}_\blacktriangle(\text{g})_\blacktriangle i}} \right), \tag{5.3}$$

using the porosity $Po_{\%}$ of the media and an empirical fitting coefficient τ called *tortuosity*. It compares the length of the gas path through the pores per unit of length with a direct connection. For spherical pores the effective Knudsen diffusion coefficient can be derived from kinetic gas theory as (Bozic et al. 2009, p. 62):

$$D_{\text{Knud}_\blacktriangle(\text{g})_\blacktriangle i} = \frac{2 \cdot \iota_{\text{pore}}}{3} \sqrt{\frac{8\Re_{\text{En}_\blacktriangle\text{mol}} T}{\pi M_{\text{Mass}_\blacktriangle\text{mol}_\blacktriangle i}}}. \tag{5.4}$$

Here $M_{\text{Mass}_\blacktriangle\text{mol}_\blacktriangle i}$ is the molar mass of the i-th species in $\text{kg}_{\text{species}_\blacktriangle i}/\text{mol}_{\text{species}_\blacktriangle i}$, and ι_{pore} the average pore radius in m.

Both tortuosity τ and average pore radius ι_{pore} are strongly dependent on the final PEN. Therefore, following the theoretical study of Iwai et al. (Iwai et al. 2010), for the anode a value of $\tau = 1.94$ (cathode: $\tau = 1.29$ (Leonide 2010, p. 58)) and an average pore radius of $\iota_{\text{pore}} = 3.75 \cdot 10^{-6}$ m (Garcia-Camprubi, Sanchez-Insa, and Fueyo 2010) (cathode: $\iota_{\text{pore}} = 2 \cdot 10^{-6}$ m (Liu et al. 2010b)) are assumed. Figure 5.7 verifies the temperature dependent values of the effective diffusion coefficients $D_{\text{mole}_\blacktriangle(\text{g})_\blacktriangle i/j}$ for binary mixtures by comparing them with literature data.

[13] See appendix C for a summary of the values used for $Ь_{\text{scat}_\blacktriangle i/j}$ and $\epsilon_{i/j}$

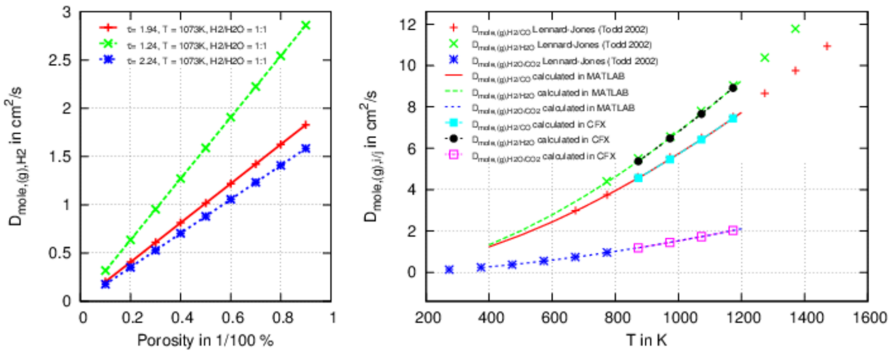

Figure 5.7.: **Effective diffusion coefficients of pure substances and gas-mixtures:** The values are calculated in dependence of the temperature T in K. While the right figure compares the calculated results for selected binary diffusion coefficients with values from the literature (Todd and Young 2002), the left one shows the porosity and tortuosity dependence of a binary gas mixture.

For the non-isothermal simulations, the effective diffusion coefficients from equations 5.2 and 5.3 must be replaced by the average diffusion coefficient of an ideal mixture of ideal gases. The reason for this is not physical, but an imperfect implementation of the energy equation in the CFX solver. During calculation, along with a decay in the RMS residuals, a constant increase in the MAX residuals can be observed. Finally, the latter not only leads to a termination of the calculation, but also to unphysical "thermal halos" of elevated temperature close to the boundaries of the solid parts. This behavior can be observed for both variable and fixed values of $D_{\mathrm{eff}_{\blacktriangle}(\mathrm{g})_{\blacktriangle}i}$ in all geometries and can only be solved by the process described above.

Using the results of the previous subsection and those of section 2.4.1, for the porosity a constant value of $Po_{\%_{\blacktriangle}\mathrm{CAT}} = 0.35$ (Bossel 1992; Mücke 2009b; Tietz 1999)[14] for the cathode, and $Po_{\%_{\blacktriangle}\mathrm{ANO}} = 0.32$ with a fixed volume ratio of Ni/YSZ = 0.55/0.45 for the anode are assumed. Additionally, the model parameter *permeability* $\mathbb{k}$ is also required for the ANSYS/CFX solver. In accordance to measurements and simulations made by Huang et al. (Huang et al. 2010) a value of $\mathbb{k} = 10^{-11}$ m^2 is applied for both electrodes.

[14] in the literature the values vary between 0.3 and 0.4 (Kilius and Krstic 2009; Shi et al. 2007b; Sleiti 2010)

5.2.2. Fluid flow

A standard test case for the fluid flow is the flow channel with a square cross-section. Figure 5.8 illustrates the velocity profiles along a line through the middle of the outlet plane in dependence of the number of CVs. Analytical solution (Stemich 2006, p. 144 et. seqq.) and CFD results show a high correlation which equals almost unity for higher numbers of CVs. Concerning the

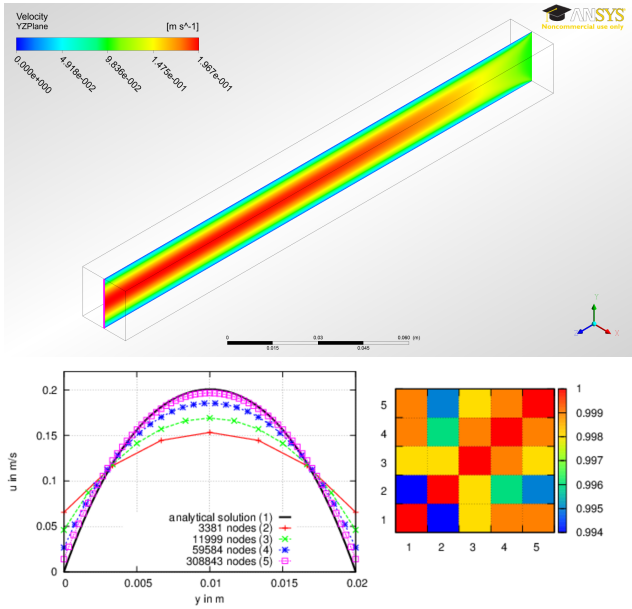

Figure 5.8.: **Fluid flow test results:** The velocity profile is evaluated at a line through the outlet plane of the flow channel (upper image). The velocity profiles (left) show increasing correlation with the analytical result for growing numbers of CVs (bottom).

inlet velocity profile, the results of the work of Schild (Schild 2011, p. 129) can be applied. He showed that by adjusting the inlet manifold, a very high flow uniformity for every flow channel[15] is possible. Therefore, for the final geometry, a parabola shaped velocity profile[16] is assumed at the inlet. In his investigation of the fluid flow through channels of small dimension[17] in a plate

[15] and among them

[16] the profile of a laminar flow through two parallel plates

[17] approximately 3 mm in diameter

heat-exchanger Schild also compared the results obtained by different turbulence models. For his situation of velocities in the range of 4 m/s[18] the Shear Stress Transport (SST) turbulence model[19] (Schild 2011, p. 76) showed optimal results. In the current case the grid study gives only low fluid velocities with values below 3.3 m/s and Reynolds numbers[20] below 100 (see Figure 5.9). Therefore, turbulence modeling can be neglected and the usual assumption[21] of laminar flow is made.

Table 5.1.: **Inlet BCs:** If not otherwise noted, the tabulated values are used for the subsequent flow simulations. Gas quantities that are not listed in a domain have a mass fraction of zero $kg_{species}/kg_{tot}$.

Quantity	**Value**	**Dimension**	**Reference/Note**
anode gas-channel			
T	973	K	assumed
$\langle \vec{u} \rangle$	1	m/s	assumed, perpendicular to the inlet plane
CH_4	0.3	kg_{CH_4}/kg_{tot}	assumed
CO	0.15	kg_{CO}/kg_{tot}	assumed
CO_2	0.01	kg_{CO_2}/kg_{tot}	assumed
H_2	0.44	kg_{H_2}/kg_{tot}	assumed
H_2O	0.1	kg_{H_2O}/kg_{tot}	assumed
cathode gas-channel			
T	973	K	assumed
$\langle \vec{u} \rangle$	2	m/s	assumed, perpendicular to the inlet plane
N_2	0.77	kg_{N_2}/kg_{tot}	(Lefebvre 2011)
O_2	0.23	kg_{O_2}/kg_{tot}	(Lefebvre 2011)

[18] mass flows of about $5 \cdot 10^{-7}$ kg/s

[19] The basis of this turbulence model are wall-scale functions to generate a transition between the $k_{turb} - \omega_{turb}$ turbulence model ($k_{TURB} - \omega_{TURB}$) and the $k_{turb} - \varepsilon_{turb}$ turbulence model ($k_{TURB} - \varepsilon_{TURB}$). The former gives better results for the flow near the surface at low *Re*, whereas the latter is more suitable for high *Re* numbers and bulk flow. Details on all models can be found in (Bozic et al. 2009, p. 36 et. seqq.)(Schild 2011, p. 46 et seqq.)(Menter 1994; Wilcox 1988).

[20] The calculation of local values for *Re* is explained in subsection 4.1.4. For the gas channels an hydraulic diameter of $\sqrt{L_x^2 + L_y^2}$ with $L_x = 2.3 \cdot 10^{-3}$ m (maximal width between two fins) and $L_y = 2.4 \cdot 10^{-3}$ m (maximal height) is assumed.

[21] e.g. (Bi, Li, and Lin 2010; Chyou et al. 2005)

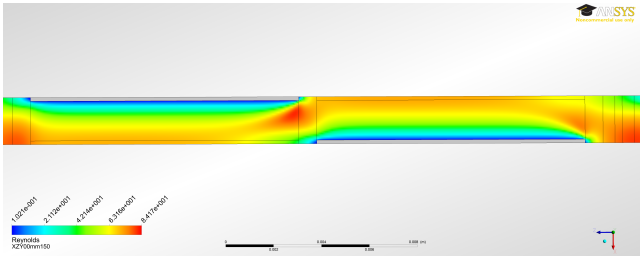

Figure 5.9.: **Reynolds numbers in the cathode flow channel:** For the given inlet conditions (see Table 5.1) the highest Reynolds numbers are obtained in the cathode's gas channel. Here the results of a simulation with the "simplified geometry" in a x-z-plane at $y = 0.15$ mm are shown. Since the values are below 100, laminar flow can be assumed.

5.2.3. Reformation of methane

For the reformation of methane (see section 2.5) during the last decades numerous kinetic models have been proposed (Andersson, Yuan, and Sundén 2012). In contrast to others,[22] the models of Xu and Fromet (Xu and Fromet 1989b; Xu and Fromet 1989a) and Snoeck and Fromet (Snoeck and Froment 2002) explicitly take the catalyst loading of the porous cermet into consideration. Since these models are the basis for successful adoptions to fuel cell problems (Lehnert, Meusinger, and Thom 2000), they are chosen for this thesis.

The models are based on empirical expressions for the reaction rates of the reformation reactions (Xu and Fromet 1989b) in mol/m^3 s:

$$r_{\text{reac}\,1} = \frac{A_{\text{eff}\blacktriangle\text{vol}\blacktriangle\text{Ni}}}{A_{\text{cata}\blacktriangle\text{mass}}} \cdot c_{\%\blacktriangle\text{Ni}} \cdot \frac{\Re_{\text{reac}\blacktriangle 1}}{p_{\text{H}_2}^{2.5} \cdot \text{DEN}^2} \cdot \left(p_{\text{CH}_4} p_{\text{H}_2\text{O}} - \frac{p_{\text{H}_2}^3 p_{\text{CO}}}{K_{\text{equi}\blacktriangle 1}} \right), \tag{5.5}$$

$$r_{\text{reac}\,2} = \frac{A_{\text{eff}\blacktriangle\text{vol}\blacktriangle\text{Ni}}}{A_{\text{cata}\blacktriangle\text{mass}}} \cdot c_{\%\blacktriangle\text{Ni}} \cdot \frac{\Re_{\text{reac}\blacktriangle 2}}{p_{\text{H}_2} \cdot \text{DEN}^2} \cdot \left(p_{\text{CO}} p_{\text{H}_2\text{O}} - \frac{p_{\text{H}_2} p_{\text{CO}_2}}{K_{\text{equi}\blacktriangle 2}} \right), \tag{5.6}$$

$$r_{\text{reac}\,3} = \frac{A_{\text{eff}\blacktriangle\text{vol}\blacktriangle\text{Ni}}}{A_{\text{cata}\blacktriangle\text{mass}}} \cdot c_{\%\blacktriangle\text{Ni}} \cdot \frac{\Re_{\text{reac}\blacktriangle 3}}{p_{\text{H}_2}^{3.5} \cdot \text{DEN}^2} \cdot \left(p_{\text{CH}_4} p_{\text{H}_2\text{O}}^2 - \frac{p_{\text{H}_2}^4 p_{\text{CO}_2}}{K_{\text{equi}\blacktriangle 3}} \right), \tag{5.7}$$

in dependence of the Ni catalyst's effective surface per volume $A_{\text{eff}\blacktriangle\text{vol}\blacktriangle\text{Ni}}$ in m^2/m^3, the effective surface per mass catalyst $A_{\text{cata}\blacktriangle\text{mass}}$ in m^2/g$_{\text{cata}}$, the relative

[22] e.g. Wang et al. (Wang et al. 2008)

concentration of nickel surface sites:

$$c_{\%\blacktriangle\mathrm{Ni}} = 1 - \frac{c_{\mathrm{Mol}\blacktriangle\mathrm{vol}\blacktriangle\mathrm{C,ad}\blacktriangle\mathrm{Ni}}}{A_{\mathrm{eff}\blacktriangle\mathrm{vol}\blacktriangle,\mathrm{Ni}}\Xi_{\mathrm{mol}\blacktriangle(\mathrm{ad,Ni})}}\ , \tag{5.8}$$

the reaction rate coefficient $\Re_{\mathrm{reac}\blacktriangle 1}$ in $\mathrm{bar}^{2.5}\,\mathrm{mol/g_{cata}\,s}$, the partial pressures p_i of the reactants and products in bar, and the equilibrium constant $K_{\mathrm{equi}\blacktriangle 1}$ in bar. The reaction rate coefficients of the reactions two and three are $\Re_{\mathrm{reac}\blacktriangle 2}$ and $\Re_{\mathrm{reac}\blacktriangle 3}$ in $\mathrm{bar\,mol/g_{cata}\,s}$, respectively $\mathrm{bar}^{2.5}\mathrm{mol/g_{cata}\,s}$. $K_{\mathrm{equi}\blacktriangle 2}$ and $K_{\mathrm{equi}\blacktriangle 3}$ are the respective equilibrium constants[23]. The denominator DEN is the same for equation 5.5 and the following equations 5.6 and 5.7. It is determined in dependence of the equilibrium constants of the reactants[24]:

$$\mathrm{DEN} = 1[\mathrm{bar}] + K_{\mathrm{equi}\blacktriangle\mathrm{CO}}p_{\mathrm{CO}} + K_{\mathrm{equi}\blacktriangle\mathrm{H_2}}p_{\mathrm{H_2}} + K_{\mathrm{equi}\blacktriangle\mathrm{CH_4}}p_{\mathrm{CH_4}} + \frac{K_{\mathrm{equi}\blacktriangle\mathrm{H_2O}}p_{\mathrm{H_2O}}}{p_{\mathrm{H_2}}}\ . \tag{5.9}$$

Finally, the Boudouard reaction rate $r_{\mathrm{reac}\blacktriangle\mathrm{Boudouard}}$ is calculated in dependence of the rate coefficient $\Re_{\mathrm{reac}\blacktriangle\mathrm{Boudouard}\blacktriangle 1}$ in $\mathrm{bar\,mol/g_{cata}\,s}$ and the equilibrium constants of the reaction[25] (Snoeck and Froment 2002):

$$r_{\mathrm{reac}\blacktriangle\mathrm{Boudouard}} = \frac{A_{\mathrm{eff}\blacktriangle\mathrm{vol}\blacktriangle\mathrm{Ni}}}{A_{\mathrm{cata}\blacktriangle\mathrm{mass}}} \cdot c_{\%\blacktriangle\mathrm{Ni}} \cdot \left(\frac{\Re_{\mathrm{reac}\blacktriangle\mathrm{Boudouard}\blacktriangle 1} K_{\mathrm{equi}\blacktriangle\mathrm{Boudouard}\blacktriangle\mathrm{CO}} \cdot \left(p_{\mathrm{CO}} c_{\%\blacktriangle\mathrm{Ni}} - \frac{p_{\mathrm{CO_2}} c_{\%\blacktriangle\mathrm{C}}}{K_{\mathrm{equi}\blacktriangle\mathrm{Boudouard}} p_{\mathrm{CO}}} \right)}{\left(1[\mathrm{bar}] + K_{\mathrm{equi}\blacktriangle\mathrm{Boudouard}\blacktriangle\mathrm{CO}} p_{\mathrm{CO}} + \frac{p_{\mathrm{CO_2}} c_{\%\blacktriangle\mathrm{C}}}{K_{\mathrm{equi}\blacktriangle\mathrm{Boudouard}\blacktriangle\mathrm{CO_2}} K_{\mathrm{equi}\blacktriangle\mathrm{Boudouard}\blacktriangle\mathrm{CO}} p_{\mathrm{CO}}} \right)^2} \right). \tag{5.10}$$

The reaction rate coefficients $\Re_{\mathrm{reac}\blacktriangle 1}$, $\Re_{\mathrm{reac}\blacktriangle 2}$, $\Re_{\mathrm{reac}\blacktriangle 3}$, and $\Re_{\mathrm{reac}\blacktriangle\mathrm{Boudouard}\blacktriangle 1}$ as well as the equilibrium constants $K_{\mathrm{equi}\blacktriangle\mathrm{CH_4}}$, $K_{\mathrm{equi}\blacktriangle\mathrm{CO}}$, $K_{\mathrm{equi}\blacktriangle\mathrm{Boudouard}\blacktriangle\mathrm{CO}}$, $K_{\mathrm{equi}\blacktriangle\mathrm{CO_2}}$, $K_{\mathrm{equi}\blacktriangle\mathrm{Boudouard}\blacktriangle\mathrm{CO_2}}$, $K_{\mathrm{equi}\blacktriangle\mathrm{H_2}}$, and $K_{\mathrm{equi}\blacktriangle\mathrm{H_2O}}$ are determined by an Arrhenius approach of the form[26]:

$$\Re_{\mathrm{reac}\blacktriangle i} = a_i \cdot \exp\left(-\frac{\mathrm{d}G_{\mathrm{En}\blacktriangle\mathrm{mol},\mathrm{act}\blacktriangle i}}{\Re_{\mathrm{En}\blacktriangle\mathrm{mol}} T} \right). \tag{5.11}$$

Here a_i are the constant pre-exponential coefficients and $\mathrm{d}G_{\mathrm{En}\blacktriangle\mathrm{mol},\mathrm{act}\blacktriangle i}$ the molar activation energy of the i-th species. For the equilibrium constants $K_{\mathrm{equi}\blacktriangle 1}$,

[23] dimensionless for reaction two, in units of bar^2 for reaction three

[24] all dimensionless despite of $K_{\mathrm{equi}\blacktriangle\mathrm{H_2O}}$ which is in units of bars

[25] $K_{\mathrm{equi}\blacktriangle\mathrm{Boudouard}\blacktriangle\mathrm{CO}}$ is dimensionless, $K_{\mathrm{equi}\blacktriangle\mathrm{Boudouard}\blacktriangle\mathrm{CO_2}}$ and $K_{\mathrm{equi}\blacktriangle\mathrm{Boudouard}}$ are in units of 1/bar

[26] for the evaluation the activation energy $\mathrm{d}G_{\mathrm{En}\blacktriangle\mathrm{mol},\mathrm{act}}$ is replaced by the heat of adsorption $\mathrm{d}H_{\mathrm{En}\blacktriangle\mathrm{mol},\mathrm{ad}}$.

$K_{\text{equi}_\blacktriangle 2}$, and $K_{\text{equi}_\blacktriangle 3}$ the following empirical expressions are applied (Adris, Lim, and Grace 1997):

$$K_{\text{equi}_\blacktriangle 1} = a_{\text{equi}_\blacktriangle 1_\blacktriangle 1} \exp\left(a_{\text{equi}_\blacktriangle 1_\blacktriangle 2} - \frac{a_{\text{equi}_\blacktriangle 1_\blacktriangle 3}}{T}\right), \tag{5.12}$$

$$K_{\text{equi}_\blacktriangle 2} = \exp\left(-a_{\text{equi}_\blacktriangle 2_\blacktriangle 1} + \frac{a_{\text{equi}_\blacktriangle 2_\blacktriangle 2}}{T}\right), \tag{5.13}$$

$$K_{\text{equi}_\blacktriangle 3} = K_{\text{equi}_\blacktriangle 1} \cdot K_{\text{equi}_\blacktriangle 2} \tag{5.14}$$

Numerical values for all coefficients are summarized in Table 5.2.

Table 5.2.: **Constants of the reformation model:** The table summarizes the constants of the reformation models .

quantity	**dimension**	**value**	**reference / note**
effective surface per volume $A_{\text{cata}_\blacktriangle \text{mass}}$	m^2/m^3	$33.9 \cdot 10^4$	assumed
number of Ni surface sites per square meter $\Xi_{\text{mol}_\blacktriangle \text{(ad,Ni)}}$	mol/m^2	$19.9 \cdot 10^{-6}$	estimated for Ni's Van der Waals radius $\iota_{\text{Ni}} = 1.63 \cdot 10^{-10}$ m (Bondi 1964)
pre-exponential coefficients			
a_1	bar$^{2.5}$ mol/g_{cata} s	$1.174 \cdot 10^{12}$	(Xu and Fromet 1989b)
a_2	bar mol/g_{cata} s	$5.431 \cdot 10^2$	(Xu and Fromet 1989b)
a_3	bar$^{2.5}$ mol/g_{cata} s	$2.833 \cdot 10^{11}$	(Xu and Fromet 1989b)
$a_{\text{Boudouard}_\blacktriangle 1}$	bar mol/g_{cata} s	$7.425 \cdot 10^3$	(Snoeck and Froment 2002)
$a_{\text{equi}_\blacktriangle \text{CH}_4}$		$6.650 \cdot 10^{-4}$	(Xu and Fromet 1989b)
$a_{\text{equi}_\blacktriangle \text{CO}}$		$8.230 \cdot 10^{-5}$	(Xu and Fromet 1989b)
$a_{\text{equi}_\blacktriangle \text{Boudouard}_\blacktriangle \text{CO}}$		$2.847 \cdot 10^{-10}$	(Snoeck and Froment 2002)
$a_{\text{equi}_\blacktriangle \text{Boudouard}_\blacktriangle \text{CO}_2}$	1/bar	$8.386 \cdot 10^3$	(Snoeck and Froment 2002)
$a_{\text{equi}_\blacktriangle \text{H}_2}$		$8.120 \cdot 10^{-9}$	(Xu and Fromet 1989b)
$a_{\text{equi}_\blacktriangle \text{H}_2\text{O}}$	bar	$1.770 \cdot 10^5$	(Xu and Fromet 1989b)
fitting coefficients			
$a_{\text{equi}_\blacktriangle 1_\blacktriangle 1}$	bar^2	$1.030 \cdot 10^{10}$	(Adris, Lim, and Grace 1997)
$a_{\text{equi}_\blacktriangle 1_\blacktriangle 2}$		$304.197 \cdot 10^{-1}$	(Adris, Lim, and Grace 1997)
$a_{\text{equi}_\blacktriangle 1_\blacktriangle 3}$	K	$271.062 \cdot 10^2$	(Adris, Lim, and Grace 1997)
$a_{\text{equi}_\blacktriangle 2_\blacktriangle 1}$		$379.762 \cdot 10^{-2}$	(Adris, Lim, and Grace 1997)
$a_{\text{equi}_\blacktriangle 2_\blacktriangle 2}$	K	$415.954 \cdot 10^1$	(Adris, Lim, and Grace 1997)

Continued on next page

Continued from previous page

quantity	dimension	value	reference / note
activation energies and heat of adsorption			
$dG_{En_\blacktriangle mol,act_\blacktriangle 1}$	J/mol	$240.100 \cdot 10^3$	(Xu and Fromet 1989b)
$dG_{En_\blacktriangle mol,act_\blacktriangle 2}$	J/mol	$67.130 \cdot 10^3$	(Xu and Fromet 1989b)
$dG_{En_\blacktriangle mol,act_\blacktriangle 3}$	J/mol	$243.900 \cdot 10^3$	(Xu and Fromet 1989b)
$dG_{En_\blacktriangle mol,act_\blacktriangle Boudouard_\blacktriangle 1}$	J/mol	$108.379 \cdot 10^3$	(Snoeck and Froment 2002)
$dH_{En_\blacktriangle mol,ad,equi_\blacktriangle CH_4}$	J/mol	$-38.280 \cdot 10^3$	(Xu and Fromet 1989b)
$dH_{En_\blacktriangle mol,ad,equi_\blacktriangle CO}$	J/mol	$70.650 \cdot 10^3$	(Xu and Fromet 1989b)
$dH_{En_\blacktriangle mol,ad,equi_\blacktriangle Boudouard_\blacktriangle CO}$	J/mol	$-92.543 \cdot 10^3$	(Snoeck and Froment 2002)
$dH_{En_\blacktriangle mol,ad,equi_\blacktriangle Boudouard_\blacktriangle CO_2}$	J/mol	$89.805 \cdot 10^3$	(Snoeck and Froment 2002)
$dH_{En_\blacktriangle mol,ad,equi_\blacktriangle H_2}$	J/mol	$-82.900 \cdot 10^3$	(Xu and Fromet 1989b)
$dH_{En_\blacktriangle mol,ad,equi_\blacktriangle H_2O}$	J/mol	$88.68 \cdot 10^3$	(Xu and Fromet 1989b)

The source terms for the different species in $mol/m^3\,s$ are subsequently obtained via:

$$\gamma_{Mol,vol_\blacktriangle C,ad_\blacktriangle Ni} = r_{reac\,C,ad_\blacktriangle Ni} = r_{reac_\blacktriangle Boudouard}\,, \tag{5.15}$$

$$\gamma_{Mol,vol_\blacktriangle CH_4} = r_{reac\,CH_4} = -r_{reac\,1} - r_{reac\,3}\,, \tag{5.16}$$

$$\gamma_{Mol,vol_\blacktriangle CO} = r_{reac\,CO} = r_{reac\,1} - r_{reac\,2} - 2r_{reac_\blacktriangle Boudouard}\,, \tag{5.17}$$

$$\gamma_{Mol,vol_\blacktriangle CO_2} = r_{reac\,CO_2} = r_{reac\,2} + r_{reac\,3} + r_{reac_\blacktriangle Boudouard}\,, \tag{5.18}$$

$$\gamma_{Mol,vol_\blacktriangle H_2} = r_{reac\,H_2} = 3r_{reac\,1} + r_{reac\,2} + 4r_{reac\,3}\,, \tag{5.19}$$

$$\gamma_{Mol,vol_\blacktriangle H_2O} = r_{reac\,H_2O} = -r_{reac\,1} - r_{reac\,2} - 2r_{reac\,3}\,. \tag{5.20}$$

The test case is given by a rectangular flow channel with a porous catalytic bed (see Figure 5.10). At the inlet a homogeneous mixture of 0.33/0.66 $kg_{species}/kg_{tot}$ CH_4/H_2O with an average fluid velocity of 1.5 m/s is assumed. To save computation time it is necessary to source out the fast reaction kinetics to a "UserFortran" routine which extends the ordinary CFD solver setup by self written code. Figure 5.11 shows a block diagram of the algorithm which evaluates the rates of the reformation reactions. The algorithm starts with an input set of the reactants molar concentrations at the current temperature T. Since the fluid is moving through the finite volumes of the computational grid the algorithm cannot proceed with its calculations until a steady-state is attained. It rather has to stop when the residence-time of the fluid τ_{fl}[27] in each CV is reached (see Figure 5.12).

[27] $\tau_{fl} = \min\left(\frac{A_{y,z}}{\vec{u}_x}, \frac{A_{x,z}}{\vec{u}_y}, \frac{A_{x,y}}{\vec{u}_z}\right)$ in s.

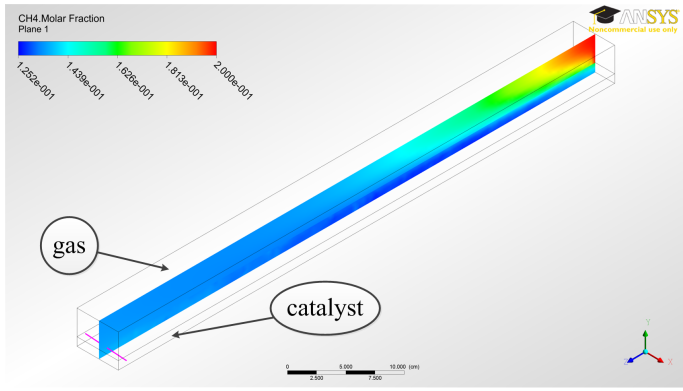

Figure 5.10.: **Test geometry for the reformation submodel:** As a test case a rectangular flow channel with a porous catalytic bed is assumed. Here the case for $T = 800\,\mathrm{K}$ is presented.

For smaller times the reaction rates are calculated according to equations 5.5, 5.6, and 5.7. Since they are the first derivatives of the concentrations at the time t, only a linear approximation of the time dependency around t is possible. In order to minimize both, the computation time and the residual error, the time step dt after which the concentrations and reaction rates are calculated again is determined by the time needed to change the concentration of one of the reactants by 15 %[28] (see Figure 5.13).

When either a steady-state or the residence time are reached, the difference of the final concentrations and the input values divided by the total time t_{tot} are calculated to give the reaction rates per second. This result is passed back to the CFD solver which finally calculates the energy balance[29] by the difference of the molar enthalpies $\Delta H_{\mathrm{En}_{\blacktriangle}\mathrm{mol}}$ per CV at the beginning and at the end[30] of each iteration step.

To check the validity of the model it has to prove its ability to finally calculate the right equilibrium composition of the reactants after a sufficient amount of time for the reaction. Therefore, on the one hand the temperature and com-

[28] A comparison of a linear approximation at $t = 0\,\mathrm{s}$ and a standard PT_1 element gives an error of about 8 % to the real solution for a 15 % change relative to the inlet conditions. If $t + \mathrm{d}t$ is greater than τ_{fl}, dt is altered to $\mathrm{d}t = \tau_{\mathrm{fl}}$.

[29] and sets up the respective sources and sinks

[30] after undergoing chemical reactions

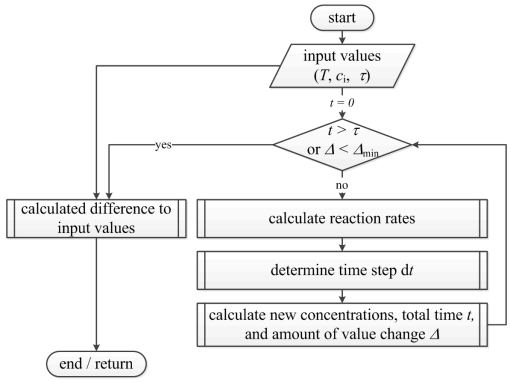

Figure 5.11.: **Block diagram of the reformation algorithm:** The "UserFortran" subroutine calculates the reaction progress until either a steady-state ($\Delta \leq \Delta_{\text{min}}$) or the residence time of the fluid ($t \geq \tau$) is reached.

position are evaluated at a pre-defined location in the CFD model and on the other hand a 0D version of the algorithm is implemented in MATLAB.

Figure 5.14 shows the results for concentration profiles of all species from the CFD, MATLAB, and a thermodynamic equilibrium calculation performed with the Thermochemical software and database package (FactSage) version 6.3. Despite of a slight underestimation of the hydrogen concentration in the CFD results at intermediate temperature, the models show a high correlation to the thermodynamic equilibrium calculation. It is furthermore noteworthy to mention that the C concentration is negligible in any case and thus will not be addressed in the subsequent investigation.

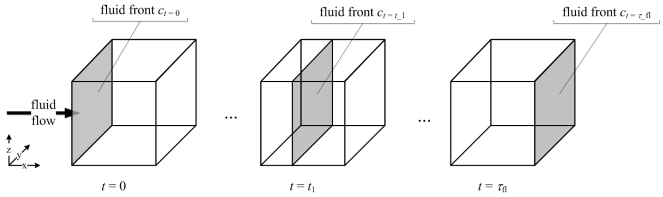

Figure 5.12.: **Movement of a fluid front through a finite volume:** In the example the fluid is moving in x-direction. The fluid front of interest enters the CV at $t = 0$ s. Until it has reached the opposite surface at $t = \tau_{\text{fl}}$ the species traveling on it experience chemical reactions.

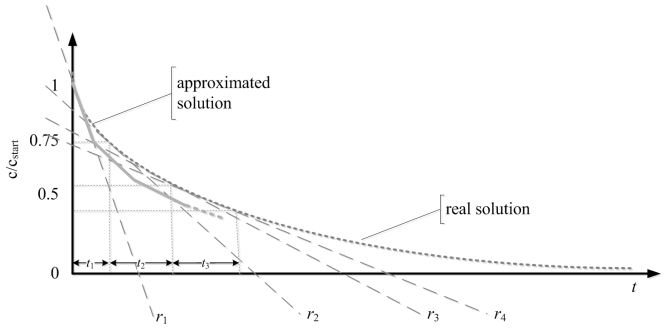

Figure 5.13.: **Time step adjustment during reaction rate calculation:** At every point in time the current reaction rate $r_{\text{reac}\,i}$ is calculated (dotted lines). The time-step is determined by a 15 % change in the reactants concentration.

5.2.4. Heat transfer

Heat transfer can be subdivided into two different aspects: heat transfer within a phase and among two phases. While the former is described by the entire energy BE[31] (see equation 4.7) the latter focuses on the continuity equation 4.9. The convective and diffusive terms in equation 4.7 are governed by $c_{\text{En,v}}$, λ_{En}, and $\rho_{\text{Mass}\blacktriangle\text{vol}}$ for which values and temperature dependent expressions are taken from the literature (see appendix C for a summary).

As already discussed in section 4.1.4, inter-phase heat transfer is dominated by the local convective heat transfer coefficient $\alpha_{\text{th}\blacktriangle\text{convec}}$, which is calculated in dependence of the Nußelt number Nu, the thermal conductivity of the gas phase $\lambda_{\text{En}\blacktriangle(\text{g})}$, and the hydraulic diameter L_{dia} (see equation 4.10). According to the literature (Verein Deutscher Ingenieure 2006, p. Gb 6), for the latter the average channel diameter[32] is used.

Since the fluid flow simulations allow the assumption of laminar flow, empirical correlations to calculate Nu for turbulent flow are not necessary, and from Sanchez, Muñoz, and Sanchez (Sánchez, Muñoz, and Sánchez 2007) a value of $Nu = 3.607$ for fully developed laminar flow is applied. According to Todd and Young (Todd and Young 2002), Wassiljewas's expression for the average thermal conductivity $\lambda_{\text{En}\blacktriangle(\text{g})}$ of a n component gas mixture in W/m K

[31] for solids the convective term is zero; for steady-state situations the storage term is zero
[32] $L_{\text{dia}} = 2.3 \cdot 10^{-3}$ m

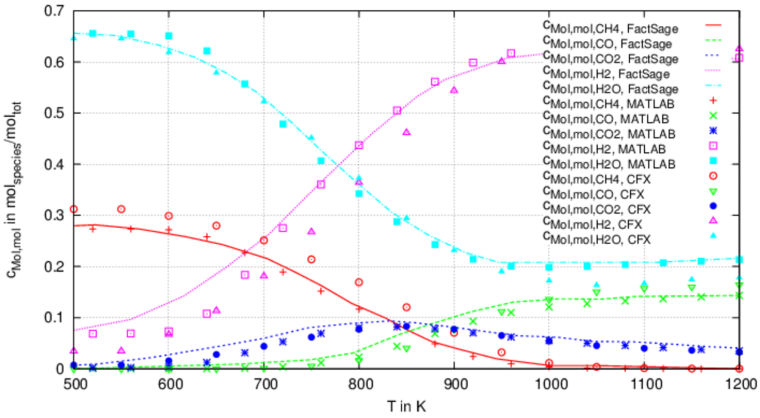

Figure 5.14.: **Concentration profiles of the reformation reactions:** The composition of the reactants in the CFD simulation has almost reached the equilibrium composition (index: CFX). In particular the equilibrium (index: FactSage) and the 0D MATLAB simulations (index: MATLAB) show a high correlation.

(Poling, Prausnitz, and O'Connell 2001, p. 10.30):

$$\lambda_{\mathrm{En,(g)}} = \sum_{i=1}^{n} \frac{y_{\mathrm{Mol}_\blacktriangle \mathrm{mol}_\blacktriangle i} \lambda_{\mathrm{En}_\blacktriangle i}}{\sum_{j=1}^{n} y_{\mathrm{Mol}_\blacktriangle \mathrm{mol}_\blacktriangle j} \text{Ð}_{i/j}} \tag{5.21}$$

is very suitable for SOFCs and thus is selected for in this thesis. Here $y_{\mathrm{Mol}_\blacktriangle \mathrm{mol}_\blacktriangle i}$ is the molar fraction of the i-th species in $\mathrm{mol}_{\mathrm{species}_\blacktriangle i}/\mathrm{mol}_{\mathrm{tot}}$ and $\lambda_{\mathrm{En}_\blacktriangle i}$ its thermal conductivity in W/m K. The Mason and Saxena modification of the interaction parameter $\text{Ð}_{i/j}$:

$$\text{Ð}_{i/j} = \frac{a_1 \left(1 + \sqrt{\frac{\Gamma_{\mathrm{visc}_\blacktriangle i}}{\Gamma_{\mathrm{visc}_\blacktriangle j}}} \cdot \left(\frac{M_{\mathrm{Mass}_\blacktriangle \mathrm{mol}_\blacktriangle j}}{M_{\mathrm{Mass}_\blacktriangle \mathrm{mol}_\blacktriangle i}}\right)^{\frac{1}{4}}\right)^2}{\sqrt{8 \cdot \left(1 + \frac{M_{\mathrm{Mass}_\blacktriangle \mathrm{mol}_\blacktriangle i}}{M_{\mathrm{Mass}_\blacktriangle \mathrm{mol}_\blacktriangle j}}\right)}} \qquad \text{with } \text{Ð}_{i/i} = 1 \tag{5.22}$$

for the i-th and the j-th component is calculated in dependence of the thermal conductivities $\lambda_{\mathrm{En}_\blacktriangle i}$, the molar masses $M_{\mathrm{Mass}_\blacktriangle \mathrm{mol}_\blacktriangle i}$ and $M_{\mathrm{Mass}_\blacktriangle \mathrm{mol}_\blacktriangle j}$ in kg/kmol, and a dimensionless numerical fitting coefficient a_1 which is usually taken as

unity. The required thermal conductivities of the pure substances are available e.g. from the PTPPC handbook. A comparison of calculated values with literature data is shown in Figure 5.15. (Todd and Young 2002)

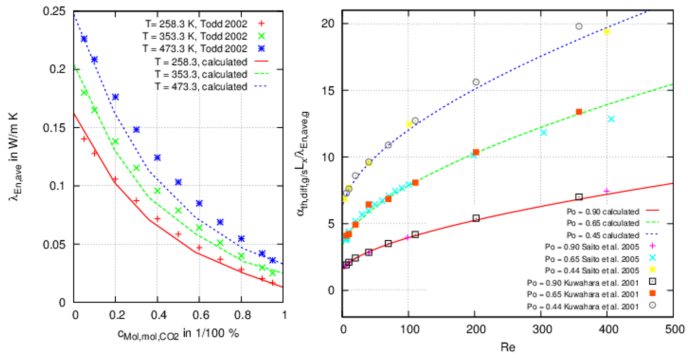

Figure 5.15.: **Thermal conductivity and heat transfer coefficient:** The left figure compares the thermal conductivity of a H_2-CO_2 mixture in dependence of the fluid temperature T in K and the mixture composition with literature data from Todd and Young (Todd and Young 2002). The right figure references the calculations to literature data (Kuwahara, Shirota, and Nakayama 2001; Saito and de Lemos 2005) by illustrating the influence of the porosity and the Reynolds number on the heat transfer coefficient $\alpha_{\text{th,diff}_{\blacktriangle}\text{(g)/(s)}}$ of the porous medium ($Pr = 1$).

Using the results in Figure 5.15, values in the range of $10 \leq \alpha_{\text{th}_{\blacktriangle}\text{convec}} \leq 250\,\text{W/m K}$ can be derived from equation 4.10 for a binary H_2-CO mixture. Since heat transfer literature often focuses on the estimation of Nu and empirical correlations for the heat transfer of certain heat exchanger geometries, specific literature data on the current setup is limited. Hence the literature data for calculated values of the convective heat transfer through the rips of a finned tube bundle, which are in the same order of magnitude (Verein Deutscher Ingenieure 2006, p. Mb 3 et seqq.), allow only a rough verification.

While ANSYS/CFX can solve equation 4.10 for heat transfer between solid and fluid phases (e.g. gas channel and IC) it is necessary to give an expression for T_{fl}, calculating the solid-fluid heat transfer at a boundary between porous and fluid domains. Since the temperature changes between in- and outlet are not expected to be very high, the respective inlet temperatures $T_{\text{ANO}_{\blacktriangle}\text{in}}$ and $T_{\text{CAT}_{\blacktriangle}\text{in}}$ are set as fixed references.[33]

[33] Attempts to find better approximations by averaging between inlet and outlet values or

As mentioned earlier, in the porous electrodes inter-phase conduction is dominant. Unfortunately, the number of macroscopic approaches for a determination of $\alpha_{\text{th,diff}_{\blacktriangle}(g)/(s)}$ is very small (Martynenko and Pavlyukevich 1998; Saito and de Lemos 2005). Since real porous media are build from (almost) chaotic random structures, analytical approaches usually start from idealized physical models. One of these approaches is the one of Kuwahara, Shirota, and Nakayama (Kuwahara, Shirota, and Nakayama 2001). They assume an infinite number of solid square rods of $L_\chi \cdot L_\chi$[34] in a regular triangular pattern (see Figure 5.16).

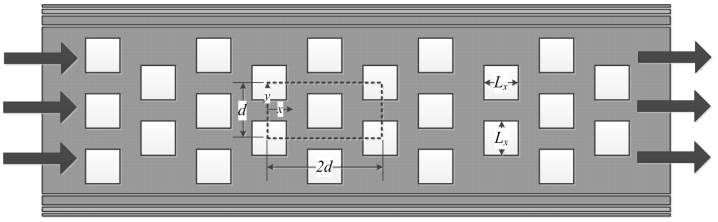

Figure 5.16.: **Simplified model of the heat transfer in a porous medium:** Kuwahara, Shirota, and Nakayama (Kuwahara, Shirota, and Nakayama 2001) investigated an infinite regular pattern of solid square rods around which a fluid is moving in order to obtain an expression for the interfacial heat transfer coefficient $\alpha_{\text{th,diff}_{\blacktriangle}(g)/(s)}$; modified from (Saito and de Lemos 2005).

Starting from solutions for the governing transport equations for the surrounding gas volume, the authors obtained a correlation for the interfacial heat transfer coefficient:

$$\alpha_{\text{th,diff}_{\blacktriangle}(g)/(s)} = \frac{\lambda_{\text{En}_{\blacktriangle}(g)}}{L_\chi} \cdot \left\{ 1 + \frac{4 \cdot (1 - Po_{\%})}{Po_{\%}} + \frac{1}{2} \cdot \sqrt{1 - Po_{\%}} \cdot Re^{0.6} Pr^{\frac{1}{3}} \right\} \qquad (5.23)$$

in dependence of the local Reynolds Re and Prandtl Pr numbers, the porosity $Po_{\%}$[35], and the hydrodynamic diameter L_χ[36]. While $\lambda_{\text{En}_{\blacktriangle}(g)}$ is again calculated using equation 5.21, the Prandtl number Pr is given by (Meschede 2006, p. 1122):

$$Pr = \frac{\Gamma_{\text{visc}_{\blacktriangle}(g)} c_{\text{En,p,mass}_{\blacktriangle}(g)_{\blacktriangle}\text{ave}}}{\lambda_{\text{En}_{\blacktriangle}(g)}} .$$

referencing to the values at certain locations during calculation, lead to numerical instability.

[34] average particle sizes of 5 µm for the anode (first 20 µm: 2.5 µm) and 2.5 µm for the cathode (Mücke 2009b) are assumed

[35] $0.2 < Po_{\%} < 0.9$ (Kuwahara, Shirota, and Nakayama 2001)

[36] Here the average pore diameters are used.

Here equation 4.4 can be used to calculate the average heat capacity at constant pressure
$c_{\mathrm{En,p,mass}_{\blacktriangle}(\mathrm{g})_{\blacktriangle}\mathrm{ave}}$ in J/kg K from the pure substance values of its constituents.

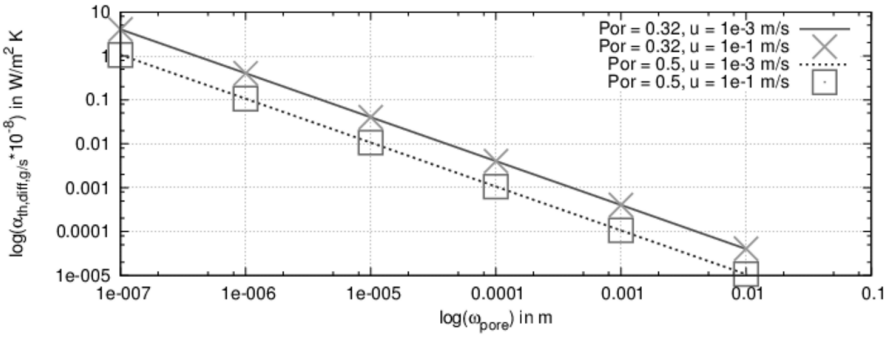

Figure 5.17.: **Porous media heat transfer coefficient:** In the Kuwahara, Shirota, and Nakayama (Kuwahara, Shirota, and Nakayama 2001) model of a porous medium, the heat transfer coefficient shows an exponential dependency on the average pore radius. For $T = 973$ K, $\iota_{\mathrm{pore}} = 7.5{\cdot}10^{-6}$ m, a 0.97/0.03 $\mathrm{mol_{species}/mol_{tot}}$ H_2/H_2O mixture, and a fixed value of $Pr = 0.002$, $\alpha_{\mathrm{th,diff}_{\blacktriangle}(\mathrm{g})/(\mathrm{s})}$ increases with decreasing porosity. Within the investigated velocity range the influence of the fluid velocity is negligible.

Figure 5.17 shows the normalized heat transfer coefficient $\alpha_{\mathrm{th,diff}_{\blacktriangle}(\mathrm{g})/(\mathrm{s})}$ in dependence of the average pore radius ι_{pore} for different porosities $Po_{\%}$ and fluid velocities $\vec{u}$ inside the porous medium. It it obvious that the fluid velocity is negligible, but the pore radius and the porosity show strong influences. In both cases an increase is followed by a reduction of $\alpha_{\mathrm{th,diff}_{\blacktriangle}(\mathrm{g})/(\mathrm{s})}$, leading to the conclusion that a rather dense material penetrated by small pores is beneficial for heat transfer. This agrees well with experimental findings of Brendelberger et al. (Brendelberger et al. 2012), who investigated heat transfer in a porous catalytic burner. Their electron microscope images show a highly porous structure[37] consisting of large primary pores[38] which are covered by numerous secondary pores[39]. Since Kim's (Kim 1991) statement about the limited number of available publications on $\alpha_{\mathrm{th,diff}_{\blacktriangle}(\mathrm{g})/(\mathrm{s})}$ is still valid, the cal-

[37] a little pressure drop was intended by the authors
[38] $\iota_{\mathrm{pore}} = 0.05$ - 0.5 mm
[39] $\iota_{\mathrm{pore}} \approx 10\,\mu$m

culated results of the Kuwahara, Shirota, and Nakayama (Kuwahara, Shirota, and Nakayama 2001) model in equation 5.23 are adjusted to Brendelberger et al.'s (Brendelberger et al. 2012) measurements by multiplying the former with an empirical correlation function:

$$\begin{aligned} \text{TJ} =& 110.969 \cdot 10^{-6}\ [\text{K}] \cdot T^{-2} + 291.599 \cdot 10^{-8}\ [\text{K}] \cdot T^{-1} + 606.885 \cdot 10^{-11} \\ & - 394.904 \cdot 10^{-14} \left[\frac{1}{\text{K}}\right] \cdot T + 12.732 \cdot 10^{-16} \left[\frac{1}{\text{K}^2}\right] T^2 \ . \end{aligned}$$

Figure 5.18 shows a comparison of the volumetric heat transfer coefficients $\alpha_{\text{th,diff}_\blacktriangle\text{vol}_\blacktriangle\text{(g)/(s)}}$ obtained by Brendelberger et al. from their experimental data with the adjusted numerical results from the Kuwahara, Shirota, and Nakayama model.

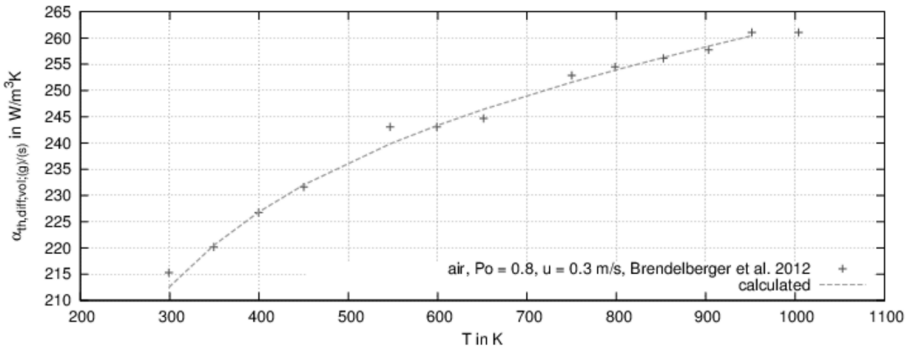

Figure 5.18.: **Volumetric heat transfer coefficients:** The results of the Kuwahara, Shirota, and Nakayama (Kuwahara, Shirota, and Nakayama 2001) model for air flowing ($\vec{u}$ = 0.3 m/s) through a porous medium with a porosity of $Po_{\%}$ = 0.8 and an effective surface of $A_{\text{eff}_\blacktriangle\text{vol}}$ = 4.6·10^6 m^2/m^3 are adjusted to the experimental results of Brendelberger et al. (Brendelberger et al. 2012).

Because surface heat transfer between the gaseous and the solid phase happens inside the entire porous domain, volumetric source terms for either of them are required:

$$\Upsilon_{\text{En,vol}_\blacktriangle\text{(g)}} = A_{\text{eff}_\blacktriangle\text{vol}} \alpha_{\text{th,diff}_\blacktriangle\text{(g)/(s)}} \left(T_{\text{(s)}} - T_{\text{(g)}}\right) \ , \tag{5.24}$$

$$\Upsilon_{\text{En,vol}_\blacktriangle\text{(s)}} = - \Upsilon_{\text{En,vol}_\blacktriangle\text{(g)}} \ . \tag{5.25}$$

Here $A_{\text{eff}\blacktriangle\text{vol}}$ in m^2/m^3 are the effective surface between the phases per volume, α_{th} in $\text{W}/\text{m}^2\,\text{K}$ the heat transfer coefficient, and $T_{(\text{g})}$ and $T_{(\text{s})}$ the temperatures of the gaseous and the solid phase. The models of this subsection are integrated into "UserFortran" routines for the final CFD model.

5.2.5. Charge transport

Charge transport (see section 4.1.5) can be subdivided into electronic and ionic transport. Because the former is to be described by a continuous "flux of electrons" Ohm's law must be implemented into the CFD code.

As a test case, a series connection of three different materials is assumed (see Figure 5.19). According to Ohm's and Kirchhoff's laws (see equation 2.28),

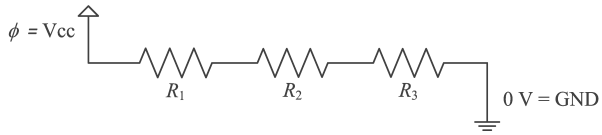

Figure 5.19.: **Block diagram of a series connection of resistors:** As a test case, a series connection of three different materials with a pre-defined difference in electric potential ϕ_{Volt} vs. GND ($\equiv$ 0 V) is compared with the CFD model.

the change in electric potential $\Delta\phi_{\text{Volt}}$ in V can be calculated as:

$$\begin{aligned} \Delta\phi_{\text{Volt}} &= R_{\text{Ohm}\blacktriangle\text{tot}} \cdot I_{\text{tot}} \,; \\ \Rightarrow R_{\text{Ohm}\blacktriangle\text{tot}} = \frac{\Delta\phi_{\text{Volt}}}{I_{\text{tot}}} &= R_{\text{Ohm}\blacktriangle 1} + R_{\text{Ohm}\blacktriangle 2} + R_{\text{Ohm}\blacktriangle 3} \,, \\ &= \frac{L_{x\blacktriangle 1}}{\underline{\underline{\sigma}}_{\text{el}\blacktriangle 1}\, L_{y\blacktriangle 1} L_{z\blacktriangle 1}} + \frac{L_{x\blacktriangle 2}}{\underline{\underline{\sigma}}_{\text{el}\blacktriangle 2}\, L_{y\blacktriangle 2} L_{z\blacktriangle 2}} + \frac{L_{x\blacktriangle 3}}{\underline{\underline{\sigma}}_{\text{el}\blacktriangle 3}\, L_{y\blacktriangle 3} L_{z\blacktriangle 3}} \,. \end{aligned}$$

In ANSYS/CFX this model is implemented as a conductor with a square cross-section, illustrated in Figure 5.20. The obtained results for the parameter set summarized in Table 5.3 are shown in Figure 5.21. It can be seen that the results from the self-implemented model are identical to the results of the ANSYS/CFX in-house electrodynamics model (Ansys Inc. 2011, p. 363 et seqq.), the values of an algebraic calculation, as well as to those of a self-written 1D-MATLAB-CFD solver. The latter is used in subsection 5.2.6 as a design tool for the electrochemical reactions and thus is explained there in more detail.

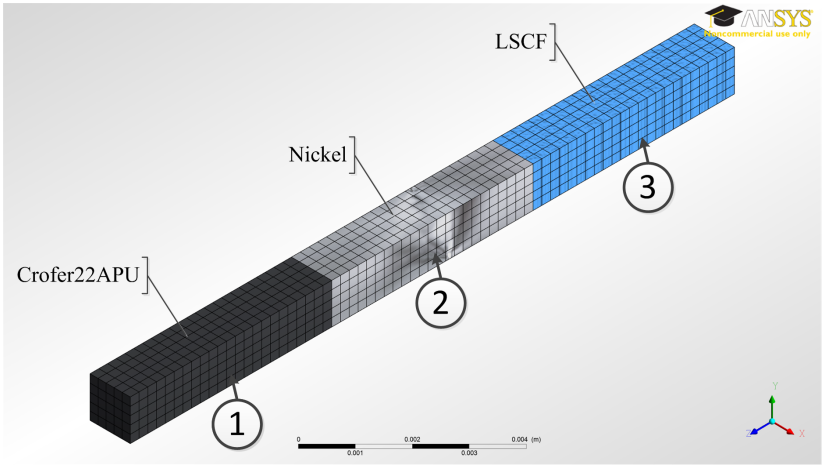

Figure 5.20.: **Electric charge transport test model:** The test model represents a conductor with a square cross-section consisting of three different materials in a series connection with pre-defined difference in electric potential $\Delta\phi_{\text{Volt}}$.

For porous media, the electrical conductivity $\underline{\underline{\sigma}}_{\text{el}}$ is strongly dependent on the porosity of the medium. Starting from the porous anode simulations in section 2.4.1, an extension to the Generalized Effective Media Theory (GEMT) for arbitrary properties of binary mixtures[40] is possible. According to McLachlan, Blaszkiewicz, and Newnham (McLachlan, Blaszkiewicz, and Newnham 1990), the average conductivity $\underline{\underline{\sigma}}_{\text{ave}}$ of a highly $\underline{\underline{\sigma}}_{\uparrow}$ and a barely $\underline{\underline{\sigma}}_{\downarrow}$ conductive species (all in S/m) is given by:

$$0 = \frac{V_{\text{Vol}_{\blacktriangle\uparrow}} \cdot \left(\underline{\underline{\sigma}}_{\downarrow}^{\frac{1}{a}} - \underline{\underline{\sigma}}_{\text{ave}}^{\frac{1}{a}}\right)}{\underline{\underline{\sigma}}_{\downarrow}^{\frac{1}{a}} + \underline{\underline{\sigma}}_{\text{ave}}^{\frac{1}{a}} \cdot \left(\frac{V_{\text{Vol}_{\blacktriangle\downarrow\blacktriangle\text{crit}}}}{1 - V_{\text{Vol}_{\blacktriangle\downarrow\blacktriangle\text{crit}}}}\right)} + \frac{\left(1 - V_{\text{Vol}_{\blacktriangle\uparrow}}\right) \cdot \left(\underline{\underline{\sigma}}_{\uparrow}^{\frac{1}{a}} - \underline{\underline{\sigma}}_{\text{ave}}^{\frac{1}{a}}\right)}{\underline{\underline{\sigma}}_{\uparrow}^{\frac{1}{a}} + \underline{\underline{\sigma}}_{\text{ave}}^{\frac{1}{a}} \cdot \left(\frac{V_{\text{Vol}_{\blacktriangle\downarrow\blacktriangle\text{crit}}}}{1 - V_{\text{Vol}_{\blacktriangle\downarrow\blacktriangle\text{crit}}}}\right)}. \tag{5.26}$$

Here $V_{\text{Vol}_{\blacktriangle\uparrow}}$ is the volume fraction of the highly conductive phase and $V_{\text{Vol}_{\blacktriangle\downarrow\blacktriangle\text{crit}}}$ the critical volume fraction of the weakly conductive phase, for which percolating clusters of the highly conductive phase are no longer existent and thus

[40] a very well and a poor conducting one

Table 5.3.: **Parameter set of the electrical test model:** The test of the electrical submodel is performed for a hypothetical series connection of Crofer22APU, Ni, and LSCF sheets.

Quantity	Dimension	Value
materials		Crofer22APU, Ni, LSCF
conductivity $\underline{\underline{\sigma}}_{\mathrm{el}}$	S/m	see appendix C
length of each layer L_x	m	0.005
width of each layer L_y	m	0.001
height of each layer L_z	m	0.001
drop in electric potential $\Delta\phi_{\mathrm{Volt}}$	V	0.01
temperature T	K	973
maximum of the residuals (CFD calculations)	var.	10^{-5}

is accompanied by a drop in conductivity. Finally, a is a dimensionless system specific design parameter. To simplify the calculation, the little conductive phase can be assumed to be an ideal insulator, what simplifies equation 5.26 to:

$$\underline{\underline{\sigma}}_{\mathrm{ave}} = \underline{\underline{\sigma}}_{\uparrow} \cdot \left(1 - \frac{1 - V_{\mathrm{Vol}_{\blacktriangle}\uparrow}}{V_{\mathrm{Vol}_{\blacktriangle}\downarrow_{\blacktriangle}\mathrm{crit}}}\right)^{a} . \tag{5.27}$$

GEMT holds several system specific parameters, what makes measurements on specimens of the system of interest crucial. Since those are not available, the influence of the Ni content on the overall conductivity is adjusted by using the results of Marinšek, Pejovnik, and Macel (Marinsek, Pejovnik, and Macel 2007), who investigated $\underline{\underline{\sigma}}_{\mathrm{el}}$ of porous Ni-10YSZ. The data points are fitted using equation 5.27, whereby special attention is paid on the one hand to a sufficient reproduction of the value of the dense material and on the other hand to the beginning of the transition region. For the same cermet the influence of the relative volume fraction on the ionic conductivity is derived from the results of Mizusaki et al. (Mizusaki et al. 1996) by using equation 5.27 again (see Figure 5.22). The empirical fitting parameters for both cases are summarized in Table 5.4. It it obvious that for the ionic conductivity the percolation threshold is significantly lower than the theoretical value of 1/3 from section 2.4.1. Next to the very limited number of experimental data points and thus a high level of uncertainty in the fit, influences of the particle size and the manufacturing process are possible.

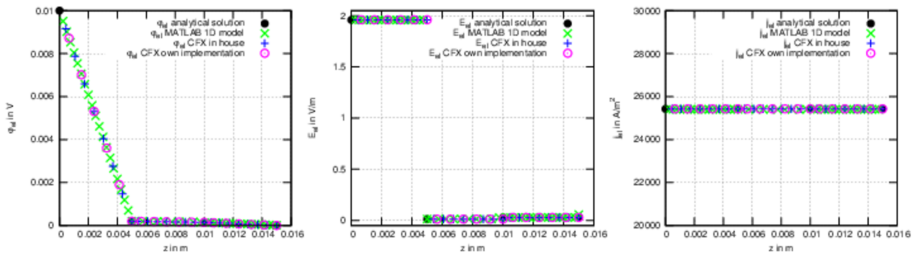

Figure 5.21.: **Electric potential, electric field, and current density:** The figures show the results for the electric potential $\Delta\phi_{\mathrm{Volt}}$ (left), the electric field $\vec{\mathbb{E}}_{\mathrm{el}}$ (middle), and the current density $\vec{j}_{\mathrm{el}}$ (right). Presented are the values of an analytical calculation (black dots), a 1D-MATLAB model (green X's), the CFX in-house electrodynamics model (blue crosses), and the self-made CFX implementation (magenta open circles). The CFX results are examined at the center line of the electric test model in z-direction.

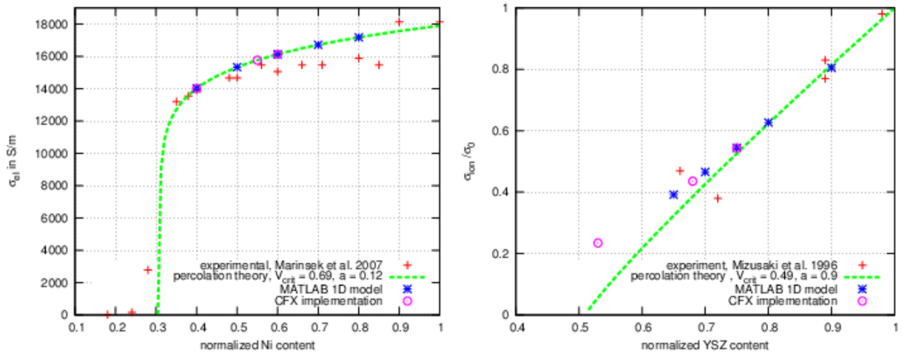

Figure 5.22.: **Conductivity versus relative volume fraction:** The figures show the values of the electric conductivity in dependence of the Ni content of the specimens (left) and the relative ionic conductivity in dependence of the YSZ content (right). Presented are measured values (red crosses), derived dependencies from percolation theory (green lines), and the results of the latter's implementation in a 1D-MATLAB model (blue stars) as well as in ANSYS/CFX (magenta open circles). The data is taken from (Marinsek, Pejovnik, and Macel 2007) and (Mizusaki et al. 1996).

Table 5.4.: **Fitting parameters for the porosity dependence of the conductivity:** Summarized are the fitting parameters for equation 5.27 for the electronic and the ionic conductivity.

Quantity	**Dimension**	**Value**
electronic conductivity		
$\underline{\underline{\sigma}}_{\uparrow}$	S/m	17,900
$V_{\mathrm{Vol}_{\blacktriangle\downarrow\blacktriangle}\mathrm{crit}}$	1/100 %	0.69
a		0.12
ionic conductivity		
$V_{\mathrm{Vol}_{\blacktriangle\downarrow\blacktriangle}\mathrm{crit}}$	1/100 %	0.79
a		1.6

To respect the temperature dependency of Nickel's electric conductivity, $\underline{\underline{\sigma}}_{\uparrow}$ from Table 5.4 is replaced by an appropriate expression obtained by Li, Shi, and Cai (Li, Shi, and Cai 2010). Altogether, it follows:

$$\underline{\underline{\sigma}}_{\mathrm{el}_{\blacktriangle}\mathrm{Ni}} = \left(3.27 \cdot 10^6 \left[\frac{\mathrm{S}}{\mathrm{m}}\right] - 1065.30 \left[\frac{\mathrm{S}}{\mathrm{m\,K}}\right] \cdot T\right) \cdot \left(1 - \frac{1 - V_{\mathrm{Vol}_{\blacktriangle}\mathrm{Ni}}}{0.69}\right)^{0.12} \text{ in } \frac{\mathrm{S}}{\mathrm{m}} \,. \tag{5.28}$$

Using a temperature dependent expression from Shi et al. (Shi et al. 2007a), for the ionic conductivity of the porous anode[41] the same approach gives[42]:

$$\underline{\underline{\sigma}}_{\mathrm{ion}_{\blacktriangle}\mathrm{YSZ}} = \left(3.34 \cdot 10^4 \left[\frac{\mathrm{S}}{\mathrm{m}}\right] \cdot \exp\left(-\frac{10,300\ [\mathrm{K}]}{T}\right)\right) \cdot \left(1 - \frac{1 - V_{\mathrm{Vol}_{\blacktriangle}\mathrm{YSZ}}}{0.79}\right)^{1.6} \text{ in } \frac{\mathrm{S}}{\mathrm{m}} \,. \tag{5.29}$$

Since the cathode is very thin, only simplified expressions without an explicit dependency on its porosity are used. While the expression for the electric conductivity is extracted from measurements made by Rembelski et al. (Rembelski et al. 2012), the ionic conductivity is derived from data obtained by Fan, Yan, and Yan (Fan, Yan, and Yan 2011) (see Figure 5.23):

$$\underline{\underline{\sigma}}_{\mathrm{el}_{\blacktriangle}\mathrm{LSCF}} = \frac{\left(1.51 \cdot 10^2 \pm 1.466\right) \cdot 10^5 \left[\frac{\mathrm{S\,K}}{\mathrm{m}}\right]}{T} \cdot \exp\left(-\frac{(1068.11 \pm 6.61)\ [\mathrm{K}]}{T}\right) \text{ in } \frac{\mathrm{S}}{\mathrm{m}} \,, \tag{5.30}$$

$$\underline{\underline{\sigma}}_{\mathrm{ion}_{\blacktriangle}\mathrm{LSCF}} = (42.65 \pm 20.41) \cdot 10^3 \left[\frac{\mathrm{S}}{\mathrm{m}}\right] \cdot \exp\left(-\frac{(85.88 \pm 4.82) \cdot 10^3 \left[\frac{\mathrm{J}}{\mathrm{mol}}\right]}{\Re_{\mathrm{En}_{\blacktriangle}\mathrm{mol}} T}\right) \text{ in } \frac{\mathrm{S}}{\mathrm{m}} \,. \tag{5.31}$$

[41] for the electrolyte the same expression with $V_{\mathrm{Vol}_{\blacktriangle}\mathrm{YSZ}} = 1$ is used

[42] For numerical reasons, the equation is multiplied by a factor of 50 during the simulations with the detailed electrochemistry model.

As discussed in section 4.1.5, the ionic conductivity is connected to the kine-

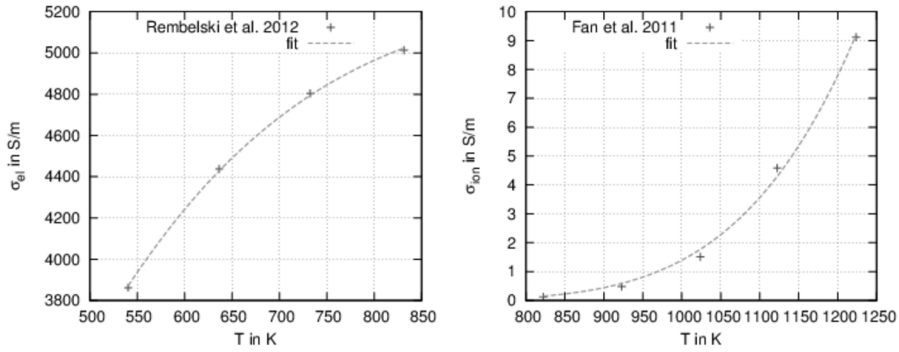

Figure 5.23.: **Electric and ionic conductivity of LSCF:** For the electric conductivity (left) data obtained by Rembelski et al. (Rembelski et al. 2012) is evaluated. The ionic conductivity (right) is derived from measurements made by Fan, Yan, and Yan (Fan, Yan, and Yan 2011).

matic diffusivity of the oxygen ions $\underline{\underline{D}}_{\text{ion}}$ via the Nernst-Einstein Equation (NEE) (Bard, Inzelt, and Scholz 2008, p. 444):

$$\underline{\underline{\sigma}}_{\text{ion}} = z^2 F_{\text{Ch}_\blacktriangle\text{mol}}{}^2 \underline{\underline{D}}_{\text{elchem}_\blacktriangle\text{mol}_\blacktriangle\text{ion}} = \frac{c_{\text{Mol}_\blacktriangle\text{vol}} z^2 F_{\text{Ch}_\blacktriangle\text{mol}}{}^2}{\Re_{\text{En}_\blacktriangle\text{mol}} T} \underline{\underline{D}}_{\text{ion}} \qquad \text{in S/m} . \quad (5.32)$$

The number of charge carriers is small compared to the number of electrons. Therefore, the current not only consists of a “continuous flux of charges”, but has to be extended by a “diffusive flux of particles”. Thus, the transport equations to be solved are[43]:

$$\begin{aligned}
\vec{j}_{\text{ion}} &= \vec{j}_{\text{ion}_\blacktriangle\text{cond}} + \vec{j}_{\text{ion}_\blacktriangle\text{diff}} , \\
\vec{j}_{\text{ion}_\blacktriangle\text{cond}} &= \underline{\underline{\sigma}}_{\text{ion}} \vec{\mathbb{E}}_{\text{ion}} , \\
\vec{j}_{\text{ion}_\blacktriangle\text{diff}} &= -zF_{\text{Ch}_\blacktriangle\text{mol}} \underline{\underline{D}}_{\text{ion}} \operatorname{grad}\left(c_{\text{Mol}_\blacktriangle\text{vol}_\blacktriangle\text{ion}}\right) , \\
&= -\frac{\underline{\underline{\sigma}}_{\text{ion}} \Re_{\text{En}_\blacktriangle\text{mol}} T}{z^2 F_{\text{Ch}_\blacktriangle\text{mol}}{}^2 c_{\text{Mol}_\blacktriangle\text{vol}_\blacktriangle\text{ion}}} \operatorname{grad}\left(\phi_{\text{ion}}\right) .
\end{aligned}$$

[43] see appendix B.4 for a derivation from thermodynamics

Experimental data on the absolute concentration of oxygen ions in LSCF and/or YSZ is rare. Thus, literature data for $\underline{\underline{\sigma}}_{ion}$ and $\underline{\underline{D}}_{ion}$ is used to determine $c_{Mol \blacktriangle vol \blacktriangle ion}$ for this test case (see Table 5.5 and Figure 5.24). Since the ion

Table 5.5.: **Ionic diffusivity:** For both materials the parameters are described by an Arrhenius approach (see equation 2.38).

Variable	Material	a_0 in m^2/s	$dG_{En \blacktriangle mol,act}$ in kJ/mol	Reference
$\underline{\underline{D}}_{ion}$	YSZ	$6.08 \cdot 10^{-9}$	57.0	(Devanathan et al. 2006)
$\underline{\underline{D}}_{ion}$	LSCF	$1.58 \cdot 10^{-6}$	73.6	(Xu and Thomson 1999)

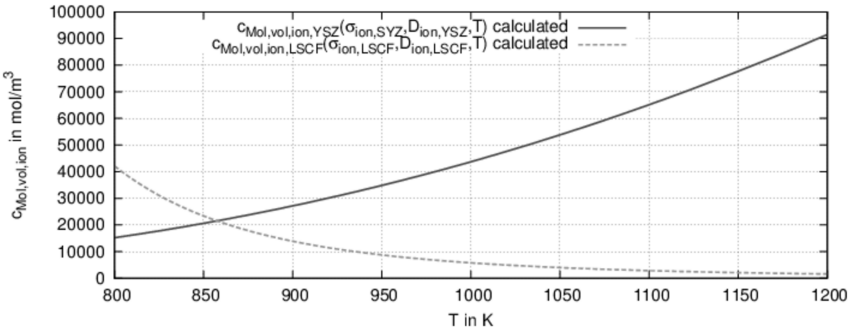

Figure 5.24.: **Concentration of oxygen ions in LSCF and YSZ taking part in the conduction process:** For an assumed porosity of 30 % the concentration of the ions, taking part in the charge conduction mechanism, is calculated according to equation 5.32.

concentration in the bulk material is finite, an appropriate maximal value is required for modeling. For this purpose, the number of charge carriers is calculated by using equation 5.32. It is expected that not all vacancies join in the conduction process, thus the maximal values have to be higher than those numbers shown in Figure 5.24. Although the literature values are well referenced[44], and equation 5.32 is an expression of Onsager's reciprocal relations and thus a fundamental law of physics (Bard, Inzelt, and Scholz 2008, p. 467), the curves in Figure 5.24 cannot be extended to infinity. Therefore, for 8YSZ a value of $c_{Mol \blacktriangle vol \blacktriangle max \blacktriangle YSZ} = 100$ kmol/m^3 and for LSCF a value of $c_{Mol \blacktriangle vol \blacktriangle max \blacktriangle LSCF} = 85$

[44] e.g. (Kim et al. 2007) for LSCF

kmol/m^3 are assumed as maximal values[45]. Finally, the source term for the thermal energy, which is released in every CV due to ohmic losses, is given by:

$$\gamma_{\mathrm{En}_\blacktriangle \mathrm{vol}_\blacktriangle(\mathrm{s})} = \left(\vec{\mathbb{E}}_{x_\blacktriangle \mathrm{el,ion}} \vec{j}_{x_\blacktriangle \mathrm{el,ion}} + \vec{\mathbb{E}}_{y_\blacktriangle \mathrm{el,ion}} \vec{j}_{y_\blacktriangle \mathrm{el,ion}} + \vec{\mathbb{E}}_{z_\blacktriangle \mathrm{el,ion}} \vec{j}_{z_\blacktriangle \mathrm{el,ion}}\right) \cdot V_{\mathrm{Vol}_\blacktriangle \mathrm{CV}} \,. \tag{5.33}$$

5.2.6. Electrochemistry

The electrochemical submodel links the chemical, electrical, and thermal models by providing expressions for their source terms. Since the coupling is bidirectional, it can be seen as the cornerstone of the SOFC model presented in this thesis. In this subsection a sophisticated 1D model, which describes the mutually coupled processes, is proposed first and subsequently adjusted to literature data. From the results of this model assumptions for a simplified model are concluded. Starting from them, a 3D model, based on the common BVE approach, is presented subsequently.

5.2.6.1. A novel approach to SOFC electrochemistry based on local reaction rates

As discussed in the previous chapters, electrochemistry deals with surface effects on very small length- and timescales. Therefore, in principle the BEs of chapter 4.1 should be extended by surface source terms for the porous electrode regions. This would also require a "reconstruction" of the topology of the latter within the CFD model, what is not feasible for cell level modeling. In consequence, the surface sources are replaced by volumetric ones for the CVs of the anode and cathode. Here, the "effective surface" $A_{\mathrm{eff}_\blacktriangle \mathrm{vol}}$ in m^2/m^3 gives a measure for the inner surface of the porous electrodes per unit of volume. While for the cathode only a single value for $A_{\mathrm{eff}_\blacktriangle \mathrm{vol}_\blacktriangle \mathrm{CAT}}$ is necessary, on the anode side the mixing of the cermet's components has to be considered. An ideal manufacturing process, any demixing during sintering, and thus a constant ratio of the cermet constituents are assumed. With this, the effective Ni surface follows as:

$$A_{\mathrm{eff}_\blacktriangle \mathrm{vol}_\blacktriangle \mathrm{Ni}_\blacktriangle \mathrm{ANO}} = A_{\mathrm{eff}_\blacktriangle \mathrm{vol}_\blacktriangle \mathrm{ANO}} \cdot \mathrm{Ni}\%_\blacktriangle \mathrm{ANO} \,,$$

[45] The calculated values agree well with those in the theoretical study of Kenney and Karan (Kenney and Karan 2010) for the anode and the one of Leonide (Leonide 2010) for the cathode.

respectively the effective YSZ surface:

$$A_{\mathrm{eff}\blacktriangle\mathrm{vol}\blacktriangle\mathrm{YSZ}\blacktriangle\mathrm{ANO}} = A_{\mathrm{eff}\blacktriangle\mathrm{vol}\blacktriangle\mathrm{ANO}} \cdot \mathrm{YSZ}\%_{\blacktriangle\mathrm{ANO}} \,.$$

The absolute values for $A_{\mathrm{eff}\blacktriangle\mathrm{vol}\blacktriangle\mathrm{ANO}}$ and $A_{\mathrm{eff}\blacktriangle\mathrm{vol}\blacktriangle\mathrm{CAT}}$ are dependent on the average diameters of the solid particles and pores, the resulting porosity and tortuosity. Experimental data on this subject is very rare (Wilson et al. 2006), thus for the cathode side a value of $A_{\mathrm{eff}\blacktriangle\mathrm{vol}\blacktriangle\mathrm{CAT}} = 3.32{\cdot}10^6\ \mathrm{m^2/m^3}$ from Leonide (Leonide 2010) and for the anode side a value of $A_{\mathrm{eff}\blacktriangle\mathrm{vol}\blacktriangle\mathrm{ANO}} = 4.6{\cdot}10^6\ \mathrm{m^2/m^3}$ obtained by Kenney et al. (Kenney et al. 2009) are used.

Since electrochemical reactions only take place at TPBs (see section 2.4.1), which are lines in a 3D environment, an effective TPB length Ъ per effective surface in $\mathrm{m/m^2}$ is required to transfer line sources to surface and subsequently to volume ones. In this context Mizusaki et al. (Mizusaki et al. 1994) reported a value of Ъ = 303 $\mathrm{m/m^2}$ from measurements on patterned model electrodes.

Starting point for the energy and species conservation processes are the electrochemical reactions on both sides of the electrolyte:

$$\mathrm{elchem}\blacktriangle\mathrm{TPB}\blacktriangle\mathbf{1}: \quad \mathrm{H_2} + \mathrm{O^{2-}_{YSZ}} + 2\,\mathrm{Ni} \longrightarrow \mathrm{H_2O} + 2\,\mathrm{Ni} + \mathrm{YSZ} + 2\,\mathrm{e^-}\,, \tag{5.34}$$

$$\mathrm{elchem}\blacktriangle\mathrm{TPB}\blacktriangle\mathbf{2}: \quad \mathrm{CO} + \mathrm{O^{2-}_{YSZ}} + 2\,\mathrm{Ni} \longrightarrow \mathrm{CO_2} + 2\,\mathrm{Ni} + \mathrm{YSZ} + 2\,\mathrm{e^-}\,, \tag{5.35}$$

$$\mathrm{elchem}\blacktriangle\mathrm{surf}\blacktriangle\mathbf{3}: \quad \mathrm{O_2} + 2\,\mathrm{LSCF} + 4\,\mathrm{e^-} \longrightarrow 2\mathrm{O^{2-}_{LSCF}}\,. \tag{5.36}$$

Moreover, when migrating from the cathode to the anode, the oxygen ions are transferred from the LSCF to the YSZ bulk, releasing LSCF vacancies and consuming YSZ ones. As a result, the following volumetric source terms for the species in dependence of the reaction rates at the TPBs $r_{\mathrm{reac}\blacktriangle\mathrm{elchem}\blacktriangle\mathrm{Mol}\blacktriangle\mathrm{TPB}\blacktriangle i}$ in mol/m s and the cathodic reaction rates $r_{\mathrm{reac}\blacktriangle\mathrm{elchem}\blacktriangle\mathrm{Mol}\blacktriangle\mathrm{surf}\blacktriangle 3}$ in $\mathrm{mol/m^2\,s}$ exist:

$$\gamma_{\mathrm{Mol}\blacktriangle\mathrm{vol}\blacktriangle\mathrm{CO}} = -\,r_{\mathrm{reac}\blacktriangle\mathrm{elchem}\blacktriangle\mathrm{Mol}\blacktriangle\mathrm{TPB}\blacktriangle 2} \cdot A_{\mathrm{eff}\blacktriangle\mathrm{vol}\blacktriangle\mathrm{ANO}} \cdot Ъ\,, \tag{5.37}$$

$$\gamma_{\mathrm{Mol}\blacktriangle\mathrm{vol}\blacktriangle\mathrm{CO_2}} = r_{\mathrm{reac}\blacktriangle\mathrm{elchem}\blacktriangle\mathrm{Mol}\blacktriangle\mathrm{TPB}\blacktriangle 2} \cdot A_{\mathrm{eff}\blacktriangle\mathrm{vol}\blacktriangle\mathrm{ANO}} \cdot Ъ\,, \tag{5.38}$$

$$\gamma_{\mathrm{Mol}\blacktriangle\mathrm{vol}\blacktriangle\mathrm{H_2}} = -\,r_{\mathrm{reac}\blacktriangle\mathrm{elchem}\blacktriangle\mathrm{Mol}\blacktriangle\mathrm{TPB}\blacktriangle 1} \cdot A_{\mathrm{eff}\blacktriangle\mathrm{vol}\blacktriangle\mathrm{ANO}} \cdot Ъ\,, \tag{5.39}$$

$$\gamma_{\mathrm{Mol}\blacktriangle\mathrm{vol}\blacktriangle\mathrm{H_2O}} = r_{\mathrm{reac}\blacktriangle\mathrm{elchem}\blacktriangle\mathrm{Mol}\blacktriangle\mathrm{TPB}\blacktriangle 1} \cdot A_{\mathrm{eff}\blacktriangle\mathrm{vol}\blacktriangle\mathrm{ANO}} \cdot Ъ\,, \tag{5.40}$$

$$\gamma_{\mathrm{Mol}\blacktriangle\mathrm{vol}\blacktriangle\mathrm{LSCF}} = -\,2r_{\mathrm{reac}\blacktriangle\mathrm{elchem}\blacktriangle\mathrm{Mol}\blacktriangle\mathrm{surf}\blacktriangle 3} \cdot A_{\mathrm{eff}\blacktriangle\mathrm{vol}\blacktriangle\mathrm{CAT}}\,, \tag{5.41}$$

$$\gamma_{\mathrm{Mol}\blacktriangle\mathrm{vol}\blacktriangle\mathrm{O_2}} = -\,r_{\mathrm{reac}\blacktriangle\mathrm{elchem}\blacktriangle\mathrm{Mol}\blacktriangle\mathrm{surf}\blacktriangle 3} \cdot A_{\mathrm{eff}\blacktriangle\mathrm{vol}\blacktriangle\mathrm{CAT}}\,, \tag{5.42}$$

$$\begin{aligned}\gamma_{\mathrm{Mol}\blacktriangle\mathrm{vol}\blacktriangle\mathrm{O^{2-}}} = {} & \left(-r_{\mathrm{reac}\blacktriangle\mathrm{elchem}\blacktriangle\mathrm{Mol}\blacktriangle\mathrm{TPB}\blacktriangle 1} - r_{\mathrm{reac}\blacktriangle\mathrm{elchem}\blacktriangle\mathrm{Mol}\blacktriangle\mathrm{TPB}\blacktriangle 2}\right) \cdot A_{\mathrm{eff}\blacktriangle\mathrm{vol}\blacktriangle\mathrm{ANO}} \cdot Ъ \\ & + 2r_{\mathrm{reac}\blacktriangle\mathrm{elchem}\blacktriangle\mathrm{Mol}\blacktriangle\mathrm{surf}\blacktriangle 3} \cdot A_{\mathrm{eff}\blacktriangle\mathrm{vol}\blacktriangle\mathrm{CAT}}\,,\end{aligned} \tag{5.43}$$

$$\gamma_{\mathrm{Mol\,vol\,YSZ}} = \left(r_{\mathrm{reac\,elchem\,Mol\,TPB}\,1} + r_{\mathrm{reac\,elchem\,Mol\,surf}\,2}\right) \cdot A_{\mathrm{eff\,vol\,ANO}} \cdot \text{Ъ} \,. \quad (5.44)$$

Using Faraday's law (see equation 2.22 in section 2.3.1.1) the source terms for the electric and ionic potentials[46], both in A/m^3, are given by[47]:

$$\begin{aligned}
\gamma_{\mathrm{Ch\,vol\,el}} &= 2F_{\mathrm{Ch\,mol}} \cdot \left(-r_{\mathrm{reac\,elchem\,Mol\,TPB}\,1} - r_{\mathrm{reac\,elchem\,Mol\,TPB}\,2}\right) \cdot A_{\mathrm{eff\,vol\,ANO}} \cdot \text{Ъ} \\
&\quad + 2r_{\mathrm{reac\,elchem\,Mol\,surf}\,3} \cdot A_{\mathrm{eff\,vol\,CAT}} \,, \\
\gamma_{\mathrm{Ch\,vol\,ion}} &= 2F_{\mathrm{Ch\,mol}} \cdot \left(r_{\mathrm{reac\,elchem\,Mol\,TPB}\,1} + r_{\mathrm{reac\,elchem\,Mol\,TPB}\,2}\right) \cdot A_{\mathrm{eff\,vol\,ANO}} \cdot \text{Ъ} \\
&\quad - 2r_{\mathrm{reac\,elchem\,Mol\,surf}\,3} \cdot A_{\mathrm{eff\,vol\,CAT}} \,.
\end{aligned}$$

Finally, a source term for the thermal energy in W/m^3 exists[48]:

$$\begin{aligned}
\gamma_{\mathrm{En\,vol}} = \Big\{ & r_{\mathrm{reac\,elchem\,Mol\,TPB}\,1} \cdot \left(\mathrm{d}H_{\mathrm{En\,mol,elchem}\,1} - 2F_{\mathrm{Ch\,mol}}\,(\phi_{\mathrm{ion}} - \phi_{\mathrm{el}})\right) \\
+ \; & r_{\mathrm{reac\,elchem\,Mol\,TPB}\,2} \cdot \left(\mathrm{d}H_{\mathrm{En\,mol,elchem}\,2} - 2F_{\mathrm{Ch\,mol}}\,(\phi_{\mathrm{ion}} - \phi_{\mathrm{el}})\right)\Big\} \cdot A_{\mathrm{eff\,vol\,ANO}} \cdot \text{Ъ} \\
+ \; & r_{\mathrm{reac\,elchem\,Mol\,surf}\,3} \cdot \left(\mathrm{d}H_{\mathrm{En\,mol,elchem}\,3} - 2F_{\mathrm{Ch\,mol}}\,(\phi_{\mathrm{el}} - \phi_{\mathrm{ion}})\right) \cdot A_{\mathrm{eff\,vol\,CAT}} \,.
\end{aligned} \quad (5.45)$$

The reaction rates itself are modeled using the Arrhenius approach from equation 4.22[49]:

$$\begin{aligned}
r_{\mathrm{reac\,elchem\,Mol\,TPB}\,1} = {} & \Re_{\mathrm{reac,elchem\,forw}\,1} \cdot c_{\mathrm{Mol\,vol\,H_2}} \cdot c_{\mathrm{Mol\,vol\,O^{2-}}} \cdot c^{2}_{\mathrm{Mol\,vol\,Ni}} \cdot \exp\left(-\frac{\mathrm{d}\mathfrak{G}_{\mathrm{En,elchem\,mol,act}\,1}}{\Re_{\mathrm{En\,mol}}\,T}\right) \\
& - \Re_{\mathrm{reac,elchem\,back}\,1} \cdot c_{\mathrm{Mol\,vol\,H_2O}} \cdot c_{\mathrm{Mol\,vol\,YSZ}} \cdot c^{2}_{\mathrm{Mol\,vol\,Ni}} \\
& \cdot \exp\left(-\frac{\mathrm{d}\mathfrak{G}_{\mathrm{En,elchem\,mol,act}\,1} - \mathrm{d}G_{\mathrm{En\,mol,reac,elchem}\,1} + 2F_{\mathrm{Ch\,mol}}\,(\phi_{\mathrm{ion}} - \phi_{\mathrm{el}})}{\Re_{\mathrm{En\,mol}}\,T}\right) \;\mathrm{in}\;\frac{\mathrm{mol}}{\mathrm{m\,s}} \,, \quad (5.46) \\
r_{\mathrm{reac\,elchem\,Mol\,TPB}\,2} = {} & \Re_{\mathrm{reac,elchem\,forw}\,2} \cdot c_{\mathrm{Mol\,vol\,CO}} \cdot c_{\mathrm{Mol\,vol\,O^{2-}}} \cdot c^{2}_{\mathrm{Mol\,vol\,Ni}} \cdot \exp\left(-\frac{\mathrm{d}\mathfrak{G}_{\mathrm{En,elchem\,mol,act}\,2}}{\Re_{\mathrm{En\,mol}}\,T}\right) \\
& - \Re_{\mathrm{reac,elchem\,back}\,2} \cdot c_{\mathrm{Mol\,vol\,CO_2}} \cdot c_{\mathrm{Mol\,vol\,YSZ}} \cdot c^{2}_{\mathrm{Mol\,vol\,Ni}} \\
& \cdot \exp\left(-\frac{\mathrm{d}\mathfrak{G}_{\mathrm{En,elchem\,mol,act}\,2} - \mathrm{d}G_{\mathrm{En\,mol,reac,elchem}\,2} + 2F_{\mathrm{Ch\,mol}}\,(\phi_{\mathrm{ion}} - \phi_{\mathrm{el}})}{\Re_{\mathrm{En\,mol}}\,T}\right) \;\mathrm{in}\;\frac{\mathrm{mol}}{\mathrm{m\,s}} \,, \quad (5.47)
\end{aligned}$$

[46] charges

[47] All potentials are referenced to the charge of an electron. Therefore, even for the ionic potential, z usually equals two.

[48] In principle, there are separate source terms for the thermal energy of the fluid and the solid phase. In this thesis, all sources are assumed to act on the fluid phase. The main reasons for this are on the one hand the lack of data on the distribution of the source terms among the phases and on the other hand the strong coupling of both sources. The latter results in numerical instabilities and prevent the convergence of the CFD models when assigning the source term to the solid.

[49] Since either electrons are released or consumed, the signs of the potential differences are opposite for the anode and the cathode.

$$r_{\text{reac}\blacktriangle\text{elchem}\blacktriangle\text{Mol}\blacktriangle\text{surf}\blacktriangle 3} = \Re_{\text{reac,elchem}\blacktriangle\text{forw}\blacktriangle 3} \cdot c_{\text{Mol}\blacktriangle\text{vol}\blacktriangle\text{O}_2} \cdot c^{2}_{\text{Mol}\blacktriangle\text{vol}\blacktriangle\text{LSCF}} \cdot \exp\left(-\frac{\mathrm{d}\mathfrak{G}_{\text{En,elchem}\blacktriangle\text{mol,act}\blacktriangle 3}}{\Re_{\text{En}\blacktriangle\text{mol}} T}\right)$$
$$- \Re_{\text{reac,elchem}\blacktriangle\text{back}\blacktriangle 3} \cdot c^{2}_{\text{Mol}\blacktriangle\text{vol}\blacktriangle\text{O}^{2-}}$$
$$\cdot \exp\left(-\frac{\mathrm{d}\mathfrak{G}_{\text{En,elchem}\blacktriangle\text{mol,act}\blacktriangle 3} - \mathrm{d}G_{\text{En}\blacktriangle\text{mol,reac,elchem}\blacktriangle 3} + 2F_{\text{Ch}\blacktriangle\text{mol}}(\phi_{\text{el}} - \phi_{\text{ion}})}{\Re_{\text{En}\blacktriangle\text{mol}} T}\right) \text{ in } \frac{\text{mol}}{\text{m}^2\,\text{s}} \,. \tag{5.48}$$

The required activation energies $\mathrm{d}\mathfrak{G}_{\text{En,elchem}\blacktriangle\text{mol,act}\blacktriangle i}$ are taken from the literature (see Table 5.6) and the reaction enthalpies $\mathrm{d}G_{\text{En}\blacktriangle\text{mol,reac,elchem}\blacktriangle i}$ are calculated using the first law of thermodynamcs (see equation 2.10 in section 2.2) as well as the NASA polynomials summarized in appendix C.

Table 5.6.: **Activation energies of the electrochemical reactions:** The tabled values are derived from e.g. molecular dynamics simulations or detailed electrochemistry models.

Quantity	Value in kJ/mol	Reference/Note
$\mathrm{d}\mathfrak{G}_{\text{En,elchem}\blacktriangle\text{mol,act}\blacktriangle 1}$	2.0	assumed
$\mathrm{d}\mathfrak{G}_{\text{En,elchem}\blacktriangle\text{mol,act}\blacktriangle 2}$	2.0	assumed
$\mathrm{d}\mathfrak{G}_{\text{En,elchem}\blacktriangle\text{mol,act}\blacktriangle 3}$	241.3	(Xu and Thomson 1999)

Since literature values for the oxygen ions are again rare, it is assumed that the ions molar Gibbs free energies are those of gaseous oxygen. In consequence, energy is only released in their electrochemical consumption at the anode. Finally, the pre-exponential coefficients $\Re_{\text{reac,elchem}\blacktriangle\text{forw}\blacktriangle i}$ and $\Re_{\text{reac,elchem}\blacktriangle\text{back}\blacktriangle i}$ are unknown too. Because of the originality of the current approach, these values are not readily available in the literature. Therefore, a discrimination of some of the coefficients is necessary in order to reduce the total number of free parameters in the system. The only known point is the current less case. Here the reaction rates are zero and thus both sides of equations 5.46 - 5.48 vanish. From section 2.3 it follows that in this situation[50] Nernst potential U_{Nernst} is apparent. With this, equations 5.46 - 5.48 can be rearranged to:

$$r_{\text{reac}\blacktriangle\text{elchem}\blacktriangle\text{Mol}\blacktriangle\text{TPB}\blacktriangle 1} = \Re_{\text{reac,elchem}\blacktriangle\text{forw}\blacktriangle 1} \cdot c_{\text{Mol}\blacktriangle\text{vol}\blacktriangle\text{H}_2} \cdot c_{\text{Mol}\blacktriangle\text{vol}\blacktriangle\text{O}^{2-}} \cdot c^{2}_{\text{Mol}\blacktriangle\text{vol}\blacktriangle\text{Ni}} \cdot \exp\left(-\frac{\mathrm{d}\mathfrak{G}_{\text{En,elchem}\blacktriangle\text{mol,act}\blacktriangle 1}}{\Re_{\text{En}\blacktriangle\text{mol}} T}\right)$$

[50] under steady-state conditions

$$\cdot \left\{ 1 - \exp\left(\frac{2F_{\mathrm{Ch}_\blacktriangle \mathrm{mol}} \cdot a_{1\blacktriangle \mathrm{elchem}\blacktriangle \mathrm{TPB}\blacktriangle 1} \cdot \left(-U_{\mathrm{Nernst,H}_{2\blacktriangle}\mathrm{ANO}} + a_{2\blacktriangle \mathrm{elchem}\blacktriangle \mathrm{TPB}\blacktriangle 1} \cdot (\phi_{\mathrm{ion}} - \phi_{\mathrm{el}}) \right)}{\Re_{\mathrm{En}_\blacktriangle \mathrm{mol}} T} \right) \right\}, \tag{5.49}$$

$$r_{\mathrm{reac}\blacktriangle \mathrm{elchem}\blacktriangle \mathrm{Mol}\blacktriangle \mathrm{TPB}\blacktriangle 2} = \Re_{\mathrm{reac,elchem}\blacktriangle \mathrm{forw}\blacktriangle 2} \cdot c_{\mathrm{Mol}\blacktriangle \mathrm{vol}_\blacktriangle \mathrm{CO}} \cdot c_{\mathrm{Mol}\blacktriangle \mathrm{vol}_\blacktriangle \mathrm{O}^{2-}} \cdot c^{2}_{\mathrm{Mol}\blacktriangle \mathrm{vol}_\blacktriangle \mathrm{Ni}} \cdot \exp\left(-\frac{\mathrm{d}\Im_{\mathrm{En,elchem}\blacktriangle \mathrm{mol},\mathrm{act}\blacktriangle 2}}{\Re_{\mathrm{En}_\blacktriangle \mathrm{mol}} T} \right)$$
$$\cdot \left\{ 1 - \exp\left(\frac{2F_{\mathrm{Ch}_\blacktriangle \mathrm{mol}} \cdot a_{1\blacktriangle \mathrm{elchem}\blacktriangle \mathrm{TPB}\blacktriangle 2} \cdot (-U_{\mathrm{Nernst,CO}_\blacktriangle \mathrm{ANO}} + a_{2\blacktriangle \mathrm{elchem}\blacktriangle \mathrm{TPB}\blacktriangle 2} \cdot (\phi_{\mathrm{ion}} - \phi_{\mathrm{el}}))}{\Re_{\mathrm{En}_\blacktriangle \mathrm{mol}} T} \right) \right\}, \tag{5.50}$$

$$r_{\mathrm{reac}\blacktriangle \mathrm{elchem}\blacktriangle \mathrm{Mol}\blacktriangle \mathrm{surf}\blacktriangle 3} = \Re_{\mathrm{reac,elchem}\blacktriangle \mathrm{forw}\blacktriangle 3} \cdot c_{\mathrm{Mol}\blacktriangle \mathrm{vol}_\blacktriangle \mathrm{O}_2} \cdot c^{2}_{\mathrm{Mol}\blacktriangle \mathrm{vol}_\blacktriangle \mathrm{LSCF}} \cdot \exp\left(-\frac{\mathrm{d}\Im_{\mathrm{En,elchem}\blacktriangle \mathrm{mol},\mathrm{act}\blacktriangle 3}}{\Re_{\mathrm{En}_\blacktriangle \mathrm{mol}} T} \right)$$
$$\cdot \left\{ 1 - \exp\left(\frac{2F_{\mathrm{Ch}_\blacktriangle \mathrm{mol}} \cdot a_{1\blacktriangle \mathrm{elchem}\blacktriangle \mathrm{surf}\blacktriangle 3} \cdot \left(-U_{\mathrm{Nernst,O}_{2\blacktriangle}\mathrm{CAT}} + a_{2\blacktriangle \mathrm{elchem}\blacktriangle \mathrm{surf}\blacktriangle 3} \cdot (\phi_{\mathrm{el}} - \phi_{\mathrm{ion}}) \right)}{\Re_{\mathrm{En}_\blacktriangle \mathrm{mol}} T} \right) \right\}. \tag{5.51}$$

Finally, the forward reaction rates $\Re_{\mathrm{reac,elchem}\blacktriangle \mathrm{forw}\blacktriangle i}$ and the dimensionless temperature dependent fitting coefficients $a_{i\blacktriangle \mathrm{elchem}\blacktriangle \mathrm{TPB/surf}\blacktriangle j}$[51] have to be evaluated by correlating calculated $\vec{j}$-U-curves with measured ones.

In order to determine the unknown model parameters for all variables BCs are necessary. Appropriate expressions for the gaseous species and the temperature are discussed elsewhere; thus here the focus lies on ϕ_{el}, ϕ_{ion}, and $c_{\mathrm{Mol}\blacktriangle \mathrm{vol}_\blacktriangle \mathrm{O}^{2-}}$. ϕ_{el} and $\vec{j}_{\mathrm{tot}}$ are correlated via the $\vec{j}$-U curve. Therefore, one of them has to be given while the other can be calculated. Since $\vec{j}_{\mathrm{tot}}$ is the sum of $\vec{j}_{\mathrm{el}}$ and $\vec{j}_{\mathrm{ion}}$ and directly associated to the volumetric sources inside the electrodes, its precise determination as BC is difficult. In consequence, the values of both ϕ_{el} as well as ϕ_{ion} are fixed at least at one of the electric contacts, respectively one of the interfaces of the electrodes with the IC. While $\phi_{\mathrm{el}_\blacktriangle \mathrm{CAT}}$ - $\phi_{\mathrm{el}_\blacktriangle \mathrm{ANO}}$ equals the cell potential, the ionic potentials are not directly measurable. It is only known that there is no ionic flux over the electrode-IC interfaces. Therefore, on the anode side $\vec{j}_{\mathrm{ion}_\blacktriangle \mathrm{ANO/IC}} = 0\ \mathrm{A/m^2}$ is assumed. Since FVM is not working with only von Neumann BCs[52] at least one fixed value is required, leading to a "mixed BC" (Patankar 1980, p. 51) with $\phi_{\mathrm{ion}_\blacktriangle \mathrm{CAT/IC}} = \phi_{\mathrm{el}_\blacktriangle \mathrm{CAT/IC}}$ and a transfer coefficient of $\alpha_{\mathrm{ion}} = 1000\ \mathrm{S/m}$ to obtain (almost) zero flux (using equation 4.14). For the oxygen ions the situation is very similar, but in contradiction to ϕ_{ion} the zero flux BC is applied to the cathode side. Since ions are consumed by the electrochemical reactions on the anode side, the smallest values of $c_{\mathrm{Mol}\blacktriangle \mathrm{vol}_\blacktriangle \mathrm{O}^{2-}}$ are expected at the interfaces of anode and

[51] which equal unity for a strict physical model

[52] the solution matrix becomes singular for this case

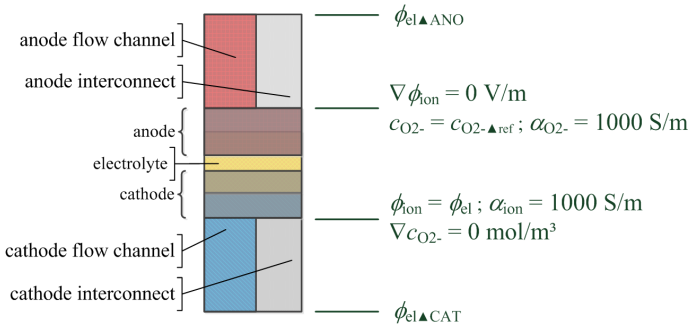

Figure 5.25.: **Boundary conditions for ϕ_{el}, ϕ_{ion}, and $c_{Mol\blacktriangle vol_{\blacktriangle}O^{2-}}$:** While $\Delta\phi_{el}$ is given by the cell voltage with an arbitrary flux through the cells external contacts, the BCs for ϕ_{ion} and $c_{Mol\blacktriangle vol_{\blacktriangle}O^{2-}}$ are determined at the interfaces of the electrodes and the ICs. Both of the latter show one von Neumann and one mixed BC.

IC. Here a "base value" for $c_{Mol\blacktriangle vol_{\blacktriangle}O^{2-}}$[53] and again a large transfer coefficient of $\alpha_{O^{2-}{}_{\blacktriangle}ANO/IC} = 1000$ S/m are assumed. The BCs for ϕ_{el}, ϕ_{ion}, and $c_{Mol\blacktriangle vol_{\blacktriangle}O^{2-}}$ are illustrated in Figure 5.25.

To adjust the model with experimental data from the literature (Tietz, Buchkremer, and Stöver 2006), a simplified 1D model of the PEN-region is developed in MATLAB[54]. During calculation the mutual couplings via:

- the number of oxygen ions[55] acting on the electrochemical reactions and the ionic conductivity as well as on the number of available YSZ and LSCF sites, and
- the electric and ionic potentials, whose difference has an exponential influence on the reaction rates as well as
- the very different values for the ionic diffusivity[56] as well as the elec-

[53] e.g. $c_{Mol\blacktriangle vol_{\blacktriangle}O^{2-}{}_{\blacktriangle}ANO/IC} = 0$ mol/m³

[54] Energy transport, convective flow through the gas-channels, and reformation as well as radiation are neglected. Also always only one type of electrochemically active species (here H_2) is apparent.

[55] very large on the cathode side while close to zero/a base value on the anode side

[56] $D_{diff\blacktriangle O^{2-}{}_{\blacktriangle}YSZ} \approx 1 \cdot 10^{-10}$ m²/s at 1000 K

tric[57] and ionic[58] conductivities, resulting in very different “reactions” on source terms of the same magnitude,

make convergent and stable solutions a very challenging task. Therefore, it is necessary that on the one hand the fitting coefficients $a_{i\_\mathrm{elchem\_TPB/surf}\_j}$ in equations 5.49 - 5.51 differ from unity and on the other hand the eventually reached steady-state between anode and cathode is “assisted” during solution.

A good starting point for this is equation 5.43, since it reveals a coupling between the anode and cathode side. Under steady-state conditions, it follows:

$$\Upsilon_{\mathrm{Mol\_vol\_O^{2-}}} = 0 = \left(-r_{\mathrm{reac\_elchem\_Mol\_TPB\_1}} - r_{\mathrm{reac\_elchem\_Mol\_TPB\_2}}\right) \cdot A_{\mathrm{eff\_vol\_ANO}} \cdot \text{Ъ} + 2r_{\mathrm{reac\_elchem\_Mol\_surf\_3}} \cdot A_{\mathrm{eff\_vol\_CAT}},$$

what can be rearranged to give an expression for the effective electrochemically active surface at the cathode:

$$A_{\mathrm{eff\_vol\_CAT}} = -\text{Ъ} A_{\mathrm{eff\_vol\_ANO}} \cdot \frac{r_{\mathrm{reac\_elchem\_Mol\_TPB\_1}} + r_{\mathrm{reac\_elchem\_Mol\_TPB\_2}}}{2r_{\mathrm{reac\_elchem\_Mol\_surf\_3}}}. \qquad (5.52)$$

Equation 5.52 couples $r_{\mathrm{reac\_elchem\_Mol\_TPB\_1}}$ and $r_{\mathrm{reac\_elchem\_Mol\_TPB\_2}}$ with $r_{\mathrm{reac\_elchem\_Mol\_surf\_3}}$ via the oxygen ions. Their number limits the active surface of the cathode. It can be increased by either raising the reaction rates at the anode or its effective surface and TPB length. With this, and an assumed reference value of $c_{\mathrm{Mol\_vol\,O^{2-}\_ANO/IC}} = 4{,}000\ \mathrm{mol/m^3}$, a high correlation (see Figure 5.26) to experimental $\vec{j}$-U-curves from Tietz, Buchkremer, and Stöver (Tietz, Buchkremer, and Stöver 2006) can be attained for the values listed in Table 5.7[59].

[57] $\underline{\sigma}_{\mathrm{el\_Ni}} \approx 2 \cdot 10^6$ S/m at 1000 K

[58] $\underline{\sigma}_{\mathrm{ion\_YSZ}} \approx 2$ S/m at 1000 K

[59] The values are measured for a 0.97/0.03 $\mathrm{mol_{species}/mol_{tot}}$ H_2/H_2O gas mixture (only H_2 electrochemistry) at the anode side and air at the cathode side; for numerical stability $\underline{\sigma}_{\mathrm{ion}}$ has to be enhanced by a factor of 50.

Table 5.7.: **Model parameters of the detailed electrochemistry model:** The tabled values are adjusted in such a way that the model fits to the experimental data obtained by Tietz, Buchkremer, and Stöver (Tietz, Buchkremer, and Stöver 2006).

Quantity	Value	Dimension
$\Re_{\text{reac,elchem}\blacktriangle\text{forw}\blacktriangle 1}$	$4.592 \cdot 10^{-11}$	$\frac{\text{mol}}{\text{m s}}$
$a_{1\blacktriangle\text{elchem}\blacktriangle\text{TPB}\blacktriangle 1}$	$2.7 \cdot 10^{-4}$ [1/K] $\cdot T - 2.48 \cdot 10^{-1}$	
$\Re_{\text{reac,elchem}\blacktriangle\text{forw}\blacktriangle 3}$	$15.06 \cdot 10^{-3}$	$\frac{\text{mol}}{\text{m}^2\text{s}}$
$a_{3\blacktriangle\text{elchem}\blacktriangle\text{surf}\blacktriangle 1}$	1	
$a_{3\blacktriangle\text{elchem}\blacktriangle\text{surf}\blacktriangle 2}$	1	

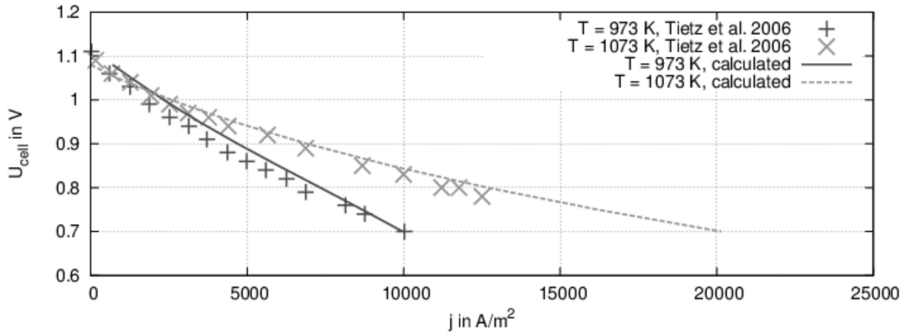

Figure 5.26.: **Experimental vs. simulated $\vec{j}$-U-curves:** The experimental curves are measured by Tietz, Buchkremer, and Stöver (Tietz, Buchkremer, and Stöver 2006) at a Ni-YSZ/YSZ/LSCF system. The models geometry and operating conditions are adjusted to meet the experiments. For both temperatures a high correlation between experiment and simulation is obvious.

The gas concentration profiles at $T = 1073$ K, $U_{\text{cell}} = 0.75$ V, and $\vec{j} = 16{,}180$ A/m^2 are illustrated in Figure 5.27.

Since it is clear that the $\vec{j}$-U curve comes to its end as soon as one of the species reaches its mass transport limit[60]. In accordance to equation 5.4, a higher porosity $Po_{\%}$ and lower tortuosity τ, and thus manufacturing aspects would help to push this limit to higher current densities. The concentration of the oxygen ions is shown in Figure 5.28. An exponential decay from the cathode to the anode side dominates the profile.

[60] zero concentration at the electrolyte interface

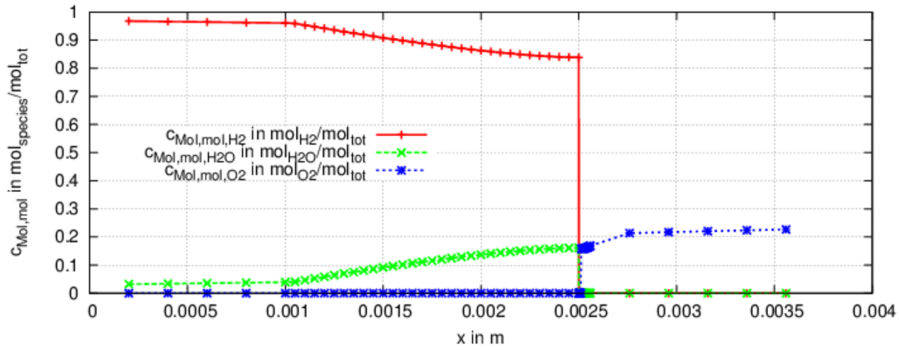

Figure 5.27.: **Species concentration profiles:** The concentration profiles are calculated at T = 1073 K, U_{cell} = 0.75 V, and $\vec{j}$ = 1.618·10^4 A/m^2. The markers indicate the values at the centroids of the CVs. While almost no change can be seen in the gas channels (anode: 0 m < χ < 1 · 10^{-3} m, cathode: 2.75 · 10^{-3} m < χ < 3.8 · 10^{-3} m), power law changes are apparent inside the electrodes (anode: 1 · 10^{-3} m < χ < 2.5 · 10^{-3} m, cathode: 2.501 · 10^{-3} m < χ < 2.75 · 10^{-3} m).

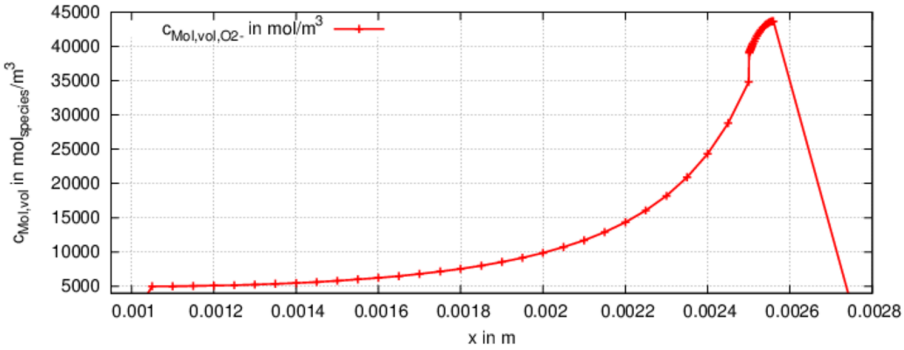

Figure 5.28.: **1D oxygen ion concentration profile:** The profile is calculated at T = 1073 K, U_{cell} = 0.7 V, and $\vec{j}$ = 2.014·10^4 A/m^2. The markers indicate the values at the centroids of the CVs. Clearly visible is an exponential decay from the cathode to the base value at the anode. Since no sources are apparent in the electrolyte, the concentration shows a linear decay in this region. In the gas channels the ion concentration is zero.

Next to the numerical issues arising from a value close to zero, respectively the base value at the anode, two other aspects are of special interest. On the one hand the absolute values are much smaller than the assumed maximal ones, and on the other hand for the entire anode almost identical to the base value.

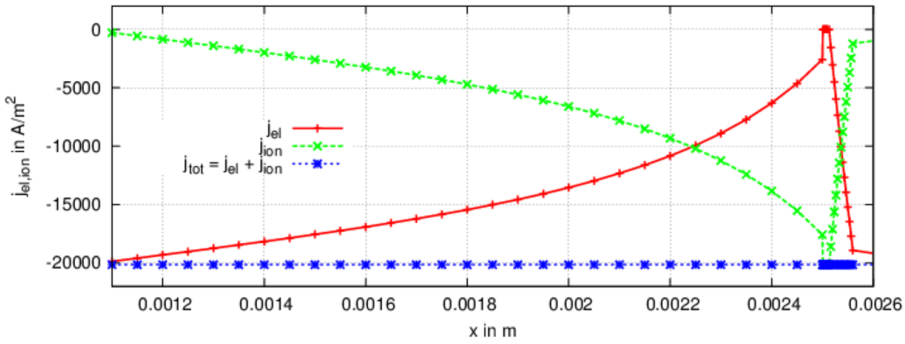

Figure 5.29.: **Electric and ionic current densities in the 1D model:** Along the PEN structure a transition between electric (red) and ionic (green) charge transport occurs, due to the electric and ionic conductivities of the different domains and the existence of electrochemical reactions. Along the entire PEN structure the total current density $\vec{j}_{tot}$ (blue) is constant. Illustrated are the values at the left boundaries of the CVs at $T = 1073\,\mathrm{K}$ and $U_{cell} = 0.7\,\mathrm{V}$.

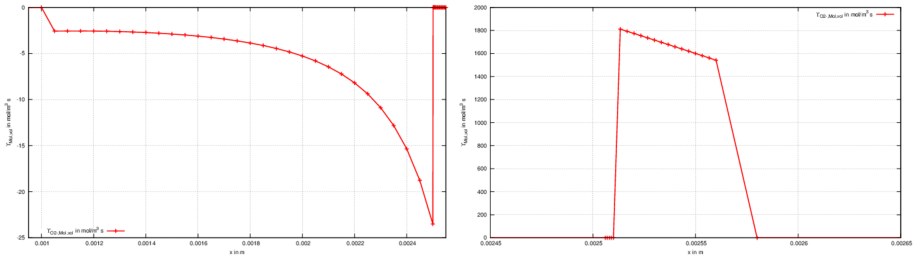

Figure 5.30.: **Electrochemical reaction rates in the 1D model:** While the cathode (right) shows an almost uniform performance, an exponential decay of the source term is apparent at the anode side (left). Here the rates are shown for O^{2-} at $T = 1073\,\mathrm{K}$, $U_{cell} = 0.7\,\mathrm{V}$, and $\vec{j} = 2.014{\cdot}10^4\,\mathrm{A/m^2}$. The markers indicate the values at the centroids of the CVs.

This means that at the cathode a shift of the equilibrium between oxygen ions and oxygen in the gas-phase towards the ion side would be possible, if

the absorption reaction is energetically facilitated. Additionally, the main part of the anode shows only a rather small electrochemical activity. The reason for this is the lack in oxygen ions, coming from an insufficient ion mobility, respectively too thick PEN layers. While the cathode shows only a slight increase in reaction rate towards the electrolyte, its pendant at the anode side shares the exponential/power law decay with the oxygen ions (see Figure 5.30). This behavior is clear since the number of the latter has a direct influence on the anode's electrochemistry. It is noteworthy to mention that the entire anode structure reveals electrochemical activity, what is a direct consequence of the base value assumption for the oxygen ions at the anode surface. If the latter is assumed to be close to zero, the electrochemical activity is limited to a small region close to the electrolyte, impeding the need for a detailed local investigation throughout the entire anode. This aspect is addressed again when the simplified 3D model is introduced below. The same trend is also illustrated in Figure 5.31 for the electric and ionic potentials. While the former shows only the expected slight in- and decrease close to the electrolyte, the latter grows logarithmic along the electrodes from the cathode to the anode. Both behaviors can be explained with the very different conductivities and the time required for a homogenization along the entire PEN structure.

In Figure 5.29 the transition between electric and ionic charge transport is illustrated. Since oxygen ions and thus ionic potential is not transferred over the boundaries to the gas channels, the ionic current density has to be zero at these interfaces. The transport of ions occurs from the cathode to the anode (in the model high values of χ to low ones), what requires the same sign of $\vec{j}_{\mathrm{ion}}$ for all domains. In the electrolyte, charge transport occurs almost only via ions, what means that $\vec{j}_{\mathrm{ion}}$ is maximal in this region. For the electric current density the situation is completely different, while $\vec{j}_{\mathrm{el}}$ is maximal at the electrode surfaces, where the current collectors are assumed; it is minimal in the electrolyte, where it even changes its direction. The latter is theoretically expected (O'Hayre et al. 2009, p. 83 et seqq.) and a consequence of the fact that negatively charged particles always travel in the direction of increasing potential. The total current density $\vec{j}_{\mathrm{tot}}$, which is the sum of $\vec{j}_{\mathrm{el}}$ and $\vec{j}_{\mathrm{ion}}$, is constant along the entire PEN structure. It expresses the total number of charges transferred per second and square meter which has to be constant under steady-state conditions.

Altogether, the novel approach works well in getting detailed information on the PEN region. In agreement with the theoretical study of Andersson, Yuan,

and Sundén (Andersson, Yuan, and Sundén 2012), it underlines the need for alternative electrolyte materials with higher ionic conductivity, which would help to extend the electrochemical reactions deep into the anode structure. As a consequence of YSZ's very limited ionic conductivity, the design of the anode can be focused on electric conductivity and gas permeability[61]. In particular the latter is very important to guarantee a sufficient supply with reactants at the reaction zones close to the electrolyte. Since the main part of the electrochemistry occurs in a direct neighborhood of the electrolyte, in a simplified model the latter can be subsequently reduced to an electrochemically Active Boundary (electrochemically active region around the electrolyte, represented by a boundary plane) (AB), separating anode and cathode.

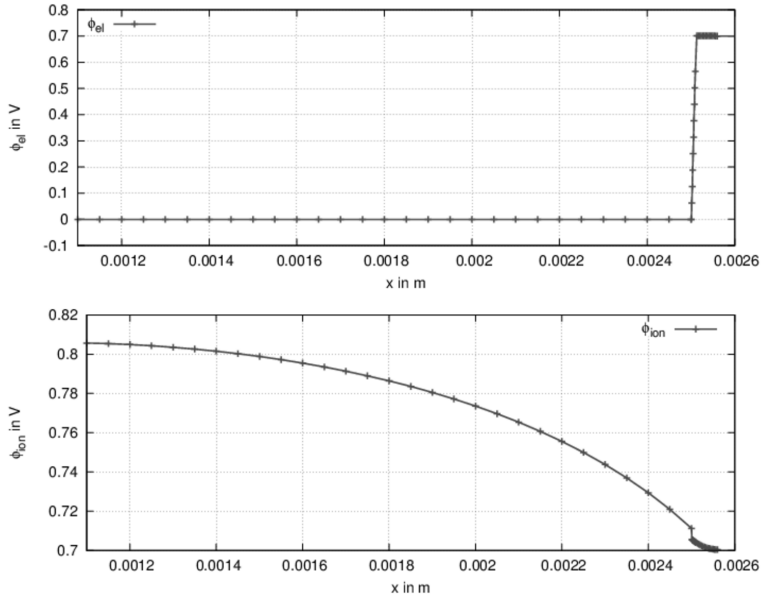

Figure 5.31.: **Electric and ionic potentials in the 1D model:** While the electric potential (top) is slightly lowered below GND close to the anode/electrolyte interface, an increase above cell potential next to the cathode/electrolyte interface occurs. In contradiction, the ionic potential (bottom) grows logarithmic from the cathode to the anode (electrolyte: $2.50 \cdot 10^{-3}\,\mathrm{m} < \chi < 2.501 \cdot 10^{-3}\,\mathrm{m}$). The displayed values are calculated for $T = 1073\,\mathrm{K}$, $U_{\mathrm{cell}} = 0.7\,\mathrm{V}$, and $\vec{j} = 2.014 \cdot 10^4\ \mathrm{A/m^2}$. The markers indicate the values at the centroids of the CVs.

[61] despite of a very thin layer close to the electrolyte

5.2.6.2. A simplified 3D model for simple geometries

To reduce the complexity of the final 3D CFD model, the electrolyte shrinks to an electrochemically active wall, separating the active parts of anode and cathode (see Figure 5.32). Under the following assumptions this leads to a significant decrease in computation time:

- Due to the little ionic diffusivity in YSZ, electrochemical reactions only take place in a direct neighborhood of the electrolyte. In this region, the reactant and product concentrations equal their respective values at the surfaces, and the reactions occur only at the boundaries separating the different domains.
- Oxygen ions pass the active region perpendicular to the electrolyte surface. In plane currents of ions are negligible. At any time there is a steady-state situation between the number of oxygen ions at the anode side and the oxygen concentration in the cathode gas.
- Outside the electrochemically active region charge is only transferred by electric current.
- Ohmic losses are homogeneously distributed over the electrolyte and can be equally assigned to anode and cathode.

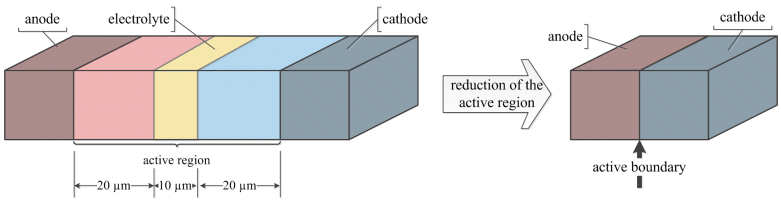

Figure 5.32.: **Reduction of the electrochemically active region:** The region around the electrolyte is reduced to an Active Boundary (electrochemically active region around the electrolyte, represented by a boundary plane) (AB) separating the anode and cathode domain in order to simplify the model.

With these assumptions and the results of the novel approach to Solid Oxide Fuel Cell (SOFC) electrochemistry from the previous subsection, the electrolyte and the first few micrometers in both electrodes shrink to a wall with reactive surfaces (Active Boundary (electrochemically active region around the

electrolyte, represented by a boundary plane) (AB)), separating the anode and cathode chambers. At the surfaces the reactions 5.34 - 5.36 take place, whereby the coupling between species conversion and electronics is again achieved by Faraday's law (see equation 2.21). In contrast to the detailed approach, the reactions are not assumed to be the sources of electric/ionic charges. They are rather seen as the consequence of an electric current density $\vec{j}_{\mathrm{el}}$ in A/m^2 which itself has its origin in the cell's internal distribution of the electric potential ϕ_{el} in V.

In accordance to subsection 2.3.1, the cell voltage U_{cell} is given by the difference of the Nernst potential and the internal losses due to the overpotentials η (equations 2.27, 2.29, and 2.31). In equation 2.27 the latter bridges the gap to $\vec{j}_{\mathrm{el}}$ by the BVE and requires an iterative solution of the system. The electric variables and their BCs are illustrated in Figure 5.33.

Theoretically, this approach has an extensive need for "global information", since in equation 2.29 η_{Ohm} requires an equivalent circuit model of the cell and U_{Nernst} is determined by using "reference values" for the concentrations somewhere in the gas channel. The need for these information can be reduced by a local calculation of U_{Nernst} at the electrolyte surface[62]. With this, the electrical problem is characterized by the BVE in equation 2.27 and[63]:

$$\begin{aligned}\eta_{\mathrm{act}} &= U_{\mathrm{Nernst}} - U_{\mathrm{cell}} - \eta_{\mathrm{Ohm}}\,, \\ &= U_{\mathrm{Nernst}_{\blacktriangle}\mathrm{local}} - \left(\phi_{\mathrm{el}_{\blacktriangle}\mathrm{CAT}} - \phi_{\mathrm{el}_{\blacktriangle}\mathrm{ANO}}\right) - \eta_{\mathrm{Ohm}_{\blacktriangle}\mathrm{ANO/ELE/CAT}}\,.\end{aligned}$$

The last term in this equation expresses the fact that the ohmic losses in fuel cells are governed by the losses in the ion conductor (Mücke 2009b). It can be expressed as:

$$\eta_{\mathrm{Ohm}_{\blacktriangle}\mathrm{ANO/ELE/CAT}} = j_{\mathrm{ion}} \cdot \left(\frac{L_{\chi_{\blacktriangle}\mathrm{ANO}}}{\underline{\underline{\sigma}}_{\mathrm{ion}_{\blacktriangle}\mathrm{ANO}}} + \frac{L_{\chi_{\blacktriangle}\mathrm{ELE}}}{\underline{\underline{\sigma}}_{\mathrm{ion}_{\blacktriangle}\mathrm{ELE}}} + \frac{L_{\chi_{\blacktriangle}\mathrm{CAT}}}{\underline{\underline{\sigma}}_{\mathrm{ion}_{\blacktriangle}\mathrm{CAT}}} \right).$$

Because of the exponential decay in the reaction rates in the electrodes, and the assumption of a linear movement of the ions between cathode and anode, the average paths $L_{\chi_{\blacktriangle}\mathrm{ANO}}$ and $L_{\chi_{\blacktriangle}\mathrm{CAT}}$ are estimated as the half of the active zone (10 µm). $L_{\chi_{\blacktriangle}\mathrm{ELE}}$ equals the width of the electrolyte (10 µm). Due to the steady-state assumption, $\vec{j}_{\mathrm{ion}}$ equals $\vec{j}_{\mathrm{el}}$ in the BVE. Using equation 2.20, for every CV

[62] because it then directly respects concentration losses

[63] since $\vec{j}_{\mathrm{el}}$ is the same, there is no distinction between anode and cathode in η_{act}

the local Nernst potential and thus $\vec{j}_{el}$ are calculated for the anode side at the interface with the cathode.

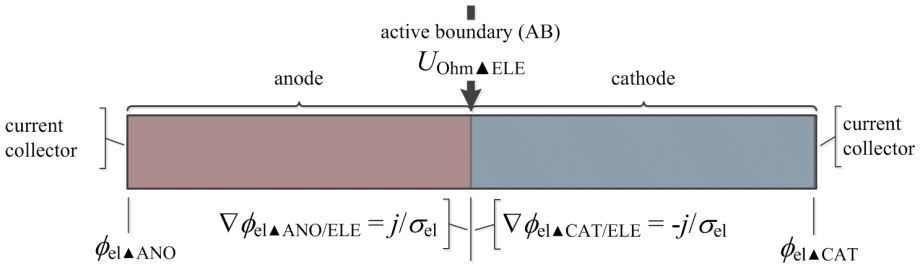

Figure 5.33.: **Variables connected to electrochemistry and their BCs in the simplified SOFC model for simple geometries:** Since j_{el} and ϕ_{el} are coupled via the BVE, an iterative solution technique is required. The current density $\vec{j}$ is calculated at the interface of the anode and the cathode whereby variable values from either side of the interface are used.

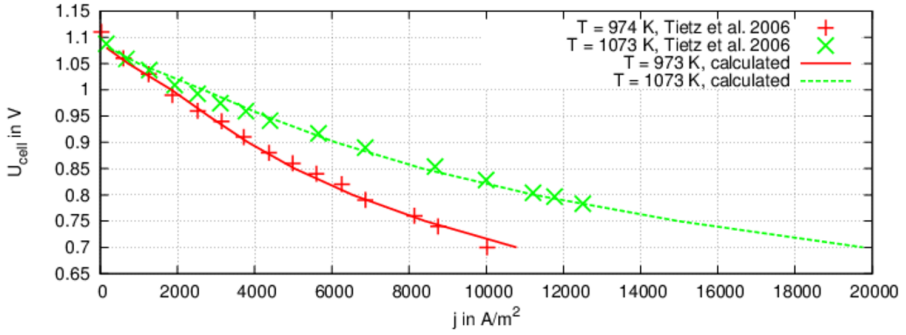

Figure 5.34.: **Experimental vs. simulated polarization curves (3D model, hydrogen electrochemistry, simple geometry model):** The experiment of Tietz, Buchkremer, and Stöver (Tietz, Buchkremer, and Stöver 2006) is reproduced with an ANSYS/CFX setup. With appropriate parameters, in a simple geometry the model is able to simulate the experimental results.

From the results of the detailed model as well as from experiments made by Raj, Atkinson, and Kilner (Raj, Atkinson, and Kilner 2009) it is known that a certain decay in oxygen ion concentration exists between anode and cath-

ode. To take this into consideration, during calculation the available oxygen concentration at the anode side of the interface is assumed to be 90 % of the oxygen's concentration at opposite side of the interface using a "User Fortran" extension of the CFX solver. With the same technique, the calculated current density $\vec{j}_{\mathrm{el}}$ is passed to the cathode side, so that it can be used at either side of the interface as a current and energy source, as well as a species sink (see equation 2.22).

In order to validate the model with experimental data, the exchange current density $\vec{j}_{\mathrm{exch}}$ and the empirical fitting coefficient β in the BVE have to be adjusted properly. With

$$\vec{j}_{\mathrm{exch}_{\blacktriangle}\mathrm{H}_{2\,\blacktriangle}\mathrm{simpl}} = 6.0 \left[\frac{\mathrm{A}}{\mathrm{m^2K}}\right] \cdot T - 4.238 \cdot 10^3 \left[\frac{\mathrm{A}}{\mathrm{m^2}}\right]$$

and

$$\beta_{\mathrm{H}_{2\,\blacktriangle}\mathrm{simpl}} = 5.0 \cdot 10^{-4} \left[\frac{1}{\mathrm{K}}\right] \cdot T - 2.36 \cdot 10^{-1}$$

the model shows a high correlation to the previously mentioned $\vec{j}$-U-curves obtained by Tietz, Buchkremer, and Stöver (Tietz, Buchkremer, and Stöver 2006) for hydrogen electrochemistry (see Figure 5.34).

Unfortunately, it is not possible to apply the model to the novel cascades cell concept introduced in section 3.2. The reasons for this are on the one hand the limitation of the "UserFortran" routines to single tasking calculation and on the the other hand the need for so called "1:1 connections" between the meshes on either side of the AB by the "User Fortran" routine. The ANSYS meshing program only generates this kind of connection for very simple geometries and fluid domains on either side of the boundary (e.g. like two flow channels with a common connection plane). Since it is not possible to simplify the novel geometry to such an extent that "1:1 connections" are generated, a second 3D model, feasible for arbitrarily complex cell geometries is required.

5.2.6.3. A simplified 3D model for complex geometries, based on diffusive exchange

To adopt the model to arbitrary geometries, the solvers intrinsic feature of defining so called "Additional variables", which can pass any boundary via a diffusive flux, is used. As shown in Figure 5.35, the process is much the same as in the previous model. Only one additional "assistant interface" close[64] to

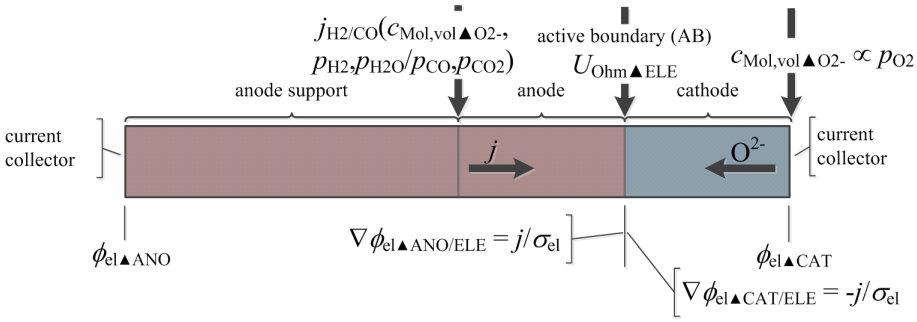

Figure 5.35.: **Variables connected to electrochemistry and their BCs in the simplified SOFC model for arbitrary geometries:** Since $\vec{j}_{el}$ and ϕ_{el} are coupled via the BVE, an iterative solution technique is required. The current density $\vec{j}$ is calculated at the anode side on a layer close to the interface with the cathode. It then migrates to the interface where it is applied on both sides. The required oxygen ion concentration is determined by $c_{Mol▲vol▲O_2}$ at the outer surface of the cathode.

the anode's side of the AB is needed. To make the required oxygen ion concentration available at the anode side, the oxygen concentration at the cathode's boundary with the gas channel/the IC is passed to an "Additional variable", which subsequently migrates to the anode[65]. Using the methodology described in the previous subsection, the local Nernst potential and thus $\vec{j}_{el}$ are calculated on the anode's "assistant layer". After that the latter is passed to the cathode via an "Additional variable". To minimize the error from gradients in the values of the "Additional variables", current, energy, and species sources are calculated from their values at either side of the AB. The CFX solver requires that perpendicular to the AB the active parts of the anode and cathode are subdivided into

[64] some micrometers distance

[65] to minimize the error, a high diffusivity of $1 \cdot 10^{-3}$ m^2/s is assumed.

at least three computational elements. As a side effect, also the other dimensions of the elements need to be shrunken too, in order to prevent "degenerated elements". Therefore, for the given dimensions, the active regions are both adjusted to a width of $1 \cdot 10^{-4}$ m and meshed with only the mentioned minimal number of subdivisions. In consequence to the rather coarse mesh, deviations between calculated values and experimental data are expected for very low as well as very high current densities. In both cases the limited mass transport leads to an overestimation of j. For the high current case, electrochemistry and mass transport might counterbalance each other during the solution process in such a way that the calculation will not converge. With

$$\vec{j}_{\mathrm{exch}_{\blacktriangle}\mathrm{H}_{2\,\blacktriangle}\mathrm{arb}} = -2.5 \left[\frac{\mathrm{A}}{\mathrm{m^2K}}\right] \cdot T + 30.325 \cdot 10^2 \left[\frac{\mathrm{A}}{\mathrm{m^2}}\right]$$

and

$$\beta_{\mathrm{H}_{2\,\blacktriangle}\mathrm{arb}} = 2.2 \cdot 10^{-3} \left[\frac{1}{\mathrm{K}}\right] \cdot T - 1.861,$$

the model shows a high correlation to the previously mentioned $\vec{j}$-U-curves obtained by Tietz, Buchkremer, and Stöver (Tietz, Buchkremer, and Stöver 2006) for hydrogen electrochemistry (see Figure 5.36).

To study CO electrochemistry, a similar model is set up and adjusted to the experimental results of Li, Shi, and Cai (Li, Shi, and Cai 2010) by using

$$\vec{j}_{\mathrm{exch}_{\blacktriangle}\mathrm{CO}_{\blacktriangle}\mathrm{arb}} = 1.2 \cdot 10^{-2} \left[\frac{\mathrm{A}}{\mathrm{m^2K^2}}\right] \cdot T^2 - 24.35 \left[\frac{\mathrm{A}}{\mathrm{m^2K}}\right] \cdot T + 1.25 \cdot 10^4 \left[\frac{\mathrm{A}}{\mathrm{m^2}}\right]$$

and

$$\beta_{\mathrm{CO}_{\blacktriangle}\mathrm{arb}} = -2.0 \cdot 10^{-6} \left[\frac{1}{\mathrm{K^2}}\right] \cdot T^2 + 4.59 \cdot 10^{-3} \left[\frac{1}{\mathrm{K}}\right] \cdot T - 2.44\,.$$

Although again correlation is attained (see Figure 5.37), this result has to be handled with some care, since only the geometry is adapted to Li, Shi, and Cai's experiment, but the materials and properties of the PEN structure are the same as for the H_2 case.

This simplification is necessary since in the final model both electrochemistry models have to work in parallel in order to give $\vec{j}_{\mathrm{el}}$:

$$\vec{j}_{\mathrm{el}} = \vec{j}_{\mathrm{el}_{\blacktriangle}\mathrm{H}_2} + \vec{j}_{\mathrm{el}_{\blacktriangle}\mathrm{CO}}.$$

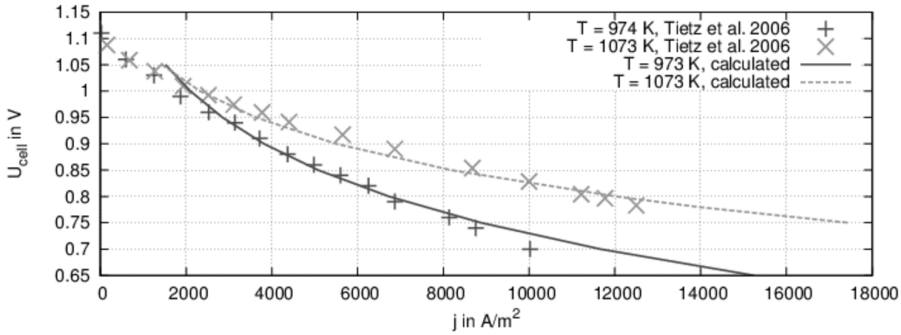

Figure 5.36.: **Experimental vs. simulated polarization curves (3D model, H_2, arbitrary geometry model):** The experiment of Tietz, Buchkremer, and Stöver (Tietz, Buchkremer, and Stöver 2006) is reproduced with an ANSYS/CFX setup. With appropriate parameters the model is able to simulate the experimental results.

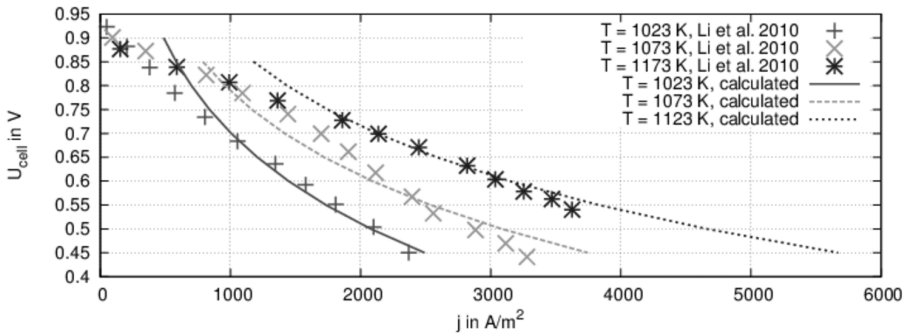

Figure 5.37.: **Experimental vs. simulated polarization curves (3D model, CO, arbitrary geometry model):** The experiment of Li, Shi, and Cai (Li, Shi, and Cai 2010) is reproduced with an ANSYS/CFX setup, whereby the structure and composition of the PEN is altered to that of Tietz, Buchkremer, and Stöver (Tietz, Buchkremer, and Stöver 2006).

The source term for the thermal energy in equation 5.45 has to be reformulated to a surface source[66] $\gamma_{\mathrm{En}_\blacktriangle\mathrm{surf}}$ in W/m^2:

$$\gamma_{\mathrm{En}_\blacktriangle\mathrm{surf}} = \vec{j}_{\mathrm{el}_\blacktriangle\mathrm{H}_2} \cdot \left(\frac{\mathrm{d}H_{\mathrm{En}_\blacktriangle\mathrm{mol},\mathrm{elchem}_\blacktriangle 1}}{2F_{\mathrm{Ch}_\blacktriangle\mathrm{mol}}} - \left(\phi_{\mathrm{el}_\blacktriangle\mathrm{CAT/ELE}} - \phi_{\mathrm{el}_\blacktriangle\mathrm{ANO/ELE}}\right) \right) + \vec{j}_{\mathrm{el}_\blacktriangle\mathrm{CO}} \cdot \left(\frac{\mathrm{d}H_{\mathrm{En}_\blacktriangle\mathrm{mol},\mathrm{elchem}_\blacktriangle 2}}{2F_{\mathrm{Ch}_\blacktriangle\mathrm{mol}}} - \left(\phi_{\mathrm{el}_\blacktriangle\mathrm{CAT/ELE}} - \phi_{\mathrm{el}_\blacktriangle\mathrm{ANO/ELE}}\right) \right) .$$

Finally, the specific ohmic losses are calculated in all domains by adjusting equation 2.28 to:

$$\gamma_{\mathrm{En}_\blacktriangle\mathrm{vol}_\blacktriangle\mathrm{Ohm}} = \frac{\vec{j}_{\mathrm{el}}^{\,2}}{\underline{\underline{\sigma}}_{\mathrm{el/ion}}} \text{ in } \frac{\mathrm{W}}{\mathrm{m}^3} .$$

5.3. Conclusions

The chapter starts with the generation of a CAD model of the novel cell concept, a definition of the different computational domains, and the limitations of the intended model. It is figured out that an extensive simplification of the original geometry is necessary in order to achieve convergent results within an acceptable computation time. Subsequently, all relevant submodels are explained and verified. For the electrochemistry a novel approach based on a local description of the phenomena is developed and applied to a 1D model. From the results, a limitation of the electrochemically active region to a thin layer around the electrolyte is figured out. Hence a reduced 3D model of the PEN region is derived in order to simplify the final model. The application of this chapters submodels to question the novel cell concept is the subject of the next chapter.

[66] It is again assumed that the sources only act on the fluid phase. The below mentioned values of $\phi_{\mathrm{el}_\blacktriangle\mathrm{CAT/ELE}}$ and $\phi_{\mathrm{el/ANO/ELE}}$ are also transported to the respective opposite side of the electrolyte by using an “Additional variable” which is transported by diffusion.

6. 3D investigation of the novel cell concept

The current chapter deals with the detailed 3D investigation of the novel cell concept. Next to the overall balances, local distributions of electric quantities, species concentrations, and temperature are discussed. In section 6.1 the basic findings are presented for a REference Case (REC). In section 6.2 the highly coupled nature of the SOFC system is emphasized by a parameter study on variations in electric potential and temperature. Finally, section 6.3 highlights fuel utilization and efficiency, before section 6.4 concludes the results of this chapter.

6.1. Results of the reference case

To study the general behavior of the system, a three cell REC with the operating conditions from Table 5.1 and a total voltage difference of 2.4 V between the external contacts of cathode ($\phi_{el} = 2{,}4\,V$) and anode ($\phi_{el} = 0\,V$, GND) is investigated. Its results are discussed subsequently.

6.1.1. Model overview and overall balances

To show the ability of the model to handle a series connection of cells and to study their influence on the state variables of the system, the final model should consist of more than one cell. Because of the large grid size it is very challenging to compute results for a complete plate of eight cells. To simplify the problem, a series connection of three cells is selected, since this setup includes at least one cell without a direct connection to a fixed BC for the electric potential (see Figure 6.1).

Tables 6.1 to 6.4 present the overall balances for mass, atoms, and energy. Summarizing the tables, the numerical results of the model show a high conver-

gence for the entire system. Therefore, it is expected that the calculated values are sufficiently reliable to interpret them for the final results of this thesis.

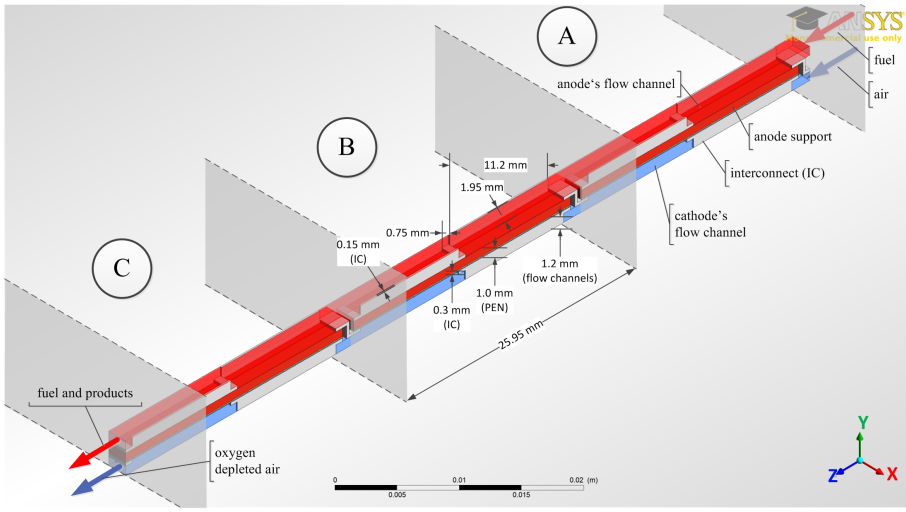

Figure 6.1.: **Final CFD geometry:** The final CFD geometry is based on the "simplified geometry" (see section 5.1) and consists of three cells (Ⓐ to Ⓒ) in a series connection. The media pass the cells in positive z-direction (top right to bottom left). For the bottom and the top as well as the front and the back of the geometry, symmetry BCs are applied.

Table 6.1.: **Overall mass balance of the REC:** The table summarizes the mass balances of the REC at either side of the AB as well as its total value. The values are calculated using $\dot{m}_{\text{Mass}} = A \cdot \rho_{\text{Mass}\blacktriangle\text{vol}} \cdot \vec{u}_{\text{fl}}$ in kg/s at each surface. Outflows are counted negative.

Location	$\dot{m}_{\text{Mass}\blacktriangle\text{ANO}}$ **[10^{-6} kg/s]**	$\dot{m}_{\text{Mass}\blacktriangle\text{CAT}}$ **[10^{-6} kg/s]**	$\sum$ **[10^{-6} kg/s]**
Inlet	$9.769 \cdot 10^{-2}$	1.057	1.154
Outlet	$-15.340 \cdot 10^{-2}$	−1.001	-1.154
$\sum$	$-5.573 \cdot 10^{-2}$	$5.573 \cdot 10^{-2}$	$-1.137 \cdot 10^{-7}$

Table 6.2.: **Overall atom balance of the REC:** The table summarizes the atom balance at either side of the AB for the REC. The values of the atomic mass flows $\dot{m}_{\text{Mass}\blacktriangle i}$ are calculated by using the results of Table 6.1 and the relationship $\dot{m}_{\text{Mass}\blacktriangle i} = \dot{m}_{\text{Mass}} \cdot \left(\sum_j X_{\text{Mass,mass}\blacktriangle j} n_{i\blacktriangle j}\right)$ in dependence of the respective mass fractions of the j gas components $X_{\text{Mass,mass}\blacktriangle j}$ in $\text{kg}_{\text{species}}/\text{kg}_{\text{tot}}$ and the number of atoms of type i in the component j. Outflows are counted negative. Quantities are given in 10^{-8} kg/s.

Anode

Location	$\dot{m}_{\text{Mass}\blacktriangle\text{C}\blacktriangle\text{ANO}}$	$\dot{m}_{\text{Mass}\blacktriangle\text{H}\blacktriangle\text{ANO}}$	$\dot{m}_{\text{Mass}\blacktriangle\text{N}\blacktriangle\text{ANO}}$	$\dot{m}_{\text{Mass}\blacktriangle\text{O}\blacktriangle\text{ANO}}$
Inlet	2.848	4.649	$4.888 \cdot 10^{-1}$	1.778
Outlet	-2.850	-4.628	$-7.178 \cdot 10^{-1}$	-7.142
$\sum$	$-2.045 \cdot 10^{-3}$	$2.172 \cdot 10^{-2}$	$-2.290 \cdot 10^{-1}$	-5.364

Cathode

Location	$\dot{m}_{\text{Mass}\blacktriangle\text{C}\blacktriangle\text{CAT}}$	$\dot{m}_{\text{Mass}\blacktriangle\text{H}\blacktriangle\text{CAT}}$	$\dot{m}_{\text{Mass}\blacktriangle\text{N}\blacktriangle\text{CAT}}$	$\dot{m}_{\text{Mass}\blacktriangle\text{O}\blacktriangle\text{CAT}}$
Inlet	0.000	0.000	81.380	24.311
Outlet	0.000	0.000	-81.290	-18.830
$\sum$	0.000	0.000	$9.480 \cdot 10^{-2}$	5.479
$\sum_{\text{tot}}$	$-2.045 \cdot 10^{-3}$	$2.172 \cdot 10^{-2}$	$-1.639 \cdot 10^{-1}$	$1.143 \cdot 10^{-1}$

Table 6.3.: **Overall species balance of the REC:** The table summarizes the species balance at either side of the AB for the REC. The values of the mass flows $\dot{m}_{\text{Mass}\blacktriangle i}$ are calculated by using the results of Table 6.1 and the relationship $\dot{m}_{\text{Mass}\blacktriangle i} = \dot{m}_{\text{Mass}} \cdot X_{\text{Mass,mass}\blacktriangle i}$ in dependence of the respective mass fraction $X_{\text{Mass,mass}\blacktriangle i}$ in $\text{kg}_{\text{species}}/\text{kg}_{\text{tot}}$ for each species i. Outflows are counted negative. Quantities are given in 10^{-8} kg/s.

Anode

Location	$\dot{m}_{\text{Mass}\blacktriangle\text{CH}_4}$	$\dot{m}_{\text{Mass}\blacktriangle\text{CO}}$	$\dot{m}_{\text{Mass}\blacktriangle\text{CO}_2}$	$\dot{m}_{\text{Mass}\blacktriangle\text{H}_2}$	$\dot{m}_{\text{Mass}\blacktriangle\text{H}_2\text{O}}$	$\dot{m}_{\text{Mass}\blacktriangle\text{N}_2}$	$\dot{m}_{\text{Mass}\blacktriangle\text{O}_2}$
Inlet	2.930	1.465	$9.778 \cdot 10^{-2}$	3.808	$9.791 \cdot 10^{-1}$	$4.888 \cdot 10^{-1}$	0.000
Outlet	-1.782	-2.808	-1.144	-3.592	-5.298	$-7.178 \cdot 10^{-1}$	0.000
$\sum$	1.148	-1.343	-1.047	$2.165 \cdot 10^{-1}$	-4.319	$-2.290 \cdot 10^{-1}$	0.000

Cathode

Location	$\dot{m}_{\text{Mass}\blacktriangle\text{CH}_4}$	$\dot{m}_{\text{Mass}\blacktriangle\text{CO}}$	$\dot{m}_{\text{Mass}\blacktriangle\text{CO}_2}$	$\dot{m}_{\text{Mass}\blacktriangle\text{H}_2}$	$\dot{m}_{\text{Mass}\blacktriangle\text{H}_2\text{O}}$	$\dot{m}_{\text{Mass}\blacktriangle\text{N}_2}$	$\dot{m}_{\text{Mass}\blacktriangle\text{O}_2}$
Inlet	0.000	0.000	0.000	0.000	0.000	81.390	24.310
Outlet	0.000	0.000	0.000	0.000	0.000	-81.290	-18.830
$\sum$	0.000	0.000	0.000	0.000	0.000	$-1.342 \cdot 10^{-1}$	5.478
$\sum_{\text{tot}}$	1.148	-1.343	-1.047	$2.165 \cdot 10^{-1}$	-4.319	$-1.342 \cdot 10^{-1}$	5.478

Table 6.4.: **Overall energy balance of the REC:** The energy balance consists on the one hand of the thermal and chemical energy of the reacting media and on the other hand of the electrical energy flowing through the electric contacts. While chemical energy/enthalpy flows are calculated by the sum of the chemical energy/enthalpy flow of each of the species i: $\dot{H}_{\mathrm{En}\blacktriangle\mathrm{in/out}} = \sum_i \frac{\dot{m}_{\mathrm{Mass}\blacktriangle\mathrm{in/out}} \cdot X_{\mathrm{Mass,mass}\blacktriangle i} \cdot H_{\mathrm{En}\blacktriangle\mathrm{mol}\blacktriangle i}}{M_{\mathrm{Mass}\blacktriangle\mathrm{mol}\blacktriangle i}}$, the thermal energy flows are calculated via $\dot{Q}_{\mathrm{En}\blacktriangle\mathrm{in/out}} = \sum_i \frac{\dot{m}_{\mathrm{Mass}\blacktriangle\mathrm{in/out}} \cdot X_{\mathrm{Mass,mass}\blacktriangle i} \cdot c_{\mathrm{En,p,mol}\blacktriangle i} \cdot T_{\blacktriangle\mathrm{in/out}}}{M_{\mathrm{Mass}\blacktriangle\mathrm{mol}\blacktriangle i}}$, and the electrical energy flows are determined by $\dot{E}_{\mathrm{En,Ch}\blacktriangle\mathrm{in/out}} = \vec{j}_{\mathrm{in/out}} \cdot A_{\mathrm{in/out}} \cdot (\phi_{\mathrm{in}} - \phi_{\mathrm{out}})$. Negative inlet values of $\dot{H}_{\mathrm{En}}$ result from negative enthalpies of the constituents relative to the reference conditions (see appendix C), negative outlet values from outflow. All quantities are given in 10^{-1} W.

	Anode		**Cathode**		**IC**	$\sum$
	$\dot{H}_{\mathrm{En}}$	$\dot{Q}_{\mathrm{En}}$	$\dot{H}_{\mathrm{En}}$	$\dot{Q}_{\mathrm{En}}$	$\dot{E}_{\mathrm{En,Ch}}$	
Inlet	1.400	7.295	7.699	11.870	$4.368 \cdot 10^{-3}$	28.268
Outlet	4.600	-8.247	-7.931	-11.980	-4.739	-28.297
$\sum$	6.000	-0.952	-0.232	-0.110	-4.735	-0.029

6.1.2. Electric aspects

Maybe the most interesting aspects of a fuel cell are its electric properties; namely the polarization curve, the distribution of current density and electric potential, as well as the fuel utilization and power density. Since the polarization curves will be the subject of section 6.3, the focus lies here on the influence of the series connection and local distribution of the state variables. Figure 6.2 shows the electric potential ϕ_{el}, the electric field $\vec{\mathbb{E}}_{\mathrm{el}}$, and the electric current density $\vec{j}_{\mathrm{el}}$ in a y-z-plane at $x = 0.1$ mm. The qualitative impression of a series connection of three batteries in Figure 6.1 can be underpinned quantitatively by evaluating the state variables at the inlet planes (and the final outlet planes) of each cell's IC (see Table 6.5). Next to almost identical potential differences $\Delta\phi_{\mathrm{el}}$ for all cells in the system, the respective electric fields $\vec{\mathbb{E}}_{\mathrm{el}}$, and electric current densities $\vec{j}_{\mathrm{el}}$ have similar values.

Table 6.5.: **Electric quantities of a three cell series connection:** The values of ϕ_{el}, $\vec{\mathbb{E}}_{el}$, and $\Delta\vec{j}_{el}$ are evaluated by averaging over the respective inlet planes of each cell and the outlet plane of the final one. The values for the current sources $\vec{j}_{el_{\blacktriangle} i_{\blacktriangle} ave}$ are calculated by averaging over the entire electrochemically active area of each cell. The power densities $\wp_{el_{\blacktriangle} i_{\blacktriangle} ave}$ are subsequently derived from these values. Finally, the values of the volumetric power densities $\wp_{vol,el_{\blacktriangle} i_{\blacktriangle} ave}$ follow by multiplying $\wp_{el_{\blacktriangle} i_{\blacktriangle} ave}$ with the quotient of the electrochemically active area $A = 1.442 \cdot 10^{-4}$ m^2 and the cell volume $V_{vol,cell} = 5.085 \cdot 10^{-7}$ m^3.

Quantity	**Dimension**	**Third cell (C)**	**Second cell (B)**	**First cell (A)**	**Inlet**
ϕ_{el}	V	2.400	1.584	0.783	$1.905 \cdot 10^{-8}$
$\Delta\phi_{el}$	V	0.816	0.801	0.783	
$\vec{\mathbb{E}}_{el}$	V/m	0.369	0.396	0.438	0.28
$\Delta\vec{\mathbb{E}}_{el}$	V/m	$-2.595 \cdot 10^{-2}$	$-4.227 \cdot 10^{-2}$	$-2.059 \cdot 10^{-2}$	
$\Delta\vec{\mathbb{E}}_{el_{\blacktriangle}\%}$	%	-7.018	-10.680	-4.701	
$\vec{j}_{el}$	A/m^2	$3.345 \cdot 10^5$	$3.580 \cdot 10^5$	$3.962 \cdot 10^5$	$4.148 \cdot 10^5$
$\Delta\vec{j}_{el}$	A/m^2	$-2.348 \cdot 10^4$	$-3.822 \cdot 10^4$	$-1.860 \cdot 10^3$	
$\Delta\vec{j}_{el_{\blacktriangle}\%}$	%	-7.018	-10.680	-4.696	
$\vec{j}_{el_{\blacktriangle} tot_{\blacktriangle} ave}$	A/m^2	$4.037 \cdot 10^3$	$4.477 \cdot 10^3$	$5.197 \cdot 10^3$	
$\vec{j}_{el_{\blacktriangle} CO_{\blacktriangle} ave}$	A/m^2	$3.324 \cdot 10^2$	$3.410 \cdot 10^2$	$3.627 \cdot 10^2$	
$\vec{j}_{el_{\blacktriangle} H_{2\,\blacktriangle} ave}$	A/m^2	$3.705 \cdot 10^3$	$4.136 \cdot 10^3$	$4.834 \cdot 10^3$	
$\wp_{el_{\blacktriangle} tot_{\blacktriangle} ave}$	W/m^2	$3.294 \cdot 10^3$	$3.586 \cdot 10^3$	$4.069 \cdot 10^3$	
$\wp_{el_{\blacktriangle} CO_{\blacktriangle} ave}$	W/m^2	$2.712 \cdot 10^2$	$2.732 \cdot 10^2$	$2.840 \cdot 10^2$	
$\wp_{el_{\blacktriangle} H_{2\,\blacktriangle} ave}$	W/m^2	$3.023 \cdot 10^3$	$3.313 \cdot 10^3$	$3.785 \cdot 10^3$	
$\wp_{vol,el_{\blacktriangle} tot_{\blacktriangle} ave}$	W/m^3	$9.341 \cdot 10^5$	$10.169 \cdot 10^5$	$11.535 \cdot 10^5$	
$\wp_{vol,el_{\blacktriangle} CO_{\blacktriangle} ave}$	W/m^3	$7.691 \cdot 10^4$	$7.746 \cdot 10^4$	$8.053 \cdot 10^4$	
$\wp_{vol,el_{\blacktriangle} H_{2\,\blacktriangle} ave}$	W/m^3	$8.572 \cdot 10^5$	$9.395 \cdot 10^5$	$10.730 \cdot 10^5$	

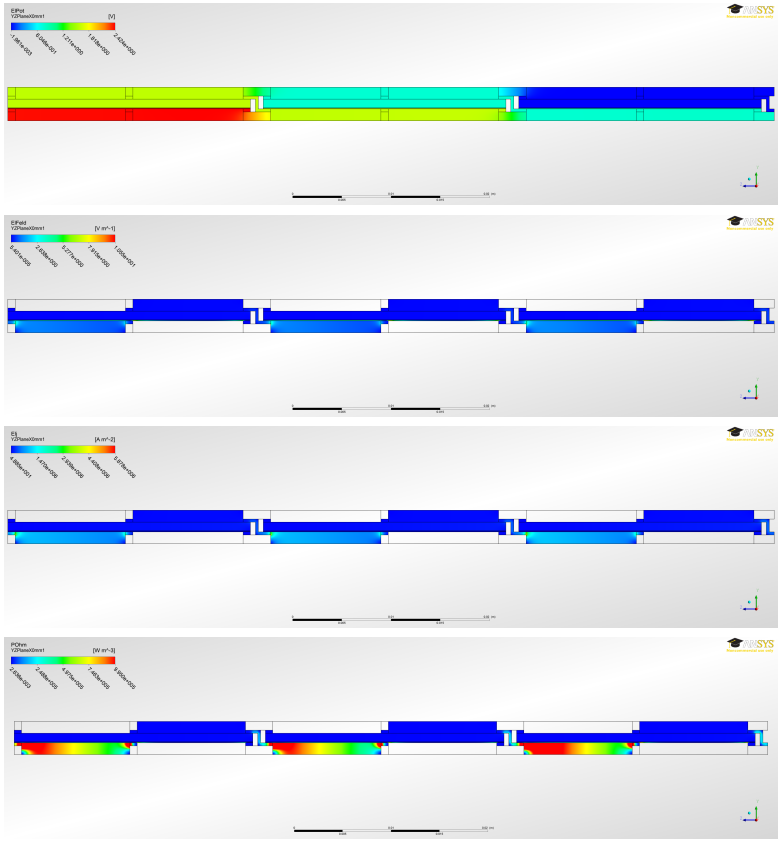

Figure 6.2.: **Local distribution of electric state variables in a y-z-plane at $x = 0.1$ mm:** Shown are the electric potential ϕ_{el} (top), the electric field $\vec{\mathbb{E}}_{el}$ (second from top, gas-phase omitted due to outstanding large values), the electric current density $\vec{j}_{el}$ (second from bottom), and the volumetric ohmic power density $\mathfrak{p}_{vol\,Ohm}$ in W/m^3 (bottom). ϕ_{el} has fixed values of 2.4 V at the cathode's contacts (bottom left) and GND at the anode's contacts (top right). It is obvious that the potential distribution is similar to a series connection of batteries. The electric field $\vec{\mathbb{E}}_{el}$ and current density $\vec{j}_{el}$ qualitatively show translational symmetry in z-direction among the cells. At each cell, the values increase at the cathode side with growing z (cells Ⓐ to Ⓒ), whereas at the same time a decrease on the anode side is recorded. Much larger average current densities ($\vec{j}_{el} \approx 1.4 \cdot 10^6$ A/m^2) are apparent at the cathode side of the AB. Thus the highest ohmic power densities are present in these regions (bottom). The values for $\vec{\mathbb{E}}_{el}$ are omitted in the gas-phase, because the gases in each cell attain the same electric potential as e.g. the ICs. Since their electrical conductivity is very weak, (almost) no current flows, resulting in very strong fields ($\vec{\mathbb{E}}_{el} \approx 500$ V/m).

6.1.2.1. Electric potential and electric field

As the driving force for the electric current, the difference in electric potential ϕ_{el} between the anode and the cathode and the distribution within them is of primary interest. Figure 6.2 and Table 6.5 reveal a high similarity to a series connection of three batteries with (nearly) the same difference in ϕ_{el} for every cell. Using the almost identical Nernst potential U_{Nernst} in Figure 6.3 as affirmation, it can be derived that the operating conditions between the cells have to be very similar. Thus stronger changes in temperature and gas composition are either not apparent or balance each other. Both aspects are addressed below in more detail.

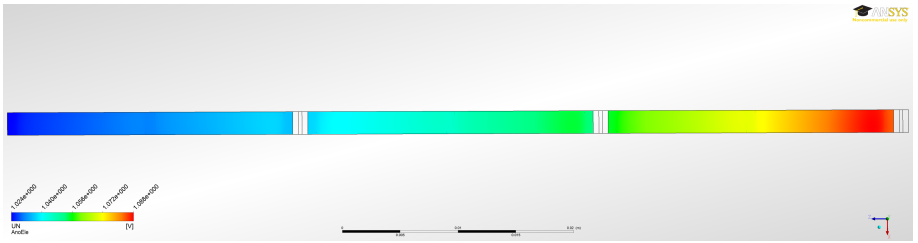

Figure 6.3.: **Distribution of the Nernst potential at the AB:** The theoretically achievable open circuit potential U_{Nernst} (see section 2.3) is almost identical for all cells in the series connection. It slowly decreases in flow direction (right to left; cells Ⓐ to Ⓒ) due to changes in reactant concentration. The areas covered by the IC can be identified by slightly decreased values of U_{Nernst} (left, middle, and right regions of each cell). Reasons for this are either temperature variations or changes in reactant composition.

In consequence to the release and consumption of electric charges at the TPBs, inside the respective electrodes, and between serially connected anodes and cathodes, differences in electric potential have to be apparent. As an example, the local distribution of ϕ_{el} inside the second cell Ⓑ of the three cell series connection in illustrated in Figure 6.4. While the potential remains almost constant inside the anode (left) it steadily increases in upstream direction inside the cathode and the IC. At the cathode side of the PEN the increase is additionally superimposed by a lateral distribution which is structured by the IC's geometry. The reason for this is the consumption of electric charges at the cathode's AB which has to be replaced through the rather poor conductive cathode. In consequence, the local electron density is slightly lower in those

regions without a direct contact to the IC and hence the electric potential is increased.

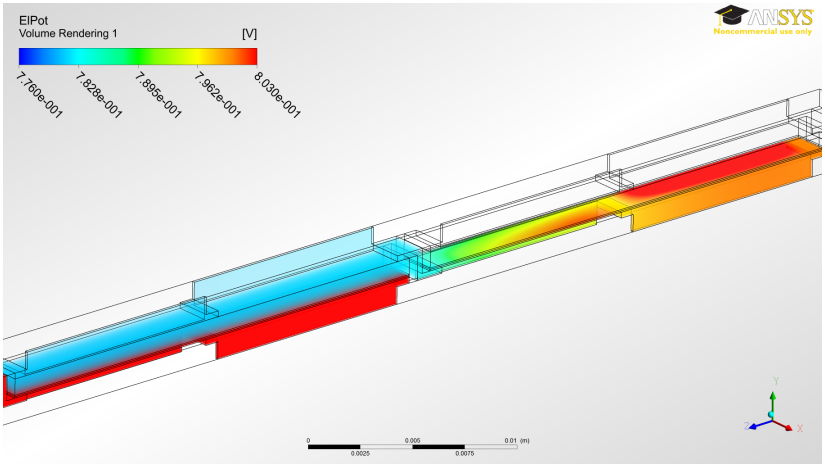

Figure 6.4.: **Electric potential distribution:** For the second cell (B) of the series connection the local values of the electric potential ϕ_{el} are shown. The potential remains almost constant inside the anode (left) and increases in upstream direction inside the cathode/IC. Here also a lateral distribution in dependence of the electrode's coverage by the IC is apparent.

This interpretation is supported by a look at the vector components of $\vec{\mathbb{E}}_{el}$ in Figure 6.5. The almost uniform distribution in z-direction[1] is overlaid by very strong fields in x- and y-direction towards the metallic IC. Close to the boundary with the IC, the orthogonal component of the field (y-direction) increases significantly. Altogether, it follows the vector plot in Figure 6.5, which reveals a direction of the electric field $\vec{\mathbb{E}}_{el}$, and thus a flow towards the metallic IC. Reasons for this behavior are discussed below together with the electric current density.

6.1.2.2. Current density

At the cathode side of each cell in flow direction an increase in electric current density $\vec{j}_{el}$ can be identified. Simultaneously, a decrease is apparent at the anode side of the AB (see Figure 6.2).

[1] in-plane currents to the subsequent anode

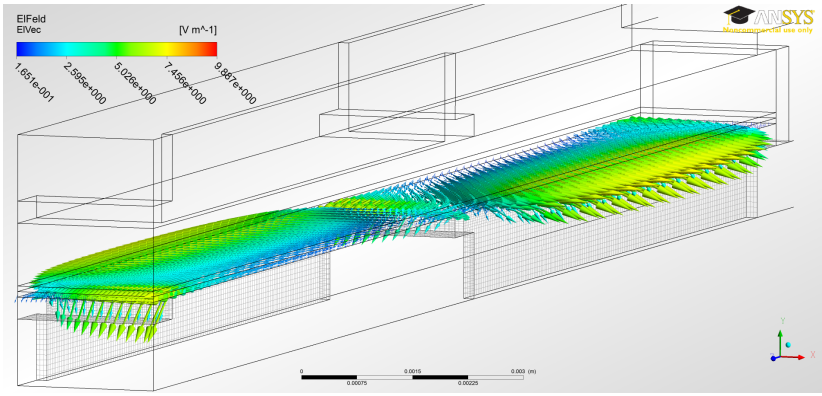

Figure 6.5.: **Vectors of the electric field inside the cathode:** For the third cell Ⓒ of the series connection the vectors of the electric field $\vec{\mathbb{E}}_{el}$ inside the cathode are displayed. The boundaries of the cathode gas-channel with the IC are highlighted as surface meshes to emphasize the direction of $\vec{\mathbb{E}}_{el}$ towards the metallic IC.

Anode's boundary regions:

Anode side:

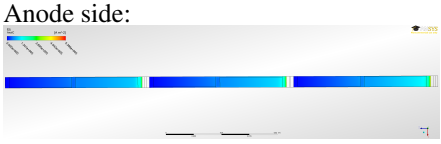

IC side:

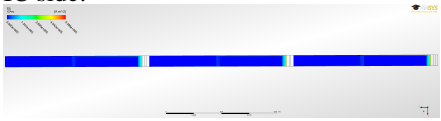

Cathode's boundary regions:

Cathode side:

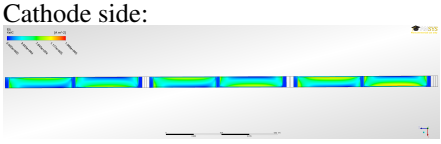

IC side:

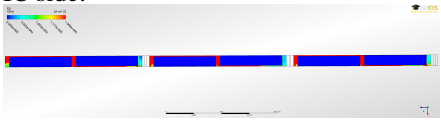

Figure 6.6.: **Electric current density distribution in the boundary region of anode/cathode and IC:** The current density is evaluated at the contact area of the anode/cathode with the respective gas channel and IC. In both cases the upper image shows $\vec{j}_{el}$ inside the electrode whereas the lower one the situation inside the IC. For the anode side of the AB (left) it is obvious that for each cell on both sides of the boundary the current density decreases along with decreasing ϕ_{el}. Since the electric conductivity of the anode is higher, in the IC $\vec{j}_{el}$ increases significantly only at the outer right finger of each cell. Since the IC is much more conductive than the cathode, the former carries the current, while the latter is mainly needed for its lateral homogenization (right images).

Reasons for this behavior are a steady "loss" of electrons in the process of ion creation at the cathode and its reversal at the anode (both in opposite direction to the flow). Further insights on the distribution of $\vec{j}_{\mathrm{el}}$ can be obtained when looking at the electrodes perpendicular to the flow direction (see Figure 6.6). For each cell the current density decreases steadily inside the anode in direction of falling electric potential ϕ_{el} (positive z-direction). The drastic increase at the outer right fingers follows from the concentrated passage of electric charges from the anode to the IC. Since only this boundary region is used for their passage, $\vec{j}_{\mathrm{el}}$ locally increases significantly in both domains (also visible in Figure 6.2).

When looking at the values of $\vec{j}_{\mathrm{el}}$ in the anode and IC (left images in Figure 6.6), it is obvious that the current is transported primarily by the anode. The reason for this behavior is the higher conductivity of the anode cermet (because of its Ni content) compared to the IC. As it can be seen in Figure 6.7, the electric conductivity $\underline{\underline{\sigma}}_{\mathrm{el}}$ of the IC is still about two orders of magnitude larger than the one of the cathode. In consequence, at the cathode side the sit-

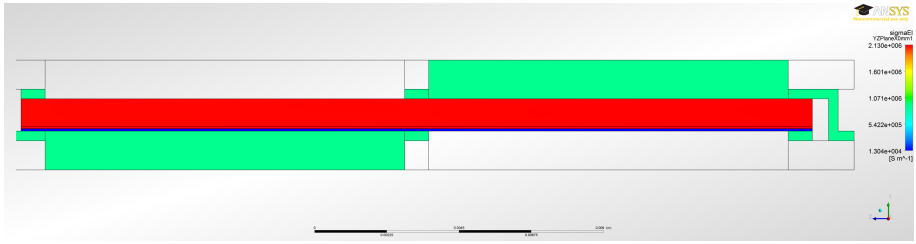

Figure 6.7.: **Electric conductivity distribution:** Because of the high Ni content, the values of $\underline{\underline{\sigma}}_{\mathrm{el}}$ are maximal in the anode. Although the IC's conductivity is only about half of that of the anode, it is still approximately two orders of magnitude larger than the cathode's one. The values are highlighted for the first cell Ⓐ in the series connection at a y-z-plane at $x = 0.1$ mm. Since the values in the gas channels are close to unity, they are suppressed.

uation is completely opposite. As the images in the right of Figure 6.6 show, the current density is much larger in the IC than in the electrode. Inside the cathode it is heavily structured by the geometry of the IC. While $\vec{j}_{\mathrm{el}}$ is almost zero under the IC and in the central regions of the cut-outs, it increases up to about $1.5 \cdot 10^5$ A/m^2 in the cut-out areas close to the IC. This structure in x-direction is a result of the need to homogeneously supply electrons to the

reaction zones. While the almost uniform distribution in χ-direction inside the cut-out areas points to a homogeneous consumption of the charges in this direction, the slight decrease in $\vec{j}_{\mathrm{el}}$ in flow direction among the cells reveals a higher electrochemical activity close to the inlet.

6.1.2.3. Sources and sinks of the electric current density

Figure 6.8 confirms the findings of the previous subsection. While CO shows only slight changes in the electrochemical reaction rate[2], $\vec{j}_{\mathrm{el}_{\blacktriangle}\mathrm{H}_2}$ reduces its value to about 64 % of its maximal value close to the inlet. Thus hydrogen in converted much faster by the system, compared to CO. When looking at the numerical values, an order of magnitude can be figured out as a guideline.

Both current densities show local minima at the covered parts of the electrodes (right, left, and center of each cell, see Figure 6.8). Since the transport of electrons is even better in these regions compared to the rest, the observed changes must originate in variations in the reactant concentration. Due to the rather thick anode, differences in the oxygen concentration at the cathode side of the AB are more likely (see below).

Although lateral currents could be expected, as the previous subsection shows, they are not very pronounced. Nevertheless, even for the high operating voltage of the REC, an influence of the PEN coverage by the IC is apparent. For higher loads this might lead to fuel starvation, large reaction rate gradients, and finally maybe an increased degradation rate.

6.1.3. Mass transport and species distribution

As already discussed in the previous chapters, it is necessary to distinguish between the mass transport in the gas channel and the electrodes. The former is dominated by convection and is intended to provide an efficient transport of the operating media and homogenization of the temperature profile. Therefore, in subsection 3.2.2 sinusoidal shaped fins for structuring the flow channels are proposed. As discussed in section 5.1.1, these fins are simplified to straight connections for the final geometry (“simplified geometry”). Since the laminar nature of the flow on both sides of the PEN has already been investigated in subsection 5.2.2, here the focus lies on the distribution of the velocity profile.

[2] about 50 A/m^2 ($\approx$ 13 %) among the three cells

CO:

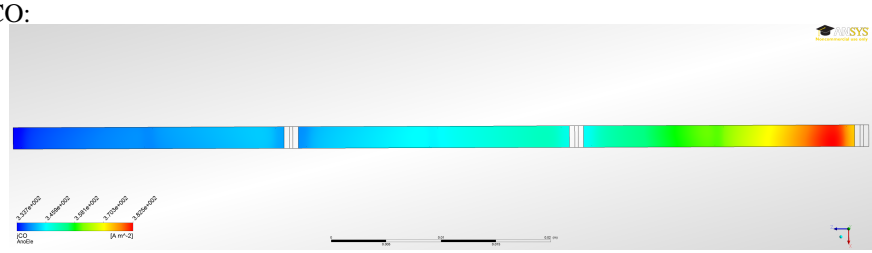

H_2:

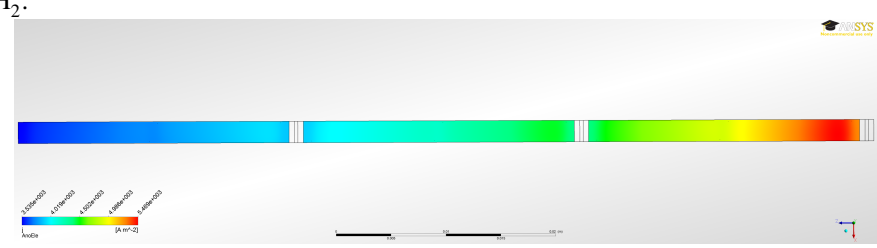

CO + H_2:

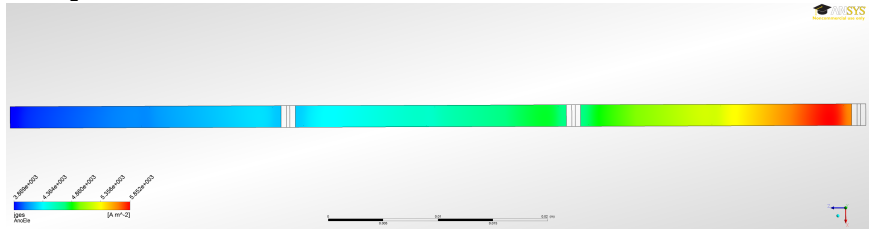

Figure 6.8.: **Current density distribution at the anode side of the AB:** The operating media pass the system in growing z-direction (cells (A) to (C) from right to left). For CO (top) as well as for H_2 (middle) the reaction rate steadily decreases from the inlet (right) to the outlet (left). While the loss is only about 13 % for CO, the electric sources from the hydrogen's electrochemical conversion are lowered by almost 36 % along the flow direction. In both cases, an influence of the electrode coverage by the IC is apparent at the end and in the middle of each cell. The sum of both current densities (bottom) shows a trend towards homogenization for each cell.

6.1.3.1. Velocity profile

Figure 6.9 shows the velocity profile of all domains in a y-z-plane at $x = 1$ mm. In both domains the velocity decreases from the center of the flow channel (top and bottom edges in Figure 6.9) to the electrodes, where it is almost zero. In the cutting plane, local maxima in those regions where the IC narrows the flow

channel can be observed. They are a consequence of the "Venturi effect" which says that for a given mass flow the fluid velocity must rise when the channels diameter decreases. (Grote and Feldhusen 2007, p. W18 et seqq.) Since the inlet velocity at the cathode side of the PEN (bottom) is higher than the anode's one, the regions of highest velocities are only in this domain. Two important aspects can be derived from the figure: On the one hand the velocity distribution among the cells is very uniform, thus subsequently only one cell needs to be investigated in more detail[3], and on the other hand a strong influence of the IC's geometry on the velocity profile. Using the example of cell three (C),

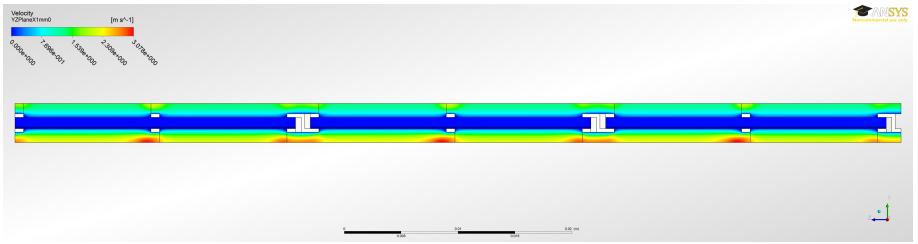

Figure 6.9.: **Overall velocity distribution in a y-z-plane at $x = 1$ mm:** Because of the higher inlet velocity (see Table 5.1 in section 5.2.2), the regions of higher average velocity are all inside the cathode's gas channel (bottom). Each cell ((A) to (C), from right to left) is structured by the IC into alternating regions of high and low average velocity. Among the cells the velocity profile is very similar, thus detailed studies are possible with a single cell.

the local distribution of the velocity profile is displayed in Figure 6.10. The figure shows that on either side of the electrolyte even the simplified fins act as baffles, by concentrating the flow to well developed laminar flow profiles with non zero velocities at the surfaces of the porous electrodes. In the middle of the cell (between planes (PA5) and (PA6)), a mixing occurs by splitting and rearrangement of the streams. To illustrate this aspect, Figures 6.11 and 6.12 show streamlines and velocity vectors inside the third cell's (C) anodic flow channel. In particular, the streamline-plot reveals a redirection of the flow by the IC. Due to the simplified geometry, the stream is only redirected parallel to the anode surface. In the "original geometry" the sinusoidal shaped fins would also redirect the flow orthogonal to the electrode surface. This would lead to an

[3]Because of the assumed parabolic inlet velocity profile, the first cell (A) shows in this region some deviations to the other cells

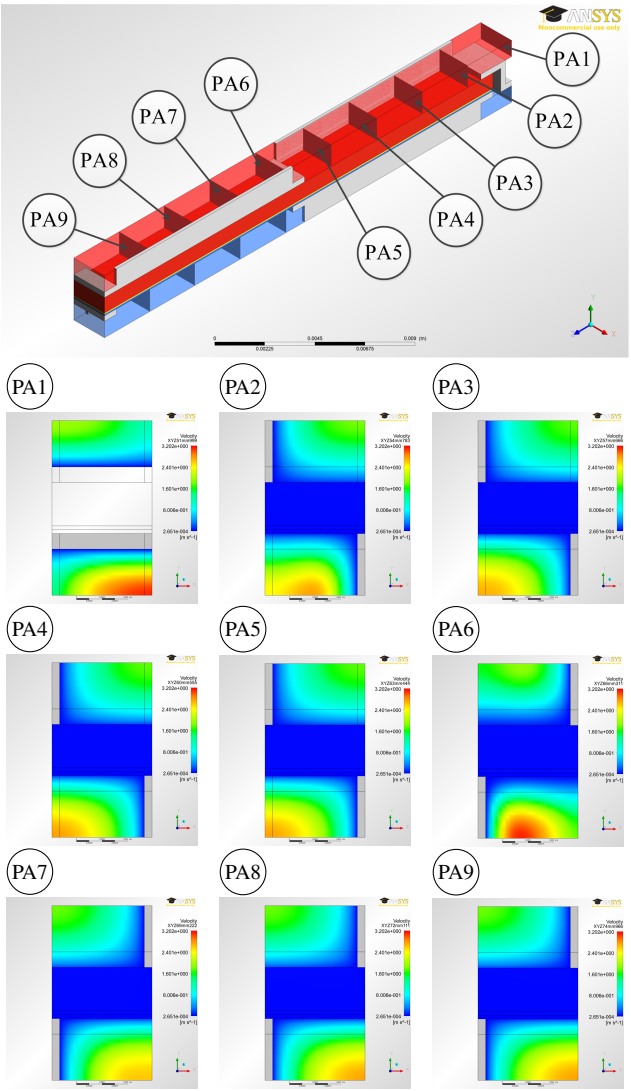

Figure 6.10.: **Velocity profiles:** The velocity profiles are evaluated in the third cell (C) at the planes (PA1) - (PA9) shown in the topmost figure. The profiles reveal highly developed laminar flow profiles inside the gas channels and almost zero velocity in the electrodes.

enhanced mixing inside the flow channel and to a shifting of the core regions of the flow towards the electrode.

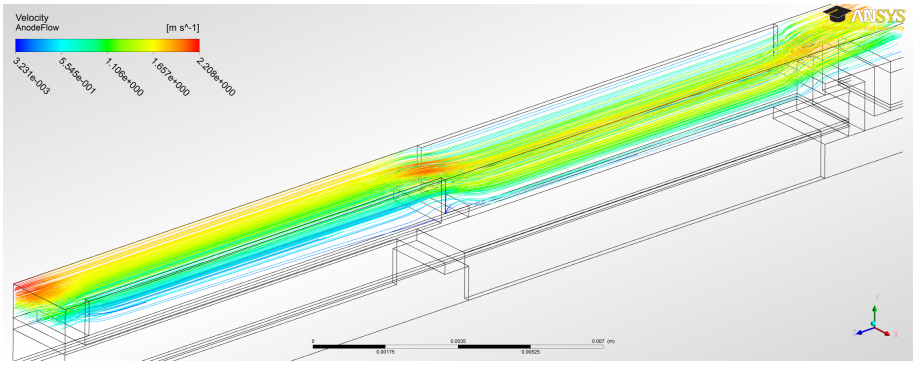

Figure 6.11.: **Streamlines inside the anode's flow channel:** At the connection of two cells, the flow almost unifies to one stream (top right corner; see also Figure 6.10), while at the center of the cell (middle) the staggered structure of the fins forces flow redistribution. The figure shows the situation inside the third cell Ⓒ of the series connection.

However, as Figure 6.13 shows, the "pressure drop" in the flow channels is almost negligible[4]. Major changes are only apparent inside the porous electrodes; while the coverage by the IC and the net mass-flow from the cathode lead to an increase inside the anode, a lid flow situation and loss of mass via the electrolyte result in a decrease inside the cathode. Altogether, from these results a homogeneous distribution of reactants and products as well as of the temperature in directions perpendicular to the flow direction are to be expected.

6.1.3.2. Species fractions

As discussed in the previous subsection, the average velocity and thus the mass flow rate is much higher in the cathode domain than in the anode's one. In consequence, the relative changes in species concentration are expected to be much more significant for the anode domain. Therefore, despite of a look at the oxygen concentration, the subsequent discussion focuses on this region.

Next to the local distribution of the different species in the operational media inside the entire gas-channel and electrode volume, the respective boundary

[4] very similar to an opened flow channel of the same length

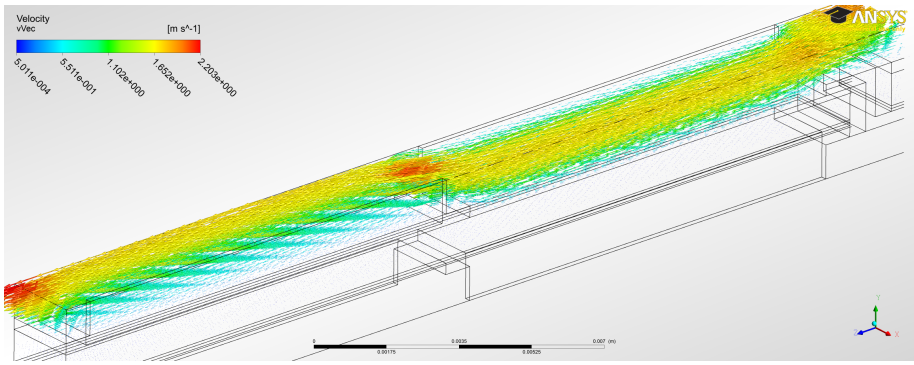

Figure 6.12.: **3D velocity vectors inside the anode's flow channel:** As in Figure 6.11 two jets which reunite at the connection of two following cells (top right corner) can be identified. The figure shows the situation inside the third cell Ⓒ of the series connection.

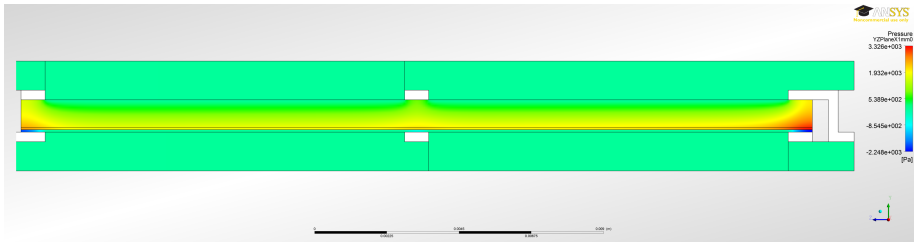

Figure 6.13.: **Pressure distribution inside the first cell:** The figure shows the pressure p inside the first cell Ⓐ in a y-z-plane at $x = 1$ mm (values relative to the inlet pressure). While the "pressure drop" inside the flow channels (anode top, cathode bottom) is almost negligible, the coverage of the anode by the IC and the net mass-flow from the cathode lead to an increase in p close to the electrolyte. Inside the cathode a lid flow situation and loss of mass via the electrolyte results in a pressure decrease.

region close to the electrochemical AB is of interest. For the anode, the former is given by a mixture with the results of the reformation reactions, whereas the latter is much more ruled by electrochemistry. To simplify the comparability of the different species, the subsequent discussion is based on "molar fractions" $y_{\mathrm{Mol}_\blacktriangle \mathrm{mol}_\blacktriangle i}$. In consequence, if not otherwise noted, in the following text the term "concentration" is used as a synonym for the molar fractions.

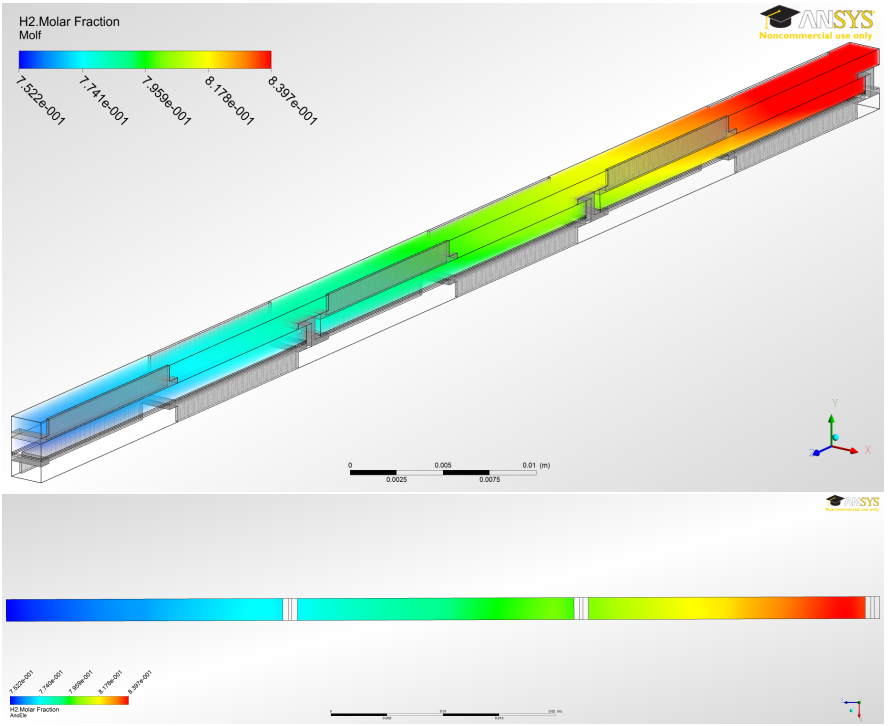

Figure 6.14.: **Molar fractions of H_2:** The operating media pass the flow channel in growing z-direction (top right to bottom left; cells Ⓐ to Ⓒ). Inside the porous anode, H_2 is created by reformation from CH_4 with H_2O and consumed by electrochemistry (at the AB). The bottom figure shows the situation at the AB (cells Ⓐ to Ⓒ in growing z-direction from right to left).

Starting with hydrogen in Figure 6.14, a steady decrease in its molar fraction from $y_{\mathrm{Mol}_\blacktriangle \mathrm{mol}_\blacktriangle \mathrm{H}_2} \approx 0.87\,\mathrm{mol}_{\mathrm{H}_2}/\mathrm{mol}_{\mathrm{tot}}$ at the inlet (top left) to $y_{\mathrm{Mol}_\blacktriangle \mathrm{mol}_\blacktriangle \mathrm{H}_2} \approx 0.75\,\mathrm{mol}_{\mathrm{H}_2}/\mathrm{mol}_{\mathrm{tot}}$ at the outlet, regardless of the reformation reactions inside the anode, is apparent. The 3D visualization reveals the limited mass trans-

port velocity inside the electrodes. Here molar fraction gradients are present between the AB and the flow channel. Also the coverage of the anode surface by the IC has an influence on the hydrogen fraction profile, which is even going down to the contact region with the electrolyte. Since transverse to the flow both electrodes are covered in the same regions, these concentration differences might originate in changes of the oxygen concentration at the cathode side of the AB.

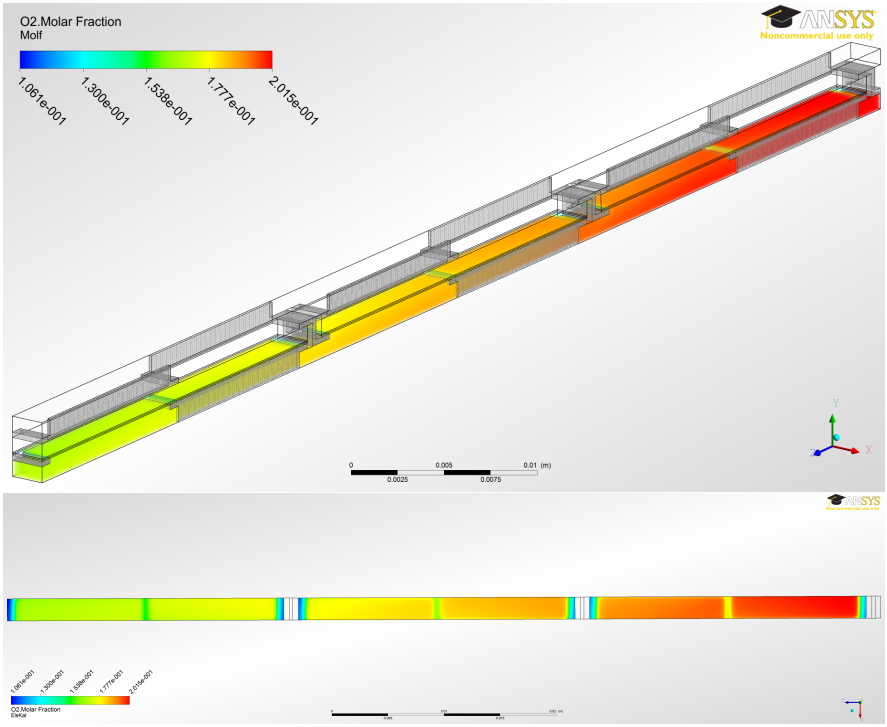

Figure 6.15.: **Molar fractions of O_2:** The operating media pass the flow channel in growing z-direction (top right to bottom left; cells Ⓐ to Ⓒ). The bottom image shows the situation at the cathode side of the AB. Under the covered parts of the cathode, significant decreases in oxygen concentration are apparent.

The oxygen molar fraction profile in the cathode domain in Figure 6.15 supports this interpretation. While the absolute value decreases only by about 20 % between in- and outlet of the system, local minima at the electrochemi-

cally AB are apparent for all covered regions (bottom image in Figure 6.15). These regions can be subdivided into those at the edges of each cell and the one in the middle. Almost independent from the cell number, the oxygen's molar fraction decreases to about $0.1\,\mathrm{mol_{O_2}/mol_{tot}}$ (about 50 % of the inlet value) at the outer edges of the cells. Here the only difference lies in the width of the region with this minimal value. In general it is thinner in the upstream regions, for each as well as among the cells. In contradiction to this rather uniform overall behavior, the total values of the minima from the center bars are dependent on the oxygen's molar fraction at the inlet of the respective cell. In any case, the oxygen fraction decreases to about 80 % of this value. Both phenomena have their origin in the diffusion controlled mass transport inside the cathode. While the edges are only connected to the gas-channel from one side, the center region is in direct contact with the main flow. Next to the reduced length the oxygen molecules have to travel through the electrode, this aspect facilitates a mass exchange. Since the dimensions of the IC transverse to the flow (χ-direction) are minimized in the "simplified geometry", coverage dependencies are not very pronounced in this direction. However, the bottom image in Figure 6.15 shows some minor effects on the oxygen's molar fraction similar to those of the center bars.

Altogether it can be said that the limited supply of the AB with oxygen from the cathode has a direct influence on the overall operational behavior of the cell. The limitation in oxygen availability can either be addressed by enhancing the transport properties of the cathode, which is difficult, since e.g. an enlarged porosity lowers the already very small electric conductivity even further, or by altering the geometry of the IC. For instance, the covered regions at the beginning and end of each cell stripe could be moved towards the middle. Maybe this would even make it possible to waive the center bar and to end up with larger uncovered regions of the cathode. However, the complexity if the IC's geometry would be increased, making manufacturing and sealing more difficult.

Going on with the other electrochemical fuel, carbon monoxide (CO), it follows a different picture than that of hydrogen. As Figure 6.16 shows, its molar fraction steadily increases from $y_{\mathrm{Mol_{\blacktriangle}mol_{\blacktriangle}CO}} \approx 2.35{\cdot}10^{-2}\,\mathrm{mol_{CO}/mol_{tot}}$ at the inlet (top left) to $y_{\mathrm{Mol_{\blacktriangle}mol_{\blacktriangle}CO}} \approx 4.41{\cdot}10^{-2}\,\mathrm{mol_{CO}/mol_{tot}}$ at the outlet of the third cell Ⓒ. The explanation for this behavior are the counteracting influences of electrochemistry and reformation.

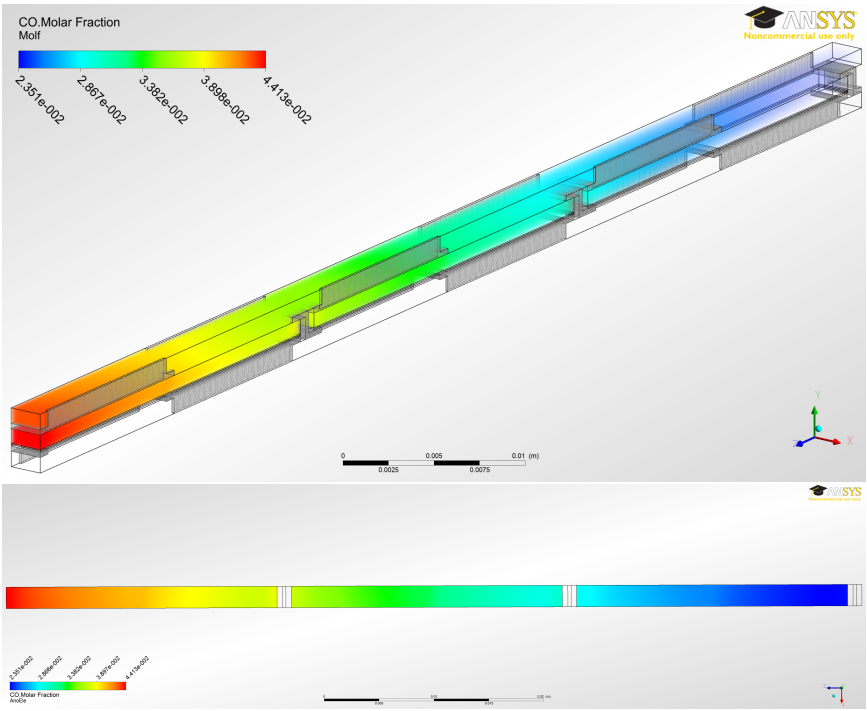

Figure 6.16.: **Molar fractions of CO:** The operating media pass the flow channel in growing z-direction (top right to bottom left; cells Ⓐ to Ⓒ). Inside the porous anode CO is created by reformation from CH_4 with H_2O and consumed by electrochemistry (at the AB).

While the former consumes CO, the latter creates it from CH_4 and H_2O (see section 2.5). Since an increase in CO is apparent in flow direction, the reformation must be strong enough to outnumber the consumption by electrochemistry. An underpinning for this interpretation is the molar fraction profile of CH_4 (see Figure 6.17), which corresponds well to the one of CO but with different signs. In those regions where local maxima of CO exist (e.g. at the upstream region of the first cell Ⓐ in Figure 6.16), local minima of CH_4 are apparent.

While the fuel concentration depletes, the ones of the products (see Figures 6.18 and 6.19) increase in flow direction. Qualitatively, both gases show a similar behavior: The amount of steam homogeneously rises by about 0.5 ·

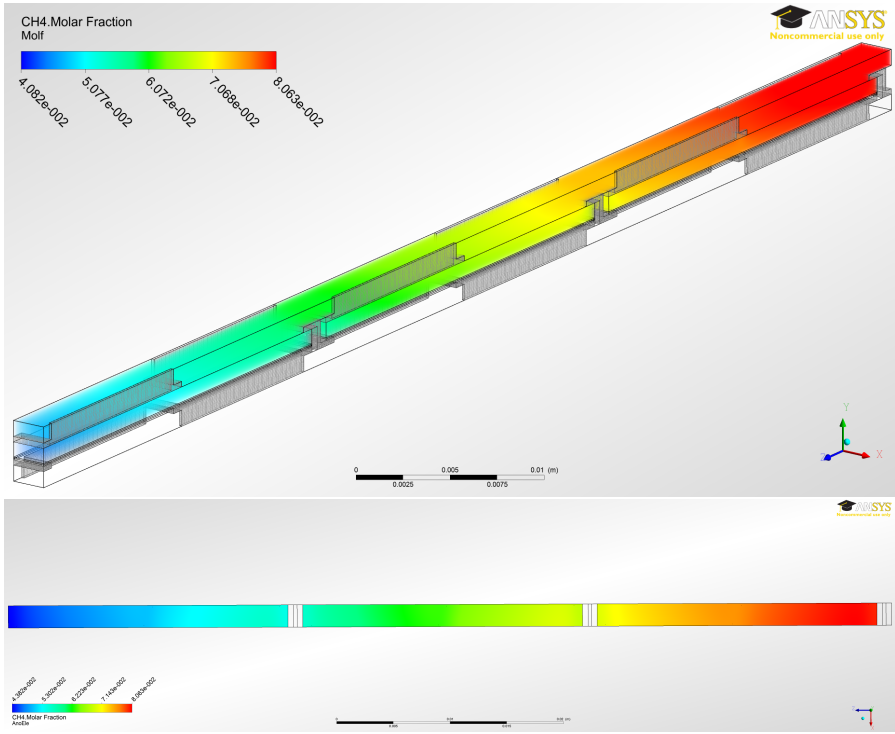

Figure 6.17.: **Molar fractions of CH_4:** The operating media pass the flow channel in growing z-direction (top right to bottom left; cells Ⓐ to Ⓒ). Inside the porous anode, CH_4 undergoes reformation reactions to form the fuel for electrochemistry.

10^{-2} mol_{H_2O}/mol_{tot} from cell to cell, the molar fraction of CO_2 increases by a factor of three from about $2.9 \cdot 10^{-3}$ mol_{CO_2}/mol_{tot} to $1.3 \cdot 10^{-2}$ mol_{CO_2}/mol_{tot} along the entire system. In contradiction to the reactants, the products show no surface dependency close to the AB (bottom images in Figures 6.18 and 6.19). For both, CO_2 and H_2O, the molar fraction in the gas-channel follows the one at the AB with some delay in upstream direction. Since the gases are efficiently transferred through the electrode to their sinks and from their sources, any changes in the electrode or the IC design are required for the anode domain. Table 6.3 in appendix A.5 summarizes the respective species mass-flows at the inlet and the outlet planes of the SOFC. As the table reveals, the total fuel consumption (referenced to the inlet mass flow of all fuels (CH_4,

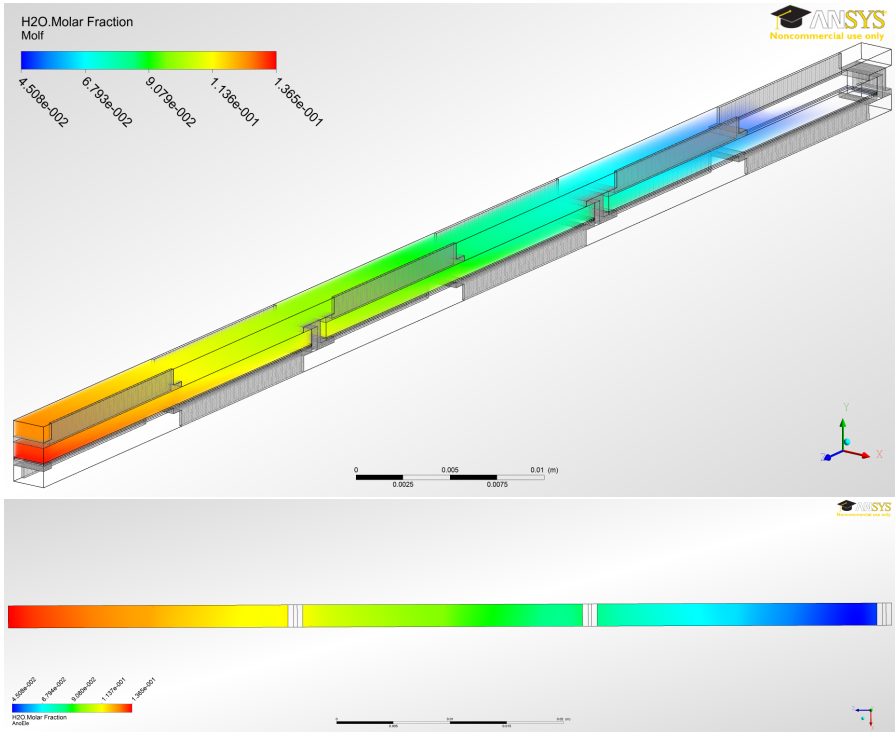

Figure 6.18.: **Molar fractions of H_2O:** The operating media pass the flow channel in growing z-direction (top right to bottom left; cells Ⓐ to Ⓒ). Inside the porous anode H_2O is consumed by the reformation reactions. The electrochemical conversion of H_2 and O^{2-} at the AB acts as source for H_2O.

CO, and H_2) is less than ten percent. Here CH_4 is consumed most (about 40 %), followed by H_2 (about 6 %), while even more CO leaves the system then enters it (about 92 %). In consequence, the three cell system is neither expected to be thermally governed by electrochemistry nor reformation, but by a balanced equilibrium between both factors.

6.1.4. Temperature distribution

Figure 6.20 shows the temperature distribution inside the system. In both domains the temperature steadily increases in flow direction by about 15 K per

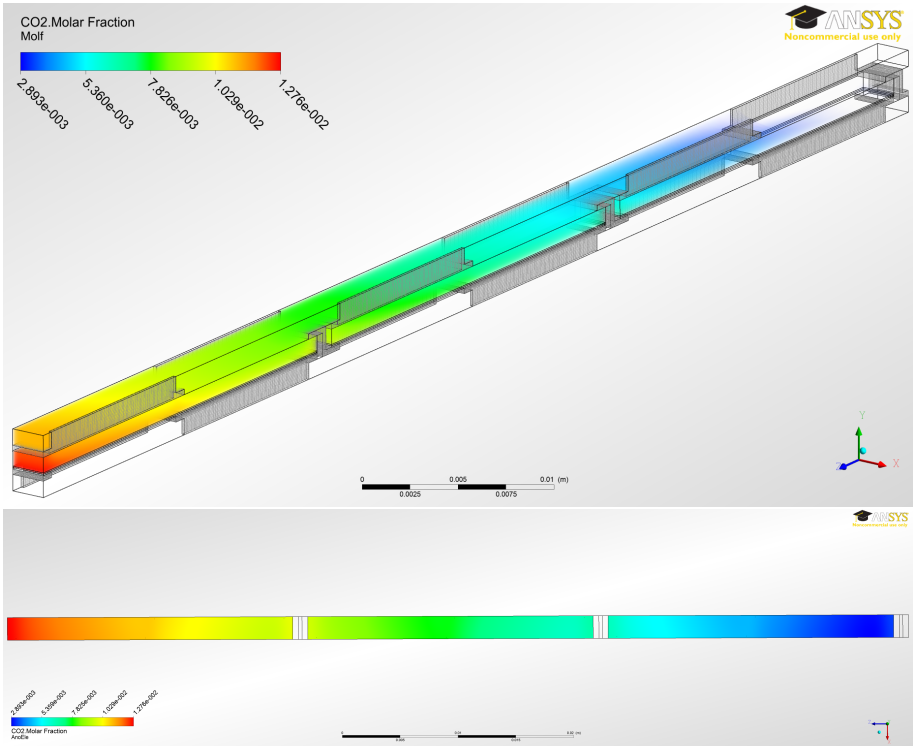

Figure 6.19.: **Molar fractions of CO_2:** The operating media pass the flow channel in growing z-direction (top right to bottom left). The electrochemical conversion of CO and O^{2-} at the AB acts as source for CO_2.

cell. In any case, the baffles of the IC act as heat exchangers, transferring the heat from the electrochemical reactions at the AB to the gas-phase. In particular in the anode domain this results on the one hand in a very fast heat up of the gases at the inlet of each cell and on the other hand in temperature differences in χ-direction, transverse to the flow direction (see Figure 6.21). Inside the anode a temperature gradient between the electrochemically AB and the electrode surface exists. Since neither a significant temperature decrease nor a complete conversion of CH_4 are apparent, the reformation reactions are rather slow and well balanced with electrochemistry. For the cathode domain the higher mass flow rate results in an extended influence of the inlet conditions on the system. Here for cells one (A) and two (B) the temperature homogenizes

in the second half of the cell. For the third cell Ⓒ this effect is no longer apparent.

In total the system is dominated by electrochemistry and the distribution of the released heat by the metallic components of the system. Since the "original geometry" has larger contact planes between gas-phase and solid, a further homogenization is to be expected. The recorded temperature differences are in the order of some Kelvins, thus significant mechanical tensions are not likely.

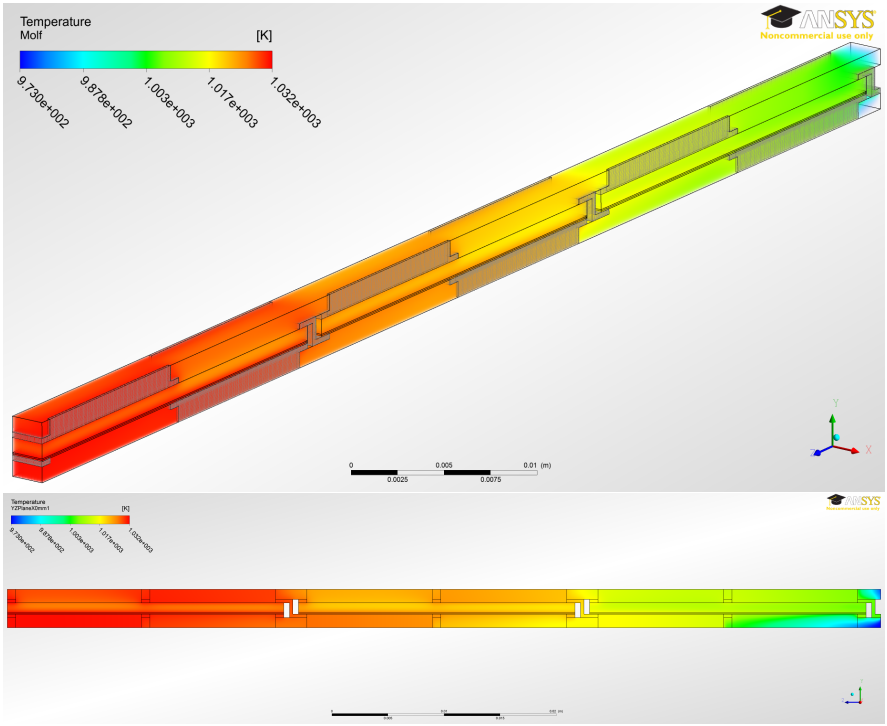

Figure 6.20.: **Temperature distribution:** The operating media pass the flow channel in growing z-direction (top right to bottom left; cells Ⓐ to Ⓒ). The electrochemical conversion of H_2, CO, and O^{2-} at the AB acts as heat source, while the reformation of methane inside the anode consumes heat. The figures show only the temperature inside the gas phase and the IC. To highlight the surfaces of the IC, in the upper image its mesh is displayed. The lower image shows a side view for a y-z-plane at $x = 1$ mm. Despite of a small inlet region, for both domains a steady increase in temperature is apparent.

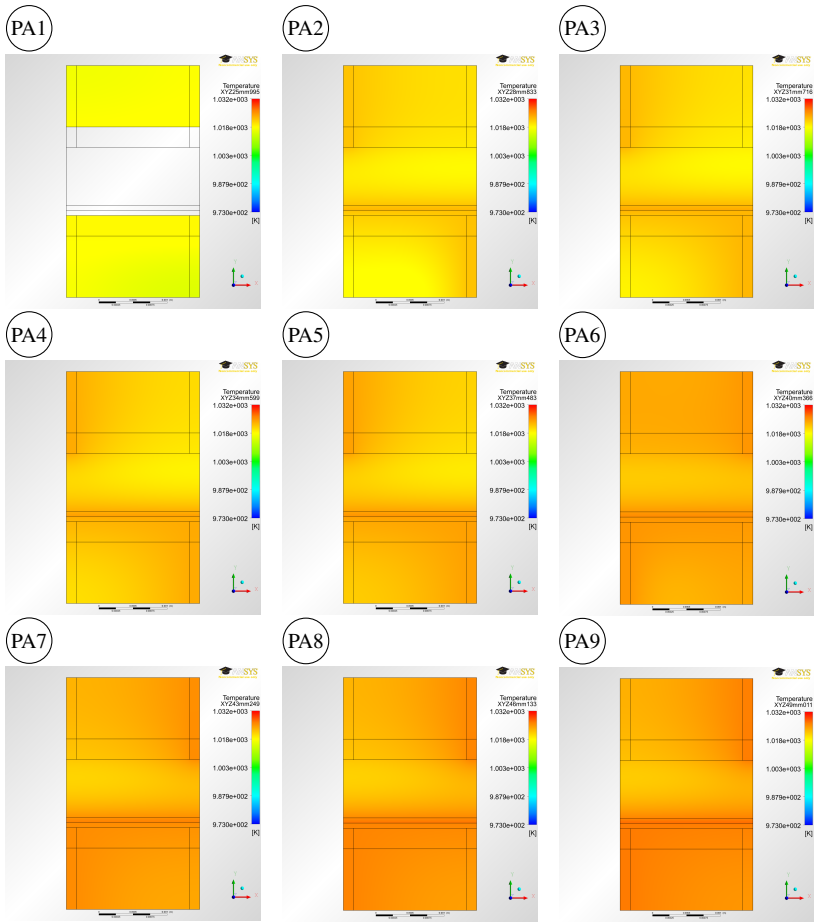

Figure 6.21.: **Temperature profiles inside the second cell:** The temperature profiles are evaluated at the second cell at the planes (PA1) - (PA9) shown in the topmost image in Figure 6.10. Displayed are the temperature in the gas-phase and the metallic IC. The values inside the solid structure of the electrodes are suppressed.

6.2. Parameter study

So far only the REC with a rather low inlet temperature and high operating voltage is discussed. Next to the inlet composition of the operating media, both parameters have a high influence on the state variables of the SOFC system. Since slight variations of the inlet composition primarily result in a shift of the REC's results in flow direction, it is assumed to be fixed for this study. Therefore, the subsequent investigation focuses on a variation in the operating voltage $\Delta\phi_{el}$ and an alternative inlet temperature T_{in}. In order to reduce the number of repetitions with the previous subsections, only the primary differences are emphasized subsequently. The balances of the subsequent investigation are summarized in appendix A.5.

6.2.1. Variation in the electric potential

Compared to the REC, here the overall difference in electric potential is varied from $\Delta\phi_{el} = 2.4\,V$ to $\Delta\phi_{el} = 2.7\,V$[5] (High Potential Case (HPC)) and to $\Delta\phi_{el} = 2.1\,V$[6] (Low Potential Case (LPC)). These variations lead to the average current and power densities summarized in Tables A.7 and A.19 in appendix A.5. The local distribution of the electric state variables ϕ_{el}, $\vec{I}_{el}$, and $\vec{j}_{el}$ under variation of $\Delta\phi_{el}$ is qualitatively similar to the situation of the REC in Figure 6.2. Deviations are apparent for the local distribution of the Nernst potential at the AB (see Figure 6.3 for the REC and Figure 6.22). While the REC shows an almost homogeneous decay from $U_{Nernst} \approx 1.06\,V$ at the inlet to $U_{Nernst} \approx 1.04\,V$ at the outlet of the system, in the HPC U_{Nernst} decays from about $U_{Nernst} \approx 1.11\,V$ to $U_{Nernst} \approx 1.06\,V$. In the LPC the values vary from $U_{Nernst} \approx 1.06\,V$ to $U_{Nernst} \approx 0.85\,V$. Since U_{Nernst} is dependent on the local concentration of the reactants and the products (see section 2.3.1.1), rather homogeneous profiles of the molar fractions of CO, CO_2, H_2, H_2O, and O_2 can be expected at the AB. Since the current densities show strong location and coverage dependent profiles (see Figure 6.23), the rather homogeneous trends are overlaid with coverage dependent effects. The Figure also shows that the profile of $\vec{j}_{el_{\blacktriangle}CO}$ changes its direction from a decrease in flow direction in the HPC and the REC to an increase in the LPC. In consequence, in the LPC either the concentration of CO must increase significantly or the electrochemical

[5] operating voltage of $\Delta\phi_{el} \approx 0.9\,V$ per cell

[6] operating voltage of $\phi_{el} \approx 0.7\,V$ per cell

$\Delta\phi_{el} = 2.7$ V (HPC):

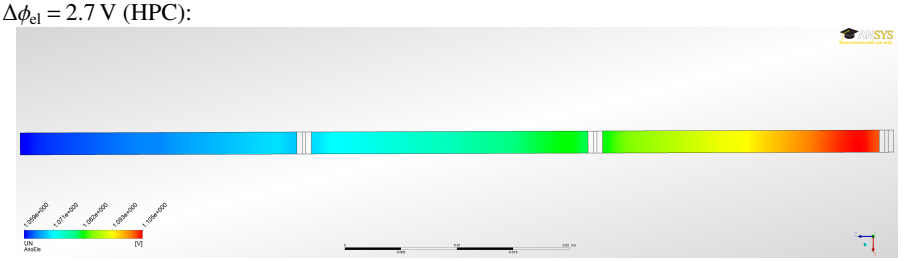

$\Delta\phi_{el} = 2.1$ V (LPC):

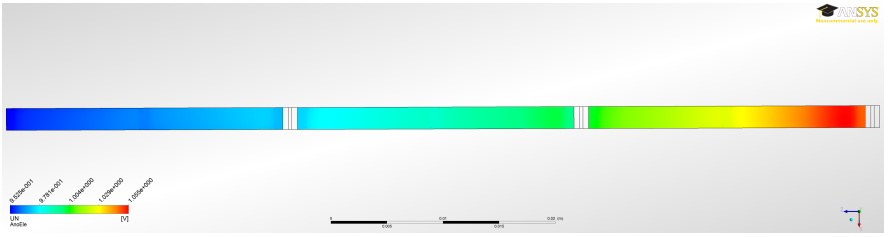

Figure 6.22.: **Distribution of the Nernst potential at the AB ($\Delta\phi_{el} = 2.7$ V and $\Delta\phi_{el} = 2.1$ V):** The operating media pass the system in growing z-direction (cells Ⓐ to Ⓒ from right to left). Including the results for the REC in Figure 6.3, U_{Nernst} is proportional to the operating voltage.

reactions switch from H_2 to CO conversion. Since $\vec{j}_{el,H_2,ave}$ is still about an order of magnitude larger than $\vec{j}_{el,CO,ave}$, the latter might occur due to either an increased CO concentration in the downstream region of the cell or a steam enrichment in the anodic off-gas. This would limit $\vec{j}_{el,H_2}$ and promote $\vec{j}_{el,CO}$ in order to provide the needed electric current.

Figures 6.24 to 6.31 show the respective values of $y_{Mol,mol,i}$ for the two cases. For both cases, the methane's molar fraction decreases in flow direction (see Figure 6.24). The absolute values scale with the operating voltage: Higher voltage results in reduced electrochemical activity with less heat production and reduced reformation, thus higher fractions of CH_4. A comparison of the relative profiles for the two cases reveals a change in CH_4 from the inlet to the outlet of the system by only about 21 % for the HPC, compared to more than 84 % in the LPC. This means that, for the given operating conditions, the cooling effect from reformation only lasts for maybe one additional cell in the latter case. In contradiction, under the HPC conditions it is even possible that unreformed CH_4 leaves the original eight cell system. In both cases the profiles

$\vec{j}_{\mathrm{el}_{\blacktriangle}\mathrm{CO}}$, $\Delta\phi_{\mathrm{el}} = 2.7$ V (HPC):

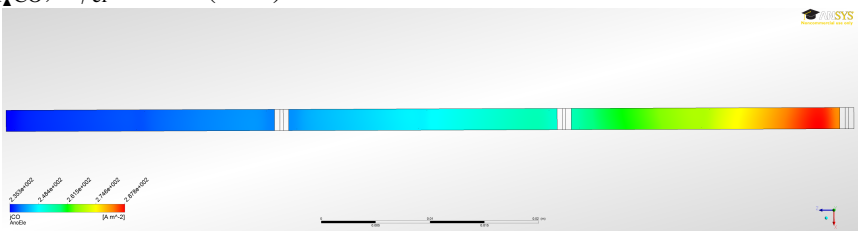

$\vec{j}_{\mathrm{el}_{\blacktriangle}\mathrm{CO}}$, $\Delta\phi_{\mathrm{el}} = 2.1$ V (LPC):

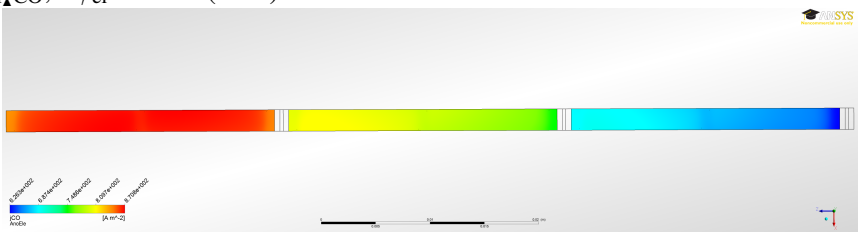

$\vec{j}_{\mathrm{el}_{\blacktriangle}\mathrm{H_2}}$, $\Delta\phi_{\mathrm{el}} = 2.7$ V (HPC):

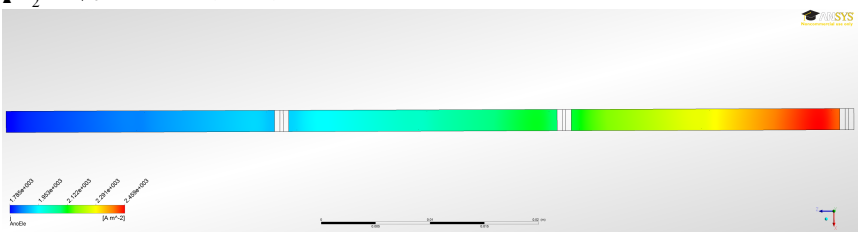

$\vec{j}_{\mathrm{el}_{\blacktriangle}\mathrm{H_2}}$, $\Delta\phi_{\mathrm{el}} = 2.1$ V (LPC):

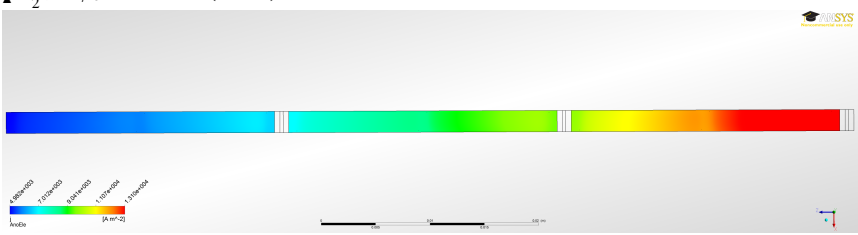

Figure 6.23.: **Current density distribution at the anode's AB at $T_{\mathrm{in}} = 973$ K and $\Delta\phi_{\mathrm{el}} = 1.8$ V:** The operating media pass the system in growing z-direction (cells Ⓐ to Ⓒ from right to left). For CO (upper two images) the variation in the operating voltage leads to a reversal in the current density profile. While $\vec{j}_{\mathrm{el}_{\blacktriangle}\mathrm{CO}}$ steadily decreases in the HPC, it increases in the LPC. For H_2 (lower two images) the reaction rate steadily decreases in flow direction. In both cases the coverage of the electrodes by the IC has an influence on $\vec{j}_{\mathrm{el}}$.

CH_4, $\Delta\phi_{el} = 2.7$ V (HPC):

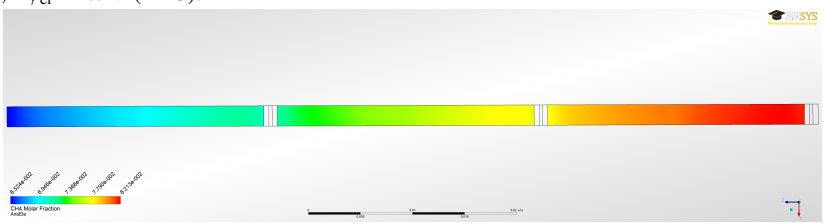

CH_4, $\Delta\phi_{el} = 2.1$ V (LPC):

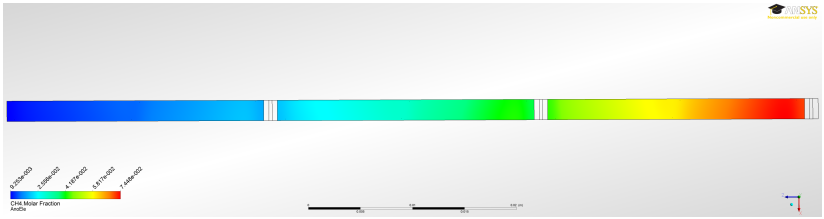

Figure 6.24.: **Molar fractions of CH_4 at the AB at $T_{in} = 973$ K:** The operating media pass the system in growing z-direction (cells Ⓐ to Ⓒ from right to left).

show local dependencies on the coverage by the IC[7]. In the covered regions at the edges of the cells local minima exist, which might either be a consequence of the limited gas transport or of local temperature maxima. Coverage dependencies are also apparent in both cases in the molar fractions of CO at the AB (see Figure 6.25). While the molar fraction of CO increases in the HPC by about 76 % between in- and outlet of the system, it is more than doubled in the LPC. Hereby, in cell three Ⓒ of the latter case $y_{\mathrm{Mol}\blacktriangle\mathrm{mol}\blacktriangle\mathrm{CO}}$ remains almost constant on a high level. Although the numbers of the LPC are much higher (factor 1.6 to 3.3), the molar fraction profiles of CO_2 look very similar for both potentials (see Figure 6.26): A steady increase with an almost uniform rate from the inlet to the outlet. In consequence, the conditions are better for CO electrochemistry in the LPC. To deal with the theory of limiting factors for H_2 electrochemistry, it is necessary to look at the molar fraction profiles of H_2 and H_2O at the AB. The former is plotted in Figure 6.28. In both cases, the profile shows a, qualitatively similar, steady decay from the inlet to the outlet.[8] The differences arise when looking at the numerical values: While $y_{\mathrm{Mol}\blacktriangle\mathrm{mol}\blacktriangle\mathrm{H_2}}$ is

[7] In particular the regions at the end of the first cell and the beginning of the second one.

[8] Slightly more pronounced coverage dependent minima at the edges of cells two Ⓑ and three Ⓒ in the LPC.

CO, $\Delta\phi_{el} = 2.7$ V (HPC):

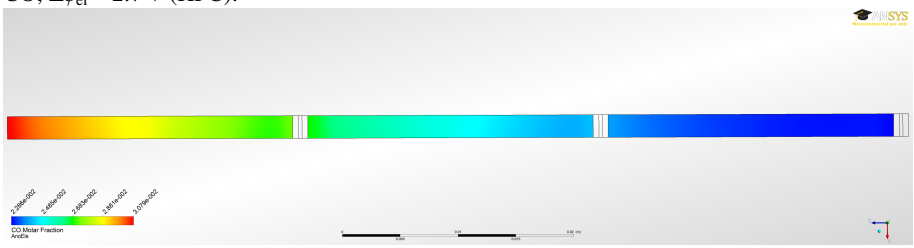

CO, $\Delta\phi_{el} = 2.1$ V (LPC):

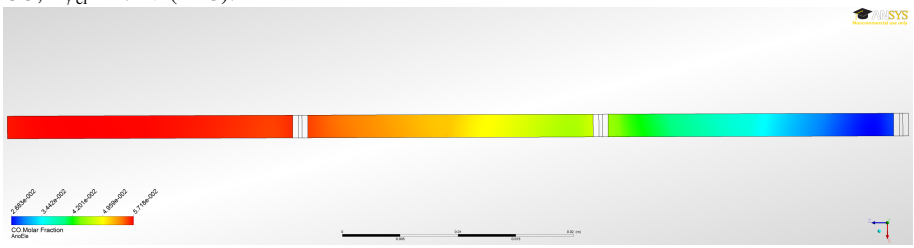

Figure 6.25.: **Molar fractions of CO at the AB at $T_{in} = 973$ K:** The operating media pass the system in growing z-direction (cells Ⓐ to Ⓒ from right to left).

CO_2, $\Delta\phi_{el} = 2.7$ V (HPC):

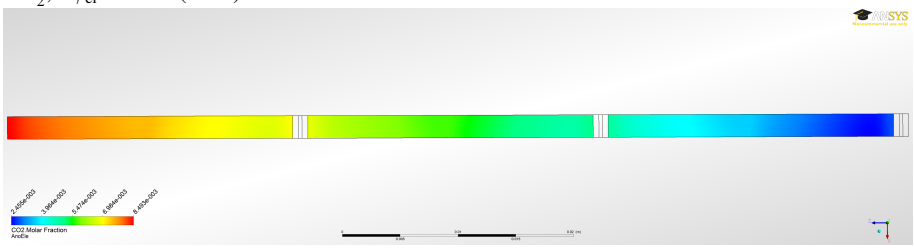

CO_2, $\Delta\phi_{el} = 2.1$ V (LPC):

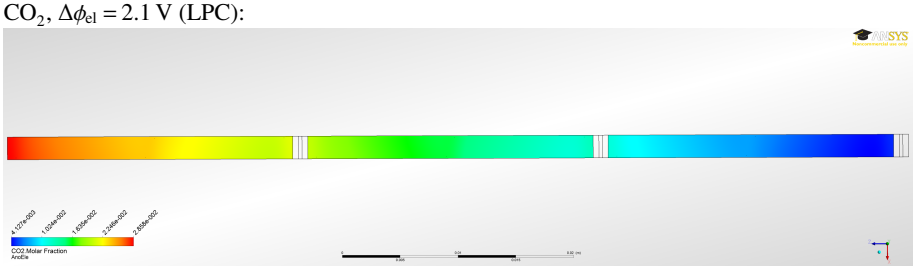

Figure 6.26.: **Molar fractions of CO_2 at the AB at $T_{in} = 973$ K:** The operating media pass the system in growing z-direction (cells Ⓐ to Ⓒ from right to left).

H_2, $\Delta\phi_{el} = 2.7$ V (HPC):

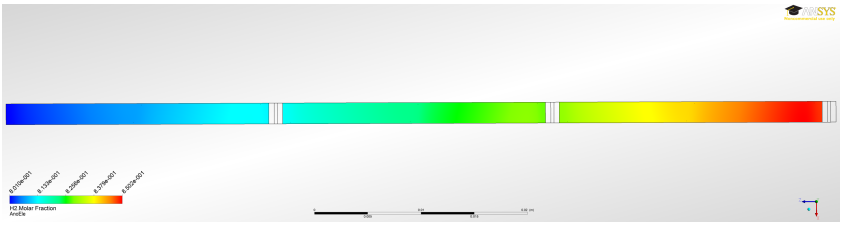

H_2, $\Delta\phi_{el} = 2.1$ V (LPC):

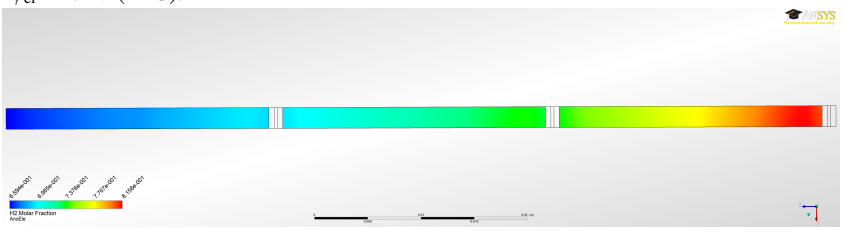

Figure 6.27.: **Molar fractions of H_2 at the AB at $T_{in} = 973$ K:** The operating media pass the system in growing z-direction (cells Ⓐ to Ⓒ from right to left).

H_2O, $\Delta\phi_{el} = 2.7$ V (HPC):

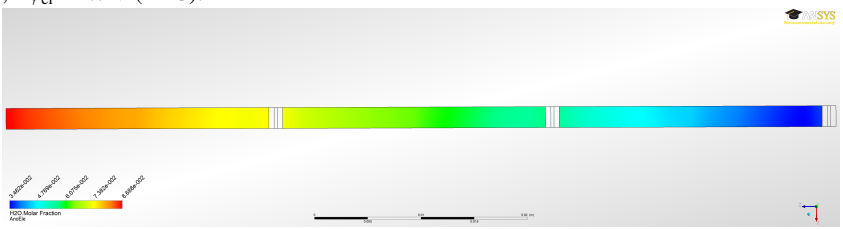

H_2O, $\Delta\phi_{el} = 2.1$ V (LPC):

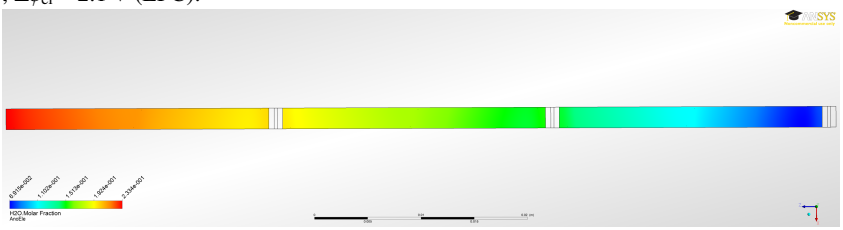

Figure 6.28.: **Molar fractions of H_2O at the AB at $T_{in} = 973$ K:** The operating media pass the system in growing z-direction (cells Ⓐ to Ⓒ from right to left).

decreased only by approximately 6 % (0.85 to 0.8 mol_{H_2}/mol_{tot}) in the HPC, it looses almost 20 % (0.82 to 0.66 mol_{H_2}/mol_{tot}) in the LPC. A look on the respective profiles for steam in Figure 6.28 completes the picture: Again similar profiles with a steady increase[9] in $y_{Mol\blacktriangle mol\blacktriangle H_2O}$ and maxima under the covered ends of the cell stripes[10]. While the steam fraction in the HPC increases only by a factor of 2.5 to about 8.7 % in flow direction, it more than triples its value to about 23.3 % in the LPC. Altogether, the species distribution hinders H_2 electrochemistry in the LPC, compared to the HPC. In consequence, the gain of the CO electrochemistry's importance in flow direction is larger in the LPC.

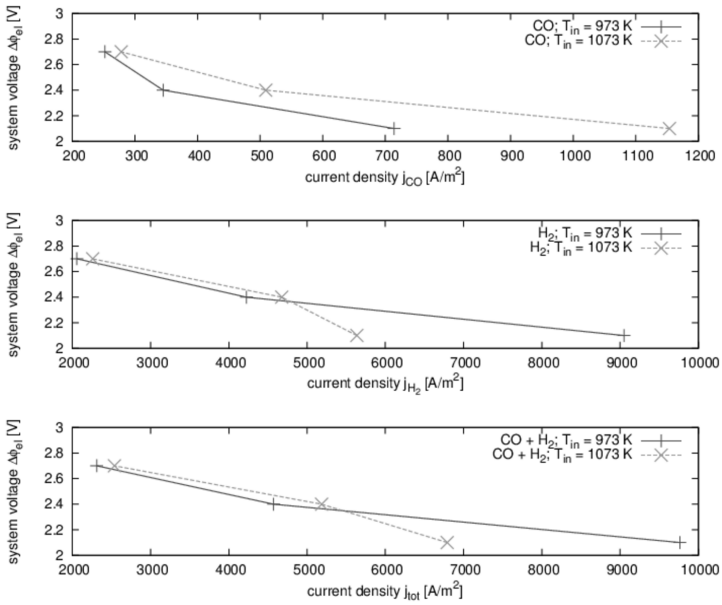

Figure 6.29.: **Polarization curves of the investigated system at different inlet temperatures:** The polarization curves show the dependence of the system's electric potential on the average of the current density over the three cells of the system. The upper image shows the curves for the electrochemical conversion of CO, the middle one the curves for hydrogen electrochemistry, and the lower one their sum. In all cases $\vec{j}_{el}$ increases with decreasing system voltage.

[9] due to electrochemistry

[10] but significant differences in the numerical values

Figure 6.29 shows the polarization curves for the average current density from CO electrochemistry (top), hydrogen electrochemistry (middle), and their sum (bottom). In all cases $\Delta\phi_{\mathrm{el}}$ decreases with increasing $\vec{j}_{\mathrm{el}}$. In any case the current density from CO is significantly smaller compared to the H_2 one. Only for the LPC at increased temperature the ratio shifts towards CO. Possible reasons for this will be addressed below in the discussion of the effects of an increased inlet temperature on the system.

Figure 6.30 shows the quotients of $\vec{j}_{\mathrm{CO}}/\vec{j}_{\mathrm{H_2}}$ in all three investigated cases and underlines the trend from the polarization curves. The ratio of $\vec{j}_{\blacktriangle \mathrm{CO}}$ to $\vec{j}_{\blacktriangle \mathrm{H_2}}$ increases steadily in flow direction. While it is rather constant for high operating voltages, the gradient increases with decreasing operating voltage. As Figure 6.31 shows, the extrema under the covered parts of the electrodes have again their roots in the limited oxygen supply from the cathode. In particular at the edges of the cell stripes even regions without any remaining oxygen are apparent in the LPC. The large changes in $y_{\mathrm{Mol}_{\blacktriangle}\mathrm{mol}_{\blacktriangle}i}$ under the covered ends of the IC make it obvious that the concept should be improved here. In particular to prevent a fuel starvation and thus concentration losses in this area, the bridges in upstream direction should be made thinner.

Neither in the HPC (see Figure 6.32) nor in the LPC (see Figure 6.33) coverage dependent effect are apparent in the temperature profile. Qualitatively, both profiles show a similar behavior to the so far discussed REC: The inlet temperature dominates the beginning of the first cell, the released heat from the electrochemical reactions and ohmic losses, leads to a system heat up in flow direction. While the overall gain in temperature is less than 20 K in the HPC, T rises by more than 150 K from 973 K up to almost 1130 K in the LPC. In particular, the first cell Ⓐ of the LPC faces temperature differences of approximately 100 K between the AB and the surfaces of the electrodes. Since the HPC is completely governed by the inlet temperature, fast changes from the HPC to the LPC would lead to significant mechanical tensions on the components. Thus the system should be heated up slowly at open circuit voltage to reduce the released heat. Subsequently, the load can be carefully adjusted to bring the system in the desired working point. As discussed, in the first cell Ⓐ strong influences of the inlet conditions as well as temperature gradients perpendicular to the electrode surfaces exist. Thus the influence of a variation of the inlet temperature is studied in the subsequent subsection.

$\vec{j}_{CO}/\vec{j}_{H_2}$, $\Delta\phi_{el} = 2.7$ V (HPC):

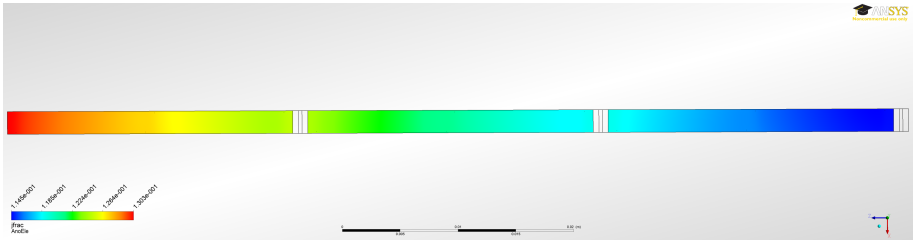

$\vec{j}_{CO}/\vec{j}_{H_2}$, $\Delta\phi_{el} = 2.4$ V (REC):

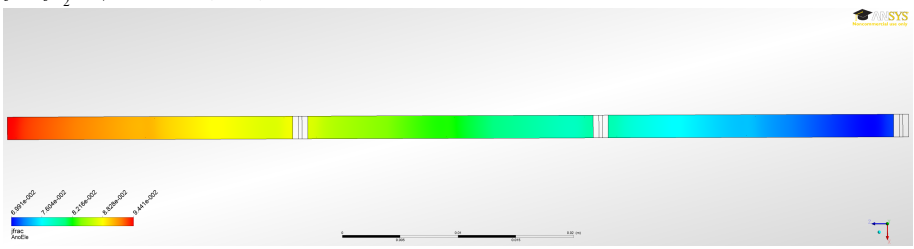

$\vec{j}_{CO}/\vec{j}_{H_2}$, $\Delta\phi_{el} = 2.1$ V (LPC):

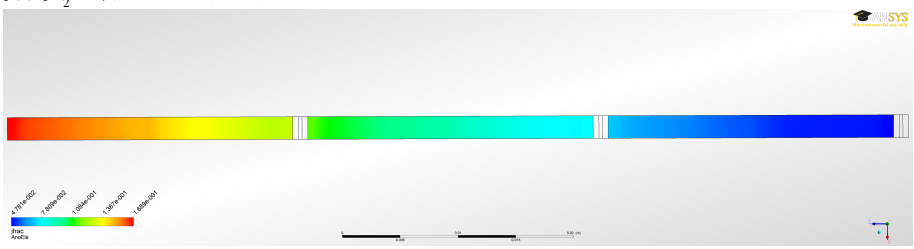

Figure 6.30.: **Quotients of $\vec{j}_{CO}/\vec{j}_{H_2}$ at different cell voltages:** The operating media pass the system in growing z-direction (cells (A) to (C) from right to left). While the ratio is almost constant in the HPC (top), the importance of $\vec{j}_{CO}$ rises in flow direction with decreased operational voltage (note the different ranges of the color bars).

O_2, $\Delta\phi_{el} = 2.7$ V (HPC):

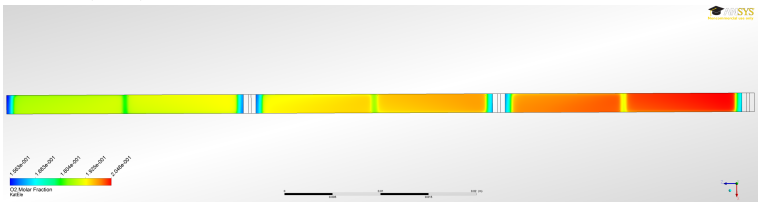

O_2, $\Delta\phi_{el} = 2.1$ V (LPC):

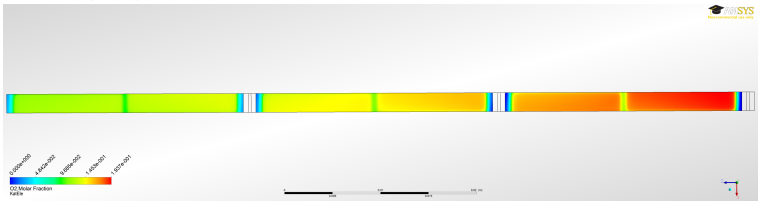

Figure 6.31.: **Molar fractions of O_2 at the AB at $T_{in} = 973$ K:** The operating media pass the system in growing z-direction (cells (A) to (C) from right to left). Under the covered parts of the cathode the oxygen's molar fraction decreases significantly, compared to the uncovered ones.

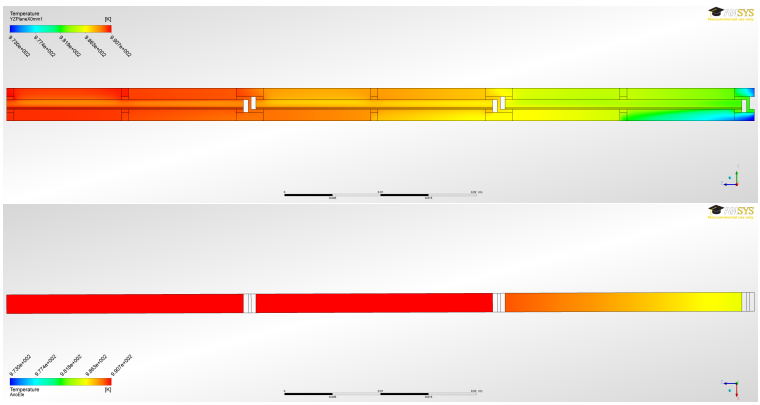

Figure 6.32.: **Temperature distribution at $T_{in} = 973$ K and $\Delta\phi_{el} = 2.7$ V (HPC):** The operating media pass the flow channel in growing z-direction (cells (A) to (C) from right to left). The electrochemical conversion of H_2, CO, and O^{2-} at the AB acts as heat source, while the reformation of methane inside the anode consumes heat. The upper image shows the situation in a y-z-plane at $\chi = 0.1$ mm. Inside the anode (upper part) cooling effects from reformation show no significant influence on the temperature. The lower image shows the temperature distribution at the anode's side of the AB. T grows only by about 8 K between in- and outlet.

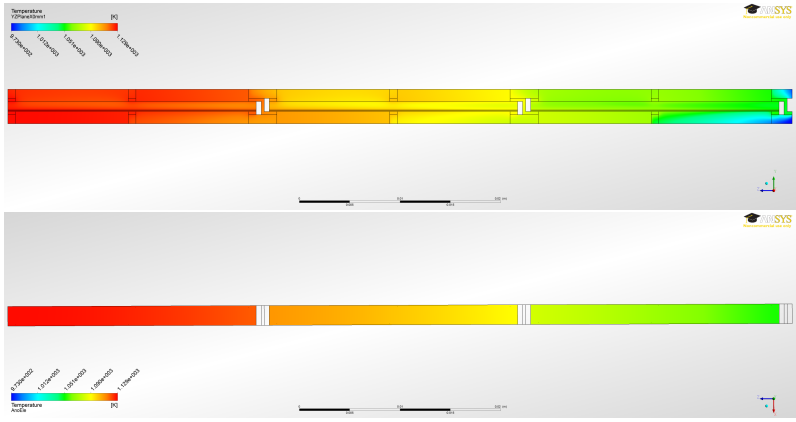

Figure 6.33.: **Temperature distribution at $T_{\mathrm{in}} = 973\,\mathrm{K}$ and $\Delta\phi_{\mathrm{el}} = 2.1\,\mathrm{V}$ (LPC):** Despite of the inlet temperature, the situation is similar to the caption of Figure 6.32. Inside the anode (upper part) cooling effects from reformation possess only inside the first cell (A) a significant effect on the temperature. The lower image shows the temperature at the anode's side of the AB. While T grows by about 40 K in the first cell (A), it is almost constant in the third cell (C).

$\Delta\phi_{\mathrm{el}} = 2.7\,\mathrm{V}$:

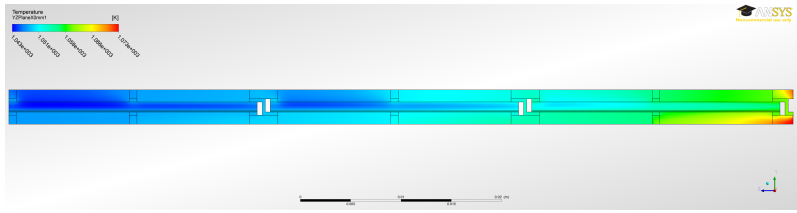

$\Delta\phi_{\mathrm{el}} = 2.1\,\mathrm{V}$:

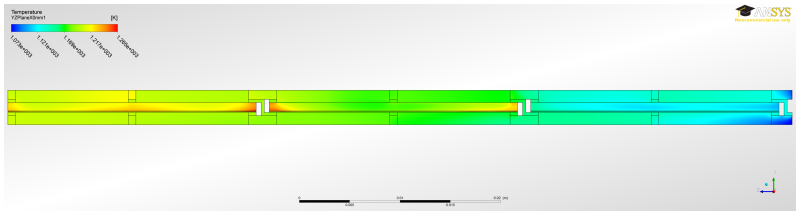

Figure 6.34.: **Temperature distribution $T_{\mathrm{in}} = 1073\,\mathrm{K}$ for different cell voltages:** Both images show the temperature distribution in a y-z-plane at $x = 0.1\,\mathrm{mm}$. While in the upper image an operating voltage of $\Delta\phi_{\mathrm{el}} = 2.7\,\mathrm{V}$ is apparent, in the lower one $\Delta\phi_{\mathrm{el}} = 2.1\,\mathrm{V}$.

6.2.2. Variation of the inlet temperature

Compared to the REC, here the inlet temperature at either side of the PEN is varied from $T_{in} = 973\,K$ to $T_{in} = 1073\,K$. This variation leads to the average current and power densities summarized in Tables A.11 to A.23 in appendix A.5.

Relative to the REC (see Table 6.5), the respective cell voltages are almost identical. Nevertheless, due to the enhanced electrochemical activity, the average current and power densities are increased by about 24 % (cell Ⓐ), 12 % (cell Ⓑ), and 2 % (cell Ⓒ). This finding correlates well with findings in the literature, whose authors intend an increase in operational temperature to counterbalance negative effects from long term degradation phenomena (de Haart 2010). In consequence, with sufficient experimental and/or simulated data, the cell voltage and power density, together with the average operating temperature, can be used for lifetime estimation.

The stepwise lowering of the gain in power density, compared to the REC, is either a consequence of a significant loss in temperature and/or changes in reactant concentration, both reducing the electrochemical activity of the system in flow direction.

The increased inlet temperature leads to a significantly accelerated reformation kinetics. While about 40 % of the inlet's methane is converted in the REC, here almost 80 % undergoes reformation reactions. As Figure 6.35 shows, this has an outstanding influence on the temperature distribution inside the system. While T increases steadily in the REC (see Figure 6.20), here temperature minima inside the anode support structure and the heating of the operating media via the IC's surfaces can be observed. Although the color scheme of Figure 6.35 suggests a more pronounced thermal profiling, compared to the REC, the variations are just in the range of 5 K to 10 K. The overall increase[11] in T is only about 50 % of the REC's one. In the REC, the increase in temperature occurs primarily inside the first cell of the series connection (more than 40 K). As the comparison of the local temperature distribution in the second cell's Ⓑ plane (PA5) shows in Figure 6.36, the relative temperature profiles are very similar. In either case the temperature varies by about 7 K between the hottest regions inside the IC and on the anode side of the AB, and the respective local minima inside the anode support structure. To generate the comparison, in both

[11] approximately 30 K

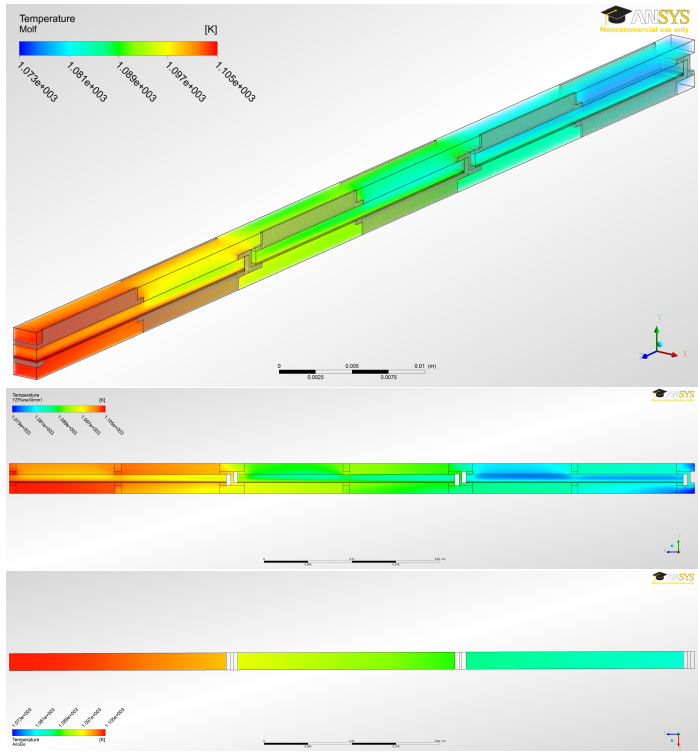

Figure 6.35.: **Temperature distribution at $T_{\mathrm{in}} = 1073\,\mathrm{K}$ and $\Delta\phi_{\mathrm{el}} = 2.4\,\mathrm{V}$:** The operating media pass the flow channel in growing z-direction (top right to bottom left; cells Ⓐ to Ⓒ). The electrochemical conversion of H_2, CO, and O^{2-} at the AB in the center plane of the cells acts as heat source, while the reformation of methane inside the anode consumes heat. The figures show only the temperature inside the gas phase. While the temperature inside the electrodes and the gas channel is highly dependent on the influences of electrochemistry and reformation (upper images), it is almost constant at the AB (bottom figure).

cases this minimal temperature is used as "reference temperature" T_{ref}. Thus, the thermomechanical tensions in cells Ⓑ and Ⓒ can expected to be in the same order of magnitude. However, as in particular the temperature profiles at the anode side of the AB show (see bottom images in Figures 6.20 and 6.35), the temperature gets more uniform in the first cell Ⓐ with increased inlet temperature. In consequence, for cell Ⓐ the current case seems to be beneficial for

$T_{in} = 973$ K: $T_{in} = 1073$ K:

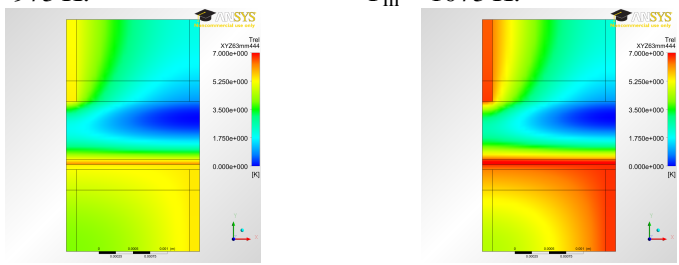

Figure 6.36.: **Relative temperature distribution at different inlet temperatures:** The images show the local temperature distribution at the (PA5) plane for $\Delta\phi_{el} = 2.4$ V and $T_{in} = 973$ K (left) and for $\Delta\phi_{el} = 2.4$ V and $T_{in} = 1073$ K (right). Both figures show the temperature difference to the respective local minimum (left: $T_{ref} = 1025$ K, right: $T_{ref} = 1095$ K). Apart from the heat up of the cathode's operating media by the IC, inside the anode the temperature variations are very similar in both cases.

reducing thermal stresses. As Figure 6.34 shows, a variation of the operating voltage results in significant changes in the temperature distribution. While an increase in the cell voltage leads to a dominance of the cooling from reformation (about 50 K in flow direction for $\Delta\phi_{el} = 2.7$ V), T increases by almost 90 K in flow direction for $\Delta\phi_{el} = 2.1$ V.

In contrast to almost 80 % of the inlet's methane, which is converted after the end of cell three (C) at $\Delta\phi_{el} = 2.4$ V, the conversion ratio is reduced to about 46 % with increasing $\Delta\phi_{el}$ to 2.7 V. While for the first case the temperature homogenization will not go much further than an additional fourth cell, it will be active for several additional cells in the second case. Altogether it can be said that an inlet temperature of about 1100 K and a cell voltage between 0.8 V and 0.9 V per cell result in a rather homogeneous temperature profile under the given inlet composition.

6.3. Fuel conversion, power density, and efficiency

This section compares the fuel conversion, power density, and efficiency of all investigated cases. Next to the fuel and voltage efficiency a "total efficiency" $\eta_{\%,tot}$ for the entire system is derived. The section ends with an investigation of the fuel conversion in longer cascades.

6.3.1. Fuel conversion

The investigated system converts CH_4, CO, and H_2 as fuels for reformation and electrochemistry, thus the fuel conversion ratio[12] for each of the species as well as a "total conversion ratio"[13], as the quotient of the sum of their mass flows at the in- and the outlet of the system[14], can be calculated. The values of the fuel efficiency[15] $\eta_{\%,\mathrm{fuel}\blacktriangle i}$ for CH_4, CO, and H_2 as well as the "total fuel efficiency" $\eta_{\%,\mathrm{fuel}\blacktriangle \mathrm{tot}}$:

$$\eta_{\%,\mathrm{fuel}\blacktriangle \mathrm{tot}} = 100 \cdot \left(1 - \frac{1}{\dot{m}^{\,0}_{\mathrm{Mass}\blacktriangle \mathrm{CH_4}} h^{\,0}_{\mathrm{mass}\blacktriangle \mathrm{CH_4}} + \dot{m}^{\,0}_{\mathrm{Mass}\blacktriangle \mathrm{CO}} h^{\,0}_{\mathrm{mass}\blacktriangle \mathrm{CO}} + \dot{m}^{\,0}_{\mathrm{Mass}\blacktriangle \mathrm{H_2}} h^{\,0}_{\mathrm{mass}\blacktriangle \mathrm{H_2}}} \cdot \left[\dot{m}_{\mathrm{Mass}\blacktriangle \mathrm{CH_4}\blacktriangle \mathrm{out}} h_{\mathrm{mass}\blacktriangle \mathrm{CH_4}\blacktriangle \mathrm{out}} + \dot{m}_{\mathrm{Mass}\blacktriangle \mathrm{CO}\blacktriangle \mathrm{out}} h_{\mathrm{mass}\blacktriangle \mathrm{CO}\blacktriangle \mathrm{out}} + \dot{m}_{\mathrm{Mass}\blacktriangle \mathrm{H_2}\blacktriangle \mathrm{out}} h_{\mathrm{mass}\blacktriangle \mathrm{H_2}\blacktriangle \mathrm{out}} \right] \right) \; [\%] \tag{6.1}$$

are illustrated in Figure 6.37. Starting with methane in the topmost figure, the fuel efficiency is inversely proportional to the cell voltage and rises with the operating temperature. For $\Delta\phi_{\mathrm{el}} = 2.1\,\mathrm{V}$ its values increase to more than 80 %, thus the cooling potential from the reformation is almost completely exhausted. The profiles for CO in the second plot in Figure 6.37 reveal a different behavior of this species, compared to CH_4. Here in every case $\eta_{\%,\mathrm{fuel}\blacktriangle \mathrm{CO}}$ is negative, what means that more fuel leaves the system than enters it. This confusing behavior can be explained by the reformation acting as a source for CO. A higher reformation rate results in a higher fuel efficiency for CH_4 and a lower one for CO. Since the values of $\eta_{\%,\mathrm{fuel}\blacktriangle \mathrm{CO}}$ are negative, this process outnumbers the consumption by CO electrochemistry. Only for the $\Delta\phi_{\mathrm{el}} = 2.1\,\mathrm{V}$ cases almost identical values for $\eta_{\%,\mathrm{fuel}\blacktriangle \mathrm{CO}}$ are obtained. This seems to be a result of the almost complete conversion of CH_4 and the increased influence of CO electrochemistry in this case[16]. Since the anode's operating media is dominated by hydrogen[17], the total fuel efficiency profiles in the bottom figure are very much those of hydrogen. The latter are illustrated in the second image from the bottom in Figure 6.37. $\eta_{\%,\mathrm{fuel}\blacktriangle \mathrm{H_2}}$ is in an inversely proportional relationship to the operating voltage too. The main difference to CH_4 is in

[12] "fuel efficiency" $\eta_{\%,\mathrm{fuel}}$ in percent, see subsection 2.3.2
[13] "total fuel efficiency"
[14] weighted with their respective enthalpies
[15] fuel conversion relative to inlet values "0"
[16] see previous subsection
[17] see e.g. Table 6.3

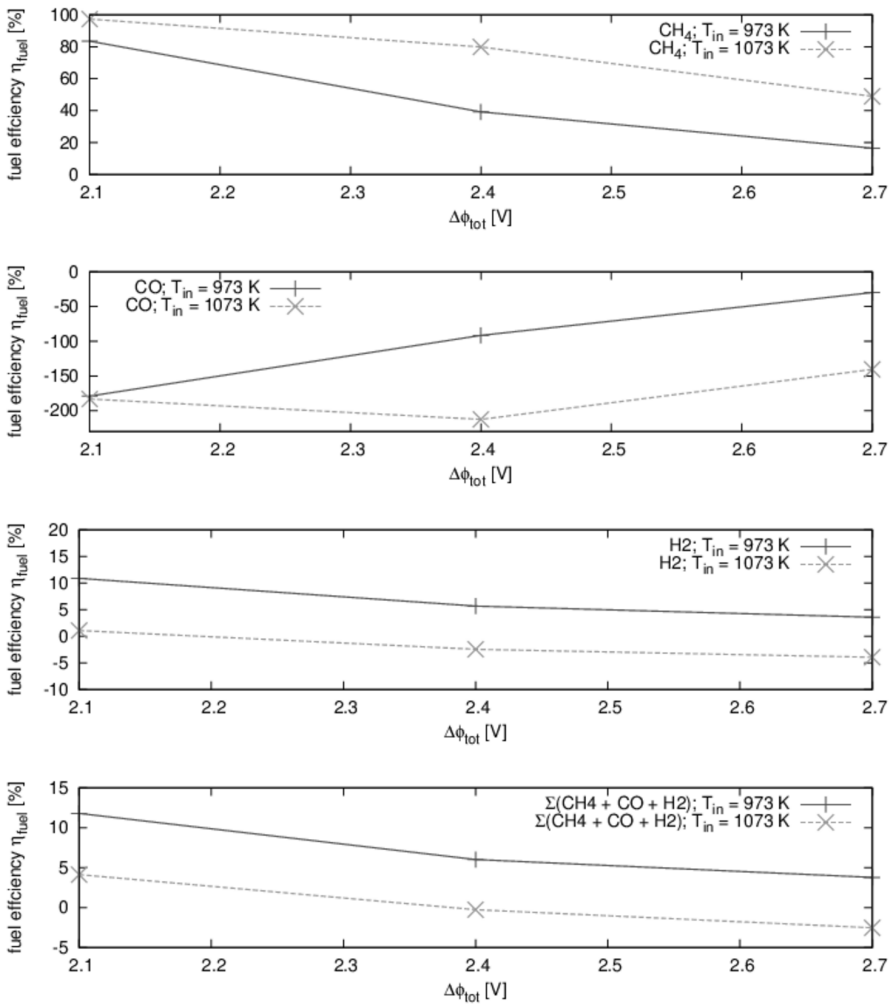

Figure 6.37.: **Fuel conversion ratios:** The figures show the fuel efficiency $\eta_{\%\,\mathrm{fuel}}$ for CH_4 (top), CO (second from top), and H_2 (second from bottom). The bottom figure shows the sum of all three components, calculated using equation 6.1. In several cases the calculated efficiency is negative, since more fuel leaves the system than enters it. The reason for this behavior is the creation of CO and H_2 by reformation.

the reversal of the temperature difference: Lower temperature leads to higher fuel efficiency. Since electrochemistry is boosted by rising T, the observed behavior must also be a consequence of a balancing effect from the H_2 creation by reformation. Altogether, the fuel efficiency of the investigated three-cell system is very small. For several cases it even becomes negative, since significantly more CO and/or H_2 leave the system[18] than enter it. Even if $\eta_{\%,\mathrm{fuel}\blacktriangle\mathrm{tot}}$ might grows with further reduction of the operating voltage, the negative effects on the temperature distribution, discussed in the previous sections, make this step not very feasible. Thus a higher fuel efficiency just seem to be possible with new materials for the PEN, increasing the oxygen supply rate, the current density, and finally the percentage of converted fuel. Alternatively, a modification of the inlet composition at the fuel gas side and/or more cells in the series connection could help to increase the fuel efficiency. Here, the effects on the local temperature distribution have to be considered. Before these aspects are highlighted in subsection 6.3.4, the electrical power density $\mathfrak{p}_{\mathrm{vol,el}}$ and the voltage efficiency $\eta_{\%,\mathrm{Volt}}$ are investigated in the next subsections.

6.3.2. Volumetric power density

The volumetric electric power density $\mathfrak{p}_{\mathrm{vol,el}}$ in $\mathrm{W_{el}/m^3}$ describes the electrical power output of the system per cubic meter. For the calculation only the active cell volume from the simulation is used. Auxiliary components, which increase the volume and lower the electrical net output of the system like housing, pipes or blowers are not considered. For the investigated cases, Figure 6.38 shows the average over the three cells of the system for the volumetric electric power density. Since $\mathfrak{p}_{\mathrm{vol,el}}$ is directly proportional to the current density $\vec{j}_{\mathrm{el}}$, the curves look similar to the polarization curves of the system. Like them, $\mathfrak{p}_{\mathrm{vol,el}}$ increases on the one hand with decreasing cell voltage and on the other hand with increasing temperature. While the power density almost doubles between the investigated electric potentials, the temperature variation just leads to minor changes of about 10 % or less. Interestingly, the point for $T_{\mathrm{in}} = 1073\,\mathrm{K}$ and $\Delta\phi_{\mathrm{el}} = 2.1\,\mathrm{V}$ doesn't follow the described trend for $\mathfrak{p}_{\mathrm{vol,el}\blacktriangle\mathrm{H_2}}$. As reported earlier, for this point the strongest limitations for hydrogen electrochemistry within the study are apparent. As discussed earlier, possible reasons might be a mass transport limitation from the cathode or interactions with the

[18] at an increased temperature

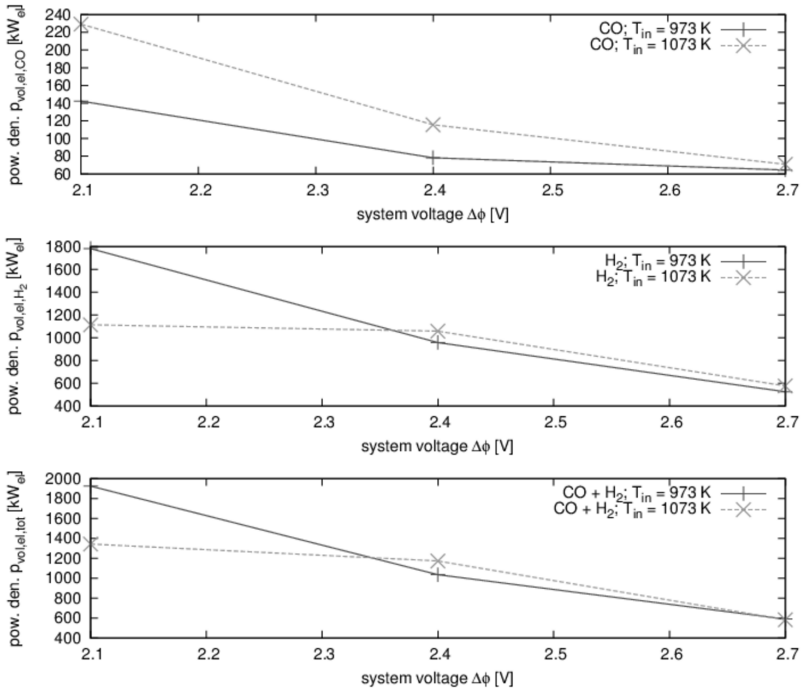

Figure 6.38.: **Volumetric power densities:** The figures show the volumetric power densities for different system voltages and inlet temperatures. The topmost figure shows the power density resulting from CO electrochemistry, the one in the middle the contribution of hydrogen, and the lowermost figure the total values, given by the sup of the upper two.

reformation reactions.

Altogether, for the investigated operating conditions volumetric electric power densities of about 1 MW_{el} per cubic meter can be derived. Compared to the giant installations in conventional power plants of several hundred MW_{el} this value sounds interesting. However, it has to be noted that it will decrease significantly when the auxiliary components from the beginning would be taken into consideration too.

6.3.3. Voltage efficiency

The voltage efficiency $\eta_{\%,\mathrm{Volt}}$ in percent is defined as the ratio of released electrical energy to the amount of converted chemical energy. Figure 6.39 shows the voltage efficiency in dependence of the systems operating voltage and temperature. As expected from theory in subsection 2.3.2 $\eta_{\%,\mathrm{Volt}}$ rises with the sys-

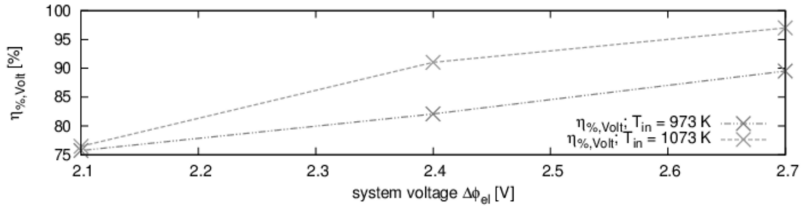

Figure 6.39.: **Voltage efficiencies:** The figure shows the average over the three cells of the system for the voltage efficiency $\eta_{\%,\mathrm{Volt}}$ in dependence of the system voltage $\Delta\phi_{\mathrm{el}}$ and the inlet temperature T_{in}. An increase of each of both factors leads to an increase in $\eta_{\%,\mathrm{Volt}}$.

tems operating voltage. Increasing the inlet temperature is also accompanied by an increase in efficiency. Although the electric conductivity of the metallic components decreases with rising T, the resulting additional ohmic losses seem to be outnumbered by the influences of the facilitated gas transport in the electrodes and the accelerated electrochemistry. In any case the values are on a high level, what is a consequence of the observed low fuel efficiency. An ideal cell operated at (almost) open circuit voltage has (almost) any losses, but shows (almost) no fuel conversion.

As in the previous subsection the case with $T_{\mathrm{in}} = 1073\,\mathrm{K}$ and $\Delta\phi_{\mathrm{el}} = 2.1\,\mathrm{V}$ shows some differences to the others. Here the drop in efficiency compared to the next potential is almost 10 %, what is much higher than the others. The growing influence of concentration losses η_{conc} seem to be the reason for this.

Altogether it follows that a high voltage efficiency is achievable by increasing the operating voltage and temperature.

6.3.4. Fuel conversion in longer cascades

So far only three cells are investigated in a a series connection, resulting in a rather low fuel conversion ratio and thus a limited “total efficiency”. In order

to study the fuel conversion efficiency of larger cascades, a virtual twenty one cell system is investigated. This is achieved by taking the REC and receptively applying the obtained outlet conditions as inlet ones for a subsequent simulation.

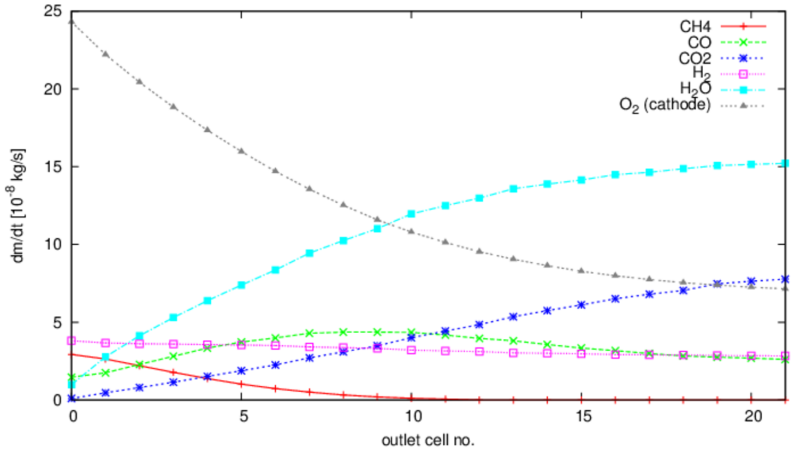

Figure 6.40.: **Species mass flows in a long cascade:** The virtual cascade is created by applying the outlet conditions of a three cell simulation as inlet ones for a subsequent simulation. Along the cells, the mass flows of the reactant CH_4, H_2, and O_2 (cathode side of the PEN) decrease, the ones of the products CO_2 and H_2O increase. In consequence to its role as product in the reformation reactions and its rather slow electrochemical conversion, CO increases up till cell eight, before it depletes as well.

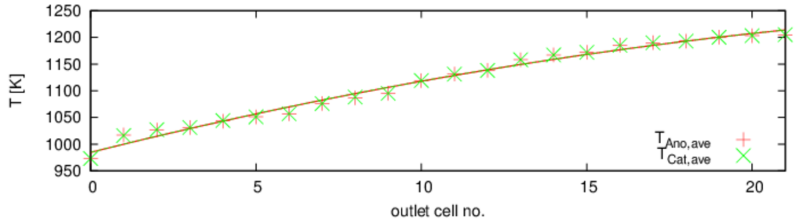

Figure 6.41.: **Gas temperatures at the cell outlets of a long cascade:** Shown are the average values over the respective outlets of the cells in the fifteen cell cascade. After a significant step in the first cell, the temperature rises almost linear by about 10 K per cell.

Figure 6.40 shows the mass flows of the different species at the outlets of the respective cell. The curves reveal a superimposition of reformation and electrochemistry. The mass flows of the "primary reacants" CH_4 and O_2, which are steadily consumed, are reduced from cell to cell. In particular CH_4 is almost completely converted after ten cells. Despite of its role as product in the reformation reactions, H_2 slowly depletes as well. In consequence, for the selected BCs it has to be consumed by electrochemistry faster than it is created by reformation. Since the H_2O mass flow rate steadily increases, there must be sufficient hydrogen to supply the electrochemical reactions. For the second electrochemical pair, CO and CO_2, the situation is much more complex. Although, the slow, but steady, increase in CO_2 reveals a constant electrochemical conversion, the mass flow of CO increases until the end of cell eight, before it declines as well. In contradiction to H_2, the beginning depletion of CO coincides with the almost complete conversion of CH_4. Therefore, it can be said that the CO concentration is defined by reformation rather than by electrochemistry.

Since the reformation reactions have almost come to an end at the outlet of cell eight, the systems thermal situation is of interest. With only electrochemistry it might heat up drastically, what would lead to significant mechanical tensions. Figure 6.41 shows the average temperature of the operating media at the respective cell outlets. Apart from a temperature step in the first cell, the temperature rises almost linear by only 10 K or less per cell. The values for the anode and the cathode side of the PEN are identical. Both aspects reveal a good temperature conduction inside the system and thus only small thermomechanical stresses. Nevertheless, it is possible to influence the temperature profile by e.g. increasing the air's mass flow rate or by introducing additional air in the downstream direction of the cascade.

To judge over the fuel efficiency of the longer cascade, the conversion ratios of the fuel gases CH_4, CO, and H_2 have to be discussed. Figure 6.42 shows the percentage of change of these gases mass flows relative to their inlet values "0". In addition, the total fuel efficiency at the outlet of each cell is calculated using equation 6.1.

While the conversion ratios for the "steadily depleating" reactants CH_4, H_2, and O_2 increase from cell to cell, the one for CO even reaches a negative value of almost -200 %, before it slowly turns towards zero at the end of cell nine. The system is dominated by hydrogen. Therefore, the values of $\eta_{\%,\text{fuel}\blacktriangle\text{H}_2}$ and $\eta_{\%,\text{fuel}\blacktriangle\text{tot}}$ are very similar.

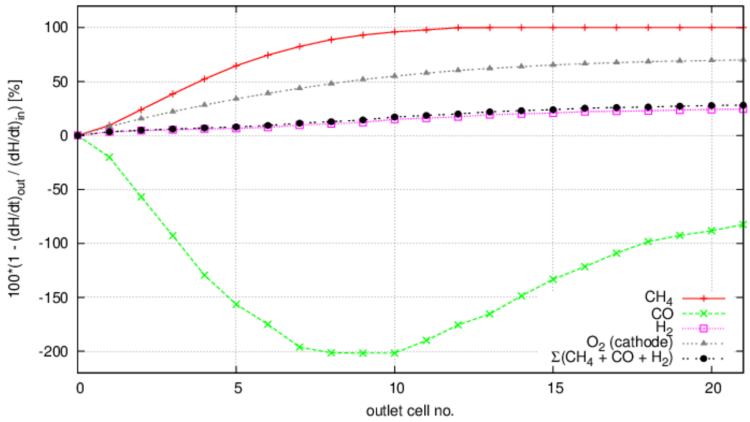

Figure 6.42.: **Fuel conversion ratios in a long cascade:** The conversion ratios are determined by the fraction of the respective mass flows at the outlet of cell i and the inlet value "0". The fuel efficiency at the outlet of cell i $\eta_{\%,\text{fuel}\blacktriangle i}$ is calculated using equation 6.1. Next to the fuel gases the ratios for oxygen are illustrated too.

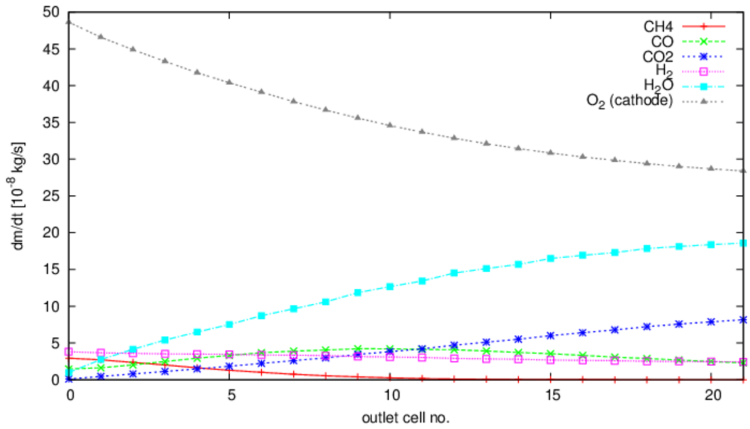

Figure 6.43.: **Species mass flows in a long cascade, enhanced oxygen mass flow:** While the enhanced oxygen mass flow rate at the cathode side of the PEN increases the H_2O mass flow rate by almost 30%, the one of CO_2 remains almost unchanged.

Since CH_4 is efficiently converted by electrochemistry, $\eta_{\%,\text{fuel}\blacktriangle\text{tot}}$ is always slightly larger than $\eta_{\%,\text{fuel}\blacktriangle\text{H}_2}$. At the end of cell twenty one the total fuel efficiency has reached a value of $\eta_{\%,\text{fuel}\blacktriangle\text{tot}} \approx 28.1\,\%$, what leads to a "total

efficiency" of:

$$\eta_{\%,\mathrm{tot}_{\blacktriangle}21} = 17.28\,\%.$$

at the outlet of the system. Since Figure 6.41 reveals a moderate temperature rising, it can be said that, if sufficient oxygen is provided in the cathode's gas-stream, theoretically even an almost complete fuel conversion, without serious thermomechanical stresses, is possible. To confirm this hypothesis, the oxygen mass flow rate at the cathode side is doubled compared to the basic settings from Table 5.1. Figures 6.43 to 6.45 show the respective species mass flows, conversion ratios, and cell temperatures.

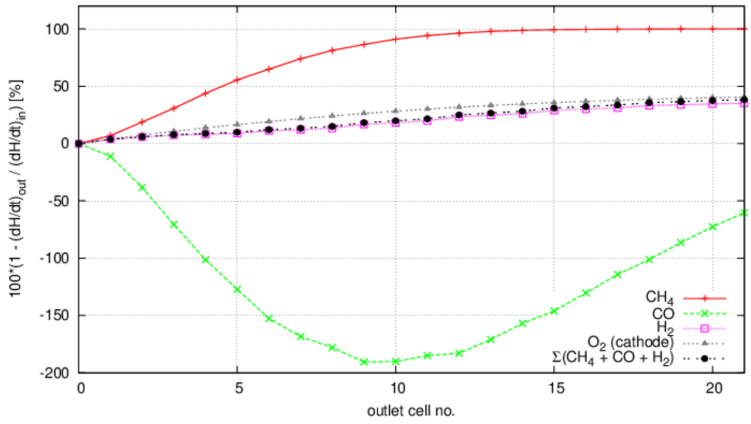

Figure 6.44.: **Fuel conversion ratios in a long cascade, enhanced oxygen mass flow:** Due to the enhanced oxygen mass flow, hydrogen is converted faster. Thus, compared to Figure 6.42, the total fuel conversion ratio at the end of cell 21 is increased.

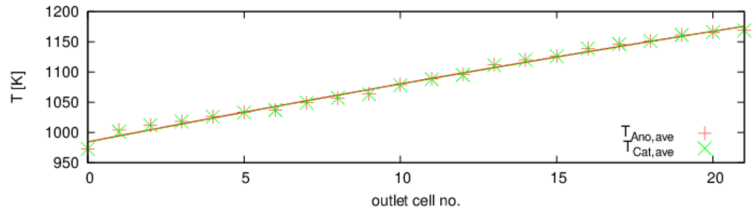

Figure 6.45.: **Gas temperatures at the cell outlets of a long cascade, enhanced oxygen mass flow:** As a consequence of the enhanced cathodic mass flow rate the cell temperature rises even slower than in Figure 6.41.

Since the hydrogen electrochemistry is significantly faster than the CO one, the mass flow rate of steam is enhanced by almost 30 % compared to the former results. On the contrary, for CO_2 hardly any changes are apparent. A comparison of Figures 6.42 and 6.44 reveals an increase of the total fuel conversion ratio to more than 38 % at the end of cell 21, what increases the "total efficiency" $\eta_{\%,\mathrm{tot}_{\blacktriangle}21}$ to almost 24 %.

Since Figure 6.45 reveals an even slower increase in temperature, the results show that with sufficient oxygen and long cascades, the results of Schlitzberger (Schlitzberger 2012) can be confirmed: Longer cascades are the key to higher fuel conversion and thus an increased total efficiency.

6.4. Conclusions

In this chapter the results of a detailed investigation of a three cell series connection of the novel cell concept with a 3D CFD model are presented. Next to the REC, the results of a parameter study on the operating voltage and inlet temperature are discussed. Apart from the operating conditions, the split and recombine fin structure of the metallic IC is found to be very effective for species homogenization. Additionally, the large interfacial area of IC and gas-phase provides an effective heat transfer from the reaction zones to the gas flow. However, the coverage of the PEN has an influence on the local species distribution inside the electrodes and even on the electrochemical reaction rates at the AB. In particular the uninterrupted bars at the beginning and the end of each cell might be modified in order to prevent fuel starvation.

For a high cell voltage the effects of electrochemistry and reformation on the temperature profile inside the electrodes balance each other in such a way that, independent of the inlet temperature, profiles with temperature differences of less than 10 K perpendicular to the flow direction can be achieved. For a cell voltage of $\Delta\phi_{\mathrm{el}_{\blacktriangle}\mathrm{cell}} = 0.9\,\mathrm{V}$ and $T_{\mathrm{in}} = 1073\,\mathrm{K}$ even a smaller outlet than inlet temperature is observed. Altogether, an inverse proportionality between cell voltage and outlet temperature is identified. Due to the coupling with the reformation, for a smaller cell voltage a decreased inlet temperature is found to be beneficial to homogenize the temperature profiles inside the anode. The contribution of CO to the total current density is found to be smaller than 10 % in any case. Since the quotients of $\vec{j}_{\mathrm{CO}}/\vec{j}_{\mathrm{H}_2}$ increase in flow direction, it can be said that, due to the different reaction kinetics, the system first converts the

hydrogen and subsequently the carbon monoxide. This trend is also visible in the volumetric power density of the system. Again a difference of an order of magnitude between the contributions of CO and H_2 to the total value is observed. The values show a proportional tendency to the cell voltage.

While CH_4 is efficiently converted in any of the investigated cases, the fuel conversion ratios of CO and H_2 are small. Due to the reformation reactions, in several cases even more CO and/or H_2 leave the system than enter it. The situation changes when the cascade becomes longer. For the REC's BCs the total conversion ratio follows a slowly increasing trend, given by hydrogen. Since the temperature rises only slowly, even after the reformation reactions have come to an end, the calculated total efficiency of more than 17 % for a twenty one cell system can easily be increased with an even longer cascade.

In summary, the setup of a DIR in combination with CO and H_2 electrochemistry and long cascades of fuel cells confirms the initial hypothesis. It is found to be effective in terms of temperature homogenization and fuel conversion efficiency.

7. Conclusions

The chapter summarizes the results of this thesis. The findings are reviewed in a global context and final conclusions are drawn. In the beginning of this thesis the basic operating principles of SOFCs are derived from thermodynamics in order to figure out key aspects for design, materials, and manufacturing. In combination with the results of a review on the current state of the art in the field of SOFC design concepts, a janiform configuration of an anode supported IP-SOFC system is developed. As preparative work for an investigation of the cell concept with a numerical model, the current state of the art in 3D-SOFC modeling and the mathematical treatment of the phenomena of interest are reviewed. Here, possible influences of the anode composition and microstructure as well as of elementary surface reactions on the overall cell performance and the numerical results are identified. The first aspect is subsequently investigated by setting up a simplified lattice based model of an anode cermet. Using the model, it is figured out that a global optimum in the number of TPBs exists for an equivolumetric mixture of the cermet's constituents. Since there is a difference of several orders of magnitude between the electronic and the ionic conductivities, this ideal composition should only be applied to a thin active region of the anode close to the electrolyte. For the anode support structure the composition should be shifted towards a facilitated transport of electrons and gaseous species. In particular, when using appropriate metals like Ni, its interface with the gas species can be used for the DIR of lower hydrocarbons. The second aspect is addressed by a cathode surface reaction model. Although the proposed simple three-path reaction process is able to explain experimental polarization curves, the model is found to be too complex for macroscopic CFD simulations. Subsequently, the CFD problem setup is addressed. To obtain an appropriate computational mesh, the original geometry is simplified in several stages. For the physical phenomena of the final model individual submodels are set up and verified. In particular the electrochemical and reformation reactions are emphasized. For the former an alternative approach, based on a local description of the potential dependent equations, is proposed and applied to a

1D-CFD model of the PEN region. It is figured out that, although theoretically the entire anode is electrochemically active, the small oxygen ion transport velocity limits the active region to a rather thin frontier close to the electrolyte. Since the models numerical stability is fragile, two alternative approaches to electrochemistry (both with CO and H_2 conversion), one for simple and one for complex geometries, are proposed too. Either of them is based on conventional electrochemical mathematics and is appropriate for 3D-CFD simulations. Reformation of methane is addressed by a reaction site availability and residence time dependent kinetic model. Here, it is figured out that the thermodynamic equilibrium is not reached directly after entering the cell's active volume and thus can be one issue of a design process. In particular in combination with the geometry of the IC, whose baffles act as split and recombine micro-mixers for the gas flows, local hot-spots and cooler areas are possible. Using a simplified geometry, a three-cell series connection is investigated in a parameter study on the operating voltage and temperature. It is figured out that for high cell voltages the thermal effects of electrochemistry and reformation balance each other in such a way that temperature gradients of less than 10 K perpendicular to the flow direction are achieved. By increasing the inlet temperature it is possible to promote the influence of the reformation reactions in such a way that the temperature remains almost unchanged between in- and outlet. For a constant inlet temperature lowering the cell voltage increases the electrochemical conversion rate and thus the average current density as well as the amount of released heat. Inside the anode, the additional heat leads to thermal gradients of several dozen Kelvin transverse and perpendicular to the fuel flow direction. In consequence to the accelerated electrochemistry, regions of fuel depletion appear. In particular under the covered parts of the cathode almost any oxygen remains in some cases. Even though it is possible to increase the contribution of CO to the current density by lowering the cell voltage, in any case its values are only about 10 % of those from hydrogen. Thus, in a cell cascade, the system in total converts the hydrogen first and subsequently the CO. While CH_4 is efficiently converted in any of the investigated three-cell systems, significantly longer cascades are required to push the fuel conversion ratio of CO and H_2. For a twenty one cell cascade, a total efficiency of more than 17 %, with only a moderate increase in temperature, is achieved. Altogether, this study shows that a parallel conversion of CO and H_2 in combination with a DIR is possible with the novel cell concept and effective in terms of temperature homogenization and fuel conversion.

A. Figures and tables

A.1. Summary of SOFC design concepts

Table A.1.: Summary of the benefits and disadvantages of several SOFC concepts discussed in the literature (Chen et al. 2011; Gardner et al. 2000; Vielstich, Lamm, and Gasteiger 2003a; Sammes, Du, and Bove 2005; Tietz, Buchkremer, and Stöver 2002)

Concept	Inventor / Research	Advantages	Disadvantages	References
HEXIS-CELL	H.C. Starck/InDEC B.V./Sulzer	- simple system design - almost no sealant planes necessary - intrinsic possibility for heat management - integrated heat exchanger	- hot-spot formation - inhomogeneous gas-distribution - thermomechanical stresses - CO_2 separation difficult - low fuel utilization	(Andreassi et al. 2008; Vielstich, Lamm, and Gasteiger 2003a; Schuler 2007)
IP-SOFC, SS-SOFC	Rolls-Royce, CFCL, MHI	- improved fuel utilization - IIR possible - no/little sealant planes - reduced thermomechanical stresses	- high manufacturing costs - brittle ceramics - high ohmic losses	(Cassidy et al. 2009; Costamagna et al. 2004; Cui and Cheng 2010; Cui, Liu, and Chen 2010; Gardner et al. 2000; Grosso, Repetto, and Pezzini 2008; Lai and Barnett 2005; Leithner 2004; Magistri et al. 2005; Magistri et al. 2007; Mounir et al. 2009; Repetto and Costamagna 2008; Schlitzberger, Leithner, and Zindler 2009; Schlitzberger 2012)

Continued from previous page

Concept	Inventor / Research	Advantages	Disadvantages	References
MT-SOFC		- (relatively) cheap manufacturing - high thermal operation dynamics - reduced thermal stresses - manifold and electrical contacts in colder part of stack - intrinsic heat management via combustion of unused fuel	- high (ohmic) losses	(Alston et al. 1998; Amiri et al. 2010; Andreassi et al. 2008; Calise, Restuccia, and Sammes 2010; Funahashi et al. 2007; Lawlor et al. 2009; Sammes, Du, and Bove 2005; Serincan, Pasaogullari, and Sammes 2009a)
planar	CFCL, Forschungszentrum Jülich, H.C. Starck, HTceramix SA, RisøDTU, Sulzer, others	- IR possible - cheap manufacturing - high power densities (due to anode support) - furthest developed among all concepts - co-, counter- and cross-flow possible	- thermal stresses - large sealant planes - bipolar operation (interconnects needed) - weight due to interconnects - slow start-up/cool down behavior - increased pressure drop - in-plane currents - low fuel utilization	(Hoffmann 2009; Lin et al. 2007; Tietz, Buchkremer, and Stöver 2006; Wang et al. 2007)
PT-SOFC		- IR possible - no bipolar plates - simple construction - reduced sealants	- high ohmic losses - brittle ceramics	(Chen et al. 2011)
SC-SOFC		- one reaction chamber - simple cell/stack design - reduced temperature - little/no sealant	- low power densities - possibility of explosions	(Vielstich, Lamm, and Gasteiger 2003a, p. 343)(O'Hayre et al. 2009, p.279)
HPD-SOFC, MOLB-type SOFC, tubular	MHI, Siemens Westinghouse, Toto, others	- reduced thermal stress - little/no sealant - easy adjustment of power output by series and parallel connection - fast start-up/cool down behavior - high fuel utilization	- high ohmic losses due to long currents paths - expensive - interconnecting difficult	(Fischer and Seume 2009b; Fischer and Seume 2009a; Hwang, Chen, and Lai 2005b; Hwang, Chen, and Lai 2005a)

A.2. Summary of fuel cell types

Table A.2.: **Summary of Fuel Cell types:** Overview over currently investigated fuel cells types, ordered by their operational temperature.

Name	Temperature in °C	Electrolyte	Fuel	Oxidant	Ions	Products	References
BFC *Biological Fuel Cell*	30	Polymer + H_2O	glucose	O_2	H^+	H_2O, CO_2	(O'Hayre et al. 2009, p. 276)
LFFC *Laminar Flow Fuel Cell*	30	liquid-liquid boundary	HCOOH	O_2	H_3O^+, OH^-	CO_2, H_2O	(Bazylak, Sinton, and Djilali 2005) (O'Hayre et al. 2009, p. 277)
MAFC *Metal Air Fuel Cell*	30	KOH	Zn	O_2	OH^-	ZnO	(O'Hayre et al. 2009, p. 278)
DMFC *Direct Methanol Fuel Cell*	30 - 90	Polymer + H_2O	CH_3OH	O_2	H^+	H_2O	(Larminie and Dicks 2003, p. 15)
SPFC/PEMFC *Solid Polymer Fuel Cell / Proton Exchange Membrane Fuel Cell*	30 - 90	Polymer + H_2O	H_2	O_2	H^+	H_2O	(Larminie and Dicks 2003, p. 15)
AFC *Alcaline Fuel Cell*	50 - 200	KOH	H_2	O_2	OH^-	H_2O	(Larminie and Dicks 2003, p. 15)

Continued on next page

Continued from previous page

Name	**Temperature in °C**	**Electrolyte**	**Fuel**	**Oxidant**	**Ions**	**Products**	**References**
PAFC *Phosphoric Acid Fuel Cell*	80 - 220	Polymer + H_3PO_4	H_2	O_2	H^+	H_2O	(Larminie and Dicks 2003, p. 15)
DCFC *Direct Carbon Fuel Cell*	450 - 900	NaOH, YSZ	C	O_2	CO_3^{2-}, O^{2-}	CO_2	(Jain et al. 2008; Kacprzak, Kobylecki, and Bis 2011)
SC-SOFC *Single Chamber-SOFC*	500 - 700	YSZ, GDC	CO, H_2	O_2	O^{2-}, H^+	H_2O, CO_2	(Akhtar, Decent, and Kendall 2010) (O'Hayre et al. 2009, p. 279)
MCFC *Molten Carbonate Fuel Cell*	650	K, Li, Na_2CO_3	CO, H_2	O_2	CO_3^{2-}	CO_2	(Larminie and Dicks 2003, p. 15 et seqq.)(O'Hayre et al. 2009, p. 12)
SOFC *Solid Oxide Fuel Cell*	650 - 1000	YSZ, GDC	H_2, CO, (lower) hydrocarbons	O_2	O^{2-}	H_2O, CO_2	(O'Hayre et al. 2009; Bove and Ubertini 2006)(Heinzel, Mahlendorf, and Roes 2006, p. 15)(Vielstich, Lamm, and Gasteiger 2003a, p. 335)
DF-SOFC *Direct Flame-SOFC*	800 - 1000	YSZ	CO, H_2, hydrocarbons	O_2	O^{2-}	H_2O, CO_2	(O'Hayre et al. 2009, p. 280)
LTA-SOFC *Liquid Tin Anode-SOFC*	900 - 1000	YSZ	H_2, hydrocarbons	O_2	O^{2-}	H_2O, CO_2, SO_2	(Larminie and Dicks 2003, p. 17) (O'Hayre et al. 2009, p. 281)

A.3. Drawings of the novel cell concept

In this section technical drawings of the novel Solid Oxide Fuel Cell (SOFC) cell concept are shown (Leithner 2004; Leithner and Schlitzberger 2007; Schlitzberger 2012; Todt 2011).

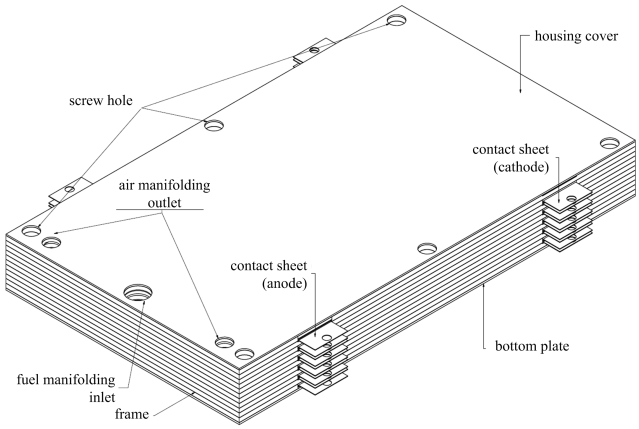

Figure A.1.: **Complete SOFC stack:** The final SOFC stack appears as a compact block with external contact sheets for the electrical connections. (Todt 2011)

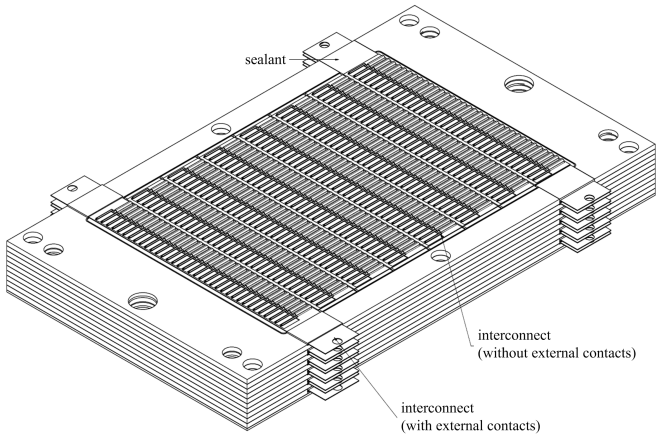

Figure A.2.: **Complete SOFC stack without cover plate:** Without the cover plate, the cascaded structure of the cell layers is visible. On the left and the right side holes for the gas manifold and screws can be seen. (Todt 2011)

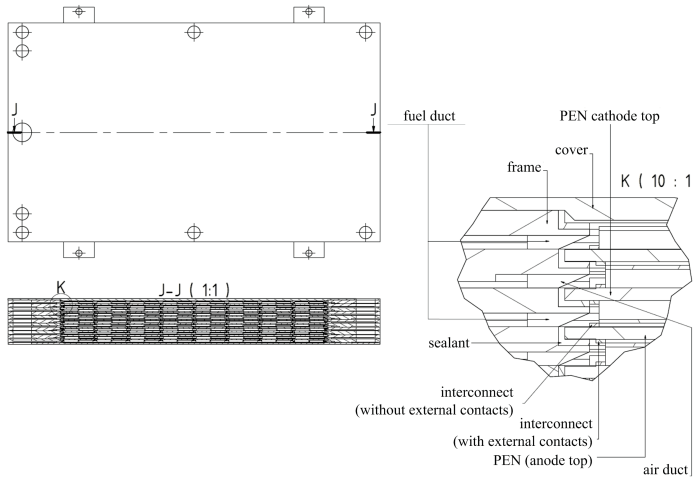

Figure A.3.: **Sectional drawing of the SOFC stack:** The stack is cut along its vertical center plane J. The detail K is located in the top left corner of the stack. Adapted from (Todt 2011).

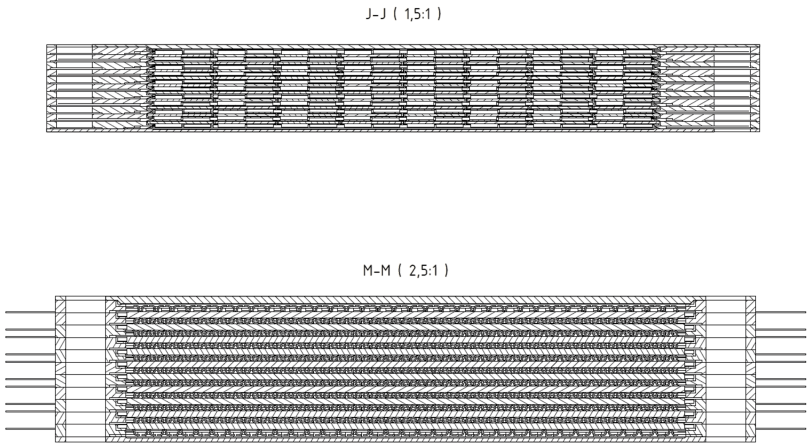

Figure A.4.: **Sectional drawings of the SOFC stack:** The stack is cut along its vertical center planes J and M. On the sides of cut M the external contact sheets are visible. (Todt 2011)

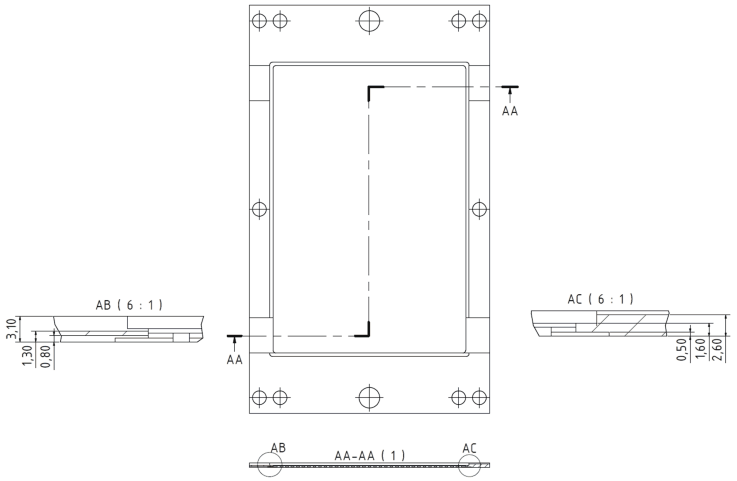

Figure A.5.: **Top view of the manifolding frame:** The details AB and AC show the contact areas of the electrochemically active areas with the housing. All dimensions are in mm. (Todt 2011)

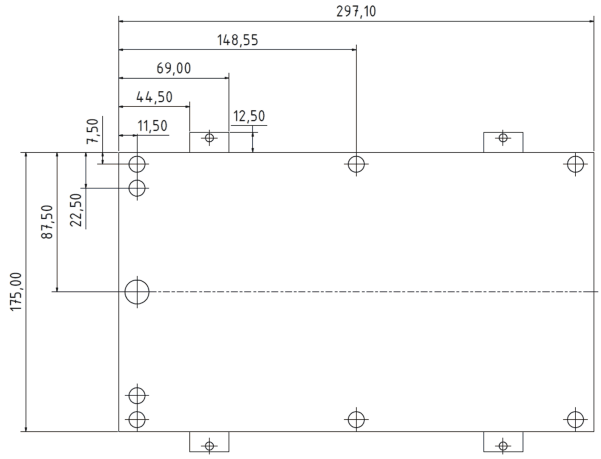

Figure A.6.: **Dimensions of the SOFC stack:** Top view of the SOFC stack. All dimensions are in mm. (Todt 2011)

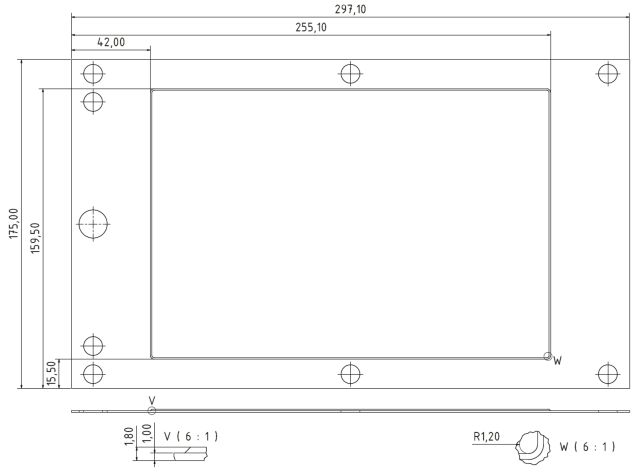

Figure A.7.: **Dimensions of the manifolding cover:** Bottom view of the manifolding cover. All dimensions are in mm. (Todt 2011)

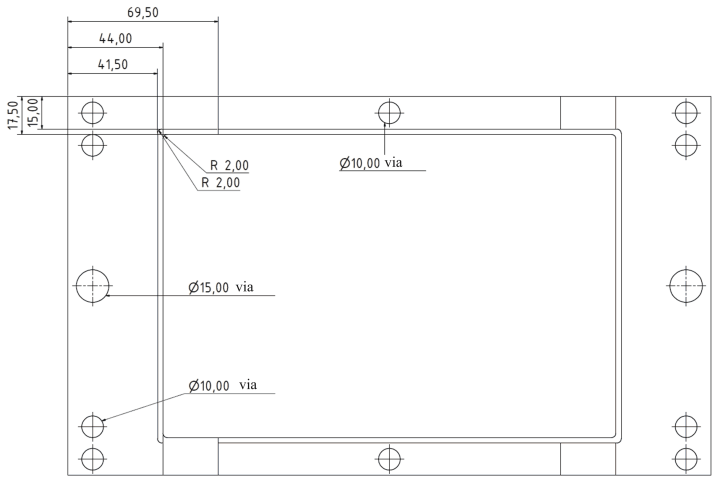

Figure A.8.: **Dimensions of the top side of the manifolding frame:** Top view of the manifolding frame. All dimensions are in mm. Modified from (Todt 2011).

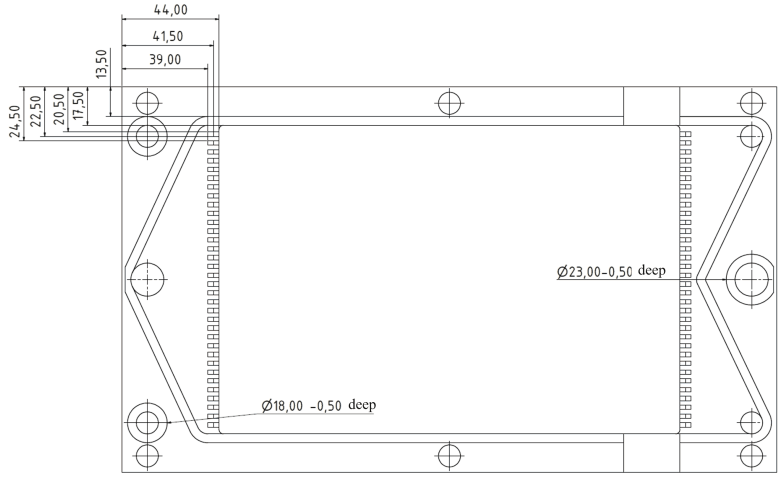

Figure A.9.: **Dimensions of the bottom side of the manifolding frame:** Bottom view of the manifolding frame. Flow homogenizers are visible at the inlet and outlet of the gas manifolding. All dimensions are in mm. Modified from (Todt 2011).

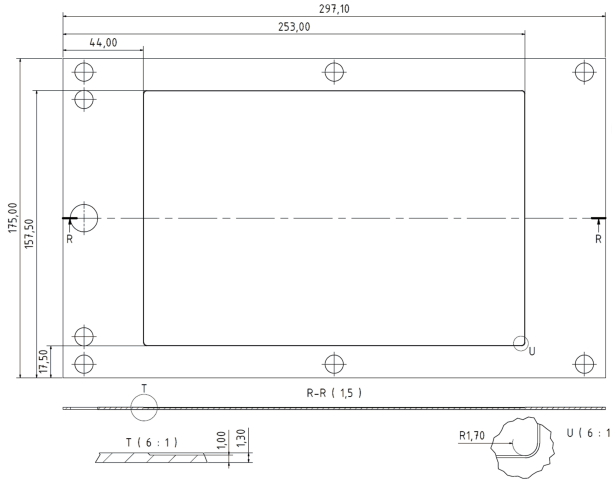

Figure A.10.: **Dimensions of the manifolding bottom plate:** Top view of the manifolding bottom plate. All dimensions are in mm. (Todt 2011)

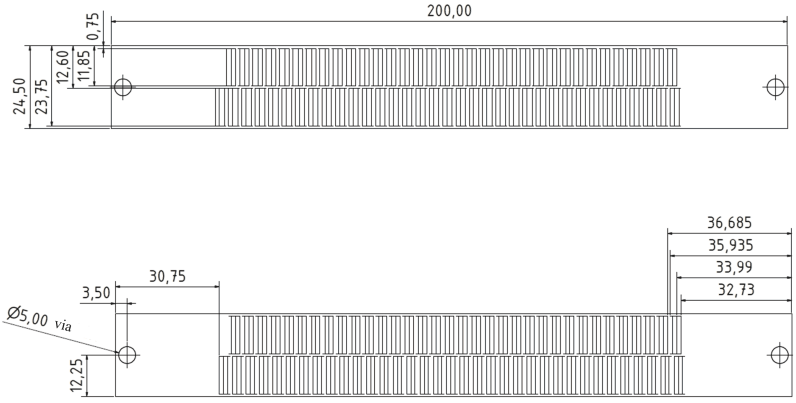

Figure A.11.: **Dimensions of the ICs with external contacts:** Top and bottom view of the ICs with external contacts. All dimensions are in mm. Modified from (Todt 2011).

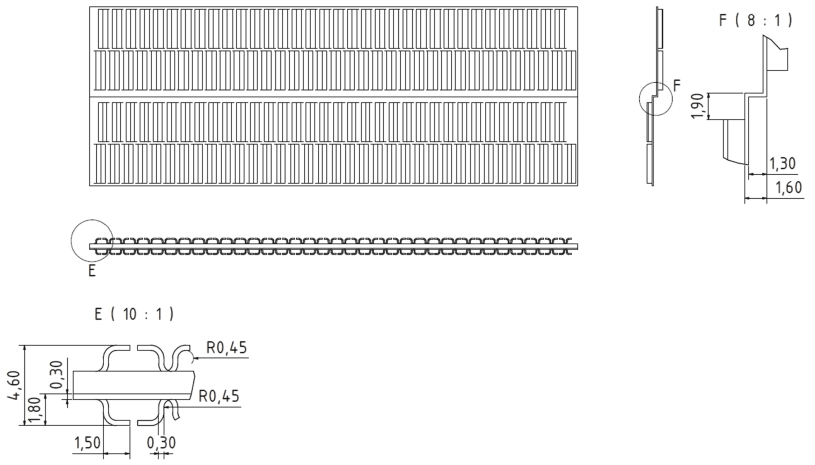

Figure A.12.: **Dimensions of the internal ICs:** Top, side and detailed view of internal ICs. Very well visible is the flow channel structure created by the sinusoidal fins. All dimensions are in mm. (Todt 2011)

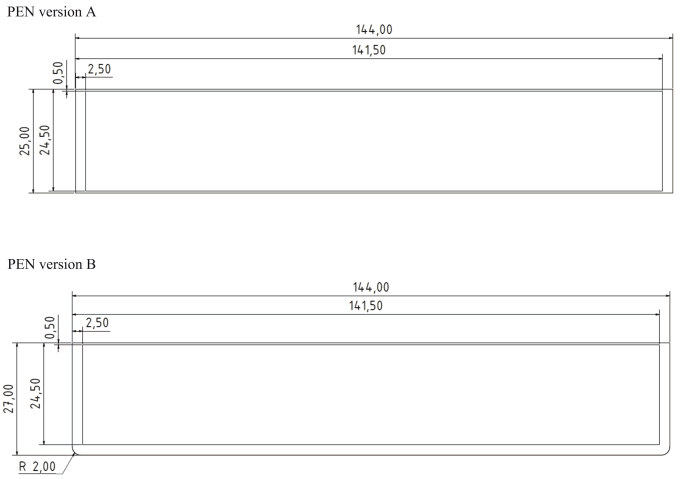

Figure A.13.: **Dimensions of the PEN structures:** To stabilize the PEN mechanically and to provide gas tightness of the domains against each other, the very first and last PENs in a layer have to be slightly larger (version B), compared to the rest (version A). All dimensions are in mm. Modified from (Todt 2011).

A.4. Three-dimensional SOFC models

Table A.3.: **Summary 3D SOFC models:** Tabulated are models which focus on a three dimensional description of SOFCs.

Author	Type	Aim	Method	Phenomena	Balance equations	Validation/verification	Electrical model	Findings	Tool
Akhtar et al. (Akhtar et al. 2009)	steady-state Single Chamber-SOFC (SC-SOFC)	basic knowledge on this type of cell	Finite Element Method (FEM)	hydrogen electrochemistry, $\sigma(T)$	energy, mass, momentum		U_{Nernst} - overpotentials, Faraday's law, j from BVE	proof of concept of SC-SOFC	COMSOL Multiph.
Autissier et al. (Autissier et al. 2004)	steady-state planar cell	operational parameter distribution for geometry optimization	FVM	hydrogen electrochemistry, radiation	energy, mass, momentum	exp. data for validation and parameter fitting	U_{Nernst} - overpotentials (ohm & activation), Faraday's law, j given	parameter distribution	FLUENT
Brus and Szmyd (Brus and Szmyd 2008)	IIR-SOFC	study radiative heat transfer		radiation and reformation					
Campanari and Iora (Campanari and Iora 2005)	planar cell	study the influence of the geometrical resolution in the PEN	FVM	hydrogen electrochemistry, $\sigma(T)$, reformation	charge, energy, mass, momentum	data from literature	U_{Nernst} - overpotentials, U_{Ohm} from equivalent circuit model, Faraday's law	more accurate temperature distribution for finer model	FLUENT

Continued on next page

Continued from previous page

Author	Type	Aim	Method	Phenomena	Balance equations	Validation/verification	Electrical model	Findings	Tool
Danilov et al. (Danilov and Tade 2009)	planar, steady-state cell plate	geometry optimization of the flow field, detailed reformation	FVM	CO and hydrogen electrochemistry, $\underline{\sigma}_{\text{ion}}(T)$, reformation	charge, energy, mass, momentum		U_{Nernst} - overpotentials, Farady's law, j from BVE	flow field optimized, non uniform surface species distribution	FLUENT, DETCHEM
Ferguson et al. (Ferguson, Fiard, and Herbin 1996)	various geometries	create multi-objective code for SOFC simulation		hydrogen electrochemistry, $\underline{\sigma}(T)$, $D(T)$	current, energy, mass	verification by other models	half-cell potentials, Ohm's law, Faraday's law	code "SOFC 3D" capable as design tool	SOFC 3D
Goldin et al. (Goldin et al. 2009)	planar button cell	influence of temperature distribution on performance	FVM	hydrogen electrochemistry, reformation	charge, energy, mass, momentum	data from literature	U_{Nernst} - overpotentials, reaction scheme from (Zhu et al. 2005)	strong temperature dependency for small flow rates of fuel/air	Gambit, Cantera, C++
Haberman and Young (Haberman and Young 2004)	IP-SOFC, steady-state	influence of porous structures on performance	FVM	hydrogen electrochemistry, reformation	charge, energy, mass, momentum		uniform j assumed	reformation kinetics have significant influence on performance	
Hwang et al. (Hwang, Chen, and Lai 2005a)	MOLB-TYPE SOFC channel	study transport in porous electrodes	FDM	hydrogen and CO electrochemistry	charge, energy, mass, momentum		Ohm's law, Faraday's law, j from BVE	spatial distribution of overpotentials	
Liu et al. (Liu, Kong, and Lin 2009)	planar SOFC, steady-state	optimize channel width in stacks to minimize contact resistance		hydrogen electrochemistry, $\underline{\sigma}(T)$	charge, energy, mass, momentum	validation by experiments	Ohm's law, BVE with fitted parameters, U_{cell} as BC	geometry optimization	COMSOL Multiph.
Lu et al. (Lu, Schaefer, and Li 2005)	HPD-SOFC, steady-state	improve overall cell performance		hydrogen electrochemistry	charge, energy, mass, momentum	data from literature	U_{cell} = sum of half-cell potentials, latter from empirical formula, Faraday's law	species- and temperature-distribution in dependence of inlet conditions	

Continued on next page

Continued from previous page

Author	Type	Aim	Method	Phenomena	Balance equations	Validation/verification	Electrical model	Findings	Tool
Nam and Jeon (Nam and Jeon 2006)	Intermediate Temperature-SOFC (IT-SOFC) electrode	study influence of micro-structural parameters on performance	FVM	hydrogen electrochemistry, $\underline{\sigma}(T)$, $D(T)$	charge, energy, mass, momentum		Ohm's law, Faraday's law, j from empirical formula	strong influence of particle size on performance	
Recknagle et al. (Recknagle et al. 2003)	planar cell	study influence of flow configuration on fuel utilization		hydrogen electrochemistry	energy, mass, momentum	UCEM for electrochemistry		similar fuel util. poss., irrespective of flow conf.	COMSOL Multiph.
Schlitzberger et al. (Schlitzberger, Leithner, and Zindler 2009)	cascaded, planar SOFC system	prove of concept, investigate electrical efficiency	FVM	hydrogen electrochemistry, reformation	charge, energy, mass, momentum		U_{Nernst} - overpotentials, Faraday's law, j from BVE	$\eta_{\%\,\text{el}} > 60\,\%$	C++, EnBiPro
Tanaka et al. (Tanaka et al. 2007)	planar, steady-state, stack	influence of radiative heat-transfer from outside on temperature distribution, code from earlier models		hydrogen electrochemistry, radiation, reformation, T dep. from JANAF (Janaf 1971)	charge, energy, mass		U_{Nernst} - overpotentials, Faraday's law, j from BVE	almost no influence of radiation from outside on cells in stack	
Wang et al. (Wang et al. 2007)	single cell, planar, steady-state	study species-, temperature-, and current density-distributions	FVM	hydrogen electrochemistry, $c_{\text{En,p}}(T)$, $D(T)$	charge, energy, mass, momentum		U_{Nernst} - overpotentials, U_{Ohm} neglected, Faraday's law, j from BVE	more uniform temp. distr. for co- than counter-flow. Influence of electrode porosity existent	ANSYS/ CFX
Yakabe and Sakurai (Yakabe and Sakurai 2004)	steady-state planar cell	study electric current path and influence of geometry on cell performance	FVM	hydrogen electrochemistry, $\underline{\sigma}(T)$	charge, energy, mass, momentum		U_{Nernst} - overpotentials (ohm & activation), Faraday's law, $\eta_{\%\,\text{act}}$ with heuristic values	geometry affects in-plane currents and hence electrical performance	FLUENT

Continued on next page

Continued from previous page

Author	Type	Aim	Method	Phenomena	Balance equations	Validation/verification	Electrical model	Findings	Tool
Yakabe et al. (Yakabe 2001)	anode supported planar cell	polarization effects from H and CO electrochemistry	FVM	hydrogen and CO electrochemistry, reformation	energy, mass, momentum			influence of WGS on concentration overpotential under high fuel utilization	
Yuan et al. (Yuan, Ji, and Chung 2009)	low temperature planar channel	temperature, geometry, microstructure influence on electrical performance	FVM	hydrogen electrochemistry, $\underline{\sigma}(T)$	charge, energy, mass, momentum		U_{Nernst} - overpotentials, Ohm's law, Faraday's law, j from BVE	strong influence of particle size and TPB length on el. performance	

A.5. Balances of the CFD results

This section summarizes the balances for the results of the different investigated cases.

A.5.1. High potential case (HPC)

The High Potential Case (HPC) is characterized by a difference of $\Delta\phi_{el} = 2.7$ V between the external contacts.

Table A.4.: **Overall mass balance of the HPC:** The table summarizes the mass balances of the HPC at either side of the AB as well as its total value. The values are determined in accordance to the description of Table 6.1

Location	$\dot{m}_{\text{Mass}\blacktriangle\text{ANO}}$ [10^{-6} kg/s]	$\dot{m}_{\text{Mass}\blacktriangle\text{CAT}}$ [10^{-6} kg/s]	total [10^{-6} kg/s]
Inlet	$9.769 \cdot 10^{-2}$	1.057	1.154
Outlet	$-12.550 \cdot 10^{-2}$	−1.029	-1.154
$\sum$	$-2.777 \cdot 10^{-2}$	$2.777 \cdot 10^{-2}$	−0.000

Table A.5.: **Overall atom balance of the HPC:** The table summarizes the atom balance at either side of the AB for the HPC. The values are determined in accordance to the annotations of Table 6.2. All quantities are given in 10^{-8} kg/s.

Anode				
Location	$\dot{m}_{\text{Mass}\blacktriangle\text{C}\blacktriangle\text{ANO}}$	$\dot{m}_{\text{Mass}\blacktriangle\text{H}\blacktriangle\text{ANO}}$	$\dot{m}_{\text{Mass}\blacktriangle\text{N}\blacktriangle\text{ANO}}$	$\dot{m}_{\text{Mass}\blacktriangle\text{O}\blacktriangle\text{ANO}}$
Inlet	2.849	4.650	$4.886 \cdot 10^{-1}$	1.777
Outlet	-2.849	-4.650	$-5.006 \cdot 10^{-1}$	-4.541
$\sum$	$-7.487 \cdot 10^{-4}$	$-1.087 \cdot 10^{-4}$	$-1.197 \cdot 10^{-2}$	-2.764
Cathode				
Location	$\dot{m}_{\text{Mass}\blacktriangle\text{C}\blacktriangle\text{CAT}}$	$\dot{m}_{\text{Mass}\blacktriangle\text{H}\blacktriangle\text{CAT}}$	$\dot{m}_{\text{Mass}\blacktriangle\text{N}\blacktriangle\text{CAT}}$	$\dot{m}_{\text{Mass}\blacktriangle\text{O}\blacktriangle\text{CAT}}$
Inlet	0.000	0.000	81.380	24.313
Outlet	0.000	0.000	-81.340	-21.580
$\sum$	0.000	0.000	$4.410 \cdot 10^{-2}$	2.733
$\sum_{\text{tot}}$	$-7.487 \cdot 10^{-4}$	$-1.087 \cdot 10^{-4}$	$3.213 \cdot 10^{-2}$	$-3.134 \cdot 10^{-2}$

Table A.6.: **Overall energy balance of the HPC:** The energy balance consists on the one hand of the thermal and chemical energy of the reacting media and on the other hand of the electrical energy flowing through the electric contacts. The values are determined in accordance to the annotations of Table 6.4. All quantities are given in 10^{-1} W.

	Anode		**Cathode**		**IC**	$\sum$
	$\dot{H}_{\text{En}}$	$\dot{Q}_{\text{En}}$	$\dot{H}_{\text{En}}$	$\dot{Q}_{\text{En}}$	$\dot{E}_{\text{En,Ch}}$	**[10^{-1} W]**
Inlet	1.372	7.260	7.659	11.820	$1.029{\cdot}10^{-3}$	28.112
Outlet	1.952	-7.657	-7.687	-11.780	-2.730	-27.902
$\sum$	3.324	-0.397	-0.276	-0.043	-2.729	-0.21

Table A.7.: **Electric properties and power densities at $T_{\text{in}} = 973$ K and $\Delta\phi_{\text{el}} = 2.7$ V (HPC):** The values are determined in the same way as described in the annotation of Table 6.5. Because of the increased operating temperature, the average current and power density increases compared to the REC in Table 6.5.

Quantity	**Dimension**	**First cell (A)**	**Second cell (B)**	**Third cell (C)**	**Outlet**
ϕ_{el}	V	2.70	1.79	0.89	$9.43 \cdot 10^{-9}$
$\Delta\phi_{\text{el}}$	V	0.91	0.90	0.89	
$\vec{\mathbb{E}}_{\text{el}}$	V/m	0.19	0.21	0.22	0.23
$\Delta\vec{\mathbb{E}}_{\text{el}}$	V/m	$-1.44 \cdot 10^{-2}$	$-1.61 \cdot 10^{-2}$	$-3.35 \cdot 10^{-3}$	
$\Delta\vec{\mathbb{E}}_{\text{el}\blacktriangle}\%$	%	-7.49	-7.78	-1.51	
$\vec{j}_{\text{el}}$	A/m^2	$1.74 \cdot 10^5$	$1.87 \cdot 10^5$	$2.01 \cdot 10^5$	$2.04 \cdot 10^5$
$\Delta\vec{j}_{\text{el}}$	A/m^2	$-1.30 \cdot 10^4$	$-1.45 \cdot 10^4$	$-2.98 \cdot 10^3$	
$\Delta\vec{j}_{\text{el}\blacktriangle}\%$	%	-7.50	-7.77	-1.48	
$\vec{j}_{\text{el}\blacktriangle\text{tot}\blacktriangle\text{ave}}$	A/m^2	$2.10 \cdot 10^3$	$2.27 \cdot 10^3$	$2.56 \cdot 10^3$	
$\vec{j}_{\text{el}\blacktriangle\text{CO}\blacktriangle\text{ave}}$	A/m^2	$2.39 \cdot 10^2$	$2.48 \cdot 10^2$	$2.71 \cdot 10^2$	
$\vec{j}_{\text{el}\blacktriangle\text{H}_2\blacktriangle\text{ave}}$	A/m^2	$1.86 \cdot 10^3$	$2.02 \cdot 10^3$	$2.29 \cdot 10^3$	
$\mathfrak{p}_{\text{el}\blacktriangle\text{tot}\blacktriangle\text{ave}}$	W/m^2	$1.91 \cdot 10^3$	$2.05 \cdot 10^3$	$2.28 \cdot 10^3$	
$\mathfrak{p}_{\text{el}\blacktriangle\text{CO}\blacktriangle\text{ave}}$	W/m^2	$2.17 \cdot 10^2$	$2.24 \cdot 10^2$	$2.42 \cdot 10^2$	
$\mathfrak{p}_{\text{el}\blacktriangle\text{H}_2\blacktriangle\text{ave}}$	W/m^2	$1.69 \cdot 10^3$	$1.82 \cdot 10^3$	$2.04 \cdot 10^3$	
$\mathfrak{p}_{\text{vol,el}\blacktriangle\text{tot}\blacktriangle\text{ave}}$	W/m^3	$5.41 \cdot 10^5$	$5.80 \cdot 10^5$	$6.48 \cdot 10^5$	
$\mathfrak{p}_{\text{vol,el}\blacktriangle\text{CO}\blacktriangle\text{ave}}$	W/m^3	$6.16 \cdot 10^4$	$6.34 \cdot 10^4$	$3.85 \cdot 10^4$	
$\mathfrak{p}_{\text{vol,el}\blacktriangle\text{H}_2\blacktriangle\text{ave}}$	W/m^3	$4.79 \cdot 10^5$	$5.17 \cdot 10^5$	$5.79 \cdot 10^5$	

Table A.8.: **Overall mass balance of the HPC at T_{in} = 1073 K:** The table summarizes the mass balances of the HPC at either side of the AB as well as its total value. The values are determined in accordance to the description of Table 6.1

Location	$\dot{m}_{\text{Mass}\blacktriangle\text{ANO}}$ [10^{-6} kg/s]	$\dot{m}_{\text{Mass}\blacktriangle\text{CAT}}$ [10^{-6} kg/s]	total [10^{-6} kg/s]
Inlet	$8.858 \cdot 10^{-2}$	$9.584 \cdot 10^{-1}$	1.047
Outlet	$-11.893 \cdot 10^{-2}$	$-9.281 \cdot 10^{-1}$	-1.047
$\sum$	$-3.035 \cdot 10^{-2}$	$3.035 \cdot 10^{-2}$	−0.000

Table A.9.: **Overall energy balance of the HPC at T_{in} = 1073 K:** The energy balance consists on the one hand of the thermal and chemical energy of the reacting media and on the other hand of the electrical energy flowing through the electric contacts. The values are determined in accordance to the annotations of Table 6.4. All quantities are given in 10^{-1} W.

	Anode		Cathode		IC	$\sum$
	$\dot{H}_{\text{En}}$	$\dot{Q}_{\text{En}}$	$\dot{H}_{\text{En}}$	$\dot{Q}_{\text{En}}$	$\dot{E}_{\text{En,Ch}}$	[10^{-1} W]
Inlet	1.889	7.371	8.006	11.940	$1.010 \cdot 10^{-3}$	29.207
Outlet	0.950	-7.691	-7.511	-11.490	-3.228	-28.970
$\sum$	2.839	-0.321	0.495	0.451	-3.227	0.237

Table A.10.: **Overall atom balance of the HPC at T_{in} = 1073 K:** The table summarizes the atom balance at either side of the AB for the HPC. The values are determined in accordance to the annotations of Table 6.2. All quantities are given in 10^{-8} kg/s.

Anode				
Location	$\dot{m}_{\text{Mass}\blacktriangle\text{C}\blacktriangle\text{ANO}}$	$\dot{m}_{\text{Mass}\blacktriangle\text{H}\blacktriangle\text{ANO}}$	$\dot{m}_{\text{Mass}\blacktriangle\text{N}\blacktriangle\text{ANO}}$	$\dot{m}_{\text{Mass}\blacktriangle\text{O}\blacktriangle\text{ANO}}$
Inlet	2.583	4.216	$4.436 \cdot 10^{-1}$	1.612
Outlet	-2.583	-4.216	$-4.565 \cdot 10^{-1}$	-4.634
$\sum$	$-5.016 \cdot 10^{-4}$	$6.629 \cdot 10^{-4}$	$-1.292 \cdot 10^{-2}$	-3.022
Cathode				
Location	$\dot{m}_{\text{Mass}\blacktriangle\text{C}\blacktriangle\text{CAT}}$	$\dot{m}_{\text{Mass}\blacktriangle\text{H}\blacktriangle\text{CAT}}$	$\dot{m}_{\text{Mass}\blacktriangle\text{N}\blacktriangle\text{CAT}}$	$\dot{m}_{\text{Mass}\blacktriangle\text{O}\blacktriangle\text{CAT}}$
Inlet	0.000	0.000	73.800	22.046
Outlet	0.000	0.000	-73.751	-19.060
$\sum$	0.000	0.000	$4.894 \cdot 10^{-2}$	2.986
$\sum_{\text{tot}}$	$-5.016 \cdot 10^{-4}$	$-6.629 \cdot 10^{-4}$	$-3.603 \cdot 10^{-2}$	$-3.630 \cdot 10^{-2}$

Table A.11.: **Electric properties and power densities of the HPC at $T_{in} = 1073$ K and $\Delta\phi_{el} = 2.7$ V:** The values are determined in the same way as described in the annotation of Table 6.5. Because of the increased operating temperature, the average current and power density increases compared to the REC in Table 6.5.

Quantity	Dimension	First cell (A)	Second cell (B)	Third cell (C)	Outlet
ϕ_{el}	V	2.70	1.79	0.89	$1.06 \cdot 10^{-8}$
$\Delta\phi_{el}$	V	0.91	0.90	0.89	
$\vec{E}_{el}$	V/m	0.20	0.22	0.24	0.25
$\Delta\vec{E}_{el}$	V/m	$-1.50 \cdot 10^{-2}$	$-2.40 \cdot 10^{-2}$	$-1.09 \cdot 10^{-3}$	
$\Delta\vec{E}_{el\blacktriangle}$%	%	-7.35	-10.95	-4.46	
$\vec{j}_{el}$	A/m^2	$1.85 \cdot 10^{5}$	$1.99 \cdot 10^{5}$	$2.20 \cdot 10^{5}$	$2.30 \cdot 10^{5}$
$\Delta\vec{j}_{el}$	A/m^2	$-1.36 \cdot 10^{4}$	$-2.18 \cdot 10^{4}$	$-9.83 \cdot 10^{3}$	
$\Delta\vec{j}_{el\blacktriangle}$%	%	-7.35	-10.96	-4.46	
$\vec{j}_{el\blacktriangle tot\blacktriangle ave}$	A/m^2	$2.24 \cdot 10^{3}$	$2.49 \cdot 10^{3}$	$2.89 \cdot 10^{3}$	
$\vec{j}_{el\blacktriangle CO\blacktriangle ave}$	A/m^2	$2.63 \cdot 10^{2}$	$2.75 \cdot 10^{2}$	$2.97 \cdot 10^{2}$	
$\vec{j}_{el\blacktriangle H_{2}\blacktriangle ave}$	A/m^2	$1.97 \cdot 10^{3}$	$2.11 \cdot 10^{3}$	$2.59 \cdot 10^{3}$	
$p_{el\blacktriangle tot\blacktriangle ave}$	W/m^2	$2.03 \cdot 10^{3}$	$2.24 \cdot 10^{3}$	$2.57 \cdot 10^{3}$	
$p_{el\blacktriangle CO\blacktriangle ave}$	W/m^2	$2.39 \cdot 10^{2}$	$2.47 \cdot 10^{2}$	$2.64 \cdot 10^{2}$	
$p_{el\blacktriangle H_{2}\blacktriangle ave}$	W/m^2	$1.79 \cdot 10^{3}$	$1.99 \cdot 10^{3}$	$2.31 \cdot 10^{3}$	
$p_{vol,el\blacktriangle tot\blacktriangle ave}$	W/m^3	$5.77 \cdot 10^{5}$	$6.36 \cdot 10^{5}$	$7.29 \cdot 10^{5}$	
$p_{vol,el\blacktriangle CO\blacktriangle ave}$	W/m^3	$6.78 \cdot 10^{4}$	$7.01 \cdot 10^{4}$	$7.49 \cdot 10^{4}$	
$p_{vol,el\blacktriangle H_{2}\blacktriangle ave}$	W/m^3	$5.09 \cdot 10^{5}$	$5.66 \cdot 10^{5}$	$6.54 \cdot 10^{5}$	

A.5.2. Reference case (REC)

The REference Case (REC) is characterized by a difference of $\Delta\phi_{el} = 2.4$ V between the external contacts.

Table A.12.: **Overall mass balance of the REC at $T_{in} = 1073$ K:** The table summarizes the mass balances of the REC at either side of the AB as well as its total value. The values are determined in accordance to the description of Table 6.1

Location	$\dot{m}_{Mass\blacktriangle ANO}$ [10^{-6} kg/s]	$\dot{m}_{Mass\blacktriangle CAT}$ [10^{-6} kg/s]	total [10^{-6} kg/s]
Inlet	$8.859 \cdot 10^{-2}$	$9.584 \cdot 10^{-1}$	1.154
Outlet	$-15.069 \cdot 10^{-2}$	$-8.964 \cdot 10^{-1}$	-1.154
$\sum$	$-6.200 \cdot 10^{-2}$	$6.200 \cdot 10^{-2}$	-0.000

Table A.13.: **Overall atom balance of the REC at T_{in} = 1073 K:** The table summarizes the atom balance at either side of the AB for the REC. The values are determined in accordance to the annotations of Table 6.2. All quantities are given in 10^{-8} kg/s.

Anode				
Location	$\dot{m}_{\text{Mass}\blacktriangle\text{C}\blacktriangle\text{ANO}}$	$\dot{m}_{\text{Mass}\blacktriangle\text{H}\blacktriangle\text{ANO}}$	$\dot{m}_{\text{Mass}\blacktriangle\text{N}\blacktriangle\text{ANO}}$	$\dot{m}_{\text{Mass}\blacktriangle\text{O}\blacktriangle\text{ANO}}$
Inlet	2.582	4.214	$4.443 \cdot 10^{-1}$	1.614
Outlet	-2.583	-4.204	$-5.619 \cdot 10^{-1}$	-7.706
$\sum$	$-1.557 \cdot 10^{-3}$	$-1.007 \cdot 10^{-2}$	$-1.175 \cdot 10^{-1}$	-6.092
Cathode				
Location	$\dot{m}_{\text{Mass}\blacktriangle\text{C}\blacktriangle\text{CAT}}$	$\dot{m}_{\text{Mass}\blacktriangle\text{H}\blacktriangle\text{CAT}}$	$\dot{m}_{\text{Mass}\blacktriangle\text{N}\blacktriangle\text{CAT}}$	$\dot{m}_{\text{Mass}\blacktriangle\text{O}\blacktriangle\text{CAT}}$
Inlet	0.000	0.000	73.800	22.040
Outlet	0.000	0.000	-73.700	-15.940
$\sum$	0.000	0.000	$1.000 \cdot 10^{-1}$	6.107
$\sum_{\text{tot}}$	$-1.557 \cdot 10^{-3}$	$-1.007 \cdot 10^{-2}$	$-1.750 \cdot 10^{-2}$	$1.586 \cdot 10^{-2}$

Table A.14.: **Overall energy balance of the REC at T_{in} = 1073 K:** The energy balance consists on the one hand of the thermal and chemical energy of the reacting media and on the other hand of the electrical energy flowing through the electric contacts. The values are determined in accordance to the annotations of Table 6.4. All quantities are given in 10^{-1} W.

	Anode		**Cathode**		**IC**	$\sum$
	$\dot{H}_{\text{En}}$	$\dot{Q}_{\text{En}}$	$\dot{H}_{\text{En}}$	$\dot{Q}_{\text{En}}$	$\dot{E}_{\text{En,Ch}}$	**[10^{-1} W]**
Inlet	1.921	7.413	8.050	11.990	$1.301 \cdot 10^{-3}$	29.375
Outlet	3.956	-8.294	-7.866	-11.610	-5.519	-29.333
$\sum$	5.877	-0.881	0.184	0.380	-5.518	-0.042

A.5.3. Low potential case (LPC)

The Low Potential Case (LPC) is characterized by a difference of $\Delta\phi_{\text{el}} = 2.1$ V between the external contacts.

Table A.15.: **Electric properties and power densities at $T_{\mathrm{in}} = 1073$ K and $\Delta\phi_{\mathrm{el}} = 2.4$ V:** The values are determined in the same way as described in the annotation of Table 6.5. Because of the increased operating temperature, the average current and power density increases compared to the REC in Table 6.5.

Quantity	Dimension	First cell (A)	Second cell (B)	Third cell (C)	Outlet
ϕ_{el}	V	2.40	1.59	0.78	$2.36 \cdot 10^{-8}$
$\Delta\phi_{\mathrm{el}}$	V	0.81	0.80	0.78	
$\vec{\mathrm{E}}_{\mathrm{el}}$	V/m	0.38	0.40	0.49	0.57
$\Delta\vec{\mathrm{E}}_{\mathrm{el}}$	V/m	$-2.60 \cdot 10^{-2}$	$-8.48 \cdot 10^{-2}$	$-8.09 \cdot 10^{-2}$	
$\Delta\vec{\mathrm{E}}_{\mathrm{el}\blacktriangle}\%$	%	-6.91	-21.04	-16.59	
$\vec{j}_{\mathrm{el}}$	A/m^2	$3.41 \cdot 10^5$	$3.65 \cdot 10^5$	$4.41 \cdot 10^5$	$5.15 \cdot 10^5$
$\Delta\vec{j}_{\mathrm{el}}$	A/m^2	$-2.36 \cdot 10^4$	$-7.68 \cdot 10^4$	$-7.32 \cdot 10^4$	
$\Delta\vec{j}_{\mathrm{el}\blacktriangle}\%$	%	-6.90	-21.05	-16.59	
$\vec{j}_{\mathrm{el}\blacktriangle\mathrm{tot}\blacktriangle\mathrm{ave}}$	A/m^2	$4.12 \cdot 10^3$	$4.99 \cdot 10^3$	$6.45 \cdot 10^3$	
$\vec{j}_{\mathrm{el}\blacktriangle\mathrm{CO}\blacktriangle\mathrm{ave}}$	A/m^2	$5.14 \cdot 10^2$	$5.05 \cdot 10^2$	$5.09 \cdot 10^2$	
$\vec{j}_{\mathrm{el}\blacktriangle\mathrm{H_2}\blacktriangle\mathrm{ave}}$	A/m^2	$3.60 \cdot 10^3$	$4.49 \cdot 10^3$	$5.94 \cdot 10^3$	
$\mathrm{p}_{\mathrm{el}\blacktriangle\mathrm{tot}\blacktriangle\mathrm{ave}}$	W/m^2	$3.36 \cdot 10^3$	$4.00 \cdot 10^3$	$5.05 \cdot 10^3$	
$\mathrm{p}_{\mathrm{el}\blacktriangle\mathrm{CO}\blacktriangle\mathrm{ave}}$	W/m^2	$4.18 \cdot 10^2$	$4.05 \cdot 10^2$	$3.99 \cdot 10^2$	
$\mathrm{p}_{\mathrm{el}\blacktriangle\mathrm{H_2}\blacktriangle\mathrm{ave}}$	W/m^2	$2.94 \cdot 10^3$	$3.60 \cdot 10^3$	$4.65 \cdot 10^3$	
$\mathrm{p}_{\mathrm{vol,el}\blacktriangle\mathrm{tot}\blacktriangle\mathrm{ave}}$	W/m^3	$9.51 \cdot 10^5$	$1.14 \cdot 10^6$	$1.43 \cdot 10^6$	
$\mathrm{p}_{\mathrm{vol,el}\blacktriangle\mathrm{CO}\blacktriangle\mathrm{ave}}$	W/m^3	$1.19 \cdot 10^5$	$1.15 \cdot 10^5$	$1.13 \cdot 10^5$	
$\mathrm{p}_{\mathrm{vol,el}\blacktriangle\mathrm{H_2}\blacktriangle\mathrm{ave}}$	W/m^3	$8.33 \cdot 10^5$	$1.02 \cdot 10^6$	$1.32 \cdot 10^6$	

Table A.16.: **Overall mass balance of the LPC:** The table summarizes the mass balances of the LPC at either side of the AB as well as its total value. The values are determined in accordance to the description of Table 6.1

Location	$\dot{m}_{\mathrm{Mass}\blacktriangle\mathrm{ANO}}$ [10^{-6} kg/s]	$\dot{m}_{\mathrm{Mass}\blacktriangle\mathrm{CAT}}$ [10^{-6} kg/s]	total [10^{-6} kg/s]
Inlet	0.098	1.057	1.155
Outlet	−0.215	−0.940	-1.155
$\sum$	−0.117	0.117	0.000

Table A.17.: **Overall atom balance of the LPC:** The table summarizes the atom balance at either side of the AB for the LPC. The values are determined in accordance to the annotations of Table 6.2. All quantities are given in 10^{-8} kg/s.

Anode				
Location	$\dot{m}_{\text{Mass}\blacktriangle\text{C}\blacktriangle\text{ANO}}$	$\dot{m}_{\text{Mass}\blacktriangle\text{H}\blacktriangle\text{ANO}}$	$\dot{m}_{\text{Mass}\blacktriangle\text{N}\blacktriangle\text{ANO}}$	$\dot{m}_{\text{Mass}\blacktriangle\text{O}\blacktriangle\text{ANO}}$
Inlet	2.847	4.647	$4.896 \cdot 10^{-1}$	1.781
Outlet	-2.848	-4.591	-1.005	-13.000
$\sum$	$-9.486 \cdot 10^{-5}$	$-5.543 \cdot 10^{-2}$	$-5.158 \cdot 10^{-1}$	-11.220
Cathode				
Location	$\dot{m}_{\text{Mass}\blacktriangle\text{C}\blacktriangle\text{CAT}}$	$\dot{m}_{\text{Mass}\blacktriangle\text{H}\blacktriangle\text{CAT}}$	$\dot{m}_{\text{Mass}\blacktriangle\text{N}\blacktriangle\text{CAT}}$	$\dot{m}_{\text{Mass}\blacktriangle\text{O}\blacktriangle\text{CAT}}$
Inlet	0.000	0.000	81.380	24.310
Outlet	0.000	0.000	-81.230	-12.780
$\sum$	0.000	0.000	$1.508 \cdot 10^{-1}$	11.530
$\sum_{\text{tot}}$	$-9.486 \cdot 10^{-5}$	$-5.543 \cdot 10^{-2}$	$-3.650 \cdot 10^{-1}$	$3.091 \cdot 10^{-1}$

Table A.18.: **Overall energy balance of the LPC:** The energy balance consists on the one hand of the thermal and chemical energy of the reacting media and on the other hand of the electrical energy flowing through the electric contacts. The values are determined in accordance to the annotations of Table 6.4. All quantities are given in 10^{-1} W.

	Anode		**Cathode**		**IC**	$\sum$
	$\dot{H}_{\text{En}}$	$\dot{Q}_{\text{En}}$	$\dot{H}_{\text{En}}$	$\dot{Q}_{\text{En}}$	$\dot{E}_{\text{En,Ch}}$	**[10^{-1} W]**
Inlet	1.461	7.373	7.787	11.970	$2.542 \cdot 10^{-2}$	28.664
Outlet	10.880	-9.761	-8.534	-12.510	-8.806	-28.731
$\sum$	12.341	-2.388	-0.747	-0.538	-8.781	-0.113

Table A.19.: **Electric properties and power densities at $T_{in} = 973$ K and $\Delta\phi_{el} = 2.1$ V (LPC):** The values are determined in the same way as described in the annotation of Table 6.5. Because of the reduced operating voltage, the average current and power density increases compared to the REC in Table 6.5.

Quantity	Dimension	Third cell (C)	Second cell (B)	First cell (A)	Inlet
ϕ_{el}	V	2.10	1.38	0.67	$4.61 \cdot 10^{-8}$
$\Delta\phi_{el}$	V	0.72	0.71	0.67	
$\vec{E}_{el}$	V/m	0.66	0.71	0.93	1.11
$\Delta\vec{E}_{el}$	V/m	$-4.44 \cdot 10^{-2}$	$-2.25 \cdot 10^{-1}$	$-1.77 \cdot 10^{-1}$	
$\Delta\vec{E}_{el\blacktriangle\%}$	%	-6.71	-31.87	-19.02	
$\vec{j}_{el}$	A/m^2	$5.99 \cdot 10^5$	$6.39 \cdot 10^5$	$8.42 \cdot 10^5$	$10.03 \cdot 10^5$
$\Delta\vec{j}_{el}$	A/m^2	$-4.02 \cdot 10^4$	$-2.04 \cdot 10^5$	$-1.60 \cdot 10^5$	
$\Delta\vec{j}_{el\blacktriangle\%}$	%	-6.72	-31.85	-19.02	
$\vec{j}_{el\blacktriangle tot\blacktriangle ave}$	A/m^2	$7.22 \cdot 10^3$	$9.53 \cdot 10^3$	$1.26 \cdot 10^4$	
$\vec{j}_{el\blacktriangle CO\blacktriangle ave}$	A/m^2	$7.89 \cdot 10^2$	$7.24 \cdot 10^2$	$6.31 \cdot 10^2$	
$\vec{j}_{el\blacktriangle H_2\blacktriangle ave}$	A/m^2	$6.43 \cdot 10^3$	$8.80 \cdot 10^3$	$1.19 \cdot 10^4$	
$p_{el\blacktriangle tot\blacktriangle ave}$	W/m^2	$5.22 \cdot 10^3$	$6.74 \cdot 10^3$	$8.40 \cdot 10^3$	
$p_{el\blacktriangle CO\blacktriangle ave}$	W/m^2	$5.70 \cdot 10^2$	$5.12 \cdot 10^2$	$4.23 \cdot 10^2$	
$p_{el\blacktriangle H_2\blacktriangle ave}$	W/m^2	$4.65 \cdot 10^3$	$6.23 \cdot 10^3$	$7.98 \cdot 10^3$	
$p_{vol,el\blacktriangle tot\blacktriangle ave}$	W/m^3	$1.48 \cdot 10^6$	$1.91 \cdot 10^6$	$2.38 \cdot 10^6$	
$p_{vol,el\blacktriangle CO\blacktriangle ave}$	W/m^3	$1.62 \cdot 10^5$	$1.45 \cdot 10^5$	$1.20 \cdot 10^5$	
$p_{vol,el\blacktriangle H_2\blacktriangle ave}$	W/m^3	$1.32 \cdot 10^6$	$1.77 \cdot 10^6$	$2.26 \cdot 10^6$	

Table A.20.: **Overall mass balance of the LPC at $T_{in} = 1073$ K:** The table summarizes the mass balances of the LPC at either side of the AB as well as its total value. The values are determined in accordance to the description of Table 6.1

Location	$\dot{m}_{Mass\blacktriangle ANO}$ [10^{-6} kg/s]	$\dot{m}_{Mass\blacktriangle CAT}$ [10^{-6} kg/s]	total [10^{-6} kg/s]
Inlet	0.088	0.959	1.047
Outlet	−0.176	−0.871	-1.047
$\sum$	−0.087	0.087	0.000

Table A.21.: **Overall atom balance of the LPC at T_{in} = 1073 K:** The table summarizes the atom balance at either side of the AB for the LPC. The values are determined in accordance to the annotations of Table 6.2. All quantities are given in 10^{-8} kg/s.

Anode				
Location	$\dot{m}_{\text{Mass}\blacktriangle\text{C}\blacktriangle\text{ANO}}$	$\dot{m}_{\text{Mass}\blacktriangle\text{H}\blacktriangle\text{ANO}}$	$\dot{m}_{\text{Mass}\blacktriangle\text{N}\blacktriangle\text{ANO}}$	$\dot{m}_{\text{Mass}\blacktriangle\text{O}\blacktriangle\text{ANO}}$
Inlet	2.580	4.211	$4.464 \cdot 10^{-1}$	1.618
Outlet	-2.556	-4.154	$-5.892 \cdot 10^{-1}$	-10.293
$\sum$	$-2.426 \cdot 10^{-2}$	$-5.691 \cdot 10^{-2}$	$-1.429 \cdot 10^{-1}$	-8.675
Cathode				
Location	$\dot{m}_{\text{Mass}\blacktriangle\text{C}\blacktriangle\text{CAT}}$	$\dot{m}_{\text{Mass}\blacktriangle\text{H}\blacktriangle\text{CAT}}$	$\dot{m}_{\text{Mass}\blacktriangle\text{N}\blacktriangle\text{CAT}}$	$\dot{m}_{\text{Mass}\blacktriangle\text{O}\blacktriangle\text{CAT}}$
Inlet	0.000	0.000	73.800	22.050
Outlet	0.000	0.000	-73.980	-13.125
$\sum$	0.000	0.000	$-1.800 \cdot 10^{-1}$	8.925
$\sum_{\text{tot}}$	$-2.426 \cdot 10^{-2}$	$-5.691 \cdot 10^{-2}$	$-3.229 \cdot 10^{-1}$	$2.500 \cdot 10^{-1}$

Table A.22.: **Overall energy balance of the LPC at T_{in} = 1073 K:** The energy balance consists on the one hand of the thermal and chemical energy of the reacting media and on the other hand of the electrical energy flowing through the electric contacts. The values are determined in accordance to the annotations of Table 6.4. All quantities are given in 10^{-1} W.

	Anode		**Cathode**		**IC**	$\sum$
	$\dot{H}_{\text{En}}$	$\dot{Q}_{\text{En}}$	$\dot{H}_{\text{En}}$	$\dot{Q}_{\text{En}}$	$\dot{E}_{\text{En,Ch}}$	**[10^{-1} W]**
Inlet	1.991	7.501	8.141	12.090	$3.201 \cdot 10^{-2}$	29.755
Outlet	6.682	-9.416	-8.450	-12.460	-6.397	-30.081
$\sum$	8.673	-1.915	-0.309	-0.370	-6.365	-0.286

Table A.23.: **Electric properties and power densities of the LPC at T_{in} = 1073 K and $\Delta\phi_{el}$ = 2.1 V:** The values are determined in the same way as described in the annotation of Table 6.5. Because of the increased operating temperature, the average current and power density increases compared to the LPC in Table A.19.

Quantity	Dimension	First cell (A)	Second cell (B)	Third cell (C)	Outlet
ϕ_{el}	V	2.10	1.40	0.69	$4.84 \cdot 10^{-8}$
$\Delta\phi_{el}$	V	0.70	0.70	0.69	
$\vec{E}_{el}$	V/m	0.31	0.33	0.63	11.02
$\Delta\vec{E}_{el}$	V/m	$-2.40 \cdot 10^{-1}$	$-2.99 \cdot 10^{-1}$	$-4.70 \cdot 10^{-1}$	
$\Delta\vec{E}_{el\blacktriangle}$%	%	-7.80	-90.08	-74.43	
$\vec{j}_{el}$	A/m^2	$2.54 \cdot 10^5$	$3.21 \cdot 10^5$	$5.88 \cdot 10^5$	$9.81 \cdot 10^5$
$\Delta\vec{j}_{el}$	A/m^2	$-6.72 \cdot 10^4$	$-26.62 \cdot 10^4$	$-39.32 \cdot 10^4$	
$\Delta\vec{j}_{el\blacktriangle}$%	%	-26.47	-82.85	-66.92	
$\vec{j}_{el\blacktriangle tot\blacktriangle ave}$	A/m^2	$3.75 \cdot 10^3$	$3.80 \cdot 10^3$	$1.28 \cdot 10^4$	
$\vec{j}_{el\blacktriangle CO\blacktriangle ave}$	A/m^2	$1.16 \cdot 10^3$	$1.29 \cdot 10^3$	$1.02 \cdot 10^3$	
$\vec{j}_{el\blacktriangle H_2\blacktriangle ave}$	A/m^2	$2.59 \cdot 10^3$	$2.52 \cdot 10^3$	$1.18 \cdot 10^4$	
$p_{el\blacktriangle tot\blacktriangle ave}$	W/m^2	$2.63 \cdot 10^3$	$2.68 \cdot 10^3$	$8.89 \cdot 10^3$	
$p_{el\blacktriangle CO\blacktriangle ave}$	W/m^2	$8.14 \cdot 10^2$	$9.06 \cdot 10^2$	$7.08 \cdot 10^2$	
$p_{el\blacktriangle H_2\blacktriangle ave}$	W/m^2	$1.82 \cdot 10^3$	$1.77 \cdot 10^3$	$8.18 \cdot 10^3$	
$p_{vol,el\blacktriangle tot\blacktriangle ave}$	W/m^3	$7.47 \cdot 10^5$	$7.59 \cdot 10^5$	$2.52 \cdot 10^6$	
$p_{vol,el\blacktriangle CO\blacktriangle ave}$	W/m^3	$2.31 \cdot 10^5$	$2.57 \cdot 10^5$	$2.01 \cdot 10^5$	
$p_{vol,el\blacktriangle H_2\blacktriangle ave}$	W/m^3	$5.16 \cdot 10^5$	$5.02 \cdot 10^5$	$2.32 \cdot 10^6$	

B. Mathematical derivations

B.1. Legendre transformation

In this appendix, a brief summary of the *Legendre transformation* is given. With the definition:

$$Б(З) = Д - Ж \cdot \frac{dД(Ж)}{dЖ}$$

it is possible to transform a function Д(Ж) into a function Б(З) without any loss of information. Since this mathematical operation is unique, the Legendre transformation of a thermodynamic potential is a thermodynamic potential too. (Motschmann 2005, p. 47 et seqq.)

Example (Leithner et al. 2010):
Find a thermodynamic potential in dependence of the temperature T instead of the entropy $S_{\mathrm{En}_\blacktriangle\mathrm{mol}}$:

$$З = T; Д = E_{\mathrm{En,int}_\blacktriangle\mathrm{mol}}(S_{\mathrm{En}_\blacktriangle\mathrm{mol}}, N_{\mathrm{Mol}_\blacktriangle\mathrm{mol}}, V_{\mathrm{Vol}_\blacktriangle\mathrm{mol}}); Ж = S_{\mathrm{En}_\blacktriangle\mathrm{mol}}$$

$$\begin{aligned} Б(T, N_{\mathrm{Mol}_\blacktriangle\mathrm{mol}}, V_{\mathrm{Vol}_\blacktriangle\mathrm{mol}}) =& E_{\mathrm{En,int}_\blacktriangle\mathrm{mol}}(S_{\mathrm{En}_\blacktriangle\mathrm{mol}}, N_{\mathrm{Mol}_\blacktriangle\mathrm{mol}}, V_{\mathrm{Vol}_\blacktriangle\mathrm{mol}}) \\ & - S_{\mathrm{En}_\blacktriangle\mathrm{mol}} \frac{dE_{\mathrm{En,int}_\blacktriangle\mathrm{mol}}(S_{\mathrm{En}_\blacktriangle\mathrm{mol}}, N_{\mathrm{Mol}_\blacktriangle\mathrm{mol}}, V_{\mathrm{Vol}_\blacktriangle\mathrm{mol}})}{dS_{\mathrm{En}_\blacktriangle\mathrm{mol}}} \\ =& E_{\mathrm{En,int}_\blacktriangle\mathrm{mol}} - S_{\mathrm{En}_\blacktriangle\mathrm{mol}} T \\ =& \mathfrak{F}_{\mathrm{En,Helm}_\blacktriangle\mathrm{mol}}(T, N_{\mathrm{Mol}_\blacktriangle\mathrm{mol}}, V_{\mathrm{Vol}_\blacktriangle\mathrm{mol}}) \,. \end{aligned}$$

B.2. Derivation of the Gibbs-Duhem relation

It is to show that the Gibbs free energy per charged particle equals the electrochemical potential (derived after (Motschmann 2005, p. 51 et seqq.)):

$$\left(\frac{\mathrm{d}G_{\mathrm{En}_{\blacktriangle}\mathrm{mol}}}{\mathrm{d}N_{\mathrm{Mol}_{\blacktriangle}\mathrm{mol}}}\right)_{T,p} = \left(\frac{\mathrm{d}E_{\mathrm{En,int}_{\blacktriangle}\mathrm{mol}}}{\mathrm{d}N_{\mathrm{Mol}_{\blacktriangle}\mathrm{mol}}}\right)_{T,p} \mathrm{d}N_{\mathrm{Mol}_{\blacktriangle}\mathrm{mol}} + \left(\frac{\mathrm{d}V_{\mathrm{Vol}_{\blacktriangle}\mathrm{mol}}}{\mathrm{d}N_{\mathrm{Mol}_{\blacktriangle}\mathrm{mol}}}\right)_{T,p} \mathrm{d}N_{\mathrm{Mol}_{\blacktriangle}\mathrm{mol}} \tag{B.1}$$

$$\underbrace{-T\left(\frac{\mathrm{d}S_{\mathrm{En}_{\blacktriangle}\mathrm{mol}}}{\mathrm{d}N_{\mathrm{Mol}_{\blacktriangle}\mathrm{mol}}}\right)_{T,p} \mathrm{d}N_{\mathrm{Mol}_{\blacktriangle}\mathrm{mol}}}_{:=\mu_{\mathrm{mol}}\,\mathrm{d}N_{\mathrm{Mol}_{\blacktriangle}\mathrm{mol}}}$$

$$= \left(\underbrace{\frac{\mathrm{d}E_{\mathrm{En,int}_{\blacktriangle}\mathrm{mol}}}{\mathrm{d}V_{\mathrm{Vol}_{\blacktriangle}\mathrm{mol}}}}_{=-p} \frac{\mathrm{d}V_{\mathrm{Vol}_{\blacktriangle}\mathrm{mol}}}{\mathrm{d}N_{\mathrm{Mol}_{\blacktriangle}\mathrm{mol}}}\right)_{T,p} \mathrm{d}N_{\mathrm{Mol}_{\blacktriangle}\mathrm{mol}} + p\left(\frac{\mathrm{d}V_{\mathrm{Vol}_{\blacktriangle}\mathrm{mol}}}{\mathrm{d}N_{\mathrm{Mol}_{\blacktriangle}\mathrm{mol}}}\right)_{T,p} \mathrm{d}N_{\mathrm{Mol}_{\blacktriangle}\mathrm{mol}} \tag{B.2}$$

$$+ \mu_{\mathrm{mol}}\,\mathrm{d}N_{\mathrm{Mol}_{\blacktriangle}\mathrm{mol}}$$

$$= -p\left(\frac{\mathrm{d}V_{\mathrm{Vol}_{\blacktriangle}\mathrm{mol}}}{\mathrm{d}N_{\mathrm{Mol}_{\blacktriangle}\mathrm{mol}}}\right)_{T,p} \mathrm{d}N_{\mathrm{Mol}_{\blacktriangle}\mathrm{mol}} + p\left(\frac{\mathrm{d}V_{\mathrm{Vol}_{\blacktriangle}\mathrm{mol}}}{\mathrm{d}N_{\mathrm{Mol}_{\blacktriangle}\mathrm{mol}}}\right)_{T,p} + \mu_{\mathrm{mol}}\,\mathrm{d}N_{\mathrm{Mol}_{\blacktriangle}\mathrm{mol}}$$

$$= \mu_{\mathrm{mol}}\,\mathrm{d}N_{\mathrm{Mol}_{\blacktriangle}\mathrm{mol}}$$

$$\Rightarrow G_{\mathrm{En}_{\blacktriangle}\mathrm{mol}} = \mu_{\mathrm{mol}} N_{\mathrm{Mol}_{\blacktriangle}\mathrm{mol}}.$$

In case of a homogeneously charged system using the definition of the electrochemical potential $\mu_{\mathrm{elchem}_{\blacktriangle}\mathrm{mol}}$ (see equation 2.2) the last term in equation B.2 might be rewritten as:

$$\Rightarrow T\left(\frac{\mathrm{d}S_{\mathrm{En}_{\blacktriangle}\mathrm{mol}}}{\mathrm{d}N_{\mathrm{Mol}_{\blacktriangle}\mathrm{mol}}}\right)_{T,p} \mathrm{d}N_{\mathrm{Mol}_{\blacktriangle}\mathrm{mol}} = (\mu_{\mathrm{elchem}_{\blacktriangle}\mathrm{mol}} - zF_{\mathrm{Ch}_{\blacktriangle}\mathrm{mol}}\phi)\mathrm{d}N_{\mathrm{Mol}_{\blacktriangle}\mathrm{mol}}$$

$$\left(\frac{\mathrm{d}G_{\mathrm{En}_{\blacktriangle}\mathrm{mol}}}{\mathrm{d}N_{\mathrm{Mol}_{\blacktriangle}\mathrm{mol}}}\right)_{T,p} = \mu_{\mathrm{elchem}_{\blacktriangle}\mathrm{mol}}\,\mathrm{d}N_{\mathrm{Mol}_{\blacktriangle}\mathrm{mol}} - zF_{\mathrm{Ch}_{\blacktriangle}\mathrm{mol}}\phi\mathrm{d}N_{\mathrm{Mol}_{\blacktriangle}\mathrm{mol}}$$

$$\underbrace{\left(\frac{\mathrm{d}G_{\mathrm{En}_{\blacktriangle}\mathrm{mol}}}{\mathrm{d}N_{\mathrm{Mol}_{\blacktriangle}\mathrm{mol}}}\right)_{T,p} + zF_{\mathrm{Ch}_{\blacktriangle}\mathrm{mol}}\phi\mathrm{d}N_{\mathrm{Mol}_{\blacktriangle}\mathrm{mol}}}_{:=\frac{\mathrm{d}\mathfrak{G}_{\mathrm{En,elchem}_{\blacktriangle}\mathrm{mol}}}{\mathrm{d}N_{\mathrm{Mol}_{\blacktriangle}\mathrm{mol}}}} = \mu_{\mathrm{elchem}_{\blacktriangle}\mathrm{mol}}\,\mathrm{d}N_{\mathrm{Mol}_{\blacktriangle}\mathrm{mol}}$$

$$\frac{\mathrm{d}\mathfrak{G}_{\mathrm{En,elchem}_{\blacktriangle}\mathrm{mol}}}{\mathrm{d}N_{\mathrm{Mol}_{\blacktriangle}\mathrm{mol}}} = \mu_{\mathrm{elchem}_{\blacktriangle}\mathrm{mol}}\,\mathrm{d}N_{\mathrm{Mol}_{\blacktriangle}\mathrm{mol}}$$

$$\Rightarrow \mathfrak{G}_{\mathrm{En,elchem}_{\blacktriangle}\mathrm{mol}} = \mu_{\mathrm{elchem}_{\blacktriangle}\mathrm{mol}} N_{\mathrm{Mol}_{\blacktriangle}\mathrm{mol}} = G_{\mathrm{En}_{\blacktriangle}\mathrm{mol}} + zF_{\mathrm{Ch}_{\blacktriangle}\mathrm{mol}}\phi N_{\mathrm{Mol}_{\blacktriangle}\mathrm{mol}}.$$

B.3. Derivation of the half cell potentials

Applying the *law of mass action* (see 2.15) to both half cell reactions in equation 2.12 gives:

$$\sum_{\text{products } i} \nu_{\text{ANO}\blacktriangle i}\, \mu_{\text{elchem}\blacktriangle\text{mol}\blacktriangle\text{mol}\blacktriangle\text{ANO}\blacktriangle i} - \sum_{\text{reactants } j} \nu_{\text{ANO}\blacktriangle j}\, \mu_{\text{elchem}\blacktriangle\text{mol}\blacktriangle\text{mol}\blacktriangle\text{ANO}\blacktriangle j} = \mu_{\text{elchem}\blacktriangle\text{mol}\blacktriangle\text{mol}\blacktriangle\text{ANO/ELE}} ,$$

$$\sum_{\text{products } k} \nu_{\text{CAT}\blacktriangle k}\, \mu_{\text{elchem}\blacktriangle\text{mol}\blacktriangle\text{mol}\blacktriangle\text{CAT}\blacktriangle k} - \sum_{\text{reactants } l} \nu_{\text{CAT}\blacktriangle l}\, \mu_{\text{elchem}\blacktriangle\text{mol}\blacktriangle\text{mol}\blacktriangle\text{CAT}\blacktriangle l} = \mu_{\text{elchem}\blacktriangle\text{mol}\blacktriangle\text{mol}\blacktriangle\text{ELE/CAT}} .$$

With the definition of the electrochemical potential in equation 2.2 it follows:

$$\sum_{\text{products } i} \nu_{\text{ANO}\blacktriangle i}\, \mu_{\text{mol}\blacktriangle\text{ANO}\blacktriangle i} - \sum_{\text{reactants } j} \nu_{\text{ANO}\blacktriangle j}\, \mu_{\text{mol}\blacktriangle\text{ANO}\blacktriangle j}$$
$$+ \sum_{\text{products } i} \nu_{\text{ANO}\blacktriangle i}\, z_i F_{\text{Ch}\blacktriangle\text{mol}}\, \phi_{\text{ANO}} - \sum_{\text{reactants } j} \nu_{\text{ANO}\blacktriangle j}\, z_j F_{\text{Ch}\blacktriangle\text{mol}}\, \phi_{\text{ANO}} = \mu_{\text{mol}\blacktriangle\text{ANO/ELE}} + z_{\text{tot}} F_{\text{Ch}\blacktriangle\text{mol}}\, \phi_{\text{ANO/ELE}} ,$$

$$\sum_{\text{products } k} \nu_{\text{CAT}\blacktriangle k}\, \mu_{\text{mol}\blacktriangle\text{CAT}\blacktriangle k} - \sum_{\text{reactants } l} \nu_{\text{CAT}\blacktriangle l}\, \mu_{\text{mol}\blacktriangle\text{CAT}\blacktriangle l}$$
$$+ \sum_{\text{products } k} \nu_{\text{CAT}\blacktriangle k}\, z_k F_{\text{Ch}\blacktriangle\text{mol}}\, \phi_{\text{CAT}} - \sum_{\text{reactants } l} \nu_{\text{CAT}\blacktriangle l}\, z_l F_{\text{Ch}\blacktriangle\text{mol}}\, \phi_{\text{CAT}} = \mu_{\text{mol}\blacktriangle\text{ELE/CAT}} + z_{\text{tot}} F_{\text{Ch}\blacktriangle\text{mol}}\, \phi_{\text{ELE/CAT}} ,$$

$$\phi_{\text{ANO}} \left(\sum_{\text{products } i} \nu_{\text{ANO}\blacktriangle i}\, z_i - \sum_{\text{reactants } j} \nu_{\text{ANO}\blacktriangle j}\, z_j \right) - z_{\text{tot}}\, \phi_{\text{ANO/ELE}}$$
$$=$$
$$\frac{1}{F_{\text{Ch}\blacktriangle\text{mol}}} \left(\mu_{\text{mol}\blacktriangle\text{ANO/ELE}} - \left(\sum_{\text{products } i} \nu_{\text{ANO}\blacktriangle i}\, \mu_{\text{mol}\blacktriangle\text{ANO}\blacktriangle i} - \sum_{\text{reactants } j} \nu_{\text{ANO}\blacktriangle j}\, \mu_{\text{mol}\blacktriangle\text{ANO}\blacktriangle j} \right) \right) ,$$

$$z_{\text{tot}} \phi_{\text{ELE/CAT}} -$$
$$\phi_{\text{CAT}} \left(\sum_{\text{products } k} \nu_{\text{CAT}\blacktriangle k}\, z_k - \sum_{\text{reactants } l} \nu_{\text{CAT}\blacktriangle l}\, z_l \right) = \frac{1}{F_{\text{Ch}\blacktriangle\text{mol}}} \left(\sum_{\text{products } k} \nu_{\text{CAT}\blacktriangle k}\, \mu_{\text{mol}\blacktriangle\text{CAT}\blacktriangle k} - \right.$$
$$\left. \sum_{\text{reactants } l} \nu_{\text{CAT}\blacktriangle l}\, \mu_{\text{mol}\blacktriangle\text{CAT}\blacktriangle l} - \mu_{\text{mol}\blacktriangle\text{ELE/CAT}} \right) .$$

Due to the conservation of charge, in the equilibrium case the differences of the sums over the products and reactants on the left side of the equations both have to be the total number of charges transferred per particle z_{tot}. This leads to (Leithner et al. 2010):

$$\phi_{\text{ANO}} - \phi_{\text{ANO/ELE}} = \frac{1}{z_{\text{tot}} F_{\text{Ch}\blacktriangle\text{mol}}} \left(\mu_{\text{mol}\blacktriangle\text{ANO/ELE}} - \sum_{\text{products } i} \nu_{\text{ANO}\blacktriangle i}\, \mu_{\text{mol}\blacktriangle\text{ANO}\blacktriangle i} - \sum_{\text{reactants } j} \nu_{\text{ANO}\blacktriangle j}\, \mu_{\text{mol}\blacktriangle\text{ANO}\blacktriangle j} \right) ,$$

$$\phi_{\text{ELE/CAT}} - \phi_{\text{CAT}} = \frac{1}{z_{\text{tot}} F_{\text{Ch}\blacktriangle\text{mol}}} \left(\sum_{\text{products } k} \nu_{\text{CAT}\blacktriangle k}\, \mu_{\text{mol}\blacktriangle\text{CAT}\blacktriangle k} - \sum_{\text{reactants } l} \nu_{\text{CAT}\blacktriangle l}\, \mu_{\text{mol}\blacktriangle\text{CAT}\blacktriangle l} - \mu_{\text{mol}\blacktriangle\text{ELE/CAT}} \right) .$$

If the electrolyte potential is defined to be zero[1], it follows:

$$\phi_{\mathrm{ANO}} = -\frac{1}{z_{\mathrm{tot}} F_{\mathrm{Ch}\blacktriangle\mathrm{mol}}} \left(\sum_{\text{products } i} \nu_{\mathrm{ANO}\blacktriangle i}\, \mu_{\mathrm{mol}\blacktriangle\mathrm{ANO}\blacktriangle i} - \sum_{\text{reactants } j} \nu_{\mathrm{ANO}\blacktriangle j}\, \mu_{\mathrm{mol}\blacktriangle\mathrm{ANO}\blacktriangle j} \right) , \tag{B.3}$$

$$\phi_{\mathrm{CAT}} = -\frac{1}{z_{\mathrm{tot}} F_{\mathrm{Ch}\blacktriangle\mathrm{mol}}} \left(\sum_{\text{products } k} \nu_{\mathrm{CAT}\blacktriangle k}\, \mu_{\mathrm{mol}\blacktriangle\mathrm{CAT}\blacktriangle k} - \sum_{\text{reactants } l} \nu_{\mathrm{CAT}\blacktriangle l}\, \mu_{\mathrm{mol}\blacktriangle\mathrm{CAT}\blacktriangle l} \right) . \tag{B.4}$$

B.4. Derivation of the Nernst-Planck equation

Starting from the diffusive transport of charged particles, according to Fick's law (Meschede 2006, p. 238):

$$\begin{aligned} \vec{J}_{\mathrm{diff}} &= -\underline{D}_{\mathrm{elchem}\blacktriangle\mathrm{mol}} \operatorname{grad}\left(\mu_{\mathrm{elchem}\blacktriangle\mathrm{mol}}\right) , \qquad \underline{D}_{\mathrm{elchem}\blacktriangle\mathrm{mol}} \text{ in } \frac{\mathrm{mol}^2}{\mathrm{J\,m\,s}} \\ \Rightarrow \vec{j}_{\mathrm{diff}} &= z F_{\mathrm{Ch}\blacktriangle\mathrm{mol}} \vec{J}_{\mathrm{diff}} , \\ &= -z F_{\mathrm{Ch}\blacktriangle\mathrm{mol}} \underline{D}_{\mathrm{elchem}\blacktriangle\mathrm{mol}} \operatorname{grad}\left(\mu_{\mathrm{elchem}\blacktriangle\mathrm{mol}}\right) , \\ &= -z F_{\mathrm{Ch}\blacktriangle\mathrm{mol}} \underline{D}_{\mathrm{elchem}\blacktriangle\mathrm{mol}} \left(\operatorname{grad}\left(\mu_{\mathrm{mol}}\right) + z F_{\mathrm{Ch}\blacktriangle\mathrm{mol}} \operatorname{grad}(\phi)\right) \end{aligned}$$

using

$$\operatorname{grad}\left(\mu_{\mathrm{mol}}\right) = \frac{\Re_{\mathrm{En}\blacktriangle\mathrm{mol}} T}{c_{\mathrm{Mol}\blacktriangle\mathrm{vol}}} \operatorname{grad}\left(c_{\mathrm{Mol}\blacktriangle\mathrm{vol}}\right) ,$$

it follows

$$\vec{j}_{\mathrm{diff}} = -z F_{\mathrm{Ch}\blacktriangle\mathrm{mol}} \underline{D}_{\mathrm{elchem}\blacktriangle\mathrm{mol}} \left(\frac{\Re_{\mathrm{En}\blacktriangle\mathrm{mol}} T}{c_{\mathrm{Mol}\blacktriangle\mathrm{vol}}} \operatorname{grad}\left(c_{\mathrm{Mol}\blacktriangle\mathrm{vol}}\right) + z F_{\mathrm{Ch}\blacktriangle\mathrm{mol}} \operatorname{grad}(\phi) \right) .$$

With the definition

$$\underline{D}_{\mathrm{diff}\blacktriangle\mathrm{ion}} := \frac{\underline{D}_{\mathrm{elchem}\blacktriangle\mathrm{mol}} \Re_{\mathrm{En}\blacktriangle\mathrm{mol}} T}{c_{\mathrm{Mol}\blacktriangle\mathrm{vol}}} \qquad \text{in } \mathrm{m}^2/\mathrm{s}$$

and the NEE

$$\underline{\sigma}_{\mathrm{ion}} = z^2 F_{\mathrm{Ch}\blacktriangle\mathrm{mol}}{}^2 \underline{D}_{\mathrm{elchem}\blacktriangle\mathrm{mol}} = \frac{c_{\mathrm{Mol}\blacktriangle\mathrm{vol}} z^2 F_{\mathrm{Ch}\blacktriangle\mathrm{mol}}{}^2}{\Re_{\mathrm{En}\blacktriangle\mathrm{mol}} T} \underline{D}_{\mathrm{diff}\blacktriangle\mathrm{ion}} \qquad \text{in S/m}$$

it follows the Nernst-Planck Equation (NPE)

$$\begin{aligned} \vec{j}_{\mathrm{diff}} &= -z F_{\mathrm{Ch}\blacktriangle\mathrm{mol}} \underline{D}_{\mathrm{diff}\blacktriangle\mathrm{ion}} \operatorname{grad}\left(c_{\mathrm{Mol}\blacktriangle\mathrm{vol}}\right) - \underline{\sigma}_{\mathrm{ion}} \operatorname{grad}(\phi) , \\ &= -z F_{\mathrm{Ch}\blacktriangle\mathrm{mol}} \underline{D}_{\mathrm{diff}\blacktriangle\mathrm{ion}} \operatorname{grad}\left(c_{\mathrm{Mol}\blacktriangle\mathrm{vol}}\right) + \underline{\sigma}_{\mathrm{ion}} \vec{\mathbb{E}} . \end{aligned} \tag{B.5}$$

[1] e.g. if a standard hydrogen electrode is used

C. Material properties

In this appendix, the constants as well as the equations and their coefficients used to calculate temperature dependent[1] values for the material parameters of the models of this thesis are summarized. Table C.1 lists the physical dimensions of the output values and the fitting parameters in dependence of the calculated quantities IO.

The following equation is taken from the Physical and Thermodynamic Properties of Pure Chemicals data compilation (PTPPC) (Daubert and Danner 1989, p. V-1):

- Thermal conductivity of the gas-phase $\lambda_{\mathrm{En}_{\blacktriangle}(\mathrm{g})}$ in W/m K, dynamic viscosity of the gas-phase $\Gamma_{\mathrm{visc}_{\blacktriangle}(\mathrm{g})}$ in kg/m s:

$$\mathrm{IO} = \frac{a_1 T^{a_2}}{1 + \frac{a_3}{T} + \frac{a_4}{T^2}} \,. \tag{C.1}$$

The following equation is used for polynomial fitting of literature data:

$$\mathrm{IO} = a_1 + a_2 T + a_3 T^2 + a_4 T^3 \,. \tag{C.2}$$

The following equations are taken from the National Aeronautics and Space Administration (space agency of the United States of America (USA)) (NASA) Glenn materials database (Zehe, Gordon, and Mcbride 2002):

- Molar heat capacity of the gas-/solid-phase $c_{\mathrm{En,p}_{\blacktriangle}\mathrm{mol}_{\blacktriangle}(\mathrm{g})/(\mathrm{s})}$ in J/mol K:

$$\mathrm{IO} = \Re_{\mathrm{En}_{\blacktriangle}\mathrm{mol}} \cdot \left(a_1 T^{-2} + a_2 T^{-1} + a_3 + a_4 T + a_5 T^2 + a_6 T^3 + a_7 T^4\right), \tag{C.3}$$

- Molar enthalpy of formation $\mathrm{d}H_{\mathrm{En}_{\blacktriangle}\mathrm{mol}_{\blacktriangle}\mathrm{mol}_{\blacktriangle}(\mathrm{g})}$ in J/mol:

$$\mathrm{IO} = \Re_{\mathrm{En}_{\blacktriangle}\mathrm{mol}} \cdot T \cdot \left(-a_1 T^{-2} + a_2 \frac{\ln(T)}{T} + a_3 + \frac{a_4 T}{2} + \frac{a_5 T^2}{3} + \frac{a_6 T^3}{4} + \frac{a_7 T^4}{5} + \frac{b_1}{T}\right), \tag{C.4}$$

[1] T in K

- Molar entropy of formation $\mathrm{d}S_{\mathrm{En_{\blacktriangle}mol_{\blacktriangle}mol_{\blacktriangle}(g)}}$ in J/mol K:

$$\text{IO} = \Re_{\mathrm{En_{\blacktriangle}mol}} \cdot \left(-\frac{a_1 T^{-2}}{2} - a_2 T^{-1} + a_3 \ln(T) + a_4 T + \frac{a_5 T^2}{2} + \frac{a_6 T^3}{3} + \frac{a_7 T^4}{4} + b_2 \right) . \tag{C.5}$$

The electric conductivity $\underline{\underline{\sigma}}_{\mathrm{el}}$ of Crofer22APU in S/m is fitted using the following expression:

$$\text{IO} = a_1 T^{a_2} . \tag{C.6}$$

For the ionic conductivity $\underline{\underline{\sigma}}_{\mathrm{ion}}$ of the ceramic components in S/m, different Arrhenius approaches are used:

$$\text{IO} = a_1 \exp\left(-\frac{a_2}{T} \right) , \tag{C.7}$$

$$\text{IO} = \frac{a_1}{T} \exp\left(-\frac{a_2}{T} \right) , \tag{C.8}$$

$$\text{IO} = a_1 \exp\left(-\frac{a_2}{\Re_{\mathrm{En_{\blacktriangle}mol}}} \cdot \left(\frac{1}{T} - \frac{1}{1123\,\mathrm{K}} \right) \right) . \tag{C.9}$$

$$\text{IO} = a_1 \exp\left(-\frac{a_2}{\Re_{\mathrm{En_{\blacktriangle}mol}} T} \right) , \tag{C.10}$$

Table C.1.: **Physical dimensions of the fitting parameters:** The table summarizes the dimensions of the fitting parameters used in equations C.1 - C.9.

Physical quantity	**Variable**	**Eq.**	**Dimensions**									
			IO	$\mathbf{a_1}$	$\mathbf{a_2}$	$\mathbf{a_3}$	$\mathbf{a_4}$	$\mathbf{a_5}$	$\mathbf{a_6}$	$\mathbf{a_7}$	$\mathbf{b_1}$	$\mathbf{b_2}$
dynamic viscosity	Γ_{visc}	C.1	kg/m s	kg/m s K		K	K^2					
electric conductivity	$\underline{\sigma}_{\mathrm{el}}$	C.2	S/m	S/m	S/m K							
electric conductivity	$\underline{\sigma}_{\mathrm{el}}$	C.8	S/m	S K/m	K							
ionic conductivity	$\underline{\sigma}_{\mathrm{ion}}$	C.7	S/m	S/m	K							
ionic conductivity	$\underline{\sigma}_{\mathrm{ion}}$	C.9	S/m	S/m	kJ/mol							
ionic conductivity	$\underline{\sigma}_{\mathrm{ion}}$	C.10	S/m	S/m	kJ/mol							
mass heat capacity	$c_{\mathrm{En,p\blacktriangle mass}}$	C.2	J/kg K	J/kg K	J/kg K^2	J/kg K^3	J/kg K^4					
molar enthalpy of formation	$\mathrm{d}H_{\mathrm{En\blacktriangle mol}}$	C.4	J/mol	J/K^2	K		K^{-1}	K^{-2}	K^{-3}	K^{-4}	K	
molar entropy of formation	$\mathrm{d}S_{\mathrm{En\blacktriangle mol}}$	C.5	J/mol K	J/K^2	K		K^{-1}	K^{-2}	K^{-3}	K^{-4}		
molar heat capacity	$c_{\mathrm{En,p\blacktriangle mol}}$	C.3	J/mol K	K^2	K		K^{-1}	K^{-2}	K^{-3}	K^{-4}		
thermal conductivity	λ_{En}	C.1	W/m K	W/m K^2		K	K^2					
thermal conductivity	λ_{En}	C.2	W/m K	W/m K	W/m K^2	W/m K^3	W/m K^4					

Table C.2.: **Material parameters and fitting coefficients for CH_4:** Unless otherwise noted, all material properties are listed for the gas phase.

Property	**Eq.**	**Coefficients**					**Reference/Note**
		value	$\mathbf{a_1}$	$\mathbf{a_2}$	$\mathbf{a_3}$	$\mathbf{a_4}$	
		$\mathbf{a_5}$	$\mathbf{a_6}$	$\mathbf{a_7}$	$\mathbf{b_1}$	$\mathbf{b_2}$	
critical pressure p_{crit} [bar]		45.99					(Poling, Prausnitz, and O'Connell 2001, p. A.5)
critical temperature T_{crit} [K]		190.56					(Poling, Prausnitz, and O'Connell 2001, p. A.5)
density ρ_{vol} [kg/m^3]		0.7168					(National Institute of Standards and Technology 2012, No. 74-82-8)
dipole moment δ [Debye]		0.0					(Poling, Prausnitz, and O'Connell 2001, p. A.20)
dynamic viscosity $\Gamma_{\text{visc}\blacktriangle(g)}$ [Pa s]	C.1		$1.323 \cdot 10^{-5}$	$1.798 \cdot 10^{-1}$	$7.18 \cdot 10^{2}$	$-8.9 \cdot 10^{3}$	(Daubert and Danner 1989) $T = 90.67 - 850$ K
exchange energy $\epsilon_{i/j}/k_{\text{En,B}}$ [K]		148.6					(Poling, Prausnitz, and O'Connell 2001, p. B.1)
molar heat capacity $c_{\text{En,p}\blacktriangle\text{mol}\blacktriangle(g)}$ [J/mol K]	C.3		$-1.766850998 \cdot 10^{5}$	$2.786181020 \cdot 10^{3}$	$-1.202577850 \cdot 10^{1}$	$3.917619290 \cdot 10^{-2}$	$T = 200 - 1000$ K
		$-3.619054430 \cdot 10^{-5}$	$2.026853043 \cdot 10^{-8}$	$-4.976705490 \cdot 10^{-12}$	$-2.331314360 \cdot 10^{4}$	$8.904322750 \cdot 10^{1}$	
(Zehe, Gordon, and Mcbride 2002)			$3.730042760 \cdot 10^{6}$	$-1.383501485 \cdot 10^{4}$	$2.049107091 \cdot 10^{1}$	$-1.961974759 \cdot 10^{-3}$	$T = 1000 - 6000$ K
		$4.727313040 \cdot 10^{-7}$	$-3.72881469 \cdot 10^{-11}$	$1.623737207 \cdot 10^{-15}$	$7.532066910 \cdot 10^{4}$	$-1.219124889 \cdot 10^{2}$	
molar mass $M_{\text{Mass}\blacktriangle\text{mol}}$ [kg/kmol]		16.043					(Daubert and Danner 1989)
scattering diameter $Ъ_{\text{scat}\blacktriangle i/j}$ [Å]		3.758					(Poling, Prausnitz, and O'Connell 2001, p. B.1)
thermal conductivity $\lambda_{\text{En}\blacktriangle(g)}$ [W/m K]	C.1		$1.226 \cdot 10^{-3}$	$8.031 \cdot 10^{-1}$	$9.6 \cdot 10^{2}$	$-6.12 \cdot 10^{4}$	(Daubert and Danner 1989) $T = 97 - 1400$ K

Table C.3.: **Material parameters and fitting coefficients for CO:** Unless otherwise noted, all material properties are listed for the gas phase.

Property	**Eq.**	**Coefficients**					**Reference/Note**
		value	$\mathbf{a_1}$	$\mathbf{a_2}$	$\mathbf{a_3}$	$\mathbf{a_4}$	
		$\mathbf{a_5}$	$\mathbf{a_6}$	$\mathbf{a_7}$	$\mathbf{b_1}$	$\mathbf{b_2}$	
critical pressure p_{crit} [bar]		34.94					(Poling, Prausnitz, and O'Connell 2001, p. A.5)
critical temperature T_{crit} [K]		132.85					(Poling, Prausnitz, and O'Connell 2001, p. A.5)
density ρ_{vol} [kg/m^3]		1.2505					(National Institute of Standards and Technology 2012, No. 630-08-0)
dipole moment δ [Debye]		0.1					(Todd and Young 2002)
dynamic viscosity $\Gamma_{\text{visc}\,\blacktriangle(\text{g})}$ [Pa s]	C.1		$1.1127 \cdot 10^{-6}$	$5.338 \cdot 10^{-1}$	$9.47 \cdot 10^{1}$		(Daubert and Danner 1989) $T = 68.15 - 1250$ K
exchange energy $\epsilon_{i/j}/k_{\text{En,B}}$ [K]		91.7					(Poling, Prausnitz, and O'Connell 2001, p. B.1)
molar heat capacity $c_{\text{En,p}\,\blacktriangle\text{mol}\,\blacktriangle(\text{g})}$ [J/mol K]	C.3	$1.456903469 \cdot 10^{-5}$	$1.489045326 \cdot 10^{4}$ $-1.087746302 \cdot 10^{-8}$	$-2.922285939 \cdot 10^{2}$ $3.027941827 \cdot 10^{-12}$	5.72452717 $-1.303131878 \cdot 10^{4}$	$-8.17623503 \cdot 10^{-3}$ -7.859241350	$T = 200 - 1000$ K
(Zehe, Gordon, and Mcbride 2002)		$1.39881454 \cdot 10^{-7}$	$4.61919725 \cdot 10^{5}$ $-1.78768036 \cdot 10^{-11}$	$-1.944704863 \cdot 10^{3}$ $9.62093557 \cdot 10^{-16}$	5.91671418 $-2.466261084 \cdot 10^{3}$	$-5.66428283 \cdot 10^{-4}$ $-1.387413108 \cdot 10^{1}$	$T = 1000 - 6000$ K
molar mass $M_{\text{Mass}\blacktriangle\text{mol}}$ [kg/kmol]		28.01					(Daubert and Danner 1989)
scattering diameter $Ъ_{\text{scat}\,\blacktriangle i/j}$ [Å]		3.690					(Poling, Prausnitz, and O'Connell 2001, p. B.1)
thermal conductivity $\lambda_{\text{En}\,\blacktriangle(\text{g})}$ [W/m K]	C.1		$8.39 \cdot 10^{-4}$	$6.409 \cdot 10^{-1}$	$8.605 \cdot 10^{1}$		(Daubert and Danner 1989) $T = 70 - 1250$ K

Table C.4.: **Material parameters and fitting coefficients for CO_2:** Unless otherwise noted, all material properties are listed for the gas phase.

Property	**Eq.**	**Coefficients**					**Reference/Note**
		value	$\mathbf{a_1}$	$\mathbf{a_2}$	$\mathbf{a_3}$	$\mathbf{a_4}$	
		$\mathbf{a_5}$	$\mathbf{a_6}$	$\mathbf{a_7}$	$\mathbf{b_1}$	$\mathbf{b_2}$	
critical pressure p_{crit} [bar]		73.74					(Poling, Prausnitz, and O'Connell 2001, p. A.6)
critical temperature T_{crit} [K]		304.12					(Poling, Prausnitz, and O'Connell 2001, p. A.6)
density ρ_{vol} [kg/m^3]		1.9769		(National Institute of Standards and Technology 2012, No. 124-38-9); T = 273.13 K; p = 1013.25 hPa			
dipole moment δ [Debye]		0.0					(Todd and Young 2002)
dynamic viscosity $\Gamma_{\text{visc}\blacktriangle(g)}$ [Pa s]	C.1		$2.148 \cdot 10^{-6}$	$4.6 \cdot 10^{-1}$	$2.0 \cdot 10^{2}$		(Daubert and Danner 1989) T = 194.67 − 1500 K
exchange energy $\epsilon_{i/j}/k_{\text{En,B}}$ [K]		195.2					(Poling, Prausnitz, and O'Connell 2001, p. B.1)
molar heat capacity $c_{\text{En,p}\blacktriangle\text{mol}\blacktriangle(g)}$ [J/mol K]	C.3	-2.127308728·10^{-7}	4.94365054·10^{4} -7.68998878·10^{-10}	-6.26411601·10^{2} 2.849677801·10^{-13}	5.30172524 -4.528198460·10^{4}	2.503813816·10^{-3} -7.048279440	T = 200 − 1000 K
(Zehe, Gordon, and Mcbride 2002)		$4.86367688 \cdot 10^{-9}$	$1.176962419 \cdot 10^{5}$ $-1.89105331 \cdot 10^{-12}$	$-1.788791477 \cdot 10^{3}$ $6.33003659 \cdot 10^{-16}$	8.29152319 -3.908350590·10^{4}	$-9.22315678 \cdot 10^{-5}$ -2.652669281·10^{1}	T = 1000 − 6000 K
molar mass $M_{\text{Mass}\blacktriangle\text{mol}}$ [kg/kmol]		44.01					(Daubert and Danner 1989)
scattering diameter $Ъ_{\text{scat}\blacktriangle i/j}$ [Å]		3.941					(Poling, Prausnitz, and O'Connell 2001, p. B.1)
thermal conductivity $\lambda_{\text{En}\blacktriangle(g)}$ [W/m K]	C.1		3.69	$-3.838 \cdot 10^{-1}$	9.64·10^{2}	1.86·10^{6}	(Daubert and Danner 1989) T = 194.67 − 1500 K

Table C.5.: **Material parameters and fitting coefficients for Crofer22APU:** Unless otherwise noted, all material properties are listed for the solid phase.

Property	**Eq.**	**Coefficients**					**Reference/Note**
		value a_5	a_1 a_6	a_2 a_7	a_3 b_1	a_4 b_2	
density $\rho_{\mathrm{Mass}\blacktriangle\mathrm{vol}}$ [kg/m^3]		7670					(VDM 2005; VDM 2010)
electric conductivity $\underline{\sigma}_{\mathrm{el}}$ [S/m]	C.6		$76.888 \cdot 10^{6}$	-0.64571			(VDM 2005; VDM 2010) self made fit
heat capacity $c_{\mathrm{En,p}\blacktriangle\mathrm{mass,(s)}}$ [J/kg K]	C.2		293.61	$6.522 \cdot 10^{-1}$	$-2.912 \cdot 10^{-4}$		(VDM 2005; VDM 2010) self made fit
molar mass $M_{\mathrm{Mass}\blacktriangle\mathrm{mol}}$ [kg/kmol]		55.12					(VDM 2005; VDM 2010)
thermal conductivity $\lambda_{\mathrm{En,(s)}}$ [W/m K]	C.2		8.074	$5.674 \cdot 10^{-2}$	$-7.205 \cdot 10^{-5}$	$3.076 \cdot 10^{-8}$	(VDM 2005; VDM 2010) self made fit, λ_{En}(473.13K) neglected

Table C.6.: **Material parameters and fitting coefficients for H_2:** Unless otherwise noted, all material properties are listed for the gas phase.

Property	Eq.	Coefficients					Reference/Note
		value	a_1	a_2	a_3	a_4	
		a_5	a_6	a_7	b_1	b_2	
critical pressure p_{crit} [bar]		12.97					(Poling, Prausnitz, and O'Connell 2001, p. A.19)
critical temperature T_{crit} [K		33.25					(Poling, Prausnitz, and O'Connell 2001, p. A.19)
density ρ_{vol} [kg/m^3]		0.08988					(National Institute of Standards and Technology 2012, No. 1333-74-0) T = 273.13 K; p = 1013.25 hPa
dipole moment δ [Debye]		0.0					(Poling, Prausnitz, and O'Connell 2001, p. A.34)
dynamic viscosity $\Gamma_{visc\,▲(g)}$ [Pa s]	C.1		$1.56 \cdot 10^{-7}$	$7.06 \cdot 10^{-1}$	−5.67	$2.1 \cdot 10^{2}$	(Daubert and Danner 1989) T = 15 − 1500 K
exchange energy $\epsilon_{i/j}/k_{En,B}$ [K]			59.7				(Poling, Prausnitz, and O'Connell 2001, p. B.2)
molar heat capacity $c_{En,p\,▲mol▲(g)}$ [J/mol K]	C.3	1.753605076·10^{-5}	4.078323210·10^{4} -1.20286027·10^{-8}	-8.009186040·10^{2} 3.36809349·10^{-12}	8.21470201 2.682484665·10^{3}	- 1.269714457·10^{-2} -3.043788844·10^{1}	(Zehe, Gordon, and Mcbride 2002) T = 200 − 1000 K
molar heat capacity $c_{En,p\,▲mol▲(g)}$ [J/mol K]	C.3	$-3.471 \cdot 10^{-7}$	$5.608 \cdot 10^{5}$ $5.937 \cdot 10^{-11}$	$-8.372 \cdot 10^{2}$ $-3.607 \cdot 10^{-15}$	2.975 5.339824410·10^{3}	$-1.252 \cdot 10^{-3}$ -2.202774769	(Zehe, Gordon, and Mcbride 2002) T = 1000 − 6000 K
molar mass $M_{Mass▲mol}$ [kg/kmol]		2.016					(Daubert and Danner 1989)
scattering diameter $Ъ_{scat\,▲i/j}$ [Å]		2.827					(Poling, Prausnitz, and O'Connell 2001, p. B.2)
thermal conductivity $\lambda_{En\,▲(g)}$ [W/m K]	C.1		$2.547 \cdot 10^{-3}$	$7.444 \cdot 10^{-1}$	9.0		(Daubert and Danner 1989) T = 14 − 1500 K

Table C.7.: **Material parameters and fitting coefficients for H_2O:** Unless otherwise noted, all material properties are listed for the gas phase.

Property	Eq.	Coefficients					Reference/Note
		value	a_1	a_2	a_3	a_4	
		a_5	a_6	a_7	b_1	b_2	
critical pressure p_{crit} [bar]		220.64					(Poling, Prausnitz, and O'Connell 2001, p. A.19)
critical temperature T_{crit} [K]		647.14					(Poling, Prausnitz, and O'Connell 2001, p. A.19)
density ρ_{vol} [kg/m^3]		0.598					T = 373.13 K; p = 1013.25 hPa
dipole moment δ [Debye]		1.8					(Poling, Prausnitz, and O'Connell 2001, p. A.34)
dynamic viscosity $\Gamma_{visc\,▲(g)}$ [Pa s]	C.1		$2.6986 \cdot 10^{-6}$	$4.98 \cdot 10^{-1}$	$1.2577 \cdot 10^{3}$	$-1.957 \cdot 10^{4}$	(Daubert and Danner 1989) T = 373.15 – 1073.1 K
exchange energy $\epsilon_{i/j}/k_{En,B}$ [K]		809.1					(Poling, Prausnitz, and O'Connell 2001, p. B.2)
molar heat capacity $c_{En,p\,▲mol▲(g)}$ [J/mol K]	C.3		$-3.94796083 \cdot 10^{4}$	$5.75573102 \cdot 10^{2}$	$9.31782653 \cdot 10^{-1}$	$7.22271286 \cdot 10^{-3}$	(Zehe, Gordon, and Mcbride 2002) T = 200 – 1000 K
		$-7.34255737 \cdot 10^{-6}$	$4.95504349 \cdot 10^{-9}$	$-1.336933246 \cdot 10^{-12}$	$-3.303974310 \cdot 10^{4}$	$1.724205775 \cdot 10^{1}$	
molar heat capacity $c_{En,p\,▲mol▲(g)}$ [J/mol K]	C.3		$1.034972096 \cdot 10^{6}$	$-2.412698562 \cdot 10^{3}$	4.64611078	$2.291998307 \cdot 10^{-3}$	(Zehe, Gordon, and Mcbride 2002) T = 1000 – 6000 K
		$-6.83683048 \cdot 10^{-7}$	$9.42646893 \cdot 10^{-11}$	$-4.82238053 \cdot 10^{-15}$	$-1.384286509 \cdot 10^{4}$	-7.978148510	
molar mass $M_{Mass▲mol}$ [kg/kmol]		18.015					(Daubert and Danner 1989)
scattering diameter $Ъ_{scat\,▲i/j}$ [Å]		2.641					(Poling, Prausnitz, and O'Connell 2001, p. B.2)
thermal conductivity $\lambda_{En\,▲(g)}$ [W/m K]	C.1		$6.977 \cdot 10^{-5}$	1.1243	$8.449 \cdot 10^{2}$	$-1.4885 \cdot 10^{5}$	(Daubert and Danner 1989) T = 373.15 – 1073.1 K

Table C.8.: **Material parameters and fitting coefficients for Lanthanum Strontium Cobalt Ferrite ($La_{0.2}Sr_{0.8}Co_{0.2}Fe_{0.8}O_{3-\varphi}$) (LSCF):** Unless otherwise noted, all material properties are listed for the solid phase. The oxygen non-stoechiometry coefficient φ varies in the literature. Because of a lack of literature data, during simulations for $c_{\mathrm{En,p}_{\blacktriangle}\mathrm{mass,(s)}}$ and $\lambda_{\mathrm{En,(s)}}$ the values for LSM are used.

Property	**Eq.**	**Coefficients**					**Reference/Note**
		value a_5	a_1 a_6	a_2 a_7	a_3 b_1	a_4 b_2	
density $\rho_{\mathrm{Mass}_{\blacktriangle}\mathrm{vol}}$ [kg/m^3]		5480					(Li et al. 1999) $\varphi = 0$
electric conductivity $\underline{\sigma}_{\mathrm{el}}$ [S/m]	C.8	$1.509 \cdot 10^7$	1068.11				(Fan, Yan, and Yan 2011) $T = 1173$ K
ionic conductivity $\underline{\sigma}_{\mathrm{ion}}$ [S/m]	C.10		$42.646 \cdot 10^3$	85.881			(Fan, Yan, and Yan 2011)
ion diffusion coefficient D_{ion} [m^2/s]	C.10	$1.58{\cdot}10^{-6}$	73.6				(Xu and Thomson 1999)
molar mass $M_{\mathrm{Mass}_{\blacktriangle}\mathrm{mol}}$ [kg/kmol]		202.3					(Li et al. 1999) $\varphi = 0$
molar oxygen vacancy concentration $V_{\mathrm{O}_{\blacktriangle}^{\bullet\bullet}\mathrm{Mol}_{\blacktriangle}\mathrm{vol}}$ [mol/m^3]		$1.354{\cdot}10^3$					(Armstrong et al. 2011)

Table C.9.: **Material parameters and fitting coefficients for Lanthanum Strontium Manganite $\left(La_{0.84}Sr_{0.16}MnO_3\right)$ (LSM):** Unless otherwise noted, all material properties are listed for the solid phase.

Property	Eq.	Coefficients					Reference/Note
		value a_5	a_1 a_6	a_2 a_7	a_3 b_1	a_4 b_2	
density $\rho_{\text{Mass}\blacktriangle\text{vol}}$ [kg/m^3]		6580					(Bossel 1992)
electric conductivity $\underline{\underline{\sigma}}_{\text{el}}$ [S/m]	C.8		$42 \cdot 10^6$	$1.17 \cdot 10^3$			(Bossel 1992; Li, Shi, and Cai 2010)
heat capacity $c_{\text{En,p}\blacktriangle\text{mass,(s)}}$ [J/kg K]		300					(Bossel 1992)
ionic conductivity $\underline{\underline{\sigma}}_{\text{ion}}$ [S/m]		100					(Deseure et al. 2005)
ion diffusion coefficient D_{ion} [m^2/s]		$4{\cdot}10^{-8}$					(Deseure et al. 2005)
molar mass $M_{\text{Mass}\blacktriangle\text{mol}}$ [kg/kmol]		108.49					(Riedel 1999) calculated from composition
thermal conductivity $\lambda_{\text{En,(s)}}$ [W/m K]		3					(Bossel 1992)

Table C.10.: **Material parameters and fitting coefficients for N_2:** Unless otherwise noted, all material properties are listed for the gas phase.

Property	Eq.	Coefficients					Reference/Note
		value	a_1	a_2	a_3	a_4	
		a_5	a_6	a_7	b_1	b_2	
critical pressure p_{crit} [bar]		33.98					(Poling, Prausnitz, and O'Connell 2001, p. A.19)
critical temperature T_{crit} [K]		126.2					(Poling, Prausnitz, and O'Connell 2001, p. A.19)
density ρ_{vol} [kg/m^3]		1.2503					(National Institute of Standards and Technology 2012, No. 7727-37-9) T = 273.13 K; p = 1013.25 hPa
dipole moment δ [Debye]		0.0					(Poling, Prausnitz, and O'Connell 2001, p. A.34)
dynamic viscosity $\Gamma_{visc\,▲(g)}$ [Pa s]	C.1		$7.632 \cdot 10^{-7}$	$5.8823 \cdot 10^{-1}$	$6.775 \cdot 10^{1}$		(Daubert and Danner 1989) T = 80 − 1500 K
exchange energy $\epsilon_{i/j}/k_{En,B}$ [K]		71.4					(Poling, Prausnitz, and O'Connell 2001, p. B.2)
molar heat capacity $c_{En,p\,▲mol▲(g)}$ [J/mol K]	C.3	$1.384646189 \cdot 10^{-5}$	$2.210371497 \cdot 10^{4}$ $-9.62579362 \cdot 10^{-9}$	$-3.81846182 \cdot 10^{2}$ $2.519705809 \cdot 10^{-12}$	6.08273836 $7.108460860 \cdot 10^{2}$	$-8.53091441 \cdot 10^{-3}$ $-1.076003744 \cdot 10^{1}$	(Zehe, Gordon, and Mcbride 2002) T = 200 − 1000 K
molar heat capacity $c_{En,p\,▲mol▲(g)}$ [J/mol K]	C.3	$1.491806679 \cdot 10^{-7}$	$5.87712406 \cdot 10^{5}$ $-1.923105485 \cdot 10^{-11}$	$-2.239249073 \cdot 10^{3}$ $1.061954386 \cdot 10^{-15}$	6.06694922 $1.283210415 \cdot 10^{4}$	$-6.1396855 \cdot 10^{-4}$ $-1.586640027 \cdot 10^{1}$	(Zehe, Gordon, and Mcbride 2002) T = 1000 − 6000 K
molar mass $M_{Mass▲mol}$ [kg/kmol]		28.014					(Daubert and Danner 1989)
scattering diameter $Ъ_{scat\,▲i/j}$ [Å]		3.798					(Poling, Prausnitz, and O'Connell 2001, p. B.2)
thermal conductivity $\lambda_{En\,▲(g)}$ [W/m K]	C.1		$3.51 \cdot 10^{-4}$	$7.652 \cdot 10^{-1}$	$2.5767 \cdot 10^{1}$		(Daubert and Danner 1989) T = 78 − 1500 K

Table C.11.: **Material parameters and fitting coefficients for Ni:** Unless otherwise noted, all material properties are listed for the solid phase.

Property	**Eq.**	**Coefficients**					**Reference/Note**
		value	$\mathbf{a_1}$	$\mathbf{a_2}$	$\mathbf{a_3}$	$\mathbf{a_4}$	
		$\mathbf{a_5}$	$\mathbf{a_6}$	$\mathbf{a_7}$	$\mathbf{b_1}$	$\mathbf{b_2}$	
density $\rho_{\mathrm{Mass}\blacktriangle\mathrm{vol}}$ [kg/m^3]		8910					(Verein Deutscher Ingenieure 2006, p. Dea4) T_{ref} = 273,13 K
electric conductivity $\underline{\sigma}_{\mathrm{el}}$ [S/m]	C.2		$3.27 \cdot 10^6$	-1065.3			(Li, Shi, and Cai 2010)
heat capacity $c_{\mathrm{En,p}\blacktriangle\mathrm{mass,(s)}}$ [J/kg K]	C.3	-6.98690689·10^{-4}	-7.68913109·10^5 4.90607891·10^{-7}	1.433956218·10^4	-1.042751331·10^2	3.92626132·10^{-1}	(Zehe, Gordon, and Mcbride 2002) T = 200 − 400 K
heat capacity $c_{\mathrm{En,p}\blacktriangle\mathrm{mass,(s)}}$ [J/kg K]	C.3	- 2.847789131·10^{-2}	-3.34588734·10^8 1.142789828·10^{-5}	3.42452797·10^6	-1.394425564·10^4	2.825654843·10^1	(Zehe, Gordon, and Mcbride 2002) T = 400 − 631 K
heat capacity $c_{\mathrm{En,p}\blacktriangle\mathrm{mass,(s)}}$ [J/kg K]	C.3	2.153531609·10^{-2}	1.036354737·10^9 -9.19246414·10^{-6}	-6.81327855·10^6 1.62433298·10^{-9}	1.854367615·10^4	-2.673006535·10^1	(Zehe, Gordon, and Mcbride 2002) T = 631 − 1200 K
heat capacity $c_{\mathrm{En,p}\blacktriangle\mathrm{mass,(s)}}$ [J/kg K]	C.3	6.67132091·10^{-3}	2.518440662·10^9 -1.69898816·10^{-6}	-9.89546523·10^6 1.788537986·10^{-10}	1.60973753·10^4	-1.386478566·10^1	(Zehe, Gordon, and Mcbride 2002) T = 1200 − 1728 K
molar mass $M_{\mathrm{Mass}\blacktriangle\mathrm{mol}}$ [kg/kmol]		58.69					(Riedel 1999) calculated from composition
thermal conductivity $\lambda_{\mathrm{En,(s)}}$ [W/m K]		94					(Verein Deutscher Ingenieure 2006, p. Dea4) T_{ref} = 273.13 K

Table C.12.: **Material parameters and fitting coefficients for O_2:** Unless otherwise noted, all material properties are listed for the gas phase.

Property	Eq.	Coefficients					Reference/Note
		value	a_1	a_2	a_3	a_4	
		a_5	a_6	a_7	b_1	b_2	
critical pressure p_{crit} [bar]		50.43					(Poling, Prausnitz, and O'Connell 2001, p. A.19)
critical temperature T_{crit} [K]		154.58					(Poling, Prausnitz, and O'Connell 2001, p. A.19)
density ρ_{vol} [kg/m^3]		1.429					(National Institute of Standards and Technology 2012, No. 7782-44-7) T = 273.13 K; p = 1013.25 hPa
dipole moment δ [Debye]		0.0					(Poling, Prausnitz, and O'Connell 2001, p. A.34)
dynamic viscosity $\Gamma_{visc\,▲(g)}$ [Pa s]	C.1		$8.038 \cdot 10^{-7}$	$6.0478 \cdot 10^{-1}$	$7.03 \cdot 10^{1}$		(Daubert and Danner 1989) T = 80 − 1500 K
exchange energy $\epsilon_{i/j}/k_{En,B}$ [K]		106.7					(Poling, Prausnitz, and O'Connell 2001, p. B.2)
molar heat capacity $c_{En,p\,▲mol▲(g)}$ [J/mol K]	C.3	-6.83630052·10^{-7}	-3.42556342·10^{4} -2.0233727·10^{-9}	4.84700097·10^{2} 1.039040018·10^{-12}	1.119010961 -3.391454870·10^{3}	4.29388924·10^{-3} 1.849699470·10^{1}	(Zehe, Gordon, and Mcbride 2002) T = 200 − 1000 K
molar heat capacity $c_{En,p\,▲mol▲(g)}$ [J/mol K]	C.3	$-2.188067988 \cdot 10^{-7}$	$-1.037939022 \cdot 10^{6}$ $2.053719572 \cdot 10^{-11}$	$2.344830282 \cdot 10^{3}$ $-8.19346705 \cdot 10^{-16}$	1.819732036 -1.689010929·10^{4}	$1.267847582 \cdot 10^{-3}$ 1.738716506·10^{1}	(Zehe, Gordon, and Mcbride 2002) T = 1000 − 6000 K
molar mass $M_{Mass▲mol}$ [kg/kmol]		31.999					(Daubert and Danner 1989)
scattering diameter $Ъ_{scat\,▲i/j}$ [Å]		3.467					(Poling, Prausnitz, and O'Connell 2001, p. B.2)
thermal conductivity $\lambda_{En\,▲(g)}$ [W/m K]	C.1		$4.943 \cdot 10^{-4}$	$7.34 \cdot 10^{-1}$	7.0·10^{1}		(Daubert and Danner 1989) T = 80 − 1500 K

Table C.13.: **Material parameters and fitting coefficients for sealant** $\left(\left(SiO_2\right)_{0.65}\left(Na_2O\right)_{0.2}(CaO)_{0.12}(BaO)_{0.03}\right)$**:** Unless otherwise noted, all material properties are listed for the solid phase.

Property	**Eq.**	**Coefficients**					**Reference/Note**
		value a_5	a_1 a_6	a_2 a_7	a_3 b_1	a_4 b_2	
density $\rho_{\text{Mass}\blacktriangle\text{vol}}$ [kg/m^3]	–	2690					(Salman and Gharib 1984) T = 298.13 K
heat capacity $c_{\text{En,p}\blacktriangle\text{mass,(s)}}$ [J/kg K]	–	500					(de Haart 2010) T = 1073.13 K
molar mass $M_{\text{Mass}\blacktriangle\text{mol}}$ [kg/kmol]	–	62.78					(Riedel 1999) calculated from composition
thermal conductivity $\lambda_{\text{En,(s)}}$ [W/m K]		0.9415					(Salman and Gharib 1984) T = 298.13 K

Table C.14.: **Material parameters and fitting coefficients for 8 mole% Yttrium Stabilized Zirconium (YSZ):** Unless otherwise noted, all material properties are listed for the solid phase.

Property	**Eq.**	**Coefficients**					**Reference/Note**
		value	a_1	a_2	a_3	a_4	
		a_5	a_6	a_7	b_1	b_2	
density $\rho_{\text{Mass}\blacktriangle\text{vol}}$ [kg/m^3]		5669					(He et al. 2002)
electric conductivity $\underline{\sigma}_{\text{el}}$ [S/m]		3					(de Haart 2010)
ionic conductivity $\underline{\sigma}_{\text{ion}}$ [S/m]	C.7		$1.339 \cdot 10^3$	10.9			(He et al. 2002)
heat capacity $c_{\text{En,p}\blacktriangle\text{mass,(s)}}$ [J/kg K]		500					(Bossel 1992; Tietz 1999)
molar mass $M_{\text{Mass}\blacktriangle\text{mol}}$ [kg/kmol]		131.43					(Riedel 1999) calculated from composition
thermal conductivity $\lambda_{\text{En,(s)}}$ [W/m K]		2.4					(Al-Hamamre and Al-Zoubi 2010; Bossel 1992; de Haart 2010)

D. Student works in the context of this thesis

In this appendix, the almost 60 student projects I was involved in as supervisor from 2009 to 2012 are listed. Some of the projects are directly associated, whereas others are virtually independent from this thesis. Nevertheless, without the help of all those students listed below, definitely a lot of my ideas would never have become reality. Once again thank you for all the faith you had in me. I am proud that I was able to work with you on these projects, and to all of you just the best wishes for your journey through life.

1. **Klages, Merle** *(diploma thesis, August 2009, in German)*
   Erstellung von Leistungskennfeldern einer Hochtemperatur-Polymerelektrolyt-Brennstoffzelle
2. **Schorsch, Timm Jerry** *(project work, October 2009, in German)*
   Übersicht Marktteilnehmer und Forschungseinrichtungen für Hochtemperatur-Brennstoffzellensysteme
3. **Blome, Klaus** *(diploma thesis, November 2009, in German)*
   Wertschöpfung Strom- und Wärmeerzeugung - Nutzen, Chancen und Risiken für kommunale Stadtwerke
4. **Staeck, Rune** *(diploma thesis, November 2009, in German)*
   Entwicklung eines piezogesteuerten Coanda-Druckreglers für einen Brennstoffzellenantrieb
5. **Diedrich, Johannes** *(project work, November 2009, in German)*
   Simulation eines innovativen Langzeitwärmespeichers
6. **Dahms, Manis** *(project work, January 2010, in German)*
   Konstruktion, Bau und Regelung eines Reflow-Ofens zur Bestückung von Platinen mit SMD Bauteilen
7. **Garcia, David** *(diploma thesis, January 2010, in German)*
   Simulation eines innovativen Langzeitwärmespeichers
8. **Zeidler, Conrad** *(student research project, February 2010, in German)*
   Simulation eines innovativen Langzeitwärmespeichers
9. **Fradin, Etienne** *(student research project, February 2010)*
   CFD Modeling of a Methane Steam Reformer
10. **Olsen Berenguer, Fernando Adrian** *(bachelor thesis, February 2010)*

Study of power system operation using SOFC as disperse generation

11. **Kammel, Jannes** *(diploma thesis, June 2010, in German)*
    Verfahren zur Befeuchtung des Elektrolyten einer Proton Exchange Membrane Fuel Cell (PEMFC)-Brennstoffzelle
12. **Brinkmeier, Jan-Philipp** *(student research project, September 2010, in German)*
    Konstruktion & Bau eines elektrisch nachgeführten Kollektors zur solarthermischen Heisswasserbereitung
13. **Blot, Carine** *(student research project, August 2010, in German)*
    Simulation und Optimirung der Kanalstruktur einer Hochtemperatur Brennstoffzelle
14. **Enge, Tobias** *(project work, June 2010, in German)*
    Stand der Technik im Bereich von Mikro- und Mini-Blockheizkraftwerk mit Brennstoffzellen
15. **Zeidler, Conrad** *(project work, September 2010, in German)*
    Stand der Technik im Bereich keramischer Materialien für Hochtemperatur-Brennstoffzellen
16. **Ilchuk, Michael** *(project work, November 2010, in German)*
    Anpassung eines Modells einer PEMFC-Brennstoffzelle zur Massdatenvalidierung und Simulation verschiedener Betriebsfälle
17. **Hübner, Stefan** *(student research project, December 2010)*
    Analysis of the technical and economical viability of a hydrogen production system based on renewable energy sources
18. **Scheufen, Sven** *(diploma thesis, January 2011, in German)*
    Weiterentwicklung eines PEMFC-Brennstoffzellenmodells zur Erstellung von Leistungskennfeldern
19. **Schlegel, Jan-Rickmer** *(diploma thesis, January 2011, in German)*
    Leistungscharakterisierung des Brennstoffzellensystems im Antriebsstrang einer B-Klasse
20. **Stellfeld, Patrick; Radkowitsch, Florian; Baak, Christian; Suermann, Michel** *(project work, February 2011, in German)*
    Konzeption eines SOFC-Prüfstands
21. **Baudis, Meike** *(project work, February 2011, in German)*
    Bewertung von solaren Kühlsystemen für Nichtwohngebäude unter verschiedenen Klimabedingungen
22. **Lefebvre, Jonathan** *(student research project, March 2011, in German)*
    Simulation der elektrochemischen Vorgänge in einer Hochtemperatur-Brennstoffzelle
23. **Böker, Anabel; Falk, Sabine** *(project work, April 2011, in German)*
    Konzept zur regennerativen Energieversorgung einer Modellregion
24. **Jocher, Yvonne** *(student research project, April 2011, in German)*
    Modellierung der elektrochemischen Reaktion im Anodenbereich einer SOFC
25. **Hanke, Victoria** *(project work, May 2011, in German)*
    Modelle der Reformierung von Kohlenwasserstoffen für den Einsatz als Brenngas in einer Solid Oxide Fuel Cell

26. **Todt, Helge** *(project work, May 2011, in German)*
Konstruktion einer Hochtemperatur Brennstoffzelle
27. **Lippky, Gesa** *(student research project, May 2011, in German)*
Stand der Technik im Bereich der Modellierung und Simulation von Brennstoffzellen und Brennstoffzellensystemen
28. **Arteagar, Zubiri Itziar** *(diploma thesis, June 2011)*
Optimization of a solar thermal concentrator for hot water production
29. **Baumbach, Sabine** *(bachelor thesis, July 2011, in German)*
Entwicklungsbegleitende Untersuchungen und Optimierungen der Wärmeverteilung in der Umhausung eines Blockheizkraftwerks mit 3D-Strömungssimulation
30. **Enge, Tobias** *(diploma thesis, August 2011, in German)*
Energieeffizienz im Presswerk - Analyse von Energiewertströmen und Überprüfung von Energieeffizienzmaßnahmen an einer Warmumformungspresse
31. **Femppel, Yannick** *(bachelor thesis, August 2011, in German)*
Verifizierung eines CFD-Modells einer solid oxide fuel cell
32. **Zirkel, Felix** *(project work, August 2011, in German)*
Analyse von solarthermischen Kühlsystemen für Wohn- und Nichtwohngebäude in Deutschland
33. **Langenhorst, Lukas** *(bachelor thesis, August 2011, in German)*
Analyse der Möglichkeit zur Direktvermarktung von Stromerzeugungseinheiten mit Energiespeichern
34. **Stellfeld, Patrick** *(bachelor thesis, August 2011, in German)*
Geometrieerstellung für die CFD Simulation einer Solid Oxide Fuel Cell
35. **Kuppe, Sebastian** *(bachelor thesis, September 2011, in German)*
Analyse des Vermarktungsansatzes der Regelleistung für dezentrale Stromerzeugungseinheiten mit gekoppelten elektrischen Energiespeichern
36. **Heinke, Steffen** *(student project, September 2011, in German)*
CFD Modellierung und Simulation der porösen Struktur und der elektrochemischen Reaktion im Anodenbereich einer SOFC
37. **Wagner, Eduard** *(bachelor thesis, September 2011, in German)*
Modellierung und Simulation einer kaskadierten Solid Oxide Fuel Cell (SOFC) mit Matlab/Simulink
38. **Smit, Felix** *(student research project, September 2011, in German)*
Temperaturregelung eines Brennstoffzellenprüfstands
39. **Schneider, Elisabeth** *(bachelor thesis, September 2011, in German)*
Projektierung einer regennerativen Wärmeversorgung unter Berücksichtigung der energetischen Sanierung der Gebäudehülle eines denkmalgeschützten Gebäudes
40. **Ghodhbani, Walid** *(student research project, September 2011, in German)*
Umbau eines Reflow-Ofens als Demonstrationsversuch
41. **Kubannek, Fabian** *(project work, September 2011, in German)*
Fuel Cells in Germany and Japan - A comparative study on the current market situation and its possible development in the future

42. **Woschny, Immo; Meyer, Doreen; Kellner, Robert; Jantschik, Kyra; Schwindt, Clemens; Rischbieter** *(project work, October 2011, in German)*
Praxisprojekt: Energie-/Ökobilanz des ÖPNV
43. **Ackermann, Tilmar** *(project work, November 2011, in German)*
Modellierung und Simulation eines Holz-Heizkraftwerks unter ökonomischen und ökologischen Aspekten
44. **Barrio, Daniel Antello** *(project work, December 2011, in German)*
Geschichte der Brennstoffzellen
45. **Hanke, Victoria** *(student project, December 2011, in German)*
Modellierung und Simulation der heterogenen katalytischen Reformierung von niederen Kohlenwasserstoffen mittels eines finiten Volumen-Verfahrens
46. **Schild, Christian** *(student project, February 2012, in German)*
CFD-Simulation eines Hochtemperatur-Plattenwärmeübertragers für die Luftvorwärmung in einem SOFC-Brennstoffzellensystem
47. **Baak, Christian** *(bachelor thesis, February 2012, in German)*
Modellierung eines Fernwärmenetzes als Kurzzeitwärmespeicher
48. **Kellner, Robert** *(bachelor thesis, March 2012, in German)*
Inbetriebnahme eines Brennstoffzellenprüfstands
49. **Horn, Birte** *(student project, April 2012, in German)*
Modellierung der elektrochemischen Katalyse in Solid Oxide Fuel Cells
50. **Jonscher, Michael; Kusta Konstantin** *(project work, April 2012, in German)*
Modellierung und Simulation einer kaskadierten Hochtemperatur-Brennstoffzelle
51. **Ghodhbani, Walid** *(diploma thesis, April 2012, in German)*
Basisinbetriebnahme einer Prototypensteuergeräteplatine für die Ansteuerung von Elektroantrieben und Prüfung der Grundfunktionalität einer Schnittstelle zum Infineon Hybrid-Kit II
52. **Schmidt, Stefanie; Nürnberg, Eva; Suermann, Michel; Krautstrunk, Isabell** *(research project, April 2012, in German)*
Modellierung des Sorptionsvorgangs in Membranen von PEMFC-Brennstoffzellenantrieben
53. **Clark, Wiebke; Loellhoeffel, Thomas; Kleinschmidt, Kristina; Krull, Susan** *(research project, April 2012, in German)*
Anpassung eines PEMFC-Brennstoffzellenmodells
54. **Franz, Marco** *(project work, May 2012, in German)*
Modellierung des Protonentransports durch die Membran einer Polymer-Elektrolyt-Membran-Brennstoffzelle (PEMFC) in Matlab/Simulink
55. **Melzer, Marcel** *(bachelor thesis, April 2012, in German)*
Untersuchung zur Kombination von Anlagen zur Erzeugung von Strom aus erneuerbaren Energien zur Optimierung von Energiespeichern in MATLAB
56. **Arth, M.; Becker, F.; Effner, S.; Fasig, T.; Heiduk, M.; Hinrichsmeyer, N.; Koch, S.; Schütz, J.; Thomitzek, T.** *(project work, April 2012, in German)*
Energie-/Ökobilanz des ÖPNV II

Bibliography

Achenbach, E. 1994. "Three-dimensional and time-dependent simulation of a planar solid oxide fuel cell stack." *Journal of Power Sources* 49 (1-3): 333–348.

Achenbach, E., and E. Riensche. 1994. "Methane/Steam Reforming Kinetics for Solid Oxide Fuel Cells." *Journal of Power Sources* 52 (2): 283–288.

Achenbach, Elmar. 1995. "Response of a solid oxide fuel cell to load change." *Journal of Power Sources* 57 (1-2): 105–109.

Adler, Stuart B. 2004. "Factors governing oxygen reduction in solid oxide fuel cell cathodes." *Chemical reviews* 104 (10): 4791–843.

Adris, A. M., C. J. Lim, and J. R. Grace. 1997. "The fluidized-bed membrane reactor for steam methane reforming: model verification and parametric study." *Chemical Engineering Science* 52 (10): 1609–1622.

Aguiar, P., C. S. Adjiman, and N. P. Brandon. 2004. "Anode-supported intermediate temperature direct internal reforming solid oxide fuel cell. I: model-based steady-state performance." *Journal of Power Sources* 138 (1-2): 120–136 (November).

Ahmed, Sohail. 2010. "Condition monitoring, diagnostic and controlling tool for boiler feed pump." PhD thesis, Mitteilungen des Pfleiderer-Instituts für Strömungsmaschinen, Fakultät für Maschinenbau, Technische Universität Braunschweig.

Ajanovic, Amela. 2011. "Biofuels versus food production: Does biofuels production increase food prices?" *Energy* 36 (4): 2070–2076.

Akhtar, N., S. P. Decent, and K. Kendall. 2010. "Numerical modelling of methane-powered micro-tubular, single-chamber solid oxide fuel cell." *Journal of Power Sources* 195 (23): 7796–7807.

Akhtar, N., S. P. Decent, D. Loghin, and K. Kendall. 2009. "A three-dimensional numerical model of a single-chamber solid oxide fuel cell." *Chemical Engineering Scienc, International Journal of Hydrogen Energy* 34:8645–8663.

Al-Hamamre, Z., and A. Al-Zoubi. 2010. "The use of inert porous media based reactors for hydrogen production." *International Journal of Hydrogen Energy* 35 (3): 1971–1986.

Alman, D. E., and Paul D. Jablonski. 2007. "Effect of minor elements and a Ce surface treatment on the oxidation behavior of an Fe-22Cr-0.5Mn (Crofer 22 APU) ferritic stainless steel." *International Journal of Hydrogen Energy* 32 (16): 3743–3753.

Alston, T., K. Kendall, M. Palin, M. Prica, and P. Windibank. 1998. "A 1000-cell SOFC reactor for domestic cogeneration." *Journal of Power Sources* 71 (1-2): 271–274 (March).

Al-Sulaiman, Fahad A., Ibrahim Dincer, and Feridun Hamdullahpur. 2010. "Exergy analysis of an integrated solid oxide fuel cell and organic Rankine cycle for cooling, heating and power production." *Journal of Power Sources* 195:2346–2354.

Alzate-Restrepo, Vanesa, and Josephine M Hill. 2010. "Carbon deposition on Ni/YSZ anodes exposed to CO/H_2 feeds." *Journal of Power Sources* 195 (5): 1344–1351.

Amiri, Saeid, R. E. Hayes, K. Nandakumar, and Partha Sarkar. 2010. "Mathematical modeling of a novel tubular micro-solid oxide fuel cell and experimental validation." *Chemical Engineering Science* 65 (22): 6001–6013.

Anderson, Harlan U., Rob J. F. van Gerwen, Peter Vang Hendriksen, Teruhisa Horita, Tatsumi Ishihara, Ellen Ivers-Tiffée, Kevin Kendall, Mohammad A. Khaleel, Augustin J. Mcevov, Nguyen Q. Minh, and Ha Möbius. 2003. *High Temperature Solid Oxide Fuel Cells. Fundamentials, Design and Applications*. Edited by Subhash C. Singhal and Kevin Kendall. Oxford, UK: Elsevier Advanced Technology.

Andersson, Martin, Hedvig Paradis, Jinliang Yuan, and Bengt Sunden. 2011. "Modeling Analysis of Different Renewable Fuels in an Anode Supported SOFC." *Journal of Fuel Cell Science and Technology* 8 (3): 031013–1–9.

Andersson, Martin, Jinliang Yuan, and Bengt Sunden. 2010. "Review on modeling development for multiscale chemical reactions coupled transport phenomena in solid oxide fuel cells." *Applied Energy* 87 (5): 1461–1476.

Andersson, Martin, Jinliang Yuan, and Bengt Sundén. 2012. "SOFC modeling considering electrochemical reactions at the active three phase boundaries." *International Journal of Heat and Mass Transfer* 55 (4): 773–788 (January).

Andreassi, L., S. Ubertini, R. Bove, and N.M. Sammes. 2008. "CFD-Based Results for Planar and Micro-Tubular Single Cell Designs." Chapter 4 of *Modeling Solid Oxide Fuel Cells: Methods, Procedures and Techniques*, edited by Roberto Bove and Stefano Ubertini, 1st ed., 97–122. Cleveland: Spinger.

Angelis-Dimakis, Athanasios, Markus Biberacher, Javier Dominguez, Giulia Fiorese, Sabine Gadocha, Edgard Gnansounou, Giorgio Guariso, Avraam Kartalidis, Luis Panichelli, and Irene Pinedo. 2010. "Methods and tools to evaluate the availability of renewable energy sources." *Renewable and Sustainable Energy Reviews* 15 (2): 1182–1200.

Ansys Inc. 2011. "ANSYS CFX-Solver Theory Guide (version 14.0)." Technical Report, ANSYS Inc., Canonsburg, PA, USA.

Ansys Inc. 2011. "ANSYS CFX-Solver Modeling Guide (version 14.0)." Technical Report, Ansys, Inc., Canonsburg, PA, USA.

Antoni, Laurent. 2004. "Materials for Solid Oxide Fuel Cells: the challenge of their stability." *Materials Science Forum* 461-464:1073–1090.

Antunes, Renato A, Mara Cristina, L Oliveira, Gerhard Ett, and Volkmar Ett. 2010. "Corrosion of metal bipolar plates for PEM fuel cells: A review." *International Journal of Hydrogen Energy* 35 (8): 3632–3647.

Aparicio, L. 1997. "Transient Isotopic Studies and Microkinetic Modeling of Methane Reforming over Nickel Catalysts." *Journal of Catalysis* 165 (2): 262–274 (January).

Araki, Wakako, Takao Koshikawa, Akihiko Yamaji, and Tadaharu Adachi. 2009. "Degradation mechanism of scandia-stabilised zirconia electrolytes: Discussion based on annealing effects on mechanical strength, ionic conductivity, and Raman spectrum." *Solid State Ionics* 180:1484–1489.

Armstrong, E. N., K. L. Duncan, D. J. Oh, J. F. Weaver, and E. D. Wachsman. 2011. "Determination of Surface Exchange Coefficients of LSM, LSCF, YSZ, GDC Constituent Materials in Composite SOFC Cathodes." *Journal of The Electrochemical Society* 158 (5): B492.

Aruna, S. T., M. Muthuraman, and K. C. Patil. 1998. "Synthesis and properties of Ni-YSZ cermet: anode material for solid oxide fuel cells." *Solid State Ionics* 111:45–51.

Ashcroft, Neil W., and David N. Mermin. 2007. *Festkörperphysik*. 3. Oldenbourg-Verlag.

Autissier, N., D. Larrain, Jan van Herle, and Daniel Favrat. 2004. "CFD Simulation tool for solid oxide fuel cells." *Journal of Power Sources* 131:313–319.

Baehr, Hans Dieter. 2005. *Thermodynamik*. 12th ed. Berlin: Springer Verlag (in German).

Baerns, M., A. Baehr, A. Brehm, J. Gmehling, H. Hofmann, U. Onken, and A. Renken. 2006. *Technische Chemie (in German)*. 1st. Weinheim: Wiley-VCH Verlag GmbH & Co. KGaA.

Bagotsky, Vladimir S. 2009. *Fuel Cells. Problems and Solutions*. 1st. Hoboken: John Wiley & Sons.

Bai, Yaohui, Chuanling Wang, Jiao Ding, Chao Jin, and Jiang Liu. 2010. "Direct operation of cone-shaped anode-supported segmented-in-series solid oxide fuel cell stack with methane." *Journal of Power Sources* 195 (12): 3882–3886.

Balakrishnan, A., P. Pizette, C. L. Martin, S. V. Joshi, and B. P. Saha. 2010. "Effect of particle size in aggregated and agglomerated ceramic powders." *Acta Materialia* 58 (3): 802–812.

Bard, Allen J., György Inzelt, and Fritz Scholz, eds. 2008. *Electrochemical Dictionary*. 1st ed. Berlin: Springer.

Barrio, Daniel Antelo. 2011. "Geschichte der Brennstoffzelle." project work (in German), Institut für Wärme- und Brennstofftechnik, Fakultät für Maschinenbau, Technische Universität Braunschweig.

Batfalsky, P., Vincent A. C. Haanappel, Jürgen Malzbender, Norbert H. Menzler, V. Shemet, Izaak C. Vinke, and R. Steinbrech. 2006. "Chemical interaction between glass-ceramic sealants and interconnect steels in SOFC stacks." *Journal of Power Sources* 155:128–137.

Baur, E., and H. Ehrenberg. 1912. "Über neue Brennstoffketten." *Zeitschrift für Elektrochemie* 18 (Oktober): 1002–1011 (in German).

Baur, E., and H. Preis. 1938. "Brennstoff-Ketten mit Festleitern." *Zeitschrift für Elektrochemie* 44 (Juli): 695–698.

Bazylak, Aimy Ming Jii, D Sinton, and N Djilali. 2005. "Improved fuel utilization in microfluidic fuel cells: A computational study." *Journal of Power Sources* 143 (1-2): 57–66.

Bebelis, Simeon, Andonis Zeritis, Constantina Tiropani, and Stylianos G Neophytides. 2000. "Intrinsic Kinetics of the Internal Steam Reforming of CH 4 over a Ni-YSZ-Cermet Catalyst-Electrode." *Industrial & Engineering Chemistry Research* 39 (12): 4920–4927.

Behr, Arno, David W. Agar, and Jakob Jörissen. 2010. *Einführung in die Technische Chemie*. Heidelberg: Spektrum Akademischer Verlag (in German).

Bi, Wuxi, Jiayu Li, and Zijing Lin. 2010. "Flow uniformity optimization for large size planar solid oxide fuel cells with U-type parallel channel designs." *Journal of Power Sources* 195 (10): 3207–3214.

Bieberle, Anja. 2000, September. "The Electrochemistry of Solid Oxide Fuel Cell Anodes: Experiments, Modeling, and Simulations." PhD thesis, ETH Zürich.

Bieberle, Anja, and Ludwig J. Gauckler. 2002. "State-space modeling of the anodic SOFC system Ni, H_2-H_2O|YSZ." *Solid State Ionics* 146 (1-2): 23 – 41.

Blome, Klaus. 2008. "Simulation von Kraftwerkskreisläufen mit Hochtemperaturbrennstoffzellen (SOFC) und integrierter allothermer Biomassevergasung." Studienarbeit, Technische Universität Braunschweig (in German).

Boder, M., and R. Dittmeyer. 2006. "Catalytic modification of conventional SOFC anodes with a view to reducing their activity for direct internal reforming of natural gas." *Journal of Power Sources* 155 (1): 13–22.

Boer, Baukje De. 1998. "SOFC Anode:. Hydrogen oxidation at porous nickel and nickel/yttria- stabilised zirconia cermet electrodes." PhD Thesis, Universiteit Twente.

Boeyens, Jan C. A. 2008. *Chemistry from first principles*. New York: Springer.

Bondi, A. 1964. "van der Waals Volumes and Radii." *The Journal of Physical Chemistry* 68 (3): 441–451.

Bossel, Ulf G. 1992. "Final report on SOFC Data, Facts & Figures." Technical Report, International Energy Agency, Berne.

Bove, Roberto, and Stefano Ubertini. 2006. "Modeling solid oxide fuel cell operation: Approaches, techniques and results." *Journal of Power Sources* 159:543–559.

———. 2008. Pages 51–93 in *Mathematical Models: A General Overview*, edited by Roberto Bove and Stefano Ubertini, Volume 1 of *Fuel Cells and hydrogen energy*, 1st. ed. Cleveland: Springer.

Bozic, Ognjan, Bernd Epple, Reinhard Leithner, Wladimir Linzer, Horst Müller, Karl Ponweiser, Heimo Walter, Andreas Werner, Adam Witkowski, and Henning Zindler. 2009. *Simulation von Kraftwerken und wärmetechnischen Anlagen*. 1. Edited by Bernd Epple, Reinhard Leithner, Wladimir Linzer, and Heimo Walter. Wien, New York: Springer.

Brendelberger, S., S. Hötker, T. Fend, and R. Pitz-Paal. 2012. "Macroscopic foam model with effective material properties for high heat load applications." *Applied Thermal Engineering* 47 (December): 34–40.

Brivio, G. P., and T. B. Grimley. 1993. "Dynamics of adsorption/desorption at solid surfaces." *Surface Science Reports* 17:1–84.

Bronstein, I. N. 2008. *Taschenbuch der Mathematik*. 7th. Frankfurt am Main: Verlag Harri Deutsch (in German).

Brundtland, Gro Harlem, Mansour Khalid, Susanna Agnelli, Saleh A. Al-Athel, Bernard Chidzero, Lamine Mohammed Fadika, and Volker Hauff. 1987. *Report of the World Commission on Environment and Development: Our Common Future*. New York, USA: Oxford University Press.

Brus, Grzegorz, and Janusz S. Szmyd. 2008. "Numerical modelling of radiative heat transfer in an internal indirect reforming-type SOFC." *Journal of Power Sources* 181 (1): 8–16.

Cain, Tyler, Bo-Kuai Lai, Subramanian Sankaranarayanan, and Shriram Ramanathan. 2010. "Photo-excitation enhanced high temperature conductivity and crystallization kinetics in ultra-thin $La_{0.6}Sr_{0.4}Co_{0.8}Fe_{0.2}O_{3-\delta}$ film." *Journal of Power Sources* 195 (10): 3145–3148.

Calise, F., G. Restuccia, and N. M. Sammes. 2010. "Experimental analysis of micro-tubular solid oxide fuel cell fed by hydrogen." *Journal of Power Sources* 195:1163–1170.

Campanari, S., and P. Iora. 2005. "Comparision of finite volume SOFC models for the simulation of a planar cell geometry." *Fuel Cells* 5:34–51.

Cassidy, M., S. Boulfrad, John T. S. Irvine, C. Chung, M. Jorger, C. Munnings, and S. Pyke. 2009. "Integration of Oxide Anodes into the Rolls-Royce IP-SOFC Concept." *Fuel Cells* 9 (6): 891–898.

Chan, S. H., H. K. Ho, and Y. Tian. 2003. "Multi-level modeling of SOFC-gas turbine hybrid system." *International Journal of Hydrogen Energy* 28 (8): 889–900 (August).

Chen, Shaofei. 2013. "Simulation eines SOFC-Brennstoffzellensystems mit Anodenabgasrückführung." PhD thesis, Technische Universität Braunschweig.

Chen, Xuan, Peggy Y Hou, Craig P Jacobsen, Steven J Visco, and Lutgard C De Jonghe. 2005. "Protective coating on stainless steel interconnect for SOFCs: oxidation kinetics and electrical properties." *Solid State Ionics* 176:425–433.

Chen, Y., F. Chen, D. Ding, and J. Gao. 2011. "Development and Fabrication of a New Concept Planar-tubular Solid Oxide Fuel Cell (PT-SOFC)." *Fuel Cells*, no. 11.

Chiang, Lieh-Kwang, Hui-Chung Liu, Yao-Hua Shiu, Chien-Hsiung Lee, and Ruey-Yi Lee. 2010. "Thermal stress and thermo-electrochemical analysis of a planar anode-supported solid oxide fuel cell: Effects of anode porosity." *Journal of Power Sources* 195:1895–1904.

Choi, Yongman, Matthew E. Lynch, M. C. Lin, and Meilin Liu. 2009. "Prediction of O_2 dissociation kinetics on $LaMnO_3$-based cathode materials for solid oxide fuel cells." *Solid State Ionics* 113:7290–7297.

Chyou, Yau-Pin, Tsang-Dong Chung, Jong-Sheng Chen, and Ri-Fong Shie. 2005. "Integrated thermal engineering analyses with heat transfer at periphery of planar solid oxide fuel cell." *Journal of Power Sources* 139:126–140.

Co, Anne C., Shen Jiang Xia, and Viola I. Birss. 2005. "A Kinetic Study of the Oxygen Reduction Reaction at $LaSrMnO_3$-YSZ Composite Electrodes." *Journal of The Electrochemical Society* 152 (3): A570–A576.

Colpan, C. Ozgur, Feridun Hamdullahpur, and Ibrahim Dincer. 2010. "Heat-up and start-up modeling of direct internal reforming solid oxide fuel cells." *Journal of Power Sources* 195 (11): 3579–3589.

Costamagna, P., A. Selimovic, M. Delborghi, and G. Agnew. 2004. "Electrochemical model of the integrated planar solid oxide fuel cell (IP-SOFC)." *Chemical Engineering Journal* 102 (1): 61–69.

Cui, Daan, and Mojie Cheng. 2009. "Thermal stress modeling of anode supported micro-tubular solid oxide fuel cell." *Journal of Power Sources* 192:400–407.

———. 2010. "Design for segmented-in-series solid oxide fuel cell through mathematical modeling." *Journal of Power Sources* 195:1435–1440.

Cui, Daan, Qiang Liu, and Fanglin Chen. 2010. "Modeling of anode-supported SOFCs with samaria doped-ceria electrolytes operating at 500 - 600 °C." *Journal of Power Sources* 195 (13): 4160–4167.

Danilov, Valery A., and Moses O. Tade. 2009. "A CFD-based model of a planar SOFC for anode flow field design." *International Journal of Hydrogen Energy* 34:8998–9006.

Daubert, T. E., and R. P. Danner, eds. 1989. *Physical and Thermodynamic Properties of Pure Chemicals - Data Compilation*. New York, Washington, Philadelphia, London: Hemisphere Publ. Corp.

Daun, K.J ., S. B. Beale, F. Liu, and G. J. Smallwood. 2006. "Radiation heat transfer in planar SOFC electrolytes." *Journal of Power Sources* 157 (1): 302–310 (June).

de Haart, L. G. J. 2009a, September. "Introduction to fuel cells: Electrochemistry & Thermodynamics. Introduction for Newbies." *6th International Solid Oxide Fuel Cell Summer School - Participant Book*, SOFC System Technology. Large SOFC, Ancona, Italy: Forschungszentrum Jülich GmbH, Germany; VTT, Finland.

de Haart, Lambertus G. J. 2009b, September. "A basic introduction to fuel cells: Electrochemistry and Thermodynamics." *6th International Large Solid Oxide Fuel Cell Summer School*. Ancona, Italy: University of Genova and Forschungszentrum Jülich, 1–63.

———. 2009c, September. "An introduction to Solid Oxide Fuel Cells materials: properties and manufacturing." *6th International Large Solid Oxide Fuel Cell Summer School*. Ancona, Italy: University of Genova and Forschungszentrum Jülich, 1–63.

———. 2009d, September. "Solid Oxide Fuel Cells: cell and stack technology." *6th International Large Solid Oxide Fuel Cell Summer School*. Ancona, Italy: University of Genova and Forschungszentrum Jüllich, 1–52.

———. 2010, August. "SOFC degradation mechanisms and their mitigation: stack degradation Contents." *HyFC Academy School*. Roskilde, Danmark, 61.

Demin, A. K., V. Alderucci, I. Ielo, G. I. Fadeev, G. Maggio, N. Giordano, and V. Antonucci. 1992. "Thermodynamic analysis of methane fueled solid oxide fuel cell system." *International Journal of Hydrogen Energy* 17 (6): 451–458.

Demtröder, Wolfgang. 2008. *Experimentalphysik 1*. 5th. ed. Springer (in German).

Der Bundesminister für Forschung und Technologie. 1977. *Programm Energieforschung und Energietechnologien 1977 - 1980*. Edited by Der Bundesminister für Forschung und Technologie. Bonn: Der Bundesminister für Forschung und Technologie.

Deseure, J, Y Bultel, L Dessemond, and E Siebert. 2005. "Theoretical optimisation of a SOFC composite cathode." *Electrochimica Acta* 50 (10): 2037–2046 (March).

de Souza, R. A., and J. A. Kilner. 1998. "Oxygen transport in $La_{1-x}Sr_xMn_{1-y}Co_yO_{3-\delta}$ perovskites Part I. Oxygen tracer diffusion." *Solid State Ionics* 106:175–187.

Deutschmann, Olaf, Steffen Tischer, Stefan Kleditzsch, Vinod M. Janardhanan, Chrys Correa, Daniel Chatterjee, Nikolay Mladenov, and Hoang Duc Minh. 2011. "DETCHEM User Manual." Technical Report, STZ Reaktive Strömungen, Heidelberg.

Devanathan, R., W. Weber, S. Singhal, and J. Gale. 2006. "Computer simulation of defects and oxygen transport in yttria-stabilized zirconia." *Solid State Ionics* 177 (15-16): 1251–1258 (June).

Dietrich, Ralph-Uwe, Andreas Lindermeir, Jana Oelze, Christian Spitta, Michael Steffen, Shaofei Chen, and Christian Schlitzberger. 2009. "Using Anode-Offgas Recycling for a Propane Operated Solid Oxide Fuel Cell." *Proceedings of the 7th International Conference on Fuel Cell Science, Engineering and Technology - FuelCell09*. American Society of Mechanical Engineers, New Port Beach, California, USA.

Dokmaingam, P., S. Assabumrungrat, A. Soottitantawat, and N. Laosiripojana. 2010. "Modelling of tubular-designed solid oxide fuel cell with indirect internal reforming operation fed by different primary fuels." *Journal of Power Sources* 195:69–78.

Drescher, I., W. Lehnert, and J Meusinger. 1998. "Structural properties of SOFC anodes and reactivity." *Electrochim. Acta* 43 (19-20): 3059–3068.

Durst, Franz. 2006. *Grundlagen der Strömungsmechanik. Eine Einführung in die Theorie der Strömung von Fluiden*. Berlin, Heidelberg: Springer (in German).

Eisenbeiß, Gerd. 2006. "Energie der Zukunft - Zukunft der Energien." In *Die Zukunft der Erde. Was verträgt unser Planet noch?*, edited by Ernst Peter Fischer and Klaus Wiegandt, Forum für Verantwortung (in German), 2nd ed., 159–181. Frankfurt am Main: Fischer Taschenbuch Verlag.

Evans, Anna, Anja Bieberle-Hütter, Jennifer L M Rupp, and Ludwig J Gauckler. 2009. "Review on microfabricated micro-solid oxide fuel cell membranes." *Journal of Power Sources* 194 (1): 119–129.

Fan, Baoan, Jiabao Yan, and Xiaochao Yan. 2011. "The ionic conductivity, thermal expansion behavior, and chemical compatibility of $La_{0.54}Sr_{0.44}Co_{0.2}Fe_{0.8}O_{3-\delta}$ as SOFC cathode material." *Solid State Sciences* 13 (10): 1835–1839.

Fergus, Jeffrey W. 2005. "Metallic interconnects for solid oxide fuel cells." *Materials Science and Engineering A* A 397:271–283.

———. 2006. "Electrolytes for solid oxide fuel cells." *Journal of Power Sources* 162 (1): 30–40.

Ferguson, R., M. Fiard, and R. Herbin. 1996. "Three-dimensional numerical simulation for various geometries of solid oxide fuel cells." *Journal of Power Sources* 58 (2): 109–122.

Ferziger, Joel H., and Milovan Perić. 2008. *Numerische Strömungsmechanik*. Berlin, Heidelberg: Springer (in German).

Fischer, Katharina, and Jörg R. Seume. 2009a. "Location and Magnitude of Heat Sources in Solid Oxide Fuel Cells." *Journal of Fuel Cell Science and Technology* 6:1–11.

Fischer, Katharina, and Jörg R Seume. 2009b. "Impact of the Temperature Profile on Thermal Stress in a Tubular Solid Oxide Fuel Cell." *Journal of Fuel Cell Science and Technology* 6:1–9.

Fleig, Jürgen. 2003. "Solid Oxide Fuel Cell Cathodes: Polarization Mechanisms and Modeling of the Electrochemical Performance." *Annual Review of Materials Research* 33 (1): 361–382.

Fontana, S., R. Amendola, S. Chevalier, P. Piccardo, G. Geboche, M. Viviani, R. Molins, and M. Sennour. 2007. "Metallic interconnects for SOFC: Characterisation of corrosion resistance and conductivity evaluation at operating temperature of differently coated alloys." *Journal of Power Sources* 171:652–662.

Funahashi, Y., T. Shimamori, T. Suzuki, Y. Fujishiro, and M. Awano. 2007. "Fabrication and characterization of components for cube shaped micro tubular SOFC bundle." *Journal of Power Sources* 163 (2): 731–736.

Garbayo, I., A. Tarancón, J. Santiso, F. Peiró, E. Alarcón-lladó, A. Cavallaro, and I. Gràcia. 2010. "Electrical characterization of thermomechanically stable YSZ membranes for micro solid oxide fuel cells applications." *Solid State Ionics* 181 (5-7): 322–331.

Garcia-Camprubi, M., A. Sanchez-Insa, and N. Fueyo. 2010. "Multimodal mass transfer in solid-oxide fuel-cells." *Chemical Engineering Science* 65 (5): 1668–1677.

Gardner, F. J., M. J. Day, N. P. Brandon, M. N. Pashley, and M. Cassidy. 2000. "SOFC technology development at Rolls-Royce." *Journal of Power Sources* 86 (1-2): 122–129.

Gemmen, R.S., and J. Trembly. 2006. "On the mechanisms and behavior of coal syngas transport and reaction within the anode of a solid oxide fuel cell." *Journal of Power Sources* 161 (2): 1084–1095 (October).

Goel, Ashutosh, Maria J Pascual, and Jose M. F. Ferreira. 2010. "Stable glass-ceramic sealants for solid oxide fuel cells: Influence of Bi_2O_3 doping." *International Journal of Hydrogen Energy* 35:6911–6923.

Goldin, Graham M., Huayang Zhu, Robert J. Kee, David Bierschenk, and Scott A. Barnett. 2009. "Multidimensional flow, thermal, and chemical behavior in solid-oxide fuel cell button cells." *Journal of Power Sources* 187 (1): 123–135 (February).

Goodwin, David G., Huayang Zhu, Andrew M. Colclasure, and Robert J. Kee. 2009. "Modeling Electrochemical Oxidation of Hydrogen on Ni-YSZ Pattern Anodes." *Journal of The Electrochemical Society* 156 (9): B1004.

Graça Carvalho, Maria Da, Matteo Bonifacio, and Pierre Dechamps. 2011. "Building a low carbon society." *Energy* 36 (4): 1842–1847.

Grosso, Simone, Laura Repetto, and Paola Pezzini. 2008. "IP-SOFC Model." Chapter 6 of *Modeling Solid Oxide Fuel Cells: Methods, Procedures and Techniques*, edited by Roberto Bove and Stefano Ubertini, 1st ed., 183–205. Cleveland: Spinger.

Grote, K.-H., and J. Feldhusen, eds. 2007. *Dubbel - Taschenbuch für den Maschinenbau*. 22. Berlin, Heidelberg, New York: Springer (in German).

Haanappel, V. A. C., V. Shemet, I. C. Vinke, S. M. Gross, Th. Koppitz, N. H. Menzler, M. Zahid, and W. J. Quadakkers. 2005. "Evaluation of the suitability of various glass sealant-alloy combinations under SOFC stack conditions." *Journal of Materials Science* 40 (7): 1583–1592.

Haberman, B. A., and J. B. Young. 2004. "Three-dimensional simulation of chemically reacting gas flows in the porous support structure of an integrated-planar solid oxide fuel cell." *International Journal of Heat and Mass Transfer* 47 (17-18): 3617–3629.

Haga, Tsuyoshi, Norio Komiyama, Hitoshi Nakatomi, Kinhei Konishi, Tetsuo Sutou, and Tetsuo Kikuchi. 2009. "Prototype SOFC CHP System (SOFIT) Development and Testing." *ECS Transactions* 25 (2): 71–76.

Hagen, Anke. 2010. "Cell degradation mechanisms." *Presentations from the Academy School on Fuel Cell and Hydrogen 2010*. Roskilde, Denmark, 45.

Hahlbrock, Klaus. 2007. *Kann unsere Erde die Menschen noch ernähren?: Bevölkerungsexplosion - Umwelt - Gentechnik*. 1st ed. Forum für Verantwortung (in German). Edited by Klaus Wiegandt. Frankfurt am Main: Fischer Taschenbuch Verlag.

Haile, Sossina M. 2003. "Fuel cell materials and components." *Acta Materialia* 51:5981–6000.

Hanke, Victoria. 2011a. "Modellierung und Simulation der heterogenen katalysierten Reformierung von niederen Kohlenwasserstoffen mittels eines finiten Volumen Verfahrens." studen research project (in German), Institut für Wärme- und Brennstofftechnik, Fakultät für Maschinenbau, Technische Universität Braunschweig.

———. 2011b. "Stand der Technik im Bereich der Modellierung der Reformierung von Kohlenwasserstoffen für den Einsatz als Brenngas in einer Solid Oxide Fuel Cell." Project work (in German), Institut für Wärme- und Brennstofftechnik, Fakultät für Maschinenbau, TU Braunschweig.

Hattori, Masatoshi, Yasuo Takeda, Yoshinori Sakaki, Akihiro Nakanishi, Satoshi Ohara, Kazuo Mukai, Jin-ho Lee, and Takehisa Fukui. 2004. "Effect of aging on conductivity of yttria stabilized zirconia." *Journal of Power Sources* 126:23–27.

Hauch, Anne, and Mogens Mogensen. 2010. "Ni/YSZ electrode degradation studied by impedance spectroscopy Effects of gas cleaning and current density." *Solid State Ionics* 181 (15-16): 745–753.

He, Tianmin, Zhe Lu, Li Pei, Xiqiang Huang, Zhiguo Liu, and Weihui Su. 2002. "Electrical properties of thin-walled 8 mol % yttria-stabilized zirconia electrolyte tubes prepared by an improved slip casting method." *Journal of Alloys and Compounds* 333:231–236.

Hecht, Ethan S., Gaurav K. Gupta, Huayang Zhu, Anthony M. Dean, Robert J. Kee, Luba Maier, and Olaf Deutschmann. 2005. "Methane reforming kinetics within a Ni-YSZ SOFC anode support." *Applied Catalysis A: General* 295:40–51.

Heinzel, Angelika, Falko Mahlendorf, and Jürgen Roes, eds. 2006. *Brennstoffzellen. Entwicklung, Technologie, Anwendung.* 3rd ed. Heidelberg: C. F. Müller Verlag (in German).

Hexis. 2007. "Galileo - decentralised energy and heat supply with fuel cells." Technical Report, Hexis GmbH, Winterthur.

Ho, Thinh X, Pawel Kosinski, Alex C Hoffmann, and Arild Vik. 2010. "Effects of heat sources on the performance of a planar solid oxide fuel cell." *International Journal of Hydrogen Energy* 35 (9): 4276–4284.

Hoffmann, Jan. 2009. "Market prospects and applications of SOFC's - close-up on mCHP." *6th International Large Solid Oxide Fuel Cell Summer School*. Ancona, Italy: University of Genova and Forschungszentrum Jülich, 1 – 32.

Hoinkins, Jan, and Ebehard Lindner. 2007. *Chemie für Ingenieure (in German)*. 13th ed. Weinheim: Wiley-VCH Verlag GmbH & Co. KGaA.

Holtappels, P., I. C. Vinke, L. G. J. De Haart, and U. Stimming. 1999. "Reaction of Hydrogen/Water Mixtures on Nickel-Zirconia Cermet Electrodes. II. AC Polarization Characteristics." *Materials Research* 146 (8): 2976–2982.

Holtappels, Peter, Lambertus G. J. de Haart, and U. Stimming. 1999. "Reaction of Hydrogen / Water Mixtures on Nickel-Zirconia Cermet Electrodes. I. DC Polarization Characteristics." *Materials Research* 146 (5): 1620–1625.

Horita, T., H. Kishimoto, K. Yamaji, Y. Xiong, N. Sakai, M. Brito, and H. Yokokawa. 2006. “Materials and reaction mechanisms at anode/electrolyte interfaces for SOFCs.” *Solid State Ionics* 177 (19-25): 1941–1948.

Horn, Birte. 2012, September. “Modellierung der elektrochemischen Katalyse in Solid Oxide Fuel Cells.” Student reasearch project (in German), Technische Universität Braunschweig, Fakultät für Maschinenbau, Institut für Wärme- und Brennstofftechnik.

Hornby, A. S. 1995. *Oxford Advanced Learners's Dictionary of Current English*. 5th. Edited by Jonathan Crowther, Kathryn Kavanagh, and Michael Ashby. Oxford: Oxford University Press Inc.

Hoshen, J., and R. Kopelman. 1976. “Percolation and cluster distribution. I. Cluster multiple labeling technique and critial concentration algorithm.” *Physical Review B* 14 (8): 3438–3445.

Huang, C. M., S. S. Shy, C. W. Chien, and Chien-Hsiung Lee. 2010. “Parametric study of anodic microstructures to cell performance of planar solid oxide fuel cell using measured porous transport properties.” *Journal of Power Sources* 195:2260–2265.

Hwang, J. J., C. K. Chen, and D. Y. Lai. 2005a. “Computational analysis of species transport and electrochemical characteristics of a MOLB-type SOFC.” *Journal of Power Sources* 140:235–242.

———. 2005b. “Detailed characteristic comparison between planar and MOLB-type SOFCs.” *Journal of Power Sources* 143:75–83.

Irvine, and A. Sauvet. 2001. “Improved Oxidation of Hydrocarbons with New Electrodes in High Temperature Fuel Cells.” *Fuel Cells* 1 (3-4): 205–210.

Ishihara, Tatsumi, ed. 2008. *Perovskite Oxide for Solid Oxide Fuel Cells*. Fuel Cells and Hydrogen Energy. Dordrecht: Springer.

Iwai, Hiroshi, Naoki Shikazono, Toshiaki Matsui, Hisanori Teshima, Masashi Kishimoto, Ryo Kishida, Daisuke Hayashi, Katsuhisa Matsuzaki, Daisuke Kanno, Motohiro Saito, Hiroki Muroyama, Koichi Eguchi, and Kas. 2010. “Quantification of SOFC anode microstructure based on dual beam FIB-SEM technique.” *Journal of Power Sources* 195:955–961.

Jablonski, P. D., C. J. Cowen, and J. S. Sears. 2010. “Exploration of alloy 441 chemistry for solid oxide fuel cell interconnect.” *Journal of Power Sources* 195:813–820.

Jablonski, Paul D, and Christopher J Cowen. 2009. “Homogenizing a Nickel-Based Superalloy: Thermodynamic and Kinetic Simulation and Experimental Results.” *Metallurgical and Materials Transactions B* 40 (2): 182–186.

Jäger, Jill. 2007. *Was verträgt unsere Erde noch?: Wege in die Nachhaltigkeit*. 3rd ed. Forum für Verantwortung (in German). Edited by Klaus Wiegandt. Frankfurt am Main: Fischer Taschenbuch Verlag.

Jain, Sneh L., Yuta Nabae, Barry J. Lakeman, Kevin D. Pointon, and John T. S. Irvine. 2008. “Solid state electrochemistry of direct carbon/air fuel cells.” *Fuel Cells Bulletin*, no. 10:10–13.

Janaf. 1971. *Janaf Thermochemical Tables*. Nat. Stand. Ref. Data Sys. NSRDS-NBS 37.

Janardhanan, Vinod M. 2007. “A detailed approach to model transport, heterogeneous chemistry, and electrochemistry in solid-oxide fuel cells.” PhD thesis, Universität Karlsruhe.

Janardhanan, Vinod M., and Olaf Deutschmann. 2006. “CFD analysis of a solid oxide fuel cell with internal reforming: Coupled interactions of transport, heterogeneous catalysis and electrochemical processes.” *Journal of Power Sources* 162 (2): 1192–1202.

Janardhanan, Vinod M., Vincent Heuveline, and Olaf Deutschmann. 2007. “Performance analysis of a SOFC under direct internal reforming conditions.” *Journal of Power Sources* 172 (1): 296–307 (October).

Ji, Y., J. A. Kilner, and M. F. Carolan. 2005. "Electrical properties and oxygen diffusion in yttria-stabilised zirconia (YSZ)-$La_{0.8}Sr_{0.2}MnO_{3\pm\delta}$ (LSM) composites." *Solid State Ionics* 176:937 – 943.

Ji, Yan, Kun Yuan, and J. N. Chung. 2007. "Monte-Carlo simulation and performance optimization for the cathode microstructure in a solid oxide fuel cell." *Journal of Power Sources* 165 (2): 774–785.

Jiang, S. P., and S. P. S. Badwal. 1997. "Hydrogen Oxidation at the Nickel and Platinum Electrodes on Yttria-Tetragonal Zirconia Electrolyte." *Journal of The Electrochemical Society* 144 (11): 3777–3784.

Jiang, Tsung Leo, and Ming-Hong Chen. 2009. "Thermal-stress analyses of an operating planar solid oxide fuel cell with the bonded compliant seal design." *International Journal of Hydrogen Energy* 34:8223–8243.

Jiao, Zhenjun, Naoki Shikazono, and Nobuhide Kasagi. 2010. "Performance of an anode support solid oxide fuel cell manufactured by microwave sintering." *Journal of Power Sources* 195:151–154.

Jin, T., and K. Lu. 2010. "Thermal stability of a new solid oxide fuel/electrolyzer cell seal glass." *Journal of Power Sources* 195:195–203.

Kacprzak, Andrzej, Rafal Kobylecki, and Zbigniew Bis. 2011. "Clean energy from a carbon fuel cell." *Archives of Thermodynamics* 32 (3): 145–155.

Kang, Ying-Wei, Jun Li, Guang-Yi Cao, Heng-Yong Tu, Jian Li, and Jie Yang. 2009. "A reduced 1D dynamic model of a planar direct internal reforming solid oxide fuel cell for system research." *Journal of Power Sources* 188 (1): 170–176.

Karakasidis, T., and C. Charitidis. 2007. "Multiscale modeling in nanomaterials science." *Materials Science and Engineering: C* 27 (5-8): 1082–1089.

Kee, Robert J., Huayang Zhu, and David G. Goodwin. 2005. "Solid-oxide fuel cells with hydrocarbon fuels." *Proceedings of the Combustion Institute* 30 (2): 2379–2404.

Keil, Frerich J. 1999. "Diffusion and reaction in porous networks." *Catalysis today* 53 (2): 245–258.

Kenney, B., and K. Karan. 2006. "Impact of Nonuniform Potential in SOFC Composite Cathodes on the Determination of Electrochemical Kinetic Parameters." *Journal of The Electrochemical Society* 153 (6): A1172–A1180.

Kenney, Ben, and Kunal Karan. 2010. "Estimation of Chemical and Transport Processes in Porous, Stoichiometric LSM Cathodes Using Steady-State Polarization and Impedance Modeling." *Journal of The Electrochemical Society* 157 (8): B1126.

Kenney, Ben, Mikelis Valdmanis, Craig Baker, J.G. Pharoah, and Kunal Karan. 2009. "Computation of TPB length, surface area and pore size from numerical reconstruction of composite solid oxide fuel cell electrodes." *Journal of Power Sources* 189 (2): 1051–1059 (April).

Kharton, V., F. Marques, and A. Atkinson. 2004. "Transport properties of solid oxide electrolyte ceramics: a brief review." *Solid State Ionics* 174 (1-4): 135–149.

Ki, Jeongpill, and Daejong Kim. 2010. "Computational model to predict thermal dynamics of planar solid oxide fuel cell stack during start-up process." *Journal of Power Sources* 195 (10): 3186–3200.

Kilius, L. B., and V. Krstic. 2009. "Characterization of the 75% $Gd_{0.8}Sr_{0.2}CoO_{3-\delta}$/25% $Ce_{0.9}Gd_{0.1}O_{2-\delta}$ composite cathode system for use in intermediate temperature solid oxide fuel cells." *Journal of Power Sources* 194 (2): 690–696.

Kilo, M., C. Fundenberger, Ch. Argirusis, M. A. Taylor, and G. Borchardt. 2002. "Radiation Effects and Defects in Solids Experimental and theoretical investigation of oxygen diffusion in stabilised zirconia." *Radiation Effects & Defects in Solids* 157:1077–1083.

Kim, Ju-Sik, Su-Il Pyun, Jong-Won Lee, and Rak-Hyun Song. 2006a. "Kinetics of oxygen reduction on porous mixed conducting $(La_{0.85}Sr_{0.15})_{0.9}MnO_3$ electrode by ac-impedance analysis." *Journal of Solid State Electrochemistry* 11 (1): 117–125.

Kim, L V. 1991. "Determination of heat-transfer coefficients in porous media." *Journal of Engineering Physics and Thermophysics* 59 (5): 1423–1426.

Kim, Yong-Bum, Sung-Jin Ahn, Jooho Moon, Joosun Kim, and Hae-Weon Lee. 2006b. "Direct-write fabrication of integrated planar solid oxide fuel cells." *Journal of Electroceramics* 17 (2-4): 683–687.

Kim, Yu-Mi, Su-Il Pyun, Ju-Sik Kim, and Gyoung-Ja Lee. 2007. "Mixed Diffusion and Charge-Transfer-Controlled Oxygen Reduction on Dense $La_{1-x}Sr_xCo_{0.2}Fe_{0.8}O_{3-\delta}$ Electrodes with Various Sr Contents." *Journal of The Electrochemical Society* 154 (8): B802–B809.

Kivelson, Margaret G., and Christopher T. Russel, eds. 1995. *Introduction to Space Physics*. Los Angeles: Cambridge University Press.

Klein, J, Y Bultel, S Georges, and M Pons. 2007. "Modeling of a SOFC fuelled by methane: From direct internal reforming to gradual internal reforming." *Chemical Engineering Science* 62 (6): 1636–1649 (March).

Kleis, Jesper, Glenn Jones, Frank Abild-Pedersen, Vladimir Tripkovic, Thomas Bligaard, and Jan Rossmeisl. 2009. "Trends for Methane Oxidation at Solid Oxide Fuel Cell Conditions." *Journal of The Electrochemical Society* 156 (12): B1447.

Kresse, G., and J. Hafner. 2000. "First-principles study of the adsorption of atomic H on Ni (111), (100) and (110)." *Surface Science* 459:287–302.

Kulikovsky, Andrei A. 2010. *Analytical Modeling of Fuel Cells*. 1st ed. Amsterdam, Boston, Heidelberg, London: Elsevier.

Kumar, Vimal, Marius Paraschivoiu, and K. D. P. Nigam. 2010. "Single-phase fluid flow and mixing in microchannels." *Chemical Engineering Science* 66 (7): 1329–1373.

Kusy, R. P. 1977. "Influence of particle size ratio on the continuity of aggregates." *Journal of Applied Physics* 48 (12): 5301–5305.

Kuwahara, Fujio, Mitsuhiro Shirota, and Akira Nakayama. 2001. "A numerical study of interfacial convective heat transfer coe Â? cient in two-energy equation model for convection in porous media." *International Journal of Heat and Mass Transfer* 44:1153–1159.

Kuznecov, M., P. Otschik, N. Trofimenko, and K. Eichler. 2004. "Oxygen Transport in the SOFC Cathode." *Russian Journal of Electrochemistry* 40 (11): 1162–1169.

Kwon, Oh Hyun, and Gyeong Man Choi. 2006. "Electrical conductivity of thick film YSZ." *Solid State Ionics* 177:3057 – 3062.

Lai, Tammy S., and Scott A. Barnett. 2005. "Design considerations for segmented-in-series fuel cells." *Journal of Power Sources* 147 (1-2): 85–94.

Larminie, J., and A. Dicks. 2003, May. *Fuel Cell Systems Explained*. 2nd ed. Chichester, UK: John Wiley & Sons, Inc.

Larsen, Kari. 2010. "The power of the concentrated sun." *Renewable Energy Focus* 11 (3): 54–57 (May).

Latif, Mojib. 2007. *Bringen wir das Klima aus dem Takt?: Hintergründe und Prognosen*. 3rd. Forum für Verantwortung (in German). Edited by Klaus Wiegandt. Frankfurt am Main: Fischer Taschenbuch Verlag.

Lawlor, V., S. Griesser, G. Buchinger, A. G. Olabi, S. Cordiner, and D. Meissner. 2009. "Review of the micro-tubular solid oxide fuel cell Part I. Stack design issues and research activities." *Journal of Power Sources* 193:387–399.

Le Bars, M., and M. Grae Worster. 2006. “Interfacial conditions between a pure fluid and a porous medium: implications for binary alloy solidification.” *Journal of Fluid Mechanics* 550 (-1): 149.

Lee, J., H. Moon, H. Lee, J. Kim, J. Kim, and K. Yoon. 2002. “Quantitative analysis of microstructure and its related electrical property of SOFC anode, Ni - YSZ cermet.” *Solid State Ionics* 148 (1-2): 15 – 26.

Lefebvre, Jonathan. 2011. “Simulation der elektrochemischen Vorgäange in einer Hochtemperatur-Brennstoffzelle.” project work (in German), Institut für Wärme- und Brennstofftechnik, Fakultät für Maschinenbau, Technische Universität Braunschweig.

Lehnert, W., J. Meusinger, and F. Thom. 2000. “Modelling of gas transport phenomena in SOFC anodes.” *Journal of Power Sources* 87 (1-2): 57–63 (April).

Leithner, Reinhard. 2002. *Klimakatastrophe und Energiewirtschaft*. Informationsschrift der VDI-Gesellschaft Energietechnik. Düsseldorf: Verein Deutscher Ingenieure (in German).

———. 2004. “Struktur eines SOFC Stapels.” Deutsche Patentanmeldung, DE 10 2004 015 660.

———. 2007. “Combined cycles for CO_2-capture with high efficiency.” *International Journal of Energy Technology and Policy* 5 (3): 340–354.

Leithner, Reinhard, and Christian Schlitzberger. 2007. “Verfahren zum Betrieb und Konstruktion einer SOFC mit integrierten Wärmetauschern, integrierter Reformierung oder Vergasung, integrierter Anodenabgasrückführung und integrierter Wärmeauskopplung.” Deutsche Patentanmeldung, DE 10 2007 015 079 A1.

Leithner, Reinhard, Christian Wesemeyer, Shaofei Chen, Christian Schlitzberger, Rune Staeck, and Sebastian Stenger. 2010. “Grundlagen der Brennstoffzellen.” lecture (in German), Fakultät für Maschinenbau, Institut für Wärme- und Brennstofftechnik.

Leon, Aline, ed. 2008. *Hydrogen Technology. Mobile and Portbale Applications*. Green Energy and Technology. Berlin, Heidelberg: Springer.

Leone, P., M. Santarelli, P. Asinari, M. Calì, and R. Borchiellini. 2008. “Experimental investigations of the microscopic features and polarization limiting factors of planar SOFCs with LSM and LSCF cathodes.” *Journal of Power Sources* 177 (1): 111–122.

Leonide, Andre. 2010. “SOFC Modelling and Parameter identification by means of Impedance Spectroscopy.” PhDThesis, Karlsruher Institut für Technologie.

Li, Chen, Yixiang Shi, and Ningsheng Cai. 2010. “Elementary reaction kinetic model of an anode-supported solid oxide fuel cell fueled with syngas.” *Journal of Power Sources* 195:2266–2282.

Li, J. Q., X. R. Zeng, J. N. Tang, and P. Xiao. 2003. “Fabrication and thermal properties of a YSZ-NiCr joint with an interlayer of YSZ-NiCr functionally graded material.” *Journal of the European Ceramic Society* 23 (11): 1847–1853.

Li, Jun, Ying-wei Kang, Guang-yi Cao, Xin-jian Zhu, Heng-yong Tu, and Jian Li. 2008. “Numerical simulation of a direct internal reforming solid oxide fuel cell using computational fluid dynamics method.” *Journal of Zhejiang University SCIENCE A* 9 (7): 961–969.

Li, Yihong, Randall Gemmen, and Xingbo Liu. 2010. “Oxygen reduction and transportation mechanisms in solid oxide fuel cell cathodes.” *Journal of Power Sources* 195 (11): 3345–3358.

Li, Ying, Zilong Tang, Zhongtai Zhang, and Jianghong Gong. 1999. “Electrical conductivity of zirconia stabilized with yttria and calcia.” *Journal of Materials Science Letters* 18:443–444.

Lide, David R., ed. 2010. *CRC Handbook of Chemistry and Physics*. 91st ed. Taylor & Francis.

Lin, C., T. Chen, Y. Chyou, and L. Chiang. 2007. “Thermal stress analysis of a planar SOFC stack.” *Journal of Power Sources* 164 (1): 238–251.

Lin, Jyung-Dong, and Zhao-Lun Wu. 2009. "Effect of synthesis process on the microstructure and electrical conductivity of nickel/yttria-stabilized zirconia powders prepared by urea hydrolysis." *Journal of Power Sources* 194:631–639.

Lin, Y., Z. Zhan, J. Liu, and S. Barnett. 2005. "Direct operation of solid oxide fuel cells with methane fuel." *Solid State Ionics* 176 (23-24): 1827–1835 (July).

Lin, Yuanbo, Zhongliang Zhan, and Scott a. Barnett. 2006. "Improving the stability of direct-methane solid oxide fuel cells using anode barrier layers." *Journal of Power Sources* 158 (2): 1313–1316 (August).

Lior, Noam. 2010. "Energy resources and use: The present (2008) situation and possible sustainable paths to the future." *Energy* 35 (6): 2631–2638.

Lippky, Gesa Ulrike Dorit. 2011. "Stand der Technik im Bereich Modellierung und Simulation von Brennstoffzellen und Brennstoffzellensystemen." Studienarbeit (in German), Institut für Wärme- und Brennstofftechnik, Fakultät für Maschinenbau, Technische Universität Braunschweig.

Liu, J., M. Xu, T. Nordmeyer, and F. Zaera. 1995. "Sticking Probabilities for CO Adsorption on Pt(111) Surfaces Revisited." *J. Phys. Chem.* 99:6167–6175.

Liu, Lin, Gap-Yong Kim, and S Chandra-Ambhorn. 2010. "Modeling of thermal stresses and lifetime prediction of planar solid oxide fuel cell under thermal cycling conditions." *Journal of Power Sources* 195:2310–2318.

Liu, Qiang, Xihui Dong, Chenghao Yang, Shuguo Ma, and Fanglin Chen. 2010a. "Self-rising synthesis of Ni-SDC cermets as anodes for solid oxide fuel cells." *Journal of Power Sources* 195:1543–1550.

Liu, Renzhu, Chunhua Zhao, Junliang Li, Shaorong Wang, Zhaoyin Wen, and Tinglian Wen. 2010b. "Testing of a cathode fabricated by painting with a brush pen for anode-supported tubular solid oxide fuel cells." *Journal of Power Sources* 195:541–545.

Liu, Shixue, Wei Kong, and Zijing Lin. 2009. "Three-dimensional modeling of planar solid oxide fuel cells and the rib design optimization." *Journal of Power Sources* 194:854–863.

Liu, Wenning N., Xin Sun, Brian Koeppel, Elizabeth Stephens, and Mohammad a. Khaleel. 2011. "Creep Behavior of Glass/Ceramic Sealant and its Effect on Long-Term Performance of Solid Oxide Fuel Cells." *International Journal of Applied Ceramic Technology* 8 (1): 49–59.

Liu, Y. 2008. "Performance evaluation of several commercial alloys in a reducing environment." *Journal of Power Sources* 179:286–291.

Liu, Y., and D. Y. Chen. 2009. "Protective coatings for Cr_2O_3-forming interconnects of solid oxide fuel cells." *International Journal of Hydrogen Energy* 34:9220–9226.

Lu, Yixin, Laura Schaefer, and Peiwen Li. 2005. "Numerical study of a flat-tube high power density solid oxide fuel cell Part I. Heat/mass transfer and fluid flow." *Journal of Power Sources* 140:331–339.

Ludlum, ATI Allegheny. 2007. "Stainless Steel E-BRITE. Alloy for Solid Oxide Fuel Cells. (UNS 44627, ASTM Type XM-27)." Technical Report 4, ATI Allegheny Ludlum, Pittsburg, Pennsylvania.

Lund, Henrik, Poul Alberg Östergärd, and Ingo Stadler. 2011. "Towards 100 % renewable energy systems." *Applied Energy* 88 (2): 419–421.

Lund, P. D. 2010. "Exploring past energy changes and their implications for the pace of penetration of new energy technologies." *Energy* 35 (2): 647–656.

Lv, H., Y. Wu, B. Huang, B. Zhao, and K. Hu. 2006. "Structure and electrochemical properties of $Sm_{0.5}Sr_{0.5}Co_{1-x}Fe_xO_{3-\delta}$ cathodes for solid oxide fuel cells." *Solid State Ionics* 177 (9-10): 901–906.

Magistri, L., A. Traverso, F. Cerutti, M. Bozzolo, P. Costamagna, and A. F. Massardo. 2005. "Modelling of Pressurised Hybrid Systems Based on Integrated Planar Solid Oxide Fuel Cell (IP-SOFC) Technology." *Fuel Cells* 5 (1): 80–96.

Magistri, Loredana, Michele Bozzolo, Olivier Tarnowski, Gerry Agnew, and Aristide F. Massardo. 2007. "Design and Off-Design Analysis of a MW Hybrid System Based on Rolls-Royce Integrated Planar Solid Oxide Fuel Cells." *Journal of Engineering for Gas Turbines and Power* 129 (3): 792.

Marinsek, Marjan, Stane Pejovnik, and Jadran Macel. 2007. "Modelling of electrical properties of Ni-YSZ composites." *Journal of the European Ceramic Society* 27:959–964.

Martynenko, O. G., and N. V. Pavlyukevich. 1998. "Heat and mass transfer in porous media." *Journal of Engineering Physics and Thermophysics* 71 (1): 1–13.

Matsuzaki, Yoshio, and Isamu Yasuda. 2000. "Electrochemical Oxidation of H_2 and CO in a H_2-H_2O-CO-CO_2 System at the Interface of a Ni-YSZ Cermet Electrode and YSZ Electrolyte." *Journal of The Electrochemical Society* 147 (5): 1630.

Mauser, Wolfram. 2007. *Wie lange reicht die Ressource Wasser? Vom Umgang mit dem blauen Gold*. Forum für Verantwortung (in German). Edited by Klaus Wiegandt. Frankfurt am Main: Fischer Taschenbuch Verlag.

McIntosh, Steven, and Raymond J. Gorte. 2004. "Direct hydrocarbon solid oxide fuel cells." *Chemical reviews* 104 (10): 4845–65.

McLachlan, David S., Michael Blaszkiewicz, and Robert E. Newnham. 1990. "Electrical Resistivity of Composites." *Journal of American Ceramical Society* 73 (8): 2187–2203.

Menter, F. R. 1994. "Two-Equation Eddy-Viscosity Turbulence Models for Engineering Applications." *AIAA Journal* 32 (8): 1598–1605 (August).

Meschede, D., ed. 2006. *Gerthsen Physik*. 23rd ed. Berlin, Heidelberg, New York: Springer Verlag Berlin Heidelberg (in German).

Metz, Bert, Ogunlade Davidson, Peter Bosch, Rutu Dave, and Leo Meyer, eds. 2007. *Climate Change 2007 - Mitigation*. Contribution of Working Group III to the Fourth Assessment Report of the Intergovernmental Panel on Climate Change. Cambridge, USA: Cambride University Press.

Meusinger, J., E. Riensche, and U. Stimming. 1998. "Reforming of natural gas in solid oxide fuel cell systems." *Journal of Power Sources* 71 (1-2): 315–320 (March).

Michler, Thorsten, and Joerg Naumann. 2010. "Microstructural aspects upon hydrogen environment embrittlement of various bcc steels." *International Journal of Hydrogen Energy* 35 (2): 821–832.

Mitterdorfer, A., and L. J. Gauckler. 1999a. "Identification of the reaction mechanism of the Pt ,O_2(g)|yttria-stabilized zirconia system Part II : Model implementation , parameter estimation , and validation." *Solid State Ionics* 117:203–217.

———. 1999b. "Reaction kinetics of the Pt, O_2(g)|*c*-ZrO_2 system: precursor- mediated adsorption." *Solid State Ionics* 120:211–225.

Mizusaki, Junichiro, Hiroaki Tagawa, Tamaki Yamamura, and Shaw Ehara. 1994. "Kinetic studies of the reaction at the nickel pattern electrode on YSZ in H_2-H_20 atmospheres." *Solid State Ionics* 70/71 (PART 1): 52–58.

Mizusaki, Junichiro, Soji Tsuchiya, Katsunori Waragai, Hiroaki Tagawa, Yoshihide Arai, and Yuji Kuwayama. 1996. "Simple Mathematical Model for the Electrical Conductivity of Highly Porous Ceramics." *Journal of the American Ceramic Society* 79 (1): 109–113.

Mogensen, D., J. Grunwaldt, P. V. Hendriksen, and J. U. Nielsen. 2011. "Internal steam reforming in solid oxide fuel cells: Status and opportunities of kinetic studies and their impact on modelling." *Journal of Power Sources* 196 (1): 25–38.

Mogensen, Mogens, J. Høgh, K. V. Hansen, and T. Jacobsen. 2007. "A Critical Review of Models of the H_2/H_2O/Ni/SZ Electrode Kinetics." *ECS Transactions* 7 (1): 1329–1338.

Montero, X., Frank Tietz, D. Sebold, H. P. Buchkremer, A. Ringuede, M. Cassir, A. Laresgoiti, and I. Villarreal. 2008. "$MnCo_{1.9}Fe_{0.1}O_4$ spinel protection layer on commercial ferritic steels for interconnect applications in solid oxide fuel cells." *Journal of Power Sources* 184:172–179.

Morel, B., J. Laurencin, Y. Bultel, and F. Lefebvre-Joud. 2005. "Anode-Supported SOFC Model Centered on the Direct Internal Reforming." *Journal of The Electrochemical Society* 152 (7): A1382.

Motschmann, Uwe. 2005. "Thermodynamik und Statistische Mechanik." lecture (in German), TU Braunschweig, Braunschweig.

Mounir, H., A. El Gharad, M. Belaiche, and M. Boukalouch. 2009. "Thermo-fluid and electrochemical modeling of a multi-bundle IP-SOFC - Technology for second generation hybrid application." *Energy Conversion and Management* 50 (10): 2685–2692.

Mücke, Robert. 2009a, September. "A basic introduction to SOFC Materials and Manufacturing. Introduction for Experienced." *6th International Solid Oxide Fuel Cell Summer School - Participant Book*, SOFC System Technology. Large SOFC, Ancony, Italy: Forschungszentrum Jülich GmbH, Germany; VTT, Finland.

———. 2009b, September. "SOFC Introduction - Materials & Manufacturing." *6th International Large Solid Oxide Fuel Cell Summer School*. Ancona, Italy: University of Genova and Forschungszentrum Jülich, 1 – 91.

———. 2009c, September. "SOFC Introduction - Thermodynamics & Electrochemistry." *6th International Large Solid Oxide Fuel Cell Summer School*. Ancona, Italy: University of Genova and Forschungszentrum Jülich, 68.

Mukherjee, Joydeep, and Suljo Linic. 2007. "First-Principles Investigations of Electrochemical Oxidation of Hydrogen at Solid Oxide Fuel Cell Operating Conditions." *Journal of The Electrochemical Society* 154 (9): B919–B924.

Müller-Kraenner, Sascha. 2007. *Energiesicherheit. Die neue Vermessung der Welt*. München: Verlag Antje Kunstmann (in German).

Nam, Jin Hyun, and Dong Hyup Jeon. 2006. "A comprehensive micro-scale model for transport and reaction in intermediate temperature solid oxide fuel cells." *Electrochimica Acta* 51:3446–3460.

National Energy Technology Laboratory. 2004, November. *Fuel Cell Handbook*. 7th ed. Edited by Inc. EG &G Technical Services. Morgantown: U.S. Department of Energy. Office of Fossil Energy.

National Institute of Standards and Technology. 2012. NIST Chemistry WebBook.

Ni, Meng, Dennis Y.C. Leung, and Michael K.H. Leung. 2008a. "Importance of pressure gradient in solid oxide fuel cell electrodes for modeling study." *Journal of Power Sources* 183 (2): 668–673 (September).

———. 2008b. "Modeling of methane fed solid oxide fuel cells: Comparison between proton conducting electrolyte and oxygen ion conducting electrolyte." *Journal of Power Sources* 183 (1): 133–142 (August).

Nielsen, Lasse, and Reinhard Leithner. 2009. "Modelling and Dynamic Simulation of an Underground Cavern for Operation in an Innovative Compressed Air Energy Storage Plant." *5th International Conference on Energy, Environment, Ecosystems and Sustainable Development (EEESD '09)*. Athens, Greece.

Nolting, Wolfgang. 2011. *Grundkurs Theoretische Physik 3. Elektrodynamik*. 9th. Heidelberg; Dordrecht; London; New York: Springer (in German).

O'Hayre, Ryan, Suk-Won Cha, Whitney Colella, and Fritz B. Prinz. 2009. *Fuel Cell Fundamentials*. 2nd ed. New York: John Wiley & Sons, Inc.

Oliveira, Eduardo L. G., and Carlos A. Grande. 2010. "Methane steam reforming in large pore catalyst." *Chemical Engineering Science* 65 (5): 1539–1550.

Östergärd, M. J. L., and Mogens Mogensen. 1993. "*ac* impedance study of the oxygen reduction mechanism on $La_{1-x}Sr_xMnO_3$ in solid oxide fuel cells." *Electrochimica Acta* 38 (14): 2015–2020.

Paradis, Hedvig, Martin Andersson, Jinliang Yuan, and Bengt Sunden. 2011. "CFD Modeling: Different Kinetic Approaches for Internal Reforming Reactions in an Anode-Supported SOFC." *Journal of Fuel Cell Science and Technology* 8, no. 3.

Park, Hae-Gu, Hwan Moon, Sung-Chul Park, Jong-Hin Lee, Daeil Yoon, Sang-Hoon Hyun, and Do-Heyoung Kim. 2010. "Performance improvement of anode-supported electrolytes for planar solid oxide fuel cells via a tape-casting/lamination/co-firing technique." *Journal of Power Sources* 195 (9): 2463–2469.

Parry, Martin, Osvaldo Canziani, Jean Palutikof, Paul van der Linden, and Clair Hanson, eds. 2007. *Climate Change 2007: Impacts, Adaptation and Vulnerability*. Contribution of Working Group II to the Fourth Assessment Report of the Intergovernmental Panel on Climate Change no. 6. Cambridge, USA: Cambride University Press.

Patankar, Suhas V. 1980. *Numerical heat transfer and fluid flow*. Series in Computational Methods in Mechanics and Thermal Sciences. Edited by W. J. Minkowycz and E. M. Sparrow. New York: Hemisphere Publ. Corp.

Perls, Frederick S. 1947. *Das Ich, der Hunger und die Aggression. Die Anfänge der Gestalt-Therapie. Sinneswachheit, spontane persönliche Begegnung, Phantasie, Kontemplation*. Stuttgart: Klett-Cotta (in German).

Poling, Bruce E., John M. Prausnitz, and John P. O'Connell. 2001. *The Properties of Gases and Liquids*. 5th ed. New York, Chicago, San Francisco: McGraw-Hill Book Company.

Pramuanjaroenkij, Anchasa, Sakid Kakac, and Xiang Yang Yangzhou. 2008. "Mathematical analysis of planar solid oxide fuel cells." *International Journal of Hydrogen Energy* 33 (10): 2547–2565 (May).

Prestat, Michel, Jean-François Koenig, and Ludwig J. Gauckler. 2007. "Oxygen reduction at thin dense $La_{0.52}Sr_{0.48}Co_{0.18}Fe_{0.82}O_{3-\delta}$ electrodes. Part I: Reaction model and faradaic impedance." *Journal of Electroceramics* 18 (1-2): 87–101.

PriceWaterhouseCoopers LLP. 2010. "100 % renewable electricity. A roadmap to 2050 for Europe and North Africa." Technical Report, PricewaterhouseCoopers LLP.

Printz, Alfred, ed. 2008. *Einhundert Meisterwerke der Psychotherapie. Ein Literaturführer*. Wien, New York: Springer (in German).

Radkau, Joachim. 2006. "Wendezeiten der Umweltgeschichte. Die Spuren der menschlichen Natur." In *Die Zukunft der Erde. Was verträgt unser Planet noch?*, edited by Ernst Peter Fischer and Klaus Wiegandt, Forum für Verantwortung (in German), 2nd ed., 60–97. Frankfurt am Main: Fischer Taschenbuch Verlag.

Rahmstorf, Stefan, and Katherine Richardson. 2007. *Wie bedroht sind die Ozeane? Biologische und physikalische Aspekte*. Forum für Verantwortung (in German). Edited by Klaus Wiegandt. Frankfurt am Main: Fischer Taschenbuch Verlag.

Raj, Edwin S., Alan Atkinson, and John A. Kilner. 2009. "Oxygen diffusion studies on $(Y_2O_3)_2(Sc_2O_3)_9(ZrO_2)_{89}$." *Solid State Ionics* 180 (14-16): 952–955.

Rajaram, Gukan, Salil Desai, Zhigang Xu, Devdas M. Pai, and Jagannathan Sankar. 2008. "Systematic studies on NI-YSZ anode material for Solid Oxide Fuel Cell (SOFCs) applications." *International Journal of Manufacturing Research* 3 (3): 350–359.

Recknagle, K. P., R. E. Williford, L. A. Chick, D. R. Rector, and M. A. Khaleel. 2003. "Three-dimensional thermo-fluid electrochemical modeling of planar SOFC stacks." *Journal of Power Sources* 113 (1): 109–114 (January).

Rembelski, D., J. P. Viricelle, L. Combemale, and M. Rieu. 2012. "Characterization and Comparison of Different Cathode Materials for SC-SOFC: LSM, BSCF, SSC, and LSCF." *Fuel Cells* 12 (2): 256–264 (April).

Repetto, Laura, and Paola Costamagna. 2008. "FEM model of the ohmic resistance of IP-SOFCs." *Journal of Applied Electrochemistry* 38 (7): 1005–1010.

Riedel, Erwin. 1999. *Allgemeine und Anorganische Chemie. Ein Lehrbuch für Studenten mit Nebenfach Chemie*. 7th ed. Berlin, New York: Walter de Gruyter (in German).

RisøDTU, Topsoe, and Dantherm. 2011. "RisøDTU, Topsoe, Dantherm unveil home SOFC micro CHP unit." *Fuel Cells Bulletin* 2011 (1): 7–7 (January).

Sadeghi, M, and M Molaei. 2008. "CFD simulation of a methane steam reforming reactor." *International Journal of Chemical Reactor Engineering*, vol. 6.

Sahimi, Muhammad, and Theodore Tsotsis. 1985. "A percolation model of catalyst deactivation by site coverage and pore blockage." *Journal of Catalysis* 96 (2): 552–562.

Saito, Marcelo B., and Marcelo J. S. de Lemos. 2005. "Interfacial heat transfer coefficient for non-equilibrium convective transport in porous media." *International Communications in Heat and Mass Transfer* 32 (5): 666–676 (April).

Salazar-Villalpando, Maria D., and Bryan Reyes. 2009. "Hydrogen production over Ni/ceria-supported catalysts by partial oxidation of methane." *International Journal of Hydrogen Energy* 34 (24): 9723–9729.

Salman, S. M., and S. Gharib. 1984. "Some physical properties concerning the thermal conductivity data of BaO-containing silicate glasses in relation to structure." *Thermochimica Acta* 82:345–355.

Sammes, N. M., Y. Du, and R. Bove. 2005. "Design and fabrication of a 100 W anode supported micro-tubular SOFC stack." *Journal of Power Sources* 145:428–434.

Sanchez, D., R. Chacartegui, A. Munoz, and T. Sanchez. 2008. "On the effect of methane internal reforming modelling in solid oxide fuel cells." *International Journal of Hydrogen Energy* 33 (7): 1834–1844 (April).

Sánchez, D., A. Muñoz, and T. Sánchez. 2007. "An assessment on convective and radiative heat transfer modelling in tubular solid oxide fuel cells." *Journal of Power Sources* 169 (1): 25–34 (June).

Sanyal, Jay, Graham M. Goldin, Huayang Zhu, and Robert J. Kee. 2010. "A particle-based model for predicting the effective conductivities of composite electrodes." *Journal of Power Sources* 195 (19): 6671–6679.

Sato, Kazuyoshi, Toru Kinoshita, and Hiroya Abe. 2010. "Performance and durability of nanostructured $(La_{0.85}Sr_{0.15})_{0.98}MnO_3$/yttria-stabilized zirconia cathodes for intermediate-temperature solid oxide fuel cells." *Journal of Power Sources* 195 (13): 4114–4118.

Scheufen, Sven. 2011. "Weiterentwicklung eines PEM-Brennstoffzellenmodells zur Erstellung von Leistungskennfeldern." Diploma thesis, Technische Universität Braunschweig, Fachhochschule Lübeck.

Schild, Christian. 2011. "CFD-Simulation eines Hochtemperatur-Plattenwärmeübertragers für die Luftvorwärmung in einem SOFC-Brennstoffzellensystem." student research project (in German), Institut für Wärme- und Brennstofftechnik, Fakultät für Maschinenbau, TU Braunschweig.

Schlitzberger, Christian. 2006. "Simulation von Solid Oxide Fuel Cells mit integrierter Reformierung." Master's thesis, Technische Universität Braunschweig. Institut für Wärme- und Brennstofftechnik.

———. 2012. “Solid Oxide Fuel Cell (SOFC)-Systeme mit integrierter Reformierung bzw. Vergasung von Kohlenwasserstoffen.” Ph.D. diss., Technische Universität Braunschweig.

Schlitzberger, Christian, Reinhard Leithner, and Henning Zindler. 2009. “Development and Simulation of an Innovative Planar Stack Design-Combining a Solid Oxide Fuel Cell (SOFC) With an Allothermal Steam Reformer.” *Journal of Fuel Cell Science and Technology* 6 (4): 041009.

Schmidt-Bleek, Friedrich. 2006. *Nutzen wir die Erde richtig?: Die Leistungen der Natur und die Arbeit des Menschen*. 1st. Forum für Verantwortung (in German). Edited by Klaus Wiegandt. Frankfurt am Main: Fischer Taschenbuch Verlag.

Schorsch, Tim Jerry. 2009. “Nationale, europäische und internationale Förderprogramme und Forschungsaktivitäten im Bereich von Feststoffoxidbrennstoffzellen.” Studienarbeit (in German), Technische Universität Braunschweig.

Schuler, Alexander. 2007. “Das Brennstoffzellen-Projekt Hexis.” *Gas Wasser Abwasser (in German)* 2:93–98.

Seeliger, Andreas, J. Perner, Christoph Riechmann, Nadja Trhal, Michaela Fürsch, Stephan Nagl, and Dietmar Lindenberger. 2011. “Energy Costs in Germany - Developments, Drivers and International Comparison.” *Zeitschrift für Energiewirtschaft* 35 (1): 43–52.

Serincan, Mustafa Fazil, Ugur Pasaogullari, and Nigel M Sammes. 2009a. “A transient analysis of a micro-tubular solid oxide fuel cell (SOFC).” *Journal of Power Sources* 194 (2): 864–872.

———. 2009b. “Effects of operating conditions on the performance of a micro-tubular solid oxide fuel cell (SOFC).” *Journal of Power Sources* 194:864–872.

Shaigan, N., W. Qu, D. G. Ivey, and W. Chen. 2010. “A review of recent progress in coatings, surface modifications and alloy developments for solid oxide fuel cell ferritic steel interconnects.” *Journal of Power Sources* 195:1529–1542.

Shen, Y., M. Liu, T. He, and S. P. Jiang. 2010. “A potential interconnect material for solid oxide fuel cells: $Nd_{0.5}Ca_{0.25}Cr_{0.98}O_{3-\delta}$.” *Journal of Power Sources* 195:977–983.

Shi, Yixiang, Ningsheng Cai, Chen Li, Cheng Bao, Eric Croiset, Jiqin Qian, Qiang Hu, and Shaorong Wang. 2007a. “Modeling of an anode-supported Ni-YSZ | Ni-ScSZ | ScSZ | LSM-ScSZ multiple layers SOFC cell Part I . Experiments , model development and validation.” *Journal of Power Sources* 172:235–245.

———. 2007b. “Modeling of an anode-supported Ni-YSZ | Ni-ScSZ | ScSZ | LSM-ScSZ multiple layers SOFC cell Part II . Simulations and discussion.” *Journal of Power Sources* 172:246–252.

Shiratori, Y., T. Ijichi, T. Oshima, and K. Sasaki. 2010. “Internal reforming SOFC running on biogas.” *International Journal of Hydrogen Energy* 35 (15): 7905–7912.

Simwonis, D., H. Thülen, F. J. Dias, A. Naoumidis, and D. Stöver. 1999. “Properties of Ni/YSZ porous cermets for SOFC anode substrates prepared by tape casting and coat-mix process.” *Journal of Materials Processing Technology* 92-93 (1): 107–111.

Simwonis, D., Frank Tietz, and Detlev Stöver. 2000. “Nickel coarsening in annealed Ni / 8YSZ anode substrates for solid oxide fuel cells.” *Solid State Ionics* 132:241–251.

Singhal, S. 2000. “Advances in solid oxide fuel cell technology.” *Solid State Ionics* 135 (1-4): 305–313.

Sleiti, Ahmad K. 2010. “Performance of tubular Solid Oxide Fuel Cell at reduced temperature and cathode porosity.” *Journal of Power Sources* 195 (17): 5719–5725.

Smil, Vaclav. 1994. *Energy in world history*. Boulder, Colorado: Westview Press Inc.

———. 2005. *Creating the twentieth century. Technical innovations of 1867 - 1914 and their lasting impact*. 1st ed. New York: Oxford University Press Inc.

Smith, J. R., A. Chen, K. L. Duncan, M. E. Orazem, and E. D. Wachsman. 2006. “Evaluation of time constants governing the cathodic reaction in SOFCs.” *ECS Transactions* 1 (7): 243–253.

Snoeck, J.-W., and G. F. Froment. 2002. “Steam/CO_2 Reforming of Methane. Carbon Filament Formation by the Boudouard Reaction and Gasification by CO_2, by H_2, and by Steam: Kinetic Study.” *Industrial & Engineering Chemistry Research* 41:4252–4265.

Solomon, Susan, Dahe Qin, Martin Manning, Melinda Marquis, Kristen Averyt, Melinda M.B. Tignor, Henry LeRoy Miller Jr., and Zhenlin Chen. 2007, April. *Climate change 2007 - The Physical Science Basis. Contribution of Working Group I to the Fourth Assessment Report of the IPCC*. 1st. Cambridge, USA: Cambride University Press.

Steinberger-Wilckens, Robert. 2009, September. “An introduction to Fuel Cells - Status and applications of fuell cell technology - Competing technologies.” *6th International Large Solid Oxide Fuel Cell Summer School*. Ancona, Italy: University of Genova and Forschungszentrum Jülich, 52.

———. 2010, August. “Status and applications of SOFC technology.” *Academy School on Fuel Cell and Hydrogen 2010*. Roskilde, Danmark, 59.

Stemich, Carsten. 2006. “Theoretische und numerische Untersuchung des Strömungsmischens in einem T-förmigen Mikromischer.” PhDThesis (in German), Universität Paderborn.

Stenger, Sebastian. 2014, 09. “Konstruktion und Simulation eines SOFC-Systems mit Anodenabgasrezirkulation.” PhD thesis, Technische Universität Braunschweig.

Stiller, Christoph. 2006. Design, Operation and Control Modelling of SOFC/GT Hybrid Systems.

Storjohann, Daniel, James Daggett, Neal P. Sullivan, Huayang Zhu, Robert J. Kee, Sophie Menzer, and Dustin Beeaff. 2009. “Fabrication and evaluation of solid-oxide fuel cell anodes employing reaction-sintered yttria-stabilized zirconia.” *Journal of Power Sources* 193:706–712.

Sukeshini, A. Mary, Bahman Habibzadeh, Benjamin P. Becker, Chad A. Stoltz, Bryan W. Eichhorn, and Gregory S. Jackson. 2006. “Electrochemical Oxidation of H_2, CO, and COâH_2 Mixtures on Patterned Ni Anodes on YSZ Electrolytes.” *Journal of The Electrochemical Society* 153 (4): A705–A715.

Svensson, Ann Marl. 1998. “Mathematical Modeling of Oxygen Exchange and Transport in Ai r-Perovskite-YIf rio -Stabilized Zi rconia Interface Regions.” 145 (4): 1390–1400.

Tanaka, T., Y. Inui, A. Urata, and T. Kanno. 2007. “Three dimensional analysis of planar solid oxide fuel cell stack considering radiation.” *Energy Conversion and Management* 48 (5): 1491–1498 (05).

Tietz, Frank. 1999. “Thermal Expansion of SOFC Materials.” *Ionics* 5:129–139.

———. 2003. “Materials Selection for Solid Oxide Fuel Cells.” *Materials Science Forum* 426-432:4465–4470.

Tietz, Frank, Hans-Peter Buchkremer, and Detlev Stöver. 2002. “Components manufacturing for solid oxide fuel cells.” *Solid State Ionics* 152-153:373–381.

———. 2006. “10 years of materials research for solid oxide fuel cells at Forschungszentrum Jülich.” *Journal of Electroceramics* 17:701–707.

Tietz, Frank, Qingxi Fu, Vincent A. C. Haanappel, Andreas Mai, Norbert H. Menzler, and Sven Uhlenbruck. 2007. “Materials Development for Advanced Planar Solid Oxide Fuel Cells.” *International Journal of Applied Ceramic Technology* 4 (5): 436–445.

Tietz, Frank, V. A. C. Haanappel, Andreas Mai, J. Mertens, and Detlev Stöver. 2006. “Performance of LSCF cathodes in cell tests.” *Journal of Power Sources* 156 (1): 20–22.

Timilsina, Govinda R., and Ashish Shrestha. 2010. “How much hope should we have for biofuels?” *Energy* 36 (4): 2055–2069.

Timmermann, H., W. Sawady, R. Reimert, and E. Ivers-Tiffée. 2010. "Kinetics of (reversible) internal reforming of methane in solid oxide fuel cells under stationary and APU conditions." *Journal of Power Sources* 195:214–222.

Todd, B., and J. B. Young. 2002. "Thermodynamic and transport properties of gases for use in solid oxide fuel cell modelling." *Journal of Power Sources* 110 (1): 186–200.

Todt, Helge. 2011. "Konstruktion einer Hochtemperatur Brennstoffzelle." Project work (in German), Institut für Wärme- und Brennstofftechnik, Fakultät für Maschinenbau. Technische Universität Braunschweig.

Tomida, Kazuo, Tatsuo Kabata, Nagao Hisatome, Akihiro Yamashita, Hiroshi Tsukuda, Shigeru Ohkuma, and Toshiyasu Kiyabu. 2007. "Improvement of Tubular Type Cell Stack." *ECS Transactions* 7 (1): 173–180.

Torres-Garibay, Claudia, and Desiderio Kovar. 2009. "Perovskite-related intergrowth cathode materials with thin YSZ electrolytes for intermediate temperature solid oxide fuel cells." *Journal of Power Sources* 192:396–399.

Tucker, Michael C. 2010. "Progress in metal-supported solid oxide fuel cells: A review." *Journal of Power Sources* 195 (15): 4570–4582.

Tucker, Michael C., Lei Cheng, and Lutgard C. DeJonghe. 2011. "Selection of cathode contact materials for solid oxide fuel cells." *Journal of Power Sources* 196 (20): 8313–8322.

Tucker, Michael C., Grace Y. Lau, Craig P. Jacobson, Steven J. Visco, and Lutgard C. De Jonghe. 2010. "Cu-YSZ cermet solid oxide fuel cell anode prepared by high-temperature sintering." *Journal of Power Sources* 195 (10): 3119–3123.

Utz, A., K.V. Hansen, K. Norrman, Ellen Ivers-Tiffée, and Mogens Mogensen. 2011a. "Impurity features in Ni-YSZ-H2-H2O electrodes." *Solid State Ionics* 183 (1): 60–70.

Utz, A., A. Leonide, A. Weber, and E. Ivers-Tiffée. 2011b. "Studying the CO-CO_2 characteristics of SOFC anodes by means of patterned Ni anodes." *Journal of Power Sources* 196 (17): 7217–7224.

Valov, I., V. Rührup, R. Klein, T.-C. Rödel, A. Stork, S Berendts, M Dogan, H.-D. Wiemhöfer, M. Lerch, and J. Janek. 2009. "Ionic and electronic conductivity of nitrogen-doped YSZ single crystals." *Solid State Ionics* 180 (28-31): 1463–1470.

van Herle, Jan, Augustin J. McEvoy, and Ravindranathan Thampi. 1996. "A study on the $La_{1-x}Sr_xMoO_3$ oxygen cathode." *Electrochimica Acta* 41 (9): 1447–1454.

VDM, ThyssenKrupp. 2005. "Material Data Sheet No. 4046. Crofer 22 APU. High-temperature alloy." Technical Report, ThyssenKrupp Stainless.

———. 2010. Material Data Sheet No. 4046. Crofer 22 APU. High-temperature alloy.

Verein Deutscher Ingenieure, ed. 2006. *VDI-Wärmeatlas*. 10th ed. Springer (in German).

Vielstich, Wolf, Arnold Lamm, and Hubert A. Gasteiger, eds. 2003a. *Handbook of Fuel Cells. Volume 1. Fundamentials and Survey of Systems.* Fundamentials Technology and Applications. Chichester, UK: Wiley-VCH.

———, eds. 2003b, February. *Handbook of Fuel Cells. Volume 2. Electrocatalysis*. 1st ed. Volume 26 of *Fundamentials Technology and Applications*. Chichester, UK: Wiley-VCH.

Vogler, Marcel, Anja Bieberle-Hütter, Ludwig Gauckler, Jürgen Warnatz, and Wolfgang G. Bessler. 2009. "Modelling Study of Surface Reactions, Diffusion, and Spillover at a Ni/YSZ Patterned Anode." *Journal of The Electrochemical Society* 156 (5): B663.

Wachter, Armin, and Henning Hoeber. 1998. *Repetitorium Theoretische Physik*. Berlin, Heidelberg, New York: Springer (in German).

Wagner, Hermann-Josef. 2007. *Was sind die Energien des 21. Jahrhunderts?: Der Wettlauf um die Lagerstätten*. 2nd. Forum für Verantwortung (in German). Edited by Klaus Wiegandt. Frankfurt am Main: Fischer Taschenbuch Verlag.

Waldbillig, D., and O. Kesler. 2009. "Characterization of metal-supported axial injection plasma sprayed solid oxide fuel cells with aqueous suspension plasma sprayed electrolyte layers." *Journal of Power Sources* 191:320–329.

Wang, G., Y. Yang, H. Zhang, and W. Xia. 2007. "3-D model of thermo-fluid and electrochemical for planar SOFC." *Journal of Power Sources* 167:398–405.

Wang, K., D. Hissel, M.C. Péra, N. Steiner, D. Marra, M. Sorrentino, C. Pianese, M. Monteverde, P. Cardone, and J. Saarinen. 2011. "A Review on solid oxide fuel cell models." *International Journal of Hydrogen Energy* 36 (12): 7212–7228.

Wang, Songlin, Mingfei Liu, Yingchao Dong, Kui Xie, Xingqin Liu, and Guangyao Meng. 2008. "Influence of Cr deficiency on sintering character and properties of SOFC interconnect material $La_{0.7}Ca_{0.3}Cr_{1-x}O_{3-\delta}$." *Materials Research Bulletin* 43:2607–2616.

Wang, Xiaoge, Nobuyoshi Nakagawa, and Kunio Kato. 2001. "Anodic Polarization Related to the Ionic Conductivity of Zirconia at Ni-Zirconia/Zirconia Electrodes." *Journal of The Electrochemical Society* 148 (6): A565.

Wei, Junmei, and Enrique Iglesia. 2004. "Isotopic and kinetic assessment of the mechanism of reactions of CH_4 with CO_2 or H_2O to form synthesis gas and carbon on nickel catalysts." *Journal of Catalysis* 224 (2): 370–383 (June).

Wesemeyer, Christian, Yvonne Jocher, and Reinhard Leithner. 2011. "Numerical investigation of composition- and time- dependent properties of cermets used as anodes for solid oxide fuel cells." *Sixth M.I.T. Conference on Computational Fluid and Solid Mechanics*. Cambridge, USA.

Wesemeyer, Christian, and Reinhard Leithner. 2010. "Detailed CFD simulation of a SOFC." *Hydrogen and Fuel Cell Academy School on Fuel Cells and Hydrogen*. Roskilde, Denmark, 1.

Wilcox, David C. 1988. "Reassessment of the scale-determining equation for advanced turbulence models." *AIAA Journal* 26 (11): 1299–1310 (November).

Wilson, James R., Worawarit Kobsiriphat, Roberto Mendoza, Hsun-Yi Chen, Jon M. Hiller, Dean J. Miller, Katsuyo Thornton, Peter W. Voorhees, Stuart B. Adler, and Scott A. Barnett. 2006. "Three-dimensional reconstruction of a solid-oxide fuel-cell anode." *Nature materials* 5:541–544.

Winterfeld, P. H., L. E. Scriven, and H. T. Davis. 1981. "Percolation and conductivity of random two-dimensional composites." *Journal of Physics C: Solid State Physics* 14 (17): 2361–2376.

Woodside, Chris. 2011. "It isn't easy being green." *Nature Climate Change* 1 (1): 13–15 (March).

Xu, Jianguo, and Gilbert F Fromet. 1989a. "Methane Steam Reforming: II. Diffusional Limitations and Reactor Simulation." *AIChE Journal* 35 (1): 97–103.

———. 1989b. "Methane Steam Reforming, Methanation and Water-Gas Shift: I. Intrinsic Kinetics." *AIChE Journal* 35 (1): 88–96.

Xu, Sherman J., and William J. Thomson. 1999. "Oxygen permeation rates through ion-conducting perovskite membranes." *Chemical Engineering Science* 54 (17): 3839–3850.

Yakabe, H. 2001. "3-D model calculation for planar SOFC." *Journal of Power Sources* 102 (1-2): 144–154.

Yakabe, H., M. Hishinuma, M. Uratani, Y. Matsuzaki, and I. Yasuda. 2000. "Evaluation and modeling of performance of anode-supported solid oxide fuel cell." *Journal of Power Sources* 86 (1-2): 423–431 (March).

Yakabe, H., and T. Sakurai. 2004. "3D simulation on the current path in planar SOFCs." *Solid State Ionics* 174 (1-4): 295–302.

Yoshida, Shinya, Jun Matsunami, Yukitoshi Hosokawa, Osamu Yokota, Yutaka Tamaura, and Mitsunobu Kitamura. 1999. "Coal/CO_2 Gasification System Using Molten Carbonate Salt for Solar/Fossil Energy Hybridization." *Energy & Fuels* 13 (5): 961–964 (September).

Yuan, Kun, Yan Ji, and J N Chung. 2009. "Physics-based modeling of a low-temperature solid oxide fuel cell with consideration of microstructure and interfacial effects." *Journal of Power Sources* 194 (2): 908–919.

Yurkiv, V., D. Starukhin, H.-R. Volpp, and W. G. Bessler. 2011. "Elementary Reaction Kinetics of the CO/CO_2/Ni/YSZ Electrode." *Journal of The Electrochemical Society* 158 (1): B5–B10.

Zehe, Michael J., Sanford Gordon, and Bonnie J. Mcbride. 2002. "CAP: A Computer Code for Generating Tabular Thermodynamic Functions from NASA Lewis Coefficients." Technical Report February, Glenn Research Center, Cleveland, Ohio.

Zeidler, Conrad. 2010. "Entwurf und Optimierung eines Versorgungskonzepts für eine Wohnsiedlung in Kasachstan mit Strom und Wärme." Studienarbeit (in German), Institut für Wärme- und Brennstofftechnik, Fakultät für Maschinenbau, Technische Universität Braunschweig.

Zeng, Z., and K. Natesan. 2004. "Corrosion of metallic interconnects for SOFC in fuel gases." *Solid State Ionics* 167:9–16.

Zhan, Zhongliang, and Shung Ik Lee. 2010. "Thin film solid oxide fuel cells with copper cermet anodes." *Journal of Power Sources* 195 (11): 3494–3497.

Zhao, Feng, and Anil V. Virkar. 2010. "Effect of morphology and space charge on conduction through porous doped ceria." *Journal of Power Sources* 195 (19): 6268–6279.

Zhou, Xiaoliang, Peng Wang, Limin Liu, Kening Sun, Zhiqiang Gao, and Naiqing Zhang. 2009. "Improved electrical performance and sintering ability of the composite interconnect $La_{0.7}Ca_{0.3}CrO_{3-\delta}/Ce_{0.8}Nd_{0.2}O_{1.9}$ for solid oxide fuel cells." *Journal of Power Sources* 191:377–383.

Zhu, Huayang, Andrew M. Colclasure, Robert J. Kee, Yuanbo Lin, and Scott a. Barnett. 2006. "Anode barrier layers for tubular solid-oxide fuel cells with methane fuel streams." *Journal of Power Sources* 161 (1): 413–419 (October).

Zhu, Huayang, and Robert J. Kee. 2008. "Modeling Distributed Charge-Transfer Processes in SOFC Membrane Electrode Assemblies." *Journal of The Electrochemical Society* 155 (7): B715.

Zhu, Huayang, Robert J. Kee, Vinod M. Janardhanan, Olaf Deutschmann, and David G. Goodwin. 2005. "Modeling Elementary Heterogeneous Chemistry and Electrochemistry in Solid-Oxide Fuel Cells." *Journal of The Electrochemical Society* 152 (12): A2427.

Zhu, W. Z., and S. C. Deevi. 2003a. "A review on the status of anode materials for solid oxide fuel cells." *Materials Science and Engineering A* 362 (1-2): 228–239.

———. 2003b. "Development of interconnect materials for solid oxide fuel cells." *Materials Science and Engineering A* A348:227–243.